ABSTRACT

Title of dissertation: MAGNETIZED PLANE WAVE
AND STRIPE-ORDERED PHASES
IN SPIN-ORBIT-COUPLED BOSE GASES

Andika Putra, Doctor of Philosophy, 2018

Dissertation directed by: Professor Ian Spielman
National Institute of Standards and Technology and
Joint Quantum Institute, Department of Physics
at the University of Maryland

Quantum degenerate gases have provided rich systems to simulate engineered Hamiltonians and to explore quantum many-body problems in laboratory-scale experiments. In this work, I focus on spin-orbit-coupled (SOC) Bose-Einstein condensates (BECs) of Rubidium-87 atoms realized using two-photon Raman coupling in which various novel phases are predicted to exist due to competing energies from the atomic internal structure, coupling strength, and many-body collisions.

BECs are observed primarily using the interaction between light and matter, where it is common to probe the atoms with near-resonant light and image their shadow on a camera. This absorption imaging technique measures the integrated column density of the atoms and it is crucial to focus the imaging system. I present a systematic method to bring the ultracold atom systems into an optimal focus using the power

spectral density (PSD) of the atomic density-density correlation function. The spatial frequency at which the defocus-induced artifacts first appear in the PSD is maximized at the focus. The focusing process thus identifies the range of spatial frequencies over which the PSD is uncontaminated by finite-thickness effects.

Next, I describe magnetic phases which exist in spin-1 spin-orbit-coupled condensates at a near-zero temperature. I observe ferromagnetic and unmagnetized phases which are stabilized by the locking between the spin and linear momentum of the system. Our measurements of both the first- and second-order transitions are in agreement with theory.

Finally, I discuss the stripe-ordered phase that occurs in SOC Bose gases favoring the miscibility configuration. The stripe phase is theoretically predicted to have an excitation spectrum analogous to that of a supersolid and to exhibit spatial density modulation within specific regions of parameter space. I used optical Bragg scattering to probe the small density modulation present in the atomic spatial distribution. I present for the very first time observation of the stripe phase in a Raman SOC Bose gas and its phase diagram in various parameter space. Our observations of the phase boundaries are consistent with theory and previous work.

MAGNETIZED PLANE WAVE AND STRIPE-ORDERED PHASES IN SPIN-ORBIT-COUPLED BOSE GASES

by

Andika Putra

Dissertation submitted to the Faculty of the Graduate School of the
University of Maryland, College Park in partial fulfillment
of the requirements for the degree of
Doctor of Philosophy
2018

Advisory Committee:
Professor Steven Rolston, Chair
Professor Ian B. Spielman, Advisor
Professor Frederick C. Wellstood
Professor Gretchen K. Campbell
Professor Mohammad Hafezi

Preface

The first question I asked myself when I started writing this dissertation was: "Why do I even bother doing this?" And, of course, the obvious answer was to graduate soon and obtain my Ph.D.! Finally, I am seeing the light at the end of the tunnel?! However, in the process of putting my ideas into written words, I found this was harder than expected and I needed to do serious planning.

The next step for me was to *look up in the internet* (which has become the verb *Google* nowadays) and search for a good guideline for writing a doctoral thesis. Eventually, I stumbled upon an article by Patricia Gosling and Bart Noordam on "Mastering Your Ph.D.: Writing Your Doctoral Thesis With Style" [*Science* (2007), `DOI: 10.1126/science.caredit.a0700183`] and decided to stick with it. I found this article to be very helpful and I would like to share it with my readers. One of the many reasons you might be reading this thesis is because you are in the process of writing your own thesis. If that is the case, congratulations and good luck!

To quote from the article: *"In a thesis, it is better to err on the side of being too detailed than to risk leaving out crucial information. Be generous to the next generation of researchers; a detailed description of your progress and failures will*

save them a lot of time." This gave me a sense of purpose in writing and helped me answer the question "Why do I even bother doing this?"

Last but not least, I would like to mention Chapter 4 and 6 in this dissertation are from previously published works: "Putra, A. et al., Optimally focused cold atom systems obtained using density-density correlations. *Review of Scientific Instruments* **85**, 013110 (2014)," and "Campbell, D. L. et al., Magnetic phases of spin-1 spin-orbit-coupled Bose gases. *Nature Communications* **7**, 10897 (2016)." The former published paper on optimally focused cold atom systems was a result of my research project as a requirement for advancement to doctoral candidacy. The latter paper was a Ph.D. research project led by a senior grad student, Dan Campbell. Both published articles have a Creative Commons (CC) license, which grants people the rights to share the articles with proper citation. I acknowledge Dan for responding my email and giving me permission to include his published paper in this dissertation.

As final words, I hope I did a decent job here and happy reading!

For my mother and
in the memory of my father

Acknowledgements

The very first person I would like to thank here is Dr. Ian Spielman for being such an "*awesome*" awesome[1] advisor. I express my gratitude for his guidance and support throughout research in my graduate school.

My first chapter in doing research work was spent in `RbLi` lab at UMD. I would like to thank the lab members Daniel Campbell, Ryan Price, and Ana Valdés-Curiel for all the good and bad times we spent together in the lab. They helped me grow as a person and without them this work would not have been possible.

I also thank my neighboring lab members at UMD: Varun Vaidya, Creston Herold, Jiraphat Tiamsuphat, Sean Xiao Li, Daniel Barker, Ben Reschovsky, Neal Pisenti, Matt Reed, Zach Smith, Aftaab Dewan for letting me borrow (or steal) their equipment (or the other way around). Besides, I really appreciate the exchange of ideas during our interaction times as well.

The next half of my research work was spent in the `RbChip` lab at NIST. I thank Francisco "Paco" Salces-Cárcoba for being the best labmate and soccer buddy (if I have to choose one); Seiji Sugawa, the awesome post-doc who moved out last year, for maintaining the experiment in top condition and for developing many pieces of the

[1]Yes, this is not a typo. The word "awesome" is overused and underrated, and hence I would like to emphasize the awesomeness by squaring it!

lab software (the magnetic field control system is beyond amazing!); Abigail Perry, a previous grad student, for building the original experimental apparatus. One thing I almost forgot which Paco reminded me is Seiji's famous quote: "*Everyday is Friday!*". Also, I want to thank Yuchen Yue, the latest grad student who picked up the baton of `RbChip` lab; Chris Billington, a master Python programmer; and Emine Altuntaş, a newly-minted Ph.D. who just joined our lab. I wish all of you many successes.

I also acknowledge the `RbK` people next door at NIST: Dina Genkina, Hsin-I Lu, Ming Wu Lu, Lauren Aycock, and Alina Escalera, for supplying me with readily available lab equipment. On the contrary, the bias field from your Zeeman slower while in operation is a real annoyance! Somehow, we managed to conduct our experiments with little to no problem (Seiji and Hsin-I knew this better...).

My last two years working at NIST were energized by playing pick-up soccer. I don't think I can list all of the names here because there are a lot of people and some of them go by initials. Nevertheless, particular thanks go to Richard "Dick" Gates for organizing it three times a week in all types of weather and all four seasons.

I would like to express my gratitude to my previous roommates and physicist friends: David Green for his two lovely cats (one sadly now resting in peace); Matthew Reed (and his best companion Rufus) for organizing and teaching Hapkido; Jonathan Hoffman for his spontaneous laughters; Kristen Voigt for being the best "*Mafia*"; Brian Calvert for being the cool particle physicist; Eric Kuo, Anjor Kanekar, and Rangga Budoyo for the fun times playing "*Seven Wonders*". Special thanks go to Rangga for drawing me into the world of "*Dark Souls*".

I would also thank other grad students who arrived at UMD the same year as me: Jake Smith, Cody Ballard, Kale Johnson, Jasper Drisko. I wish them the best of luck in their future endeavors.

I thank my roommates during my stay at NIST: Chandra Shahi, Chen Zhe, Claudia Salazar, Andy Cheong Tam, and Hasan Latief for providing supporting environments. My special appreciation goes to Jeremy Lee for being a responsive landlord.

Next, I want to thank Edwin Sucipto, Freddy Witarsa, Nicholas Kuo, and Pak Andang Purnama for providing vibrant Indonesian communities in College Park area.

My personal recognition goes to my previous teachers who had gradually shaped my knowledge in physics: Suhunan Nainggolan, Manaek Nababan, Yohanes Surya, Rachmat Widodo Adi, Alexander Iskandar, and Tjia May On, to mention but a few.

Many thanks go to Steve Rolston, Fred Wellstood, Gretchen Campbell, and Mohammad Hafezi for agreeing to be in my dissertation committee. I would also thank Gail Griffin-Ferris, Kim Emswiler, Jesse Anderson, Melissa Britton, Kelly Hickman, Pauline Rirksopa, Paulina Alejandro, Jane Hessing, Jessica Crosby, Peter Shawhan, Linda O'Hara and the staff both at JQI and NIST for their administrative supports. They have made my time in graduate school very smooth.

Lastly, I would like to thank my family: my parents, Suwardi and Hou Lie Tjhing; my elder brother, Adi Putra; and my younger sister, Ayu Anggreni. I express my gratitude for their constant support and tremendous patience with me while I was finishing graduate school, despite them having little ideas of what I am doing.

Contents

List of Tables

List of Figures

List of Abbreviations

The following table explains the abbreviations used throughout this dissertation.

Abbreviation	Full meaning
AC, ac	alternating current
ACF	auto-correlation function
AOM	acousto-optic modulator
ARP	adiabatic rapid passage
BCS	Bardeen-Cooper-Schrieffer
BEC	Bose-Einstein condensate
BL	Beer-Lambert
BRF	birefringent filter
CCD	charge-coupled device
CMOS	complementary metal-oxide-semiconductor
CW, cw	continuous-wave
DC, dc	direct current
DDS	direct-digital-synthesized
EFL, efl	effective focal length
EMCCD	electron-multiplying charge-coupled device
FPGA	field-programmable gate array
FWHM	full-width at half maximum
GPE	Gross-Pitaevskii equation
HDD	hard-disk-drive
LIAD	light-induced atom desorption
MOT	magneto-optical trap
OD	optical depth
PID	proportional-integral-derivative
PLL	phase-locked loop
PSD	power spectral density

Abbreviation	Full meaning
PTAI	partial-transfer absorption imaging
RF, rf	radio frequency
RHS, rhs	right-hand side
RMS, rms	root-mean-square
ROI	region-of-interest
RWA	rotating-wave approximation
SOC	spin-orbit-coupled
SSFM	split-step Fourier method
TEC	thermoelectric cooler
TF	Thomas-Fermi
TOF	time-of-flight
TTL	transistor-transistor logic
UHV	ultra-high vacuum
UV	ultraviolet
1D	one-dimensional
2D	two-dimensional
3D	three-dimensional

List of Scientific Constants

The following table shows the physical and mathematical constants used throughout this dissertation [121].

Symbol	Quantity	Numerical value	Unit
c	speed of light in vacuum	299 792 458	$\mathrm{m\ s^{-1}}$
μ_0	magnetic constant	$4\pi \times 10^{-7}$	$\mathrm{N\ A^{-2}}$
ϵ_0	electric constant $1/\mu_0 c^2$	$8.854\,187\,817\ldots \times 10^{-12}$	$\mathrm{F\ m^{-1}}$
h	Planck constant	$6.626\,070\,040\,(81) \times 10^{-34}$	J s
$\hbar$	reduced Planck constant $h/2\pi$	$1.054\,571\,800\,(13) \times 10^{-34}$	J s
e	elementary charge	$1.602\,176\,6208\,(98) \times 10^{-19}$	C
a_B	Bohr radius	$0.529\,177\,210\,67(12) \times 10^{-10}$	m
μ_B	Bohr magneton $e\hbar/2m_e$	$927.400\,9994\,(57) \times 10^{-26}$	$\mathrm{J\ T^{-1}}$
m_e	electron mass	$9.109\,383\,56\,(11) \times 10^{-31}$	kg
m_p	proton mass	$1.672\,621\,898\,(21) \times 10^{-27}$	kg
μ_N	nuclear magneton	$5.050\,783\,699\,(31) \times 10^{-27}$	$\mathrm{J\ T^{-1}}$
k_B	Boltzmann constant	$1.380\,648\,52\,(79) \times 10^{-23}$	$\mathrm{J\ K^{-1}}$
i	unit imaginary number	$\sqrt{-1}$	
e	Euler's number	$2.718\,281\,828\,459\,045\ldots$	
π	pi, Archimedes' constant	$3.141\,592\,653\,589\,793\ldots$	

CHAPTER 1

Introduction

The quest to understand the nature of light and matter has long been at the very core of physics. For example, efforts to understand the spectrum of electromagnetic radiation emitted by a "blackbody" object led to the discovery of Planck's constant, the conception of spontaneous and stimulated emission, and the quantization of light. These pursuits eventually revolutionized the theory of statistical mechanics and led to the birth of quantum mechanics.

In 1924, Satyendra Nath Bose developed the theory of the statistical mechanics of photons which allowed a theoretical derivation of Planck's law. Bose sent his work to Albert Einstein who realized the import of it and supported Bose's ideas, leading to the formulation of a new class of particles that obeyed Bose-Einstein statistics [132]. Such particles are named bosons and they have integer values of total spin. Bose predicted that a collection of such non-interacting particles can occupy the same state and most of the particles will "condense" into the lowest accessible quantum state at nearly zero temperature, which was known as Bose-Einstein condensation.

Evidence for Bose-Einstein condensate (BEC) was first linked to the observed superfluid properties in helium-4 below the temperature 2.17 K at 1 atm (below the lambda point) [105]. However, due to the strong atomic interactions in ^{4}He,

the original BEC theory must be modified in order to describe the emergence of superfluidity [132]. It was not until 1995 that a nearly pure condensate was observed in a dilute vapor of rubidium-87 atomic gases [7], and separately in sodium-23 atoms [38], where the measured occupancy number of bosons in the ground-state provided a direct evidence for BEC.

Since then, advances in technology have enabled the BEC state to be observed in many more isotopes and particles at temperatures from 10 to 100 nK [31, 56, 65, 146]. These quantum degenerate gases have provided rich systems to simulate engineered Hamiltonians and to explore quantum many-body problems in laboratory-scale experiments, which serve as benchmarks to validate or eliminate theoretical models. Experimental observations of various quantum many-body phenomena include the superfluid-Mott insulator transition in the Bose-Hubbard model [58], condensation of fermionic atom pairs in the BCS-BEC crossover regime [145], and antiferromagnetic correlations in the Hubbard model [65], to mention but a few.

In my research, I was interested in studying spin-orbit-coupled (SOC) BECs of ^{87}Rb atoms. The spin-orbit coupling scheme used counter-propagating lasers to induce two-photon Raman transitions between different spin states of the atoms, causing spin angular momentum of the atoms being locked to their linear momentum [102, 103]. In this scheme, I was able to control the detuning δ between coupled spin states by changing the Raman laser frequencies, and I could tune the coupling strength Ω by varying the laser intensities. In this system, due to competing energies between the many-body interaction and single-particle Hamiltonian, it was

predicted that there exist three different phases: the stripe-ordered phase, the magnetized plane-wave phase, and the unmagnetized zero-momentum phase [69, 98]. In this dissertation, I present my observations of these phases.

In particular, I experimentally explored the magnetic phases present in spin-1 SOC condensates [22, 90]. This system exhibits magnetized and unmagnetized phases in two-dimensional (2D) parameter space. The behavior is mainly governed by the single-particle Hamiltonian. Phase transitions between the magnetic phases are well-described by the Landau phenomenological theory [129]. Across one dimension of the 2D parameter space, the free energy dispersion of the SOC condensates has three local minima (with two of them being degenerate), which becomes a single global minimum exhibiting a first-order phase transition. Meanwhile, along the other parameter space, the free energy dispersion has two degenerate local minima which eventually merge into a single minimum, displaying a second-order phase transition.

In SOC Bose gases, where two-body collisions within the $s-$wave approximation favor miscibility [177], there exists a stripe-ordered phase in the ground state of the many-body Hamiltonian within certain regions of parameter space [69, 98]. The stripe phase has drawn interests because it has properties that are analogous to supersolidity. Specifically, the excitation spectrum of the mean-field energy exhibit a roton-maxon like feature [97, 109]. This roton-maxon character has recently been observed by Ji et al. [79] for the magnetized phase, where the roton-mode is softening near the transition to the stripe phase, in agreement with theoretical calculations.

Another important feature of the stripe phase is the existence of density modulations. For typical SOC ^{87}Rb atoms realized in the Raman coupling scheme, direct observations of these density modulations in the ground state have proven challenging for various reasons [108]. The spatial periodicity of the density modulation is relatively small, on the order of $0.4\,\mu$m, which is beyond the resolution of most imaging systems. Besides, the density contrast is predicted to be less than 5% and experimental observation requires a precise control of the magnetic field, within $10\,\mu$G.

The main objective of my Ph.D. research was to observe the long-sought stripe-ordered phase experimentally. To overcome the above challenges, I first prepared the atoms in an equal population of mixed states since the stripe phase favors miscibility. I then loaded the spinor condensates into the SOC dressed states and let the system evolved into the metastable states, which gave a detectable region of the stripe phase. I used optical Bragg scattering [17, 174] and a high-sensitivity camera to detect the scattered photons by the very small density modulation of the stripe phase. I also implemented a combined feedforward plus feedback control system to compensate for magnetic field drift.

Although there have been many efforts to enhance the stripe phase, at present there is only one experimental group that has managed to directly observe the density modulation of the stripe phase. The stripe-ordered phase was first detected by Jun-Ru Li et al. [95] in SOC Bose gases. They realized a spin-orbit coupling scheme using a

"superlattice" [1] potential [4, 5, 96], where the interaction strength between spin states can be artificially tuned to enlarge the region of the stripe phase. Unfortunately, in their work, the presence of the density modulation was only observed in a narrow region of coupling strength Ω. It was not obvious that the density modulation existed within the predicted 2D parameter space of the SOC system and their observations do not provide clear signatures of the phase boundaries of the stripe phase.

In this work, I present my observations of the stripe phase over a range of parameters in the phase diagram. I first investigated the stripe phase in the parameter space of coupling strength and detuning (Ω, δ). My results were in agreement with theoretical predictions [69, 98] and previous measurements [95, 103]. I explored the stripe phase for various hold times t_{hold} and studied the metastability condition of the system [103]. I observed the scattered Bragg signal in the stripe phase to be decaying with a time constant of about $0.1 - 1\,\text{s}$, supporting arguments that the stripe phase formation was due to a many-body spin-dependent interaction. To confirm the long-range phase coherence of the stripe phase, I did a time revival scan of the observed Bragg signal using Talbot interferometry [120, 150]. Finally, I examined the finite-temperature phase diagram of the stripe-ordered phase as a function of coupling strength and temperature (Ω, T). My observation in the (Ω, T) space had a profile consistent with previous theoretical and experimental reports [28, 78, 178].

[1] The superlattice potential was created by superimposing two standing waves (lasers), with one laser wavelength λ_1 was an integer multiple of the other $n\lambda_2 = \lambda_1$. This resulted in a spatially periodic staggered (double-well if $n = 2$) potential.

1.1. Overview of the dissertation

Chapter 2 describes the essential part of the theory of atomic physics related to this work. First, I give an overview of atomic structure, laser cooling and trapping techniques used to achieve BECs. Next, I discuss the properties of BECs within the mean-field Gross-Pitaevskii equation (GPE) and stationary solutions of the wave-function within the Thomas-Fermi approximation. I also discuss a set of coupled GPEs governing spinor BECs and atomic physics nomenclature associated with such system, particularly for multi-component BECs in the $F = 1$ hyperfine manifold of the $5\mathcal{S}_{1/2}$ electronic ground states of ^{87}Rb atoms.

Chapter 3 describes the setup and apparatus for my experiments. I discuss the hardware I used and the experimental sequences to produce ^{87}Rb BECs. I also discuss the control of magnetic field in our laboratory, including the calibration of the field, its measurement, and the feedback control to compensate for ambient field drift, which is important in the detection of the stripe phase.

Chapter 4 describes the technique I used to optimally focus cold atoms systems using the power spectral density of the atomic density-density correlations. This technique is especially useful in finding the optimal focus of time-of-flight absorption imaging, which requires no hardware changes and minimum computational effort. This chapter is taken from previous published paper [140]: "Putra, A. et al. Optimally focused cold atoms systems obtained using density-density correlations. *Review of Scientific Instruments* **85**, 013110 (2014)."

Chapter 5 describes coherent manipulation of atoms with electromagnetic waves. This chapter covers the method I used to prepare different mixtures of the spinor $F = 1$ Bose gases using a radio frequency (RF) source. I discuss the microwave-assisted partial-transfer absorption imaging technique we used to provide feedback for our dc magnetic field control. I also review the ac-Stark effect within the framework of perturbation theory. Lastly, I discuss how I used the vectorial light shift to realize various engineered Hamiltonians in our systems, along with the accompanying calibration techniques.

Chapter 6 describes observations of magnetic phases of spin-1 SOC Bose gases. I discuss the experimental setup to realize the spin-1 SOC system and its corresponding Hamiltonian. I present our measurements of the first- and second-order phase transitions between a polar BEC and a ferromagnetic BEC. This chapter is from Ref. [22]: "Campbell, D. L., et al., Magnetic phases of spin-1 spin-orbit-coupled Bose gases, *Nature Communications* **7**, 10897 (2016)."

Chapter 7 describes the optical Bragg scattering technique I used to probe atomic structure. I start by considering the theory of optical Bragg scattering and its relation to condensed matter physics and crystallography. I then discuss the geometrical properties of the Bragg signal, including the incidence angle dependence, beam waist of the probe, and the angular spread of the scattered Bragg signal. Finally, I present measurement results of optical Bragg scattering from density modulation in one-dimensional lattice and precessing spin in SOC condensates.

Chapter 8 describes my observations of stripe-ordered phase in spin-1/2 SOC condensates. I first present theoretical background of the stripe-ordered phase within mean-field theory. Next, I briefly discuss the experimental setup and sequences I used to create and observe the stripe phase. Ultimately, I demonstrate the observations of stripe phase in various parameter space and display the phase diagram.

Finally in chapter 9, I conclude with a summary of my main results and discuss prospects for future investigations.

CHAPTER 2

Bose-Einstein condensation in laser cooled rubidium-87 atoms

In this chapter, I review the essential theory of atom-light interactions, laser cooling and trapping techniques to achieve Bose-Einstein condensation (BEC). First, I discuss the important points related to the atomic structure, hyperfine levels, and optical transition selection rules within the dipole approximation. Next, I give a brief summary on laser cooling and evaporative cooling techniques that I used to produce BECs. Finally, I discuss the properties of BECs within the mean-field theory.

2.1. Interaction of atoms with the electromagnetic field

2.1.1. Atomic structure and notation. An electron moving in a spherically symmetric potential has coordinates (r, ϑ, φ) and energy E. Canonical quantization of these variables leads to conserved observables associated with discrete quantum numbers [19]:

$$\begin{aligned} r, E &\rightarrow n = 1, 2, 3, \ldots \infty && \text{(principal quantum number)} \\ \vartheta &\rightarrow l = 0, 1, 2, \ldots (n-1) && \text{(orbital quantum number)} \\ \varphi &\rightarrow m_l = 0, \pm 1, \pm 2, \ldots \pm l && \text{(magnetic quantum number)} \end{aligned}$$

In addition, the electron has an intrinsic spin of $s = \pm 1/2$. These four quantum numbers are used to describe single electron configurations in central potentials.

The above single-electron description can be expanded to describe electronic configuration of an atomic system with many electrons. In general, the electrons are arranged in closed and open shells, and the low energy atomic spectroscopic properties are determined by the outer electrons in an open shell. For the outer electrons, the total orbital angular momentum of the partially filled subshells are designated by the convention $\mathbf{L} = \sum \mathbf{l}_i$, the total spin is described by $\mathbf{S} = \sum \mathbf{s}_i$, and the total angular momentum is $\mathbf{J} = \mathbf{L} + \mathbf{S}$. The eigenvalues of the angular momentum operators are always positive or zero, and they are designated by capital letters L, S, and J. As an example, a helium atom with two electrons can have two configurations: $S = 0$ (singlet) and $S = 1$ (triplet). In alkali atoms, there is a single electron in the outer shell ($s = 1/2$) and consequently the angular momentum operators are often written in lowercase letters $\mathbf{l},\ \mathbf{s},\ \mathbf{j} = \mathbf{l} + \mathbf{s}$ [107].

The spectroscopic notation I use in this work has the form:

$$n^{2S+1}L_J \tag{2.1}$$

In this notation, the L quantum number is represented by its corresponding alphabetic character where integer values of $L = 0, 1, 2, 3, 4, 5, 6,$ etc. are denoted by $\mathcal{S}, \mathcal{P}, \mathcal{D}, \mathcal{F}, \mathcal{G}, \mathcal{H}, \mathcal{I},$ etc.[1] For alkali metals with a single outer electron, the factor $2S + 1 = 2$ is often dropped for brevity.

[1]Due to historical reason in atomic spectroscopy, the first 4 letters stand for descriptors of lines in alkali spectra: *sharp, principal, diffuse, fundamental.* The rest of the letters are continuation of alphabetical order [163].

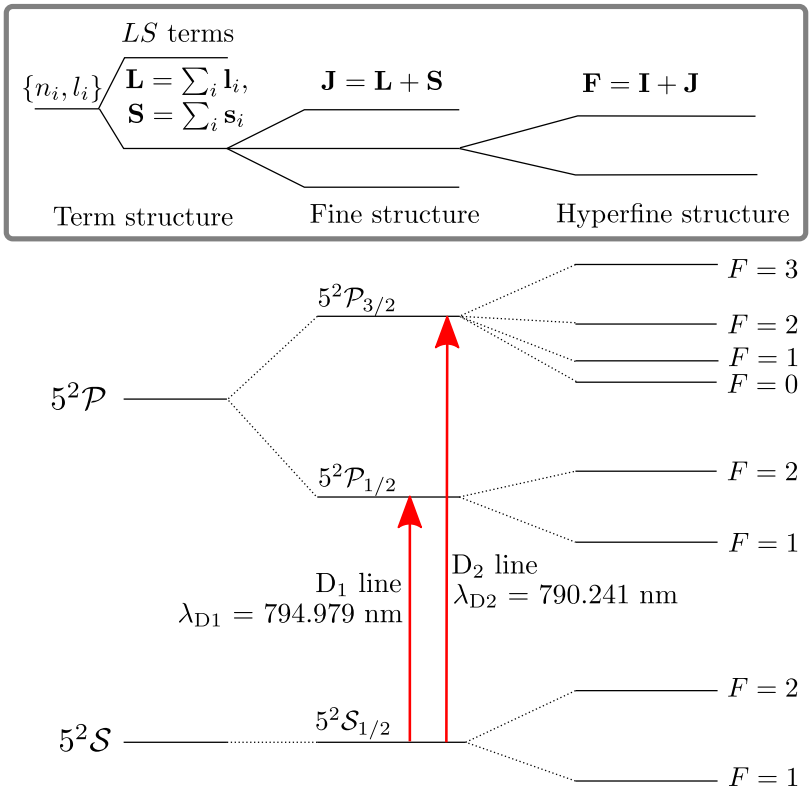

FIGURE 2.1. Atomic structure of ^{87}Rb atoms.

The spin-orbit interaction between the electron spin **S** and the orbital angular momentum **L** gives rise to the *fine structure* with total angular momentum **J**. Incorporating the spin of the nucleus, the coupling between the nuclear spin **I** and effective magnetic field due to the orbiting electron splits the energy levels further into *hyperfine structure*. This gives the total angular momentum $\mathbf{F} = \mathbf{I} + \mathbf{J}$ with quantum numbers F which describe the hyperfine splitting.

An example of the resulting atomic structure is given in Fig. 2.1. Here I consider a ^{87}Rb atom, the alkali species I used in my ultracold atom experiments, which has nuclear spin $I = 3/2$ [162]. The electronic ground state in ^{87}Rb has quantum numbers $L = 0$ and $J = 1/2$. Its first excited state with $L = 1$ is split into two energy levels

with $J = 1/2$ and $J = 3/2$. The transitions between the ground state and the two lowest excited states are labelled as the D_1 line for the $5\mathcal{S}_{1/2} \rightarrow 5\mathcal{P}_{1/2}$ transition and the D_2 line for the $5\mathcal{S}_{1/2} \rightarrow 5\mathcal{P}_{3/2}$ transition. These two separate D−line components have transition wavelengths $\lambda_{D1} = 794.979\,\text{nm}$ and $\lambda_{D2} = 790.241\,\text{nm}$, respectively, which are resolvable by commercial diode lasers.

2.1.2. Hyperfine structure. Hyperfine splitting due to interaction between the nucleus and electrons can be calculated using perturbation theory in terms of multipole expansion of the field potentials. However, the formulation of this theory is quite involved. A summary of the hyperfine calculation based on Ref. [151] is given below.

I assume the nucleus as a point source and I consider an observation point outside the nuclear matter in a spherical coordinate (r, θ, φ). The electrostatic potential V and the magnetic vector potential $\mathbf{A}$ set up by the nuclear charges, currents, and spins can be written as

$$V = \sum_{k=0}^{\infty} r^{-k-1} \mathbf{C}^{(k)} \cdot \mathbf{Q}^{(k)}, \tag{2.2}$$

$$\mathbf{A} = \sum_{k=0}^{\infty} \frac{-\mathrm{i}}{k} r^{-k-1} \left(-\mathrm{i}\mathbf{r} \times \nabla \mathbf{C}^{(k)}\right) \cdot \mathbf{M}^{(k)}, \tag{2.3}$$

where the functions $\mathbf{C}^{(k)}$ are spherical tensor operators of rank k with parity $(-1)^k$, $\mathbf{Q}^{(k)}$ are tensor operators for the electric multipole moments $Q_\mu^{(k)}$, and $\mathbf{M}^{(k)}$ are tensor operators for the magnetic multipole moments $M_\mu^{(k)}$. The scalar product of two

spherical tensor operators of rank k are defined as

$$\mathbf{T}^{(k)} \cdot \mathbf{U}^{(k)} = \sum_{\mu=-k}^{k} (-1)^{\mu} T_{\mu}^{(k)} \cdot U_{-\mu}^{(k)}. \tag{2.4}$$

The components of the spherical tensor $\mathbf{C}^{(k)}$ are given by

$$C_{\mu}^{(k)}(\theta, \varphi) = \sqrt{\frac{4\pi}{2k+1}}\, Y_{k}^{\mu}(\theta, \varphi), \tag{2.5}$$

where $Y_{k}^{\mu}(\theta, \varphi)$ are the spherical harmonics.

The nuclear electric and magnetic multipole moments of order k in Eqs. 2.2-2.3 can be expressed in terms of the spherical components $C_{\mu}^{(k)}(\theta, \varphi)$:

$$Q_{\mu}^{(k)} = e \int \Psi^{*}\, g_{l}^{\mathrm{nuc}} r^{k} C_{\mu}^{(k)}(\theta, \varphi)\ \Psi\ \mathrm{d}^{3}r, \tag{2.6}$$

$$M_{\mu}^{(k)} = \mu_{N} \int \Psi^{*}\ \left[\nabla r^{k} C_{\mu}^{(k)}(\theta, \varphi)\right] \cdot \left(g_{l}^{\mathrm{nuc}} \frac{2}{k+1} \mathbf{L}^{\mathrm{nuc}} + g_{s}^{\mathrm{nuc}} \mathbf{S}^{\mathrm{nuc}} \right)\ \Psi\ \mathrm{d}^{3}r, \tag{2.7}$$

where Ψ is the nucleus wavefunction, and μ_N is the nuclear magneton. The nucleus orbital angular momentum operator $\mathbf{L}^{\mathrm{nuc}}$ and its g-factor g_{l}^{nuc} are defined by the summation over the orbital angular momentum of each nucleon $\mathbf{L}_i$:

$$2 g_{l}^{\mathrm{nuc}} \mu_{N} \mathbf{L}^{\mathrm{nuc}} = \sum_{i=1}^{A} g_{li} \frac{e\hbar}{m_{i}c} \mathbf{L}_{i}, \tag{2.8}$$

where m_i is the mass of the i-th nucleon (either the mass of a proton or a neutron), A is the number of nucleons, and g_{li} are the orbital g-factors ($g_{li} = 1$ for a proton, and $g_{li} = 0$ for a neutron). The nucleus spin operator $\mathbf{S}^{\mathrm{nuc}}$ and its g-factor g_{s}^{nuc} are

defined by the summation over the spin of each nucleon $\mathbf{S}_i$:

$$g_s^{\mathrm{nuc}}\mu_N\mathbf{S}^{\mathrm{nuc}} = \sum_{i=1}^{A} g_{si}\frac{e\hbar}{2m_i c}\mathbf{S}_i, \tag{2.9}$$

where g_{si} are the spin g-factors ($g_{si} = 5.5857$ for a proton, and $g_{si} = -3.826$ for a neutron) [151] .

The interaction of a single electron with the nuclear potentials can be described by the relativistic Dirac equation [151, 152]. Solutions of the interaction Hamiltonian in the multipole series lead to several energy shifts in the atomic structure [163]. The $k = 0$ monopole term leads to the fine-structure of the atoms. The $k = 1$ magnetic-dipole term and the $k = 2$ electric-quadrupole term leads to the hyperfine Hamiltonian

$$H_{\mathrm{hfs}} = A_{\mathrm{hf}}\frac{\mathbf{I}\cdot\mathbf{J}}{\hbar^2} + B_{\mathrm{hf}}\frac{\frac{3}{\hbar^4}(\mathbf{I}\cdot\mathbf{J})^2 + \frac{3}{2\hbar^2}(\mathbf{I}\cdot\mathbf{J}) - I(I+1)J(J+1)}{2I(2I-1)J(2J-1)}, \tag{2.10}$$

with A_{hf} is the magnetic-dipole hyperfine constant (applicable for $I, J > 0$) and B_{hf} is the electric-quadrupole hyperfine constant (applicable for $I, J > 1/2$). Higher order expansion terms are generally omitted since they are very small and difficult to observe in alkali atoms.

In the presence of an external static magnetic field $\mathbf{B}$ along the $z-$direction, there is an additional Hamiltonian

$$H_B = -(\vec{\mu}_L + \vec{\mu}_S + \vec{\mu}_I)\cdot\mathbf{B} = \frac{\mu_B}{\hbar}(g_L L_z + g_S S_z + g_I I_z)B_z, \tag{2.11}$$

where g_L, g_S, and g_I are respectively the electron orbital, electron spin, and nuclear "$g-$factors" which account for their corresponding magnetic dipole moments $\vec{\mu}_L, \vec{\mu}_S$, and $\vec{\mu}_I$. In Eq. 2.11 we have followed the convention that the signs of the $g-$factors are opposite to the signs of the associated magnetic moments $\vec{\mu}$ [8]. For alkali atoms, the magnetic field contribution to the hyperfine structure splitting is typically small compared to the fine-structure splitting, which allows us to describe the interaction Hamiltonian H_B in terms of the good quantum number J of the electrons' total angular momentum

$$H_B = \frac{\mu_B}{\hbar} \left(g_J J_z + g_I I_z \right) B_z. \tag{2.12}$$

In order to calculate the hyperfine energy structure, one must diagonalize the total Hamiltonian $H_{\text{tot}} = H_{\text{hfs}} + H_B$, as given by Eqs. 2.10-2.12 (see Appendix A for the derivation of matrix elements of the total Hamiltonian H_{tot}). In general, the degeneracy in each hyperfine manifold is lifted by the magnetic field and the eigenstates become superpositions of the $|J, m_J, I, m_I\rangle$ basis states.[2] For a very weak magnetic field, the interaction Hamiltonian H_B can be treated as a perturbation to the hyperfine Hamiltonian H_{hfs} and the basis states $|F, m_F; I, m_I\rangle$ closely describe the eigenstates of the system. The energy shift in this weak field regime is also known as the "linear Zeeman effect" with (F, m_F) being the good quantum numbers. For very large magnetic field, where H_B dominates H_{hfs}, the basis states $|J, m_J, I, m_I\rangle$ closely describe the eigenstates of the total Hamiltonian. The energy shift in this regime is

[2]Other choices of basis states are $|F, m_F; I, m_I\rangle$ and $|F, m_F; J, m_J\rangle$ since $\mathbf{F}$ is the summation of the angular momentum operators $\mathbf{I}$ and $\mathbf{J}$.

called the "Paschen-Back effect" and (m_J, m_I) are the good quantum numbers. In the regime of intermediate magnetic fields, the eigenstates of the total Hamiltonian H_{tot} are mixtures of the basis states $|J, m_J, I, m_I\rangle$. The energy shift in this intermediate regime is called the "incomplete Paschen-Back effect" and m_F are the remaining good quantum numbers.

The hyperfine structure of ^{87}Rb in the presence of a magnetic field is shown in Fig. 2.2. Here, I consider the $5\mathcal{S}_{1/2}$ ground-state level and $5\mathcal{P}_{3/2}$ excited level of the D_2 transition. Figure 2.2 shows the hyperfine energy levels $\Delta E/h$ for magnetic field $B < 500\,\text{G}$, typical values used in our laboratories. For the values of magnetic field being considered, the energy shifts of the $5\mathcal{S}_{1/2}$ level is within the linear Zeeman effect regime, as shown in Fig. 2.2(a). Meanwhile, the energy shifts of the $5\mathcal{P}_{3/2}$ level span the whole range of the linear Zeeman effect to the Paschen-Back effect, as shown in Fig. 2.2(b).

2.1.3. Dipole matrix elements. In the dipole approximation, electromagnetic radiation with wavelength λ is assumed to have a negligible variation over the spatial extent r_{atom} of a single atom, i.e. $\lambda \gg r_{\text{atom}}$. In this limit, the interaction between an atom and a photon is given by the Hamiltonian

$$H_{\text{dip}} = -\mathbf{d} \cdot \mathbf{E} = -e\mathbf{r} \cdot E\hat{\epsilon}, \tag{2.13}$$

with the dipole moment $\mathbf{d} = e\mathbf{r}$ and electric field $\mathbf{E} = E\hat{\epsilon}$. Since the atomic wavefunctions Ψ are written in terms of the angular momentum basis states, which transform

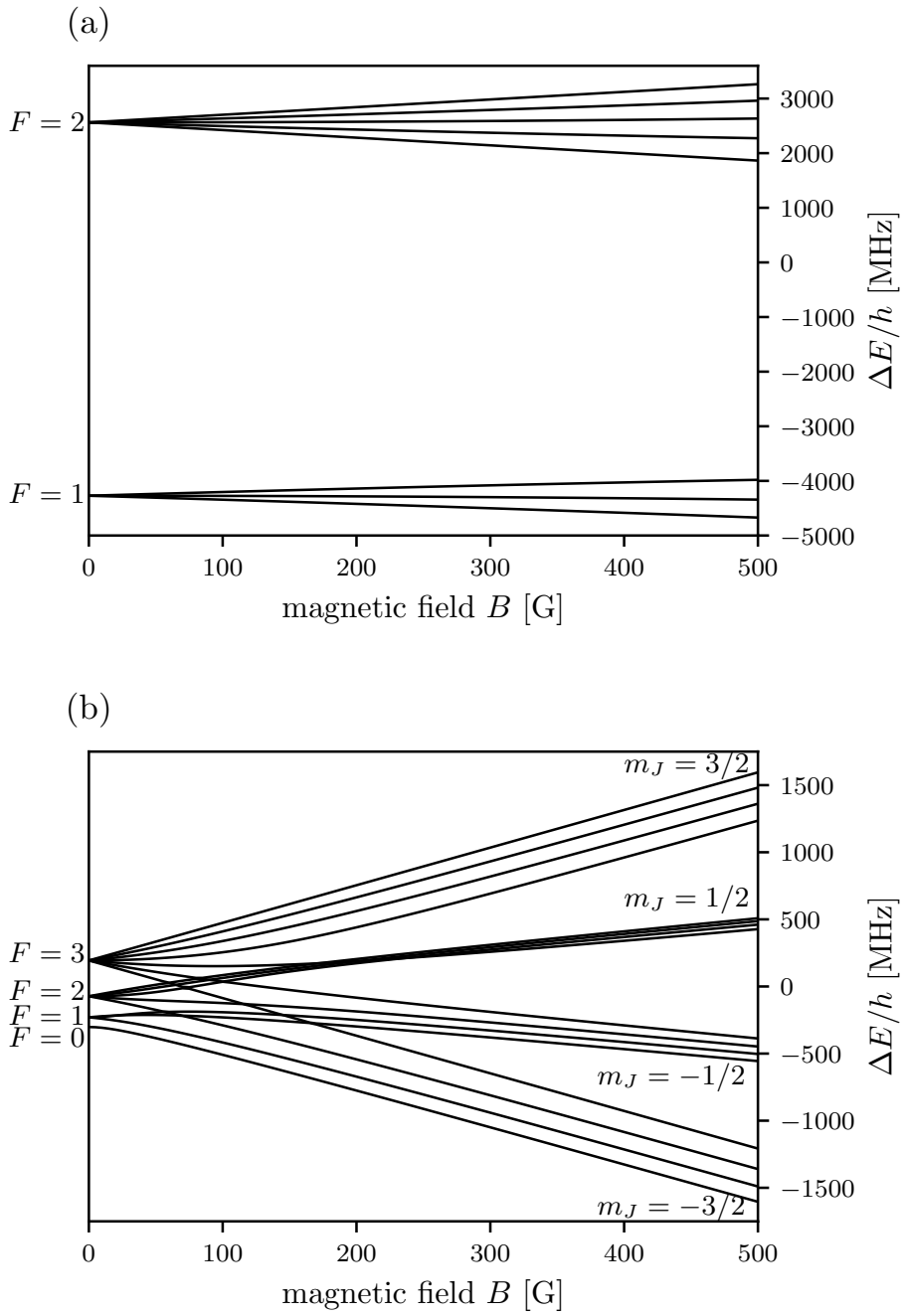

FIGURE 2.2. Hyperfine structure of ^{87}Rb atoms in an external magnetic field B. Here, we consider the fine structure levels involved in the D_2 transition: (a) $5\mathcal{S}_{1/2}$ ground level and (b) $5\mathcal{P}_{3/2}$ excited level.

in a similar way to spherical harmonics, it is natural to expand the polarization vector $\hat{\epsilon}$ in terms of the spherical unit vectors. These unit vectors are given by

$$\hat{\mathbf{u}}_{-1} = \left(\hat{\mathbf{e}}_x - \mathrm{i}\hat{\mathbf{e}}_y\right)/\sqrt{2}, \quad \hat{\mathbf{u}}_0 = \hat{\mathbf{e}}_z, \quad \hat{\mathbf{u}}_{+1} = -\left(\hat{\mathbf{e}}_x + \mathrm{i}\hat{\mathbf{e}}_y\right)/\sqrt{2}, \tag{2.14}$$

where $\hat{\mathbf{u}}_{\pm 1}$ corresponds to right- or left-circularly polarized light ($\sigma_{\pm}$-transitions) and $\hat{\mathbf{u}}_0$ corresponds to linearly polarized light (π-transition). This allows us to express the position operator in terms of spherical harmonic functions:

$$\hat{\mathbf{u}_q} \cdot \vec{\mathbf{r}} = \sqrt{\frac{4\pi}{3}} r Y_1^q\left(\theta, \phi\right) \tag{2.15}$$

where $q = 0, \pm 1$. Using the contraction rule in Eq. 2.4, we see that the dipole operator $\mathbf{d} = e\mathbf{r}$ is a spherical tensor of rank $k = 1$.

We then apply the Wigner-Eckart theorem for spherical tensor operators. For example, the fine structure transition matrix elements induced by light with angular momentum q are:

$$\begin{aligned}\left\langle Jm_J \left| d_q \right| J'm_{J'}\right\rangle &= \left\langle J \left\| \mathbf{d} \right\| J'\right\rangle \left\langle Jm_J | J'm_{J'}; 1\ q\right\rangle \\ &= \left\langle J \left\| \mathbf{d} \right\| J'\right\rangle (-1)^{J'-J+m'-m} \sqrt{\frac{2J+1}{2J'+1}} \left\langle J'm_{J'} | Jm_J; 1\ \text{-}q\right\rangle, \end{aligned} \tag{2.16}$$

where $\left|\left\langle J \left\| \mathbf{d} \right\| J'\right\rangle\right|$ are the reduced matrix elements, $\left|Jm_J\right\rangle$ is the initial atomic state, $\left|J'm_{J'}\right\rangle$ is the final atomic state, and $\left\langle Jm_J | J'm_{J'}; 1\ q\right\rangle$ are the Clebsch-Gordan coefficients for the angular momentum coupling. The reduced matrix elements are related

to the empirically determined spontaneous decay rate[3]

$$\Gamma_{JJ'} = \frac{\omega_0^3}{3\pi\epsilon_0\hbar c^3}\frac{2J+1}{2J'+1}\left|\langle J \left\|\mathbf{d}\right\| J'\rangle\right|^2, \tag{2.17}$$

where ω_0 is the transition frequency of the coupled fine structure states J and J'.

Extending the Wigner-Eckart theorem to the hyperfine structure we obtain

$$\begin{aligned}\langle Fm_F \left|d_q\right| F'm_{F'}\rangle &= \langle F \left\|\mathbf{d}\right\| F'\rangle \langle Fm_F|F'm_{F'};1\ q\rangle \\ &= \langle F \left\|\mathbf{d}\right\| F'\rangle (-1)^{F'-F+m'-m}\sqrt{\frac{2F+1}{2F'+1}}\langle F'm_{F'}|Fm_F;1\ \text{-}q\rangle \end{aligned} \tag{2.18}$$

which gives the ratio of transition strength between different $|Fm_F\rangle$ and $|F'm_{F'}\rangle$ states. The reduced matrix elements for hyperfine transition are connected to the fine structure transition by

$$\langle F \left\|\mathbf{d}\right\| F'\rangle = \langle J \left\|\mathbf{d}\right\| J'\rangle (-1)^{F'+J+1+I}\sqrt{(2F'+1)(2J+1)}\begin{Bmatrix} J & J' & 1 \\ F' & F & I \end{Bmatrix}, \tag{2.19}$$

where the last term in curly brackets is the Wigner 6-j symbol.

The dipole approximation accordingly leads to three transition selection rules

$$F' = F \quad \text{or} \quad F' = F \pm 1, \tag{2.20}$$

$$m_F = m_{F'} + q \quad \Rightarrow \quad m_{F'} = m_F \quad \text{or} \quad m_{F'} = m_F \pm 1, \tag{2.21}$$

[3]In some definitions, either the factor $(2J'+1)$ or $(2J+1)$, or both, is absorbed into the reduced dipole matrix element $|\langle J \left\|\mathbf{d}\right\| J'\rangle|$.

$$F' \neq F \quad \text{if} \quad m_{F'} = m_F = 0. \tag{2.22}$$

Considering transition to a single excited fine-structure component, the above relations result in two symmetry cases:

(1) The matrix elements that couple to any *single excited state* sublevel $|F'm_{F'}\rangle$ add up to a factor that is independent of the particular sublevel chosen:

$$\sum_{qF} |\langle F'm_{F'} |d_q| F (m_{F'} + q)\rangle|^2 = \frac{2J+1}{2J'+1} |\langle J \|\mathbf{d}\| J'\rangle|^2 . \tag{2.23}$$

The interpretation of this symmetry is simply that all of the excited state sublevels of F' energy level decay at the same spontaneous emission rate Γ, and the decaying population "branches" into various ground state sublevels.

(2) Another symmetry arises from summing the matrix elements for a *single ground-state* sublevel to all the sublevels in a particular F' energy level:

$$\begin{aligned} S_{FF'} &= \frac{\sum_q |\langle F m_F |d_q| F'm_{F'}\rangle|^2}{|\langle J \|\mathbf{d}\| J'\rangle|^2} \\ &= (2F'+1)(2J+1) \begin{Bmatrix} J & J' & 1 \\ F' & F & I \end{Bmatrix}^2 . \end{aligned} \tag{2.24}$$

The above sum $S_{FF'}$ is independent of the particular ground state sublevel chosen, and also obeys the sum rule $\sum_{F'} S_{FF'} = 1$. These factors $S_{FF'}$ provide a measure of the relative strength of each of the $F \to F'$ transitions.

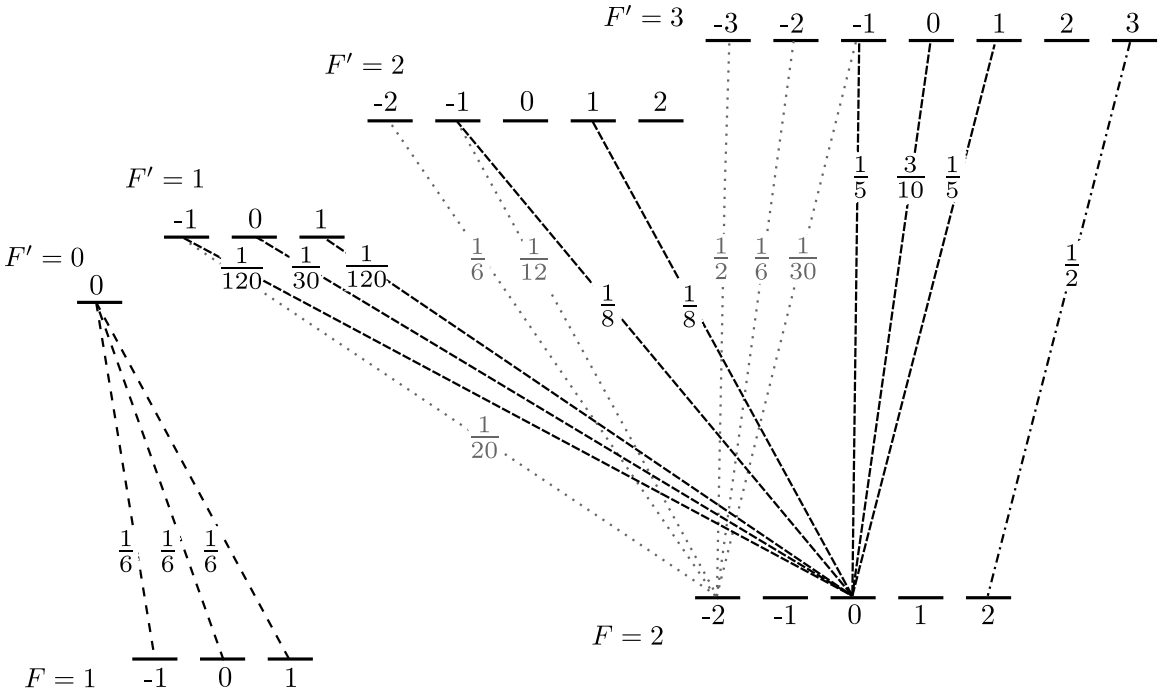

FIGURE 2.3. Examples of transition matrix elements in the D_2 line of ^{87}Rb. Symmetry cases satisfying Eq. 2.23 are shown for the $|0,0\rangle$ and $|3,3\rangle$ excited states. Symmetry cases satisfying Eq. 2.24 are shown for the $|2,-2\rangle$ and $|2,0\rangle$ ground states.

Following the transition rules described above for each distinct fine-structure component, Fig. 2.3 illustrates the strength of transition matrix elements

$$\frac{\left|\langle F m_F \left| d_q \right| F' m_{F'} \rangle\right|^2}{\left|\langle J \left\| \mathbf{d} \right\| J' \rangle\right|^2} \tag{2.25}$$

for the D_2 line of ^{87}Rb. Some of these are the transitions to the $|F', m_{F'}\rangle = |0,0\rangle$ and $|F', m_{F'}\rangle = |3,3\rangle$ excited states satisfying the first symmetry case in Eq. 2.23. I also show examples for transitions from the $|F, m_F\rangle = |2,-2\rangle$ and $|F, m_F\rangle = |2,0\rangle$ ground states satisfying Eq. 2.24.

2.2. Laser cooling and trapping

The main idea behind laser cooling techniques is to exploit the interaction of atoms and electromagnetic field to cool down the atoms to near absolute zero [115, 134]. Laser light is used to slow down the atoms through many cycles of absorption and spontaneous emission. Photons from excited atoms are spontaneously emitted in random directions with zero net contribution to the atom's average momentum. The net result is that the atomic motion is cooled by the absorbed photon recoil momentum. Unfortunately, the "randomness" of the spontaneous emission also causes unavoidable "heating" of the atomic motion, setting a threshold to the lowest velocity spread that can be achieved with this technique. The temperature limit due to this mechanism is called the Doppler temperature [24].

Ideally, atomic transitions involving the same ground state for many cycles of absorption and emission are desirable since it allows the atoms to be laser cooled indefinitely. The particular transitions used in laser cooling are known as *cycling transitions.* Due to population branching to several ground-state levels, an atom in an excited state might not return to its initial ground state after absorbing photons. This process, known as *optical pumping*, causes depletion of the number of atoms being trapped. In some cases, the atoms end up in *dark states* – ground-state levels that are transparent to the cooling light in a cycling transition. Since the linewidths of the transition (excited states) and commercial lasers used are generally much smaller than the separation between the different ground state components, a solution to this

problem is to apply another *repump* laser with a different frequency that re-excites the atoms out of the "wrong" ground states. Thus, it is a common practice to apply both *cooling* and *repump* lasers in most stages of laser cooling and trapping [115, 134].

2.2.1. Zeeman slower. In the first stage of laser cooling with a fixed laser frequency, it is common to slow down the atomic vapor originating from an oven using photon recoil from the laser beams. As the velocity decreases, the resonance condition changes due to Doppler shift. One solution to this problem is to apply a spatially varying magnetic field to alter the atomic hyperfine structure so as to compensate the Doppler shift. This technique is known as a Zeeman slower [115].

An example of a B-field profile for the slower [41] along the slowing direction z is

$$B(z) = B_b - B_t\sqrt{1 - z/z_0}, \tag{2.26}$$

where B_b is a constant bias field, B_t is the magnitude of the spatially varying component, and z_0 is the distance over which slowing takes place. Due to the recoil momentum $\hbar k_R$ imparted by the laser beam with intensity I, an atom with mass m moving at velocity v experience deceleration

$$a = \frac{\hbar k_R \Gamma}{2m} \frac{I/I_{\text{sat}}}{1 + I/I_{\text{sat}} + 4\left[\delta_0 + k_R v - \mu' B(z)/\hbar\right]^2/\Gamma^2}, \tag{2.27}$$

where Γ is the spontaneous decay rate of the excited state, I_{sat} is the saturation intensity[4], δ_0 is the laser detuning, and μ' is the magnetic moment of an atom.

[4]The saturation intensity is related to the reduced dipole matrix element of the corresponding transition and light polarization, which can be obtained by solving the optical Bloch equation [163].

To achieve the maximum possible deceleration to cool atoms with initial speed v_i to the final speed v_f, the Zeeman slower must have a length z_0 given by

$$z_0 = m\frac{v_f^2 - v_i^2}{\eta\hbar k_R\Gamma}. \tag{2.28}$$

Here the parameter η takes into account the imperfections in the Zeeman field, laser intensity and polarization, and spatial constraints. When choosing η, the designer has to bear in mind two criteria [41]:

(1) how much laser power is available

$$\frac{I}{I_{\text{sat}}} = \frac{\eta}{(1-\eta)}, \tag{2.29}$$

(2) how well the field profile (including its gradient $\mathrm{d}B/\mathrm{d}z$) can be replicated to fulfill the resonance condition at each point along the slower

$$\eta = \frac{2m\mu'}{\hbar^2 k_R^3\Gamma}\frac{\mathrm{d}B}{\mathrm{d}z}\left(\frac{\mu' B}{\hbar} - \delta_0\right). \tag{2.30}$$

2.2.2. Optical molasses – Doppler limit and sub-Doppler cooling mechanism. Optical molasses use the simplest laser cooling mechanism: a pair of counter-propagating beam with wavevectors $\pm k_R$. A two-level atom moving with velocity v is subject to the Doppler effect and observes the laser beams with detuning $\delta_{l,r} = \delta \mp k_R v$, where δ is the laser frequency detuning relative to the atomic transition. In the limit of low intensity $I \ll I_{\text{sat}}$, where stimulated emission is not important, we neglect the

interference effect between the counter-propagating lasers and we obtain the total scattering force as $\mathbf{F}_{\text{scatt}} = \mathbf{F}_{\text{left}} - \mathbf{F}_{\text{right}} = -\alpha\mathbf{v}$, where the damping coefficient α is given by [115]:

$$\alpha = \frac{2\hbar k_R^2}{\Gamma}\frac{I}{I_{\text{sat}}}\frac{-4\delta}{\left[1+(2\delta_l/\Gamma)^2\right]\left[1+(2\delta_r/\Gamma)^2\right]}. \tag{2.31}$$

With a restoring force $\mathbf{F} = -\alpha\mathbf{v}$, the damping opposes the motion of the atom in proportion to its speed, similar to drag forces in viscous media and hence this cooling technique is known as optical molasses. The cooling rate $\mathbf{F}\cdot\mathbf{v}$ is maximized for the detuning condition $\delta = -\Gamma/2$.

In optical molasses, spontaneous emission plays an essential role in dissipating energy by emission of fluorescence photons [59]. However, the random momentum recoil of the atoms $\langle \mathbf{p}^2 \rangle$ after spontaneous emission is responsible for heating. The heating can be described in an analogous way to diffusion in Brownian motion [33]:

$$\frac{\mathrm{d}}{\mathrm{d}t}\left\langle p_i^2\right\rangle_{\text{heating}} = 2D_0, \quad i = x, y, z, \tag{2.32}$$

where D_0 is the diffusion coefficient. Meanwhile, the cooling by optical forces can be described by:

$$\frac{\mathrm{d}}{\mathrm{d}t}\left\langle p_i^2\right\rangle_{\text{cooling}} = -\frac{2\alpha}{m}\left\langle p_i^2\right\rangle, \quad i = x, y, z, \tag{2.33}$$

where m is the atomic mass. The steady-state (satisfying the Fokker-Planck equation) is reached when the heating and cooling are balanced. One finds the steady-state

temperature T as $k_B T = D_0/\alpha$, where the atomic motion is associated with the temperature using the equipartition theorem $k_B T = \langle p_i^2 \rangle / m$. For very low saturation parameter $s = I/I_{\text{sat}} \ll 1$, the diffusion coefficient can be interpreted as a sum of two independent terms due to vacuum fluctuations (spontaneous emission) and fluctuations in the number of absorbed photon, and this gives the total diffusion coefficient $D_0 = (s\Gamma/2)(\hbar k_R)^2$. The minimum temperature achievable with the maximum cooling rate $\delta = -\Gamma/2$ is then given by the Doppler limit

$$T_D = \frac{\hbar\Gamma}{2k_B}. \tag{2.34}$$

In a typical D_2-line transition used in laser cooling of ^{87}Rb atoms, the Doppler temperature is $T_D = 146\,\mu$K [162].

During research on laser cooling and optical molasses, it was found that the lowest achievable temperature was colder than the Doppler cooling limit [134]. This perplexing result eventually led to a new understanding of how laser cooling could work [37]. Two counter-propagating lasers, either with orthogonal linear polarizations (lin $\perp$ lin) or orthogonal circular polarizations ($\sigma^+ - \sigma^-$), create a polarization gradient. In the first case, the lin $\perp$ lin configuration, spatially rotating ellipticity of the combined light causes spatially oscillating energy shifts in various sublevels of the atoms. Atoms which are climbing a potential hill are losing kinetic energy and have a probability to be optically pumped back to the bottom valley, transforming part of their kinetic energy into potential energy. This irreversible mechanism is known

as *Sisyphus cooling* [37]. In the second case, the $\sigma^+ - \sigma^-$ configuration, the combined polarization vector is spatially rotating with the same ellipticity. A combination of optical pumping and light shifts produces a highly sensitive motion-induced atomic orientation resulting in a large imbalance between the radiation pressures of the two counter-propagating waves.

Polarization gradient cooling works at velocities lower than the velocity capture range for Doppler cooling ($kv < \Gamma$). The equilibrium temperature T_{SD} in the sub-Doppler cooling is proportional to the laser power $T_{\mathrm{SD}} \propto \hbar\Omega^2/|\delta|$, where the dipole transition Rabi frequency Ω is related to the laser intensity via $I/I_{\mathrm{sat}} = 2\Omega^2/\Gamma^2$. The one-photon recoil energy then sets a fundamental physical limit on the lowest achievable temperature in sub-Doppler cooling to be the recoil temperature $T_R = \hbar^2 k_R^2/mk_B$ [37, 162]. As an example, for ^{87}Rb atoms in the D_2 transition with $\lambda_{\mathrm{D2}} = 780.24\,\mathrm{nm}$, the recoil temperature is $T_R \sim 362\,\mathrm{nK}$ [162].

2.2.3. Magneto-optical trap. Doppler cooling enables a quick cooling of atoms, typically in a timescale of a few ms (set by the Planck constant over the photon recoil energy). However, the atoms have a spatially diffusive motion and eventually they leave the cooling region in a timescale of a few seconds. In order to trap the atoms within a small volume, while cooling them at the same time, additional magnetic field gradients are applied. This setup is known as a magneto-optical trap (MOT).

In a MOT, quadrupole magnetic field gradient is added to the 3D standing wave configuration of the optical molasses. With the presence of a magnetic field gradient

along x such that $B = b'x$, the detuning $\delta'(\mathbf{r})$ seen by the atoms depends on the position $\mathbf{r}$ and their internal sublevel structure, i.e.

$$\delta'(\mathbf{r}) = \delta - \left(m'_{\mathrm{ex}} g_{J,\mathrm{ex}} - m'_{\mathrm{gr}} g_{J,\mathrm{gr}}\right) \frac{\mu_B}{\hbar} b'x, \tag{2.35}$$

where $m'_{\mathrm{ex}} g_{J,\mathrm{ex}}$ and $m_{\mathrm{gr}} g_{J,\mathrm{gr}}$ are respectively the magnetic moment of the excited and ground states used in the laser cooling transition. This leads to a position-dependent light force and this gives a restoring force $-\kappa\mathbf{r}$. The restoring coefficient κ scales linearly with detuning and intensity (similar to the damping coefficient α), and it is maximum for red-detuned light with $\delta = -\Gamma/2$. For cold atoms close to the center of the trap with small speed $|\mathbf{v}|$, the atoms experienced a total force $\mathbf{F} = -\alpha\mathbf{v} - \kappa\mathbf{r}$ equivalent to that of a damped oscillator.

An illustration of a MOT is shown in Fig. 2.4. This setup confines the atoms both in position and momentum, yielding a large phase-space density of atoms being trapped – the main requirement towards BEC. The main benefit of a MOT is its flexibility to convert easily into a magnetic trap or an optical molasses configuration. Also, the presence of a strong magnetic gradient is helpful for selectively trapping atoms in a specific hyperfine sub-level.

2.2.4. Magnetic trap. Once atoms are cooled close to the Doppler temperature, they need to be moved to other trapping potentials to be cooled further. One practical approach is to use a magnetic trap, where atoms are being transported by shifting the center location of the trap. One typically uses a simple magnetic field

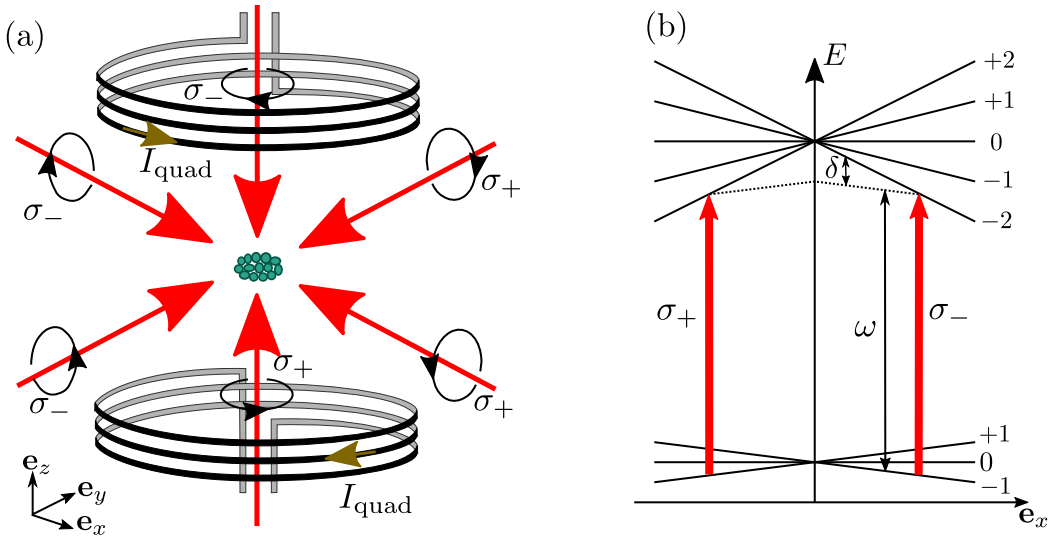

FIGURE 2.4. (a) Setup of a magneto-optical trap (MOT). Three pairs of counter-propagating laser beams with opposite circular polarizations provide the *damping force*, while magnetic field gradient from a pair of coils with opposite current provides the *restoring force*. (b) A simplified picture of different hyperfine Zeeman sublevels being cooled by the optical molasses. In common practices, both cycling and repump lasers are used to maximize the number of atoms captured in the MOT.

configuration produced by a pair of opposing anti-Helmholtz coils, with the axis along the $z-$direction, which has the form:

$$\mathbf{B} = \frac{b'}{2}\,(x, y, -2z)\,, \tag{2.36}$$

where b' is the magnitude of the field gradient and the field has an axial symmetry along the $z-$direction. This trap configuration is also known as the magnetic quadrupole trap.

In my experiments, other pairs of Helmholtz coils generate a controllable uniform magnetic field in certain directions. For simplicity, here I focus on the particular case where there is a spatially uniform magnetic field $\mathbf{B}_0 = B_0\mathbf{e}_z$ which displaces the

zero location of the magnetic trap. The magnetic trap provides a state-dependent conservative potential (in the linear Zeeman regime):

$$U(r) = -\boldsymbol{\mu} \cdot \boldsymbol{B} = \mu_B g_F m_F \frac{b'}{2} \sqrt{x^2 + y^2 + 4\,(z - z_0)^2}, \tag{2.37}$$

where $z_0 = B_0/b'$ and the strength of the magnetic field gradient in the $xy-$ plane is half the gradient along z (since $\nabla \cdot \mathbf{B} = 0$). The force experienced by the atoms can be calculated using $\mathbf{F} = -\nabla U$, and only specific atomic Zeeman sub-levels can be trapped selectively depending on the atoms' magnetic moment (depending on the sign of $g_F m_F$).

In magnetic trapping, it is crucial that the trapping force is enough to counteract the gravitational potential energy. For ^{87}Rb atoms with atomic mass $m = 1.443 \times 10^{-25}\,\mathrm{kg}$ and gravitational acceleration $g = 9.81\,\mathrm{m/s^2}$ along the z-direction, the gravitational field gradient expressed in frequency over distance is $\left|\mathrm{d}U_{\mathrm{grav}}/\mathrm{d}z\right| = mg = h \cdot 2.14\,\mathrm{kHz}/\mu\mathrm{m}$. Levitation of magnetically trappable spin states is thus achievable by selecting the appropriate field strength and position with respect to the magnetic trap center. For ^{87}Rb atoms in the $|F = 2, m_F = 2\rangle$ state, a magnetic field gradient of $b' \geq 15.3\,\mathrm{G/cm}$ is needed to levitate the atoms against gravity. If the gravity acceleration is along $x-$ or $y-$direction, twice of the field gradient is needed (i.e. $b' \geq 30.6\,\mathrm{G/cm}$).

2.2.5. Evaporative cooling. Despite having very low temperature, quantum phase transition towards BEC is not necessarily attainable unless high enough phase-space density is obtained.[5] Additional step of evaporative cooling, combined with laser cooling, is critical to achieve BEC. In evaporative cooling, energetic particles escape, carrying away their larger share of thermal energy, allowing the remaining atoms to cool down. This works for a wide range of temperatures and densities, but the process slows down as the system loses energetic particles, and hence significant number of atoms need to be trapped. Here, I summarize the evaporative cooling techniques [61, 83] which are relevant to my experiments.

2.2.5.1. *Radio-frequency induced evaporative cooling.* In magnetic traps, evaporation is done through a radio-frequency (RF) induced cooling technique [83]. The scheme uses a tunable RF radiation in conjunction with the magnetic trap to dress the atoms. Different m_F sub-level states of the atoms are mixed by the RF field, leading to a flatter potential curve at the avoided crossing of the dressed-state eigenvalues. As the atoms move away from the trap center, traversing the avoided crossing region and come into resonance with the RF field, the atomic state is adiabatically transformed into a non-trapped state (with opposite sign of magnetic moment) by stimulated emission of RF photons [83]. This process is identical to the "spilling" of the most energetic atoms out of the magnetic trap. Evaporation is then progressively

[5]The phase-space density is the ratio between the particle spatial density n and the number of significantly occupied (momentum or energy) states per unit volume. This is equivalent to the number of particles contained within a unit of volume in the thermal de Broglie wavelength, $\varpi = n\left(2\pi\hbar^2/mk_BT\right)^{3/2}$.

forced into the system by ramping down the RF frequency f_{RF} adiabatically, with a further option of also lowering the magnetic field gradient.

2.2.5.2. *Optical dipole trap.* Optical dipole traps rely on the principle that an off-resonant laser beam attracts or repels atoms, depending on whether it is red- or blue-detuned from the atomic transition [61]. Heating due to spontaneous emission with lifetime Γ is avoided if the laser light is far-detuned from the atoms' transition frequency ω_0 and a high enough laser power I is used. In the rotating-wave approximation, the dipole potential U_{dip} and scattering rate Γ_{sc} are given by [61, 132]:

$$U_{\mathrm{dip}}(\mathbf{r}) = \frac{3\pi c^2}{2\omega_0^3}\frac{\Gamma}{\Delta} I(\mathbf{r}), \qquad \Gamma_{\mathrm{sc}}(\mathbf{r}) = \frac{3\pi c^2}{2\hbar\omega_0^3}\left(\frac{\Gamma}{\Delta}\right)^2 I(\mathbf{r}), \tag{2.38}$$

where $\Delta = \omega - \omega_0$ is the detuning and ω is the laser frequency[6]. A simple relation exists between the scattering rate and the dipole potential: $\hbar\Gamma_{\mathrm{sc}} = \Gamma U_{\mathrm{dip}}/\Delta$. These results show two essential points for dipole trapping. For red-detuned traps ($\Delta < 0$), the potential minima is located at positions with maximum intensity; while for blue-detuned traps ($\Delta > 0$), the potential minima corresponds to minima of the intensity. The dipole potential scales as I/Δ, whereas the scattering rate scales as I/Δ^2 . Therefore, optical dipole traps usually use large detunings and high intensities to keep the scattering rate as low as possible for a required potential depth.

To exploit the ac-Stark shift effect to create a trapping potential, a spatially dependent intensity in the form of a Gaussian laser beam is used. A Gaussian beam

[6]In the case of multilevel atoms, one must sum all the contribution from the excited states with Clebsch-Gordan coefficients as the pre-factor, i.e. $1/\Delta \to \sum_j c_j^2/\Delta_j$.

propagating in the $y-$direction with wavelength λ and power P has the intensity profile [61]:

$$I = \frac{2P}{\pi w^2(y)} \exp\left[\frac{-2\left\{x^2 + (z - z_0)^2\right\}}{w^2(y)}\right], \tag{2.39}$$

where the spot size parameter is:

$$w(y) = w_0\sqrt{1 + \left(\frac{y}{y_R}\right)^2}. \tag{2.40}$$

Here the Rayleigh length is $y_R = \pi w_0^2/\lambda$ and the minimum beam waist w_0 is centered at $(0, 0, z_0)$. For a far red-detuned beam ($\Delta < 0$), the above intensity gives a trapping potential in the form:

$$V = -U_0 \exp\left[\frac{-2\left\{x^2 + (z - z_0)^2\right\}}{w^2(y)}\right]. \tag{2.41}$$

Evaporative cooling is achieved by lowering the total trapping potential, i.e. by ramping down the total laser power. The introduction of an offset z_0 in the dipole trap location with respect to a magnetic trap center is beneficial to limit Majorana losses during the transfer process of the atoms from the magnetic trap to the optical dipole trap [104].

Since a single focused beam only provides weak confinement along the propagation axis, it is common to cross two optical dipole beams with orthogonal polarization to create nearly isotropic atomic ensembles with tight confinement in all three dimensions. In a particular case of crossed-beam traps with 90° intersection angle in the

$xy-$plane and equal waist w_0 (where $w_0 \ll y_R$), the dipole potential near its minimum can be approximated by the Taylor series with lowest order of expansion [61]

$$V_{CB} \simeq -V_0 \left[1 - \frac{x^2 + y^2 + 2\left(z - z_0\right)^2}{w_0^2}\right]. \tag{2.42}$$

Consequently, external potential experienced by the atoms with atomic mass m can be approximated as a harmonic oscillator with trapping frequencies

$$\omega_x^2 = \frac{2V_0}{mw_0^2}, \qquad \omega_y^2 = \frac{2V_0}{mw_0^2}, \qquad \omega_z^2 = \frac{4V_0}{mw_0^2}. \tag{2.43}$$

2.3. Bose-Einstein condensation

BEC is a quantum phenomenon where an ensemble of particles with bosonic nature (integer spin) occupy the same ground-state energy level as they are cooled down to temperatures near absolute zero. In the last few decades, extensive theories of BECs have been developed [36], providing predictions of physical phenomena exhibited by these quantum gases and offering new insights. For a more comprehensive discussion, I recommend the text by Pethick and Smith [132], and the text by Pitaevskii and Stringari [135] for more advanced (curious) readers. In this section, I discuss the theory of BECs relevant to my work, particularly for neutral particles with weakly repulsive interaction such as ^{87}Rb alkali atoms.ads

2.3.1. Gross-Pitaevskii equation. The field operator $\hat{\Psi}\left(\mathbf{r}, t\right)$ describing the atomic many-body wavefunction in the Heisenberg representation is

$$\begin{aligned} \mathrm{i}\hbar\frac{\partial}{\partial t}\hat{\Psi}\left(\mathbf{r},t\right) &= \left[\hat{\Psi}\left(\mathbf{r},t\right),\hat{H}\right] \\ &= \left[-\frac{\hbar^2\nabla^2}{2m}+V_{\mathrm{ext}}\left(\mathbf{r},t\right)+\int\hat{\Psi}^{\dagger}\left(\mathbf{r}',t\right)V\left(\mathbf{r}'-\mathbf{r}\right)\hat{\Psi}\left(\mathbf{r}',t\right)\mathrm{d}^3\mathbf{r}'\right]\hat{\Psi}\left(\mathbf{r},t\right), \end{aligned} \tag{2.44}$$

where $V_{\mathrm{ext}}\left(\mathbf{r},t\right)$ is the external potential and $V\left(\mathbf{r}'-\mathbf{r}\right)$ is the many-body interaction potential [59]. At very low temperatures, a large number of bosonic atoms occupy a single state allowing us to replace the field operator $\hat{\Psi}\left(\mathbf{r},t\right)$ with a classical function $\Psi_0\left(\mathbf{r},t\right)$ which acts as the order parameter for the system. Assuming the range of the interatomic forces is much smaller than the average distance $d=n^{-1/3}$ between particles (set by the density distribution n), we need only to consider configurations involving pairs of interacting particles (configurations with three or more particles interacting simultaneously are neglected). The two-body interaction potential for dilute gases at low temperatures is given by the effective $s-$wave scattering potential

$$V\left(\mathbf{r}'-\mathbf{r}\right)=g\delta\left(\mathbf{r}'-\mathbf{r}\right)=\frac{4\pi\hbar^2a}{m}\delta\left(\mathbf{r}'-\mathbf{r}\right), \tag{2.45}$$

where a is the $s-$wave scattering length and m is the atomic mass. In other words, if the condition of diluteness $|a|\ll n^{-1/3}$ is satisfied, then the $s-$wave scattering length is sufficient to characterize all interaction effects on the atomic properties. With these

substitutions, we obtain the Gross-Pitaevskii equation (GPE)

$$\mathrm{i}\hbar\frac{\partial}{\partial t}\Psi_0\left(\mathbf{r},t\right)=\left[-\frac{\hbar^2\nabla^2}{2m}+V_{\mathrm{ext}}\left(\mathbf{r},t\right)+g\left|\Psi_0\left(\mathbf{r},t\right)\right|^2\right]\Psi_0\left(\mathbf{r},t\right). \tag{2.46}$$

Stationary solutions for the GPE give a time evolution of the condensate wave-function that follows the condition

$$\Psi_0\left(\mathbf{r},t\right)=\psi\left(\mathbf{r}\right)\exp\left(-\mathrm{i}\mu t/\hbar\right), \tag{2.47}$$

with chemical potential μ fixed by the normalization of the atoms' number. The stationary GPE reduces to

$$\mu\psi\left(\mathbf{r}\right)=\left[-\frac{\hbar^2\nabla^2}{2m}+V_{\mathrm{ext}}\left(\mathbf{r},t\right)+g\left|\psi\left(\mathbf{r}\right)\right|^2\right]\psi\left(\mathbf{r}\right). \tag{2.48}$$

For a dilute Bose gas of particles interacting with repulsive forces, or $a>0$ as in ^{87}Rb, the stationary GPE given by Eq. 2.48 describes the ground state of the system [99]. The BECs are stable and robust to increasing number of particles.

2.3.2. Thomas-Fermi approximation for Bose gases in the harmonic trap. We now consider the stationary GPE in a time-independent harmonic trap

$$V_{\mathrm{ext}}\left(\mathbf{r}\right)=\frac{1}{2}\sum_{j=x,y,z}m\omega_j^2r_j^2. \tag{2.49}$$

If the chemical potential μ and interaction energy $g\left|\psi\left(\mathbf{r}\right)\right|^2$ is larger than the energy spacing of the harmonic oscillator $\mu\simeq g\left|\psi\left(\mathbf{r}\right)\right|^2\gg\hbar\omega_j$, we can neglect the kinetic

energy term in the stationary GPE. The limit in which one ignores the kinetic energy term is called the Thomas-Fermi (TF) approximation and Eq. 2.48 reduces to:

$$\mu_{\mathrm{TF}}\psi\left(\mathbf{r}\right) \simeq \left[V_{\mathrm{ext}}\left(\mathbf{r},t\right) + g\left|\psi\left(\mathbf{r}\right)\right|^2\right]\psi\left(\mathbf{r}\right). \tag{2.50}$$

The analytical solution to the atomic density distribution is:

$$n_{\mathrm{TF}}\left(\mathbf{r}\right) = \left|\psi\left(\mathbf{r}\right)\right|^2 = \frac{1}{g}\left(\mu_{\mathrm{TF}} - \frac{1}{2}\sum_{j=x,y,z} m\omega_j^2 r_j^2\right) \tag{2.51}$$

if $\mu_{\mathrm{TF}} > V_{\mathrm{ext}}\left(\mathbf{r}\right)$, and $n_{\mathrm{TF}} = 0$ elsewhere. In the TF limit for harmonic traps, the atomic distribution has an inverted parabolic profile and the atomic cloud has an elliptical geometrical shape bounded by the condition $\mu_{\mathrm{TF}} = V_{\mathrm{ext}}\left(\mathbf{r}\right)$. The TF radii are given by

$$R_j = \sqrt{\frac{2\mu}{m\omega_j^2}}, \qquad j = x, y, z, \tag{2.52}$$

and the chemical potential constrained by the total number of condensed atoms N is accordingly [23]

$$\mu_{\mathrm{TF}} = \frac{15Ng}{8\pi R_x R_y R_z} = \frac{\hbar\bar{\omega}}{2}\left(15Na\sqrt{\frac{m\bar{\omega}}{\hbar}}\right)^{2/5}, \tag{2.53}$$

where $\bar{\omega} = \left(\omega_x\omega_y\omega_z\right)^{1/3}$. The momentum distribution of the condensate in the TF limit can be found by taking the Fourier transform of the TF wavefunction [59],

$$n_{\mathrm{TF}}\left(\mathbf{p}\right) = N\frac{15}{16\hbar^3}R_x R_y R_z\left(\frac{J_2\left(\tilde{p}\right)}{\tilde{p}^2}\right)^2, \tag{2.54}$$

where J_2 is the Bessel function of order 2 and

$$\tilde{p} = \frac{1}{\hbar}\sqrt{\sum_{j=x,y,z} p_x^2 R_x^2}. \tag{2.55}$$

It is important to note that the TF approximation breaks down near the boundary of the density profile where $n_{\mathrm{TF}}(\mathbf{r}) \to 0$ as the kinetic energy term is comparable to the interaction energy. It is then natural to define a characteristic length connected to the interactions in the system, namely the condensate healing length $\xi = h/\sqrt{2mgn_0}$, where n_0 is the peak density evaluated at the centre of the trap $n_0 = n_{\mathrm{TF}}(\mathbf{r} = 0) = \mu/g$. Within the condensate healing length region near the boundary, where $r_j \simeq R_j \pm \xi$, one must include the finite-size corrections to the TF limit [36, 132, 135].

2.3.3. Expansion of partially condensed ultracold gases. Measurements of the atomic density distribution reveals the condensation nature of an ultracold gas. In the laboratory, this is normally done by releasing the harmonic trap and letting the atomic cloud expands. The momentum distribution of the cloud is transformed into a spatial distribution. Images of the atomic cloud can be captured by the cameras. Further, the time-of-flight (TOF) expansion increases the size of the spatial structure so that it is large enough to be resolved by the imaging system.

Ultracold gases produced in the lab have a small fraction of non-condensed (thermal) atoms. While the condensed fraction of the cloud can be approximated with the TF distribution, the thermal density $n_{\mathrm{th}}(\mathbf{r})$ can be calculated using a semiclassical

expression for the Bose statistics in the grand canonical ensemble [59]

$$n_{\rm th}\left(\mathbf{r}\right)=\int\frac{{\rm d}^3\mathbf{p}}{\left(2\pi\hbar\right)^3}n_{\mathbf{p}}\left(\mathbf{r}\right)=\int\frac{{\rm d}^3\mathbf{p}}{\left(2\pi\hbar\right)^3}\frac{1}{\exp\left[\beta\left\{H\left(\mathbf{r},\mathbf{p}\right)-\mu\right\}\right]-1}, \tag{2.56}$$

where $\beta=1/k_BT$ and T is the temperature, $H\left(\mathbf{r},\mathbf{p}\right)=p^2/2m+V_{\rm eff}\left(\mathbf{r}\right)$ is the semiclassical Hamiltonian and μ is the total chemical potential.

In my work, for temperature T below the critical condensation temperature T_c, I can apply the Hartree-Fock theory to the many-body Hamiltonian [50, 135]. Since I was only interested in the expansion of thermal atoms near the tail-end of the condensate TF distribution ($n_{\rm TF}\left(\mathbf{r}\right)\approx 0$), I can approximate the effective potential experienced by the thermal atoms as $V_{\rm eff}\left(\mathbf{r}\right)-\mu\simeq V_{\rm ext}\left(\mathbf{r}\right)-\mu_{\rm TF}$ and I obtain the relation[7]

$$H\left(\mathbf{r},\mathbf{p}\right)-\mu\simeq\left|\mathbf{p}\right|^2/2m+V_{\rm ext}\left(\mathbf{r}\right)-\mu_{\rm TF}. \tag{2.57}$$

Performing the integration in Eq. 2.56 over the momentum space yields the spatial distribution of the thermal cloud [59]

$$n_{\rm th}\left(\mathbf{r}\right)=\frac{1}{\lambda_{\rm T}^3}g_{3/2}\left(\exp\left[\frac{\mu_{\rm TF}-V_{\rm ext}\left(\mathbf{r}\right)}{k_BT}\right]\right)=\frac{1}{\lambda_{\rm T}^3}g_{3/2}\left(Z\,\exp\left[-\beta V_{\rm ext}\left(\mathbf{r}\right)\right]\right), \tag{2.58}$$

where $\lambda_{\rm T}=\sqrt{2\pi\hbar^2/mk_BT}$ is the thermal de Broglie wavelength, $Z=\exp\left(\mu_{\rm TF}/k_BT\right)$ is the fugacity, and $g_m\left(x\right)=\sum_{j=1,2,\ldots}^{\infty}x^j/j^m$ is the Bose function.

[7] For $T\ll T_c$ with $n_{\rm TF}\gg n_{\rm th}$, the Hartree-Fock approximation gives $V_{\rm eff}\left(\mathbf{r}\right)-\mu\simeq V_{\rm ext}\left(\mathbf{r}\right)+2gn_{\rm TF}\left(\mathbf{r}\right)-\mu_{\rm TF}=gn_{\rm TF}\left(\mathbf{r}\right)$. This is equivalent to saying the thermal atoms experienced a "trapping" potential with an inverted parabola (TF) profile, due to interaction with BEC atoms [50].

A TOF expansion of the thermal cloud occurs after releasing the harmonic trap. The momentum distribution function in Eq. 2.56 evolves in time according to $n_{\mathbf{p}}(\mathbf{r},t) = n_{\mathbf{p}}(\mathbf{r}-\mathbf{p}t/m)$. This modifies the thermal density to:

$$n_{\mathrm{th}}(\mathbf{r},t) = \frac{1}{\lambda_{\mathrm{T}}^3}\prod_{j=x,y,z}\frac{1}{\sqrt{1+\omega_j^2 t^2}} g_{3/2}\left(Z\,\exp\left[-\beta\tilde{V}_{\mathrm{ext}}(\mathbf{r},t)\right]\right), \tag{2.59}$$

for the effective harmonic trap

$$\tilde{V}_{\mathrm{ext}}(\mathbf{r},t) = \frac{1}{2}m\sum_{j=x,y,z}\frac{\omega_j^2}{1+\omega_j^2 t^2} r_j^2. \tag{2.60}$$

To calculate the TOF expansion of the condensed part, I now generalize the frequencies of the trapping potential to be time-dependent $\omega_j(t)$. Their initial static values ω_{j0} fix the initial equilibrium configuration of the system corresponding to the TF distribution. To solve the time-dependent GPE in Eq. 2.46, I use the ansatz [23]

$$R_j(t) = \lambda_j(t) R_{j0} = \lambda_j(t)\sqrt{\frac{2\mu}{m\omega_{j0}^2}}, \qquad j=x,y,z, \tag{2.61}$$

where $\lambda_j(0) = 1$ and R_{j0} is the stationary values of the initial TF radii. In this treatment, the inverted parabolic TF profile is preserved throughout the expansion of the cloud. The scaling factors obeys $\lambda_j(t)$ the second-order differential equations

$$\frac{\mathrm{d}^2\lambda_j(t)}{\mathrm{d}t^2} = \frac{\omega_{j0}^2}{\lambda_j(t)\lambda_x(t)\lambda_y(t)\lambda_z(t)} - \omega_j^2(t)\lambda_j(t), \qquad j=x,y,z. \tag{2.62}$$

For the sudden release of a harmonic trap, $\omega_j^2(t>0)=0$, the above equation becomes

$$\frac{\mathrm{d}^2\lambda_j(t)}{\mathrm{d}t^2}=\frac{\omega_{j0}^2}{\lambda_j(t)\,\lambda_x(t)\,\lambda_y(t)\,\lambda_z(t)},\qquad j=x,y,z. \tag{2.63}$$

The expansion of the TF radii is obtained by solving Eq. 2.63 for $\lambda_j(t)$.

The total density, including both condensed and non-condensed parts, after TOF expansion for time τ is

$$\begin{aligned} n_{\mathrm{tot}}(\mathbf{r}) &= n_{\mathrm{TF}}(\mathbf{r})+n_{\mathrm{th}}(\mathbf{r}) \\ &= \frac{15N}{8\pi R_x(\tau)\,R_y(\tau)\,R_z(\tau)}\max\left(0,\left[1-\sum_{j=x,y,z}\frac{r_j^2}{R_j^2(\tau)}\right]\right)+ \\ &\prod_{j=x,y,z}\frac{1}{\lambda_T^3\sqrt{1+\omega_{j0}^2\tau^2}}\,g_{\frac{3}{2}}\left(Z\,\exp\left[-\frac{m}{2k_BT}\sum_{j=x,y,z}\frac{\omega_{j0}^2r_j^2}{1+\omega_{j0}^2\tau^2}\right]\right). \end{aligned} \tag{2.64}$$

In common imaging techniques, such as absorption imaging, the density distribution being probed is always integrated over the imaging axis, i.e. along z, and one can write the column density as

$$\rho_{\mathrm{tot}}(x,y)=\rho_{\mathrm{TF}}(x,y)+\rho_{\mathrm{th}}(x,y). \tag{2.65}$$

The TF distribution of the condensed cloud integrated over z gives the column density

$$\rho_{\mathrm{TF}}(x,y)=\frac{5N}{2\pi R_x(\tau)\,R_y(\tau)}\max\left(0,\left[1-\sum_{j=x,y}\frac{r_j^2}{R_j^2(\tau)}\right]^{3/2}\right). \tag{2.66}$$

Meanwhile, the column density for the thermal cloud is given by [26]

$$\rho_{\mathrm{th}}(x,y) = \frac{1}{\lambda_{\mathrm{T}}^3}\sqrt{\frac{2\pi k_B T}{m\omega_{zo}^2}}\prod_{j=x,y}\frac{1}{\sqrt{1+\omega_{j0}^2\tau^2}}g_2\left(Z\,\exp\left[-\sum_{j=x,y}\frac{r_j^2}{2\sigma_j^2}\right]\right), \tag{2.67}$$

where the root-mean-square (RMS) widths of the thermal density profile are

$$\sigma_j = \sqrt{\frac{1+\omega_{j0}^2\tau^2}{\omega_{j0}^2}\frac{k_B T}{m}}, \qquad j = x, y, z. \tag{2.68}$$

For a long enough time $\tau \gg 1/\omega_{j0}$, the thermal cloud expansion becomes isotropic and the temperature can be inferred from the distribution RMS width, namely $k_B T = m\left(\sigma/\tau\right)^2$. In general, to measure the temperature of the system, two different release time with durations τ_1 and τ_2 are used. The thermal wings of the released ultracold gases are fitted to yield different values of RMS widths, which provide a measure of the system temperature as

$$T = \frac{m}{k_B}\left(\frac{\sigma_{j2}^2}{\tau_2^2} - \frac{\sigma_{j1}^2}{\tau_1^2}\right). \tag{2.69}$$

Figure 2.5(a) shows an example of column density profile $\rho_{\mathrm{tot}}(x,y)$ of a ^{87}Rb Bose gas released from a harmonic trap. The column density is proportional to the optical depth (OD) obtained by absorption imaging along the $z-$direction. The squared RMS widths, σ_x^2 and σ_y^2, are obtained by fitting the thermal portions of the atomic cloud with Eqs. 2.65-2.67. Plotting σ_x^2 and σ_y^2 with respect to the square of TOF

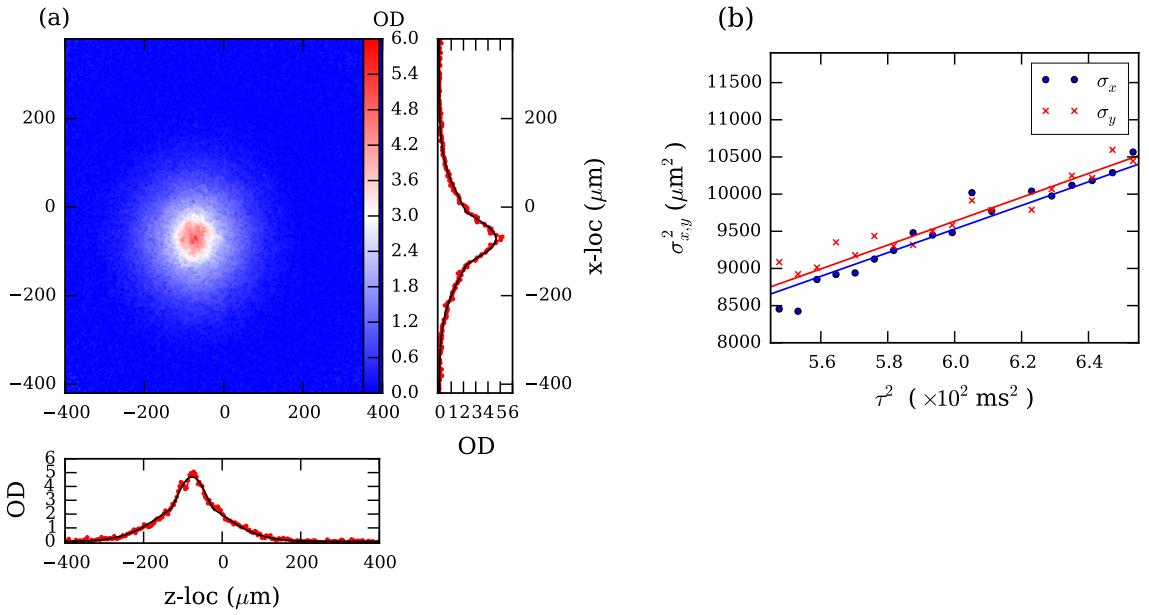

FIGURE 2.5. Temperature of a ^{87}Rb Bose gas released from a harmonic trap. (a) Fitting the column density profile $\rho_{\rm tot}(x, y)$ of a released ^{87}Rb Bose gas from a harmonic trap gives the RMS widths, σ_x and σ_y. (b) Plot of σ_x^2 and σ_y^2 with respect to the square of TOF duration τ^2. The temperature of atomic cloud $T = 165(2)$ nK is obtained using Eq. 2.68.

duration τ^2, we can then use Eq. 2.68 to obtain the temperature of the atomic cloud $T = 167(2)$ nK, as shown in Fig. 2.5(b).

2.3.4. Spinor Bose-Einstein condensates. The GPE used to describe a single component condensate in previous subsections can be extended to study the dynamics of multi-component BECs. Here I consider three-component condensates in the $F = 1$ hyperfine manifold described by the wavefunctions ψ_{-1}, ψ_0, and ψ_1 in an external potential V. A set of coupled GPEs for the mean-field dynamics is given by [68, 159] (see Appendix B for the derivation of the three-component GPEs)

$$
\begin{aligned}
\mathrm{i}\hbar\partial_t\psi_1 &= \left\{-\frac{\hbar^2\nabla^2}{2m}+V+(c_0+c_2)\left[|\psi_1|^2+|\psi_0|^2\right]+(c_0-c_2)\,|\psi_{-1}|^2\right\}\psi_1 \\
&\quad +c_2\psi_{-1}^*\psi_0^2, \qquad (2.70)\\
\mathrm{i}\hbar\partial_t\psi_{-1} &= \left\{-\frac{\hbar^2\nabla^2}{2m}+V+(c_0+c_2)\left[|\psi_{-1}|^2+|\psi_0|^2\right]+(c_0-c_2)\,|\psi_1|^2\right\}\psi_{-1} \\
&\quad +c_2\psi_1^*\psi_0^2, \qquad (2.71)\\
\mathrm{i}\hbar\partial_t\psi_0 &= \left\{-\frac{\hbar^2\nabla^2}{2m}+V+(c_0+c_2)\left[|\psi_1|^2+|\psi_{-1}|^2\right]+c_0\,|\psi_0|^2\right\}\psi_0 \\
&\quad +2c_2\psi_0^*\psi_1\psi_{-1}, \qquad (2.72)
\end{aligned}
$$

where c_0 is the spin-independent coefficient and c_2 is the spin-dependent coefficient. For repulsive gases, the spin-independent coefficient c_0 is positive. In such system, the sign of spin-independent coefficient c_2 characterizes the "magnetic" nature of the ground states of spinor Bose gases, i.e. a negative (positive) sign of c_2 represents a ferromagnetic (anti-ferromagnetic) phase.

The spinor condensates are characterized based on the miscibility and immiscibility of the different spin components. The terms used here are analogous to the mixing of liquid phases: immiscible means the two components are phase separated, as in oil and water; and miscible means the two components are phase mixed. In a simple picture of a homogenous two-component system, labeled by a and b, the mean-field

energy takes the form

$$E = \frac{1}{2}\int \mathrm{d}^3\mathbf{r}\left(g_{aa}n_a^2 + g_{bb}n_b^2 + 2g_{ab}n_a n_b\right), \tag{2.73}$$

where g_{aa}, g_{bb}, and g_{ab} are the interaction coefficients between two identical or different spins. Minimization of this energy gives the criterion for miscibility $g_{ab} < \sqrt{g_{aa}g_{bb}}$ or immiscibility $g_{ab} > \sqrt{g_{aa}g_{bb}}$ [132]. In a ferromagnetic condensate with $c_2 < 0$, one finds the states $m_F = \pm 1$ are immiscible since $g_{1,1} = g_{-1,-1} = c_0 + c_2$ and $g_{1,-1} = c_0 - c_2$; while the states $m_F = +1$ (or $m_F = -1$) and $m_F = 0$ are miscible since $g_{0,0} = c_0$ and $g_{0,1} = g_{0,-1} = c_0 + c_2$. The opposite happens for anti-ferromagnetic condensates where $c_2 > 0$. The alkali species we work with has a ferromagnetic nature since c_2 has a negative value in the $F = 1$ hyperfine manifold of ^{87}Rb $5\mathcal{S}^{1/2}$ ground state [177].

In the presence of external magnetic fields and field gradients, the spinor dynamics governed by Eqs. 2.70-2.72 exhibit a variety of phenomena, including coherent spin mixing, spin textures, spin-domain formation and coarsening [27, 165]. The spin interaction energy $|c_2|\, n$ sets the timescale for the spinor dynamics, where $|c_2|\, n/h \simeq 10\,\mathrm{Hz}$ or $h/\left(|c_2|\, n\right) \simeq 0.1\,\mathrm{s}$ in a typical ^{87}Rb condensate. In spinor condensates, a characteristic length associated with c_2 is the spin healing length $\xi_s = h/\sqrt{2m\,|c_2|\, n_0}$. When the spin healing length is larger than the size of the condensate, the interaction energy is not sufficient to create spin domains in the condensates and hence the spin dynamics in the presence of external field is largely suppressed [26]. For this reason, studies of spin dynamics in Bose gases are generally conducted in elongated quasi

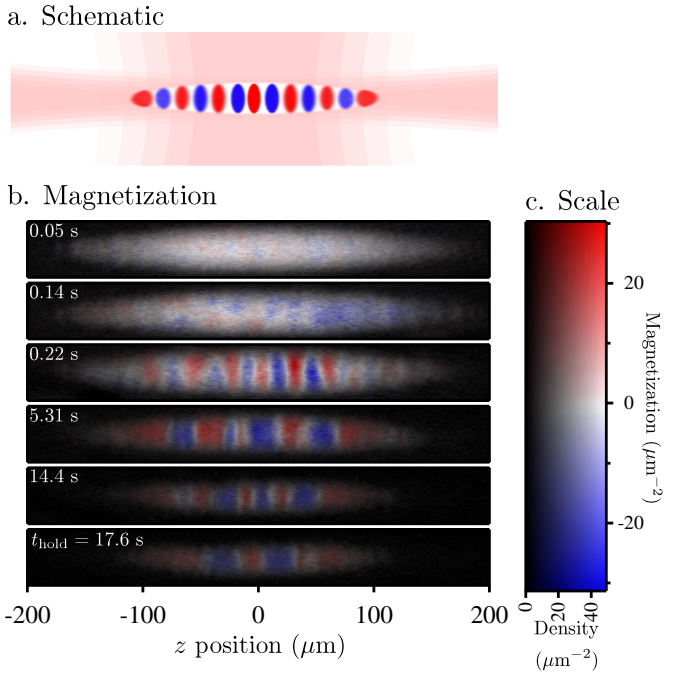

FIGURE 2.6. Magnetization $M_z(\mathbf{r})$ of two-component ^{87}Rb BECs. (a) Schematic illustrating a spinor BEC with domains in an anisotropic crossed-dipole trap. (b) Images showing the progression from a uniformly magnetized condensate (short times) in which domains appear (intermediate times), and then grow spatially (long times); during this process the condensate slowly decays away. (c) Color scale indicating the degree of magnetization (colors from blue to red), and the density (intensity from black to colored).

one-dimensional trap where spatial spin structures have a tendency to form only in the direction of the weak trap axis.

Examples of spin domain formation and coarsening, based on our previous work in Ref. [40], are shown in Figs. 2.6-2.7. Here, we explore the time-evolving magnetization of two-component ^{87}Rb BECs in the $5\mathcal{S}_{1/2}$ electronic ground state. Our BECs are well described in terms of a spinor wave-function $\Psi(\mathbf{r}) = \{\psi_\uparrow(\mathbf{r}), \psi_\downarrow(\mathbf{r})\}$, where the $|\uparrow,\downarrow\rangle$ pseudo-spins label the $|F = 1, m_F = \pm 1\rangle$ atomic spin states. The

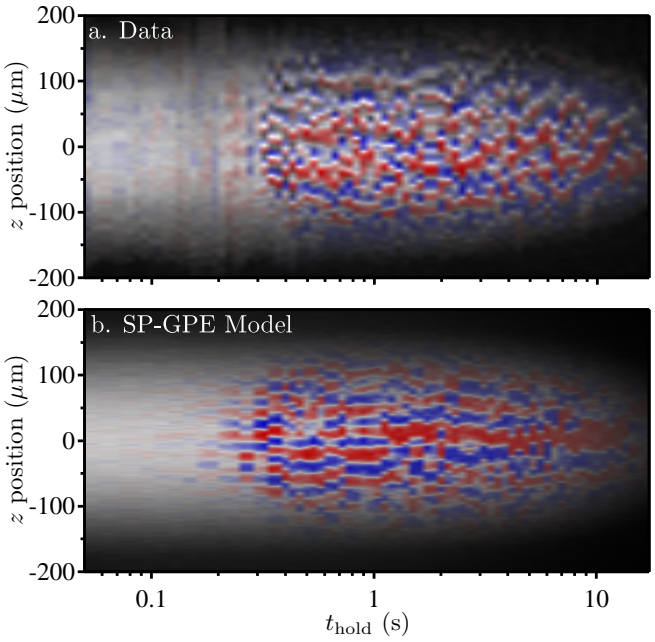

FIGURE 2.7. Time evolution of magnetization $M_z(z)$ of two-component ^{87}Rb BECs. (a) Experimental data and (b) finite temperature simulation using the stochastic-projective GPE method [18]. In both simulation and experiment, the spatial structure of $M_z(z)$ coarsens after an initial growth period as domains coalesce.

$m_F = 0$ is not populated initially, and hence the time evolution of $\psi_0(\mathbf{r}, t)$ stays zero all the time. The dynamics of the two-component BECs are governed by the spinor Gross-Pitaevskii equation

$$\mathrm{i}\hbar\partial_t\psi_{\uparrow,\downarrow}(\mathbf{r}) = \left[-\frac{\hbar^2\nabla^2}{2m} + V(\mathbf{r}) + (c_0 - c_2)\, n(\mathbf{r}) + 2c_2 N \left|\psi_{\uparrow,\downarrow}(\mathbf{r})\right|^2 \right] \psi_{\uparrow,\downarrow}(\mathbf{r}) + \frac{\Omega_\perp}{2}\psi_{\uparrow,\downarrow}(\mathbf{r}), \tag{2.74}$$

a continuum analog to the transverse field Ising model [75]. Here m is the atomic mass; $n(\mathbf{r}) = N\left[\left|\psi_\uparrow(\mathbf{r})\right|^2 + \left|\psi_\downarrow(\mathbf{r})\right|^2\right]$ is the total density; $V(\mathbf{r})$ is a spin-independent external potential; $\Omega_\perp$ describes the Zeeman shift of a "transverse" magnetic field (in

an RF-dressed state); and $c_{0,2}$ are the spin-independent and spin-dependent interaction coefficients [69, 127]. This Hamiltonian has a Z_2 symmetry describing a reversal of $|\uparrow\rangle$ and $|\downarrow\rangle$, which is absent in most binary mixtures [63, 70, 114, 176].

In ^{87}Rb's $F = 1$ manifold, $c_0 = (100.86) \times 4\pi\hbar^2 a_B/m$ vastly exceeds $c_2 \approx -4.7 \times 10^{-3} c_0$ [170]. For a static density profile and when $\Omega_\perp = 0$, each spin component in Eq. 2.74 is separately described by an attractive single-component GPE. In our spinor experiment, we initiated a 34 μs RF-pulse that puts each atom in an equal-amplitude superposition of the $|\uparrow,\downarrow\rangle$ spin states, which is the ground state of the Hamiltonian in Eq. 2.74 when $\Omega_\perp$ is large. The system then evolves according to Eq. 2.74 with $\Omega_\perp = 0$. This procedure is equivalent to rapidly quenching $\Omega_\perp$ to zero.

The quenched binary mixture is held of a variable duration $t_{\rm hold}$, up to 20 s, while spin structure forms and evolves. After $t_{\rm hold}$, we remove the confining potential and allow the atomic ensemble to expand (largely transversely) for 19.3 ms, during which time we apply a Stern-Gerlach gradient force to separate the spin components [51]. We detect the resulting density distribution of each spin component, $|\psi_\uparrow(\mathbf{r})|^2$ and $|\psi_\downarrow(\mathbf{r})|^2$, by absorption imaging. We then study the dynamics of the spin domain formation and coarsening, where the domains are quantized by spatially varying magnetization $M_z(\mathbf{r}) = |\psi_\uparrow(\mathbf{r})|^2 - |\psi_\downarrow(\mathbf{r})|^2$, as shown in Fig. 2.6. The time evolution of the domains as they grow and coalesce is displayed in Fig. 2.7. In this binary spin system, we observe the dynamical generation of spin-domains from an initially non-equilibrium system followed by their subsequent relaxation of progressively larger domains, i.e. coarsening.

CHAPTER 3

Experimental apparatus and procedure

Our experimental apparatus was originally built with a plan to conduct atom-chip experiments, where a nano-fabricated chip with micron scale wires will be placed near the atoms to generate artificial gauge field [6, 131]. However, we shifted our priority as the prototype of the chip was being bench-tested in the lab. Instead, we performed other experiments, such as observation of stripe phase in spin-orbit-coupled (SOC) condensates and study of ultracold atoms in one-dimensional (1D) trap.[1]

In this chapter, I give an overview of our experimental setup and the apparatus we used to laser cool ^{87}Rb and produce Bose-Einstein condensates (BECs) in the `RbChip` lab. I first discuss the optical layouts for each laser cooling system. I describe the green laser and Ti:sapphire laser we used for creating 1D Bose gases and SOC condensates. I next discuss the setup in the main experiment chamber, where the "science" is happening. Lastly, I give details of the control sequences we used to make BECs and the method we developed to calibrate and cancel magnetic field noise.

3.1. Apparatus for laser cooling

3.1.1. Master and cooling lasers. In laser cooling of ^{87}Rb, we use the D_2 line since it has a cycling transition ($F = 2 \rightarrow F' = 3$) for cooling and a repump

[1]As this dissertation is being revised, other lab members finally installed the chip into our main vacuum chamber!

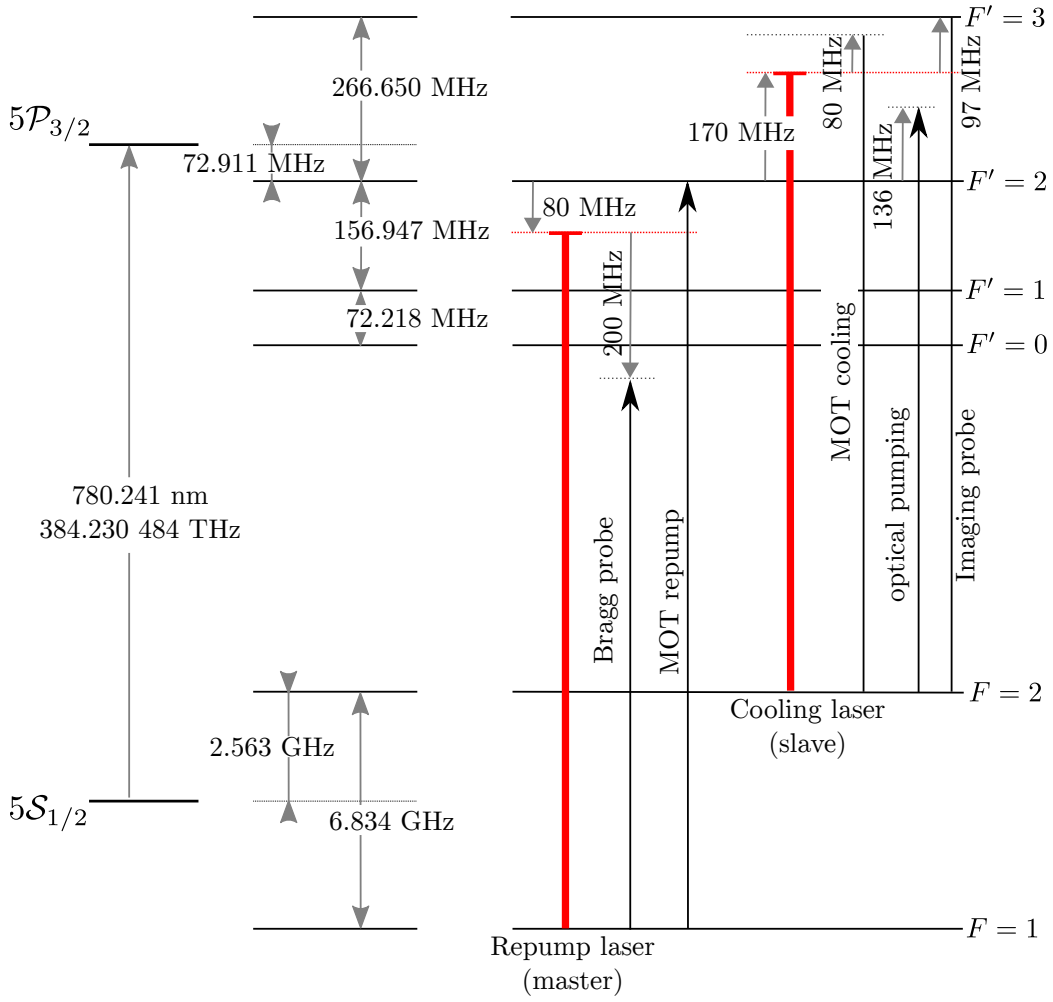

FIGURE 3.1. Schematic of laser frequencies we use in the D_2 line of ^{87}Rb.

transition ($F = 1 \rightarrow F' = 1, 2$) for recycling the atomic population back to its cooling states. The transitions used in our laser cooling setup are shown in Fig. 3.1. Here, two continuous-wave (cw) diode lasers provide the necessary power for laser cooling. Acousto-optic modulators (AOMs) are used to shift the laser frequency, to switch on and off the laser power in several 10's of ns duration, and to control the laser power being injected into optical fibers.

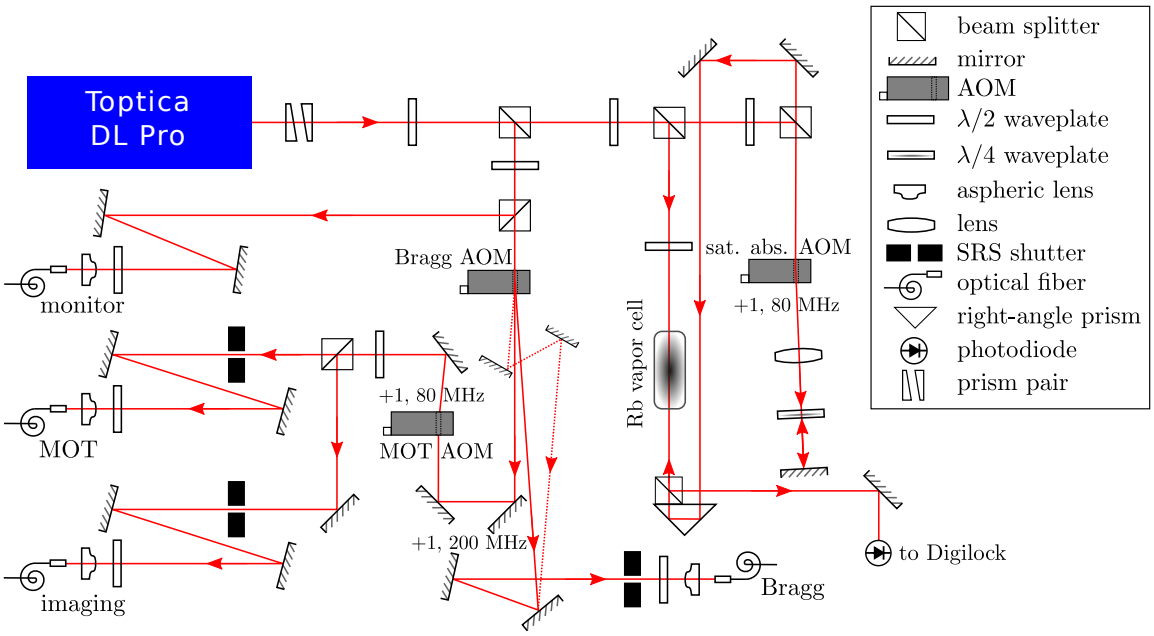

FIGURE 3.2. Optical layout of the master (repump) laser. The master laser is locked to the transition $F = 1 \rightarrow F' = 2$ using saturation absorption spectroscopy of ^{87}Rb. The master laser provides power for the MOT repump, imaging repump, and the Bragg probe.

An optical layout of the master laser which provides the repump light is shown in Fig. 3.2. The master laser `Toptica DL Pro 100` is locked to the $F = 1 \rightarrow F' = 2$ transition in the D_2 line of ^{87}Rb using saturation absorption spectroscopy [137] with an integrated `DigiLock 110` PID module. In this spectroscopy, the frequency of the pump beam is shifted by $2f_0$ with respect to the probe beam, which is performed using an AOM in the double-pass configuration [43]. The frequency commanded to the AOM is $f_0 = 80\,\text{MHz}$, which gives a detuning of $-80\,\text{MHz}$ for the actual master laser frequency from the $F = 1 \rightarrow F' = 2$ transition frequency reference. This master laser provides the repump power for the magneto-optical trap (MOT), absorption imaging, and Bragg probe. Typically, the gross repump power needed is $\sim 30\,\text{mW}$

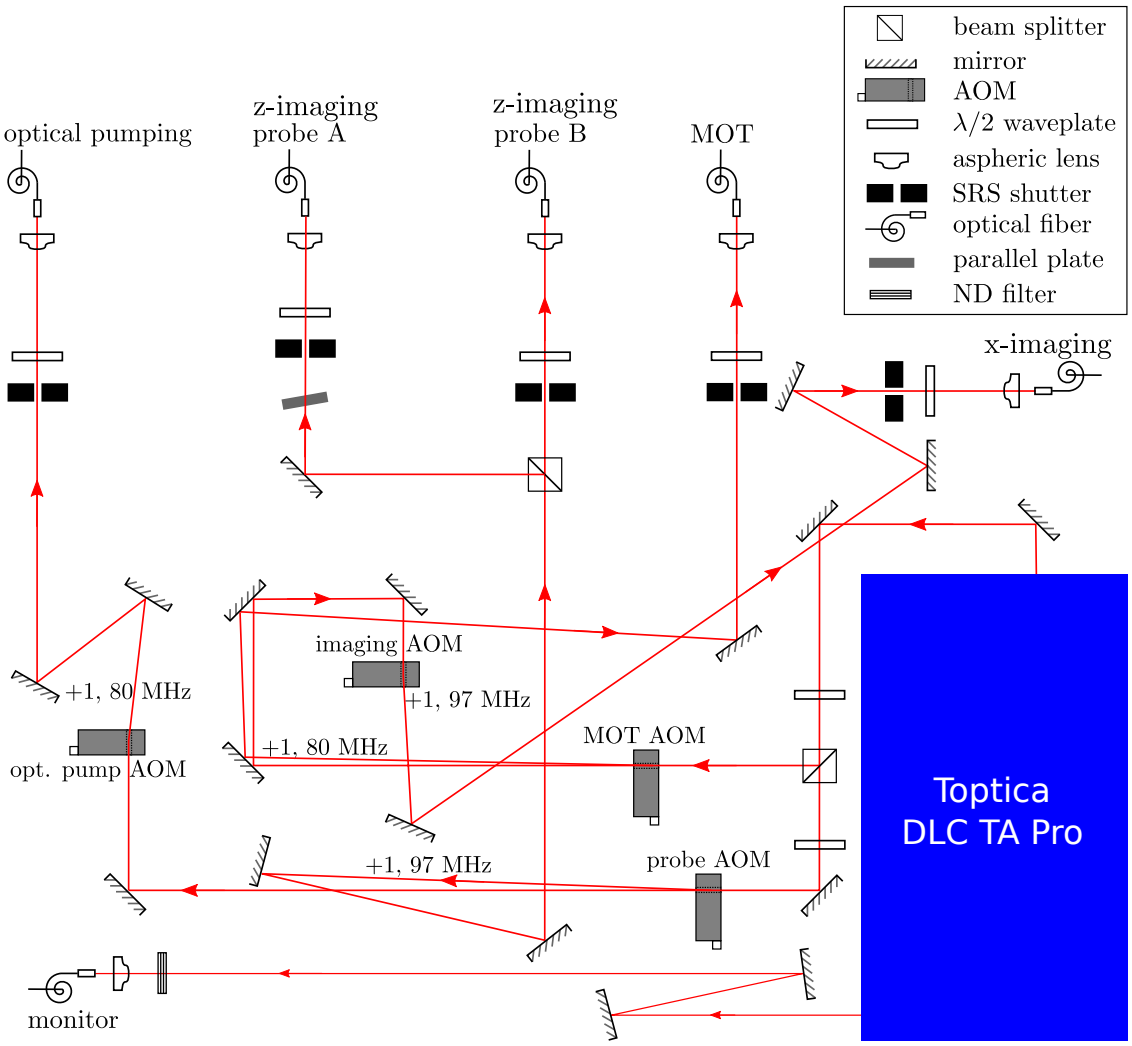

FIGURE 3.3. Optical layout of the cooling (cycling) laser. The "slave" cooling laser is beat-note locked to the master laser. The cooling provides power for the MOT cooling, optical pumping, and imaging in the cycling transition.

with a laser linewidth of $\sim 1-10$ MHz and hence a commercial diode laser is sufficient to provide the repump light.

The second laser (slave) system, an integrated diode laser and tapered amplifier (`Toptica TA Pro`) is beat-note locked [139] with respect to the master laser. The optical layout of the main cooling laser is shown in Fig. 3.3. Here, we used the analog

TABLE 3.1. Reference frequencies for the laser cooling transitions.

Laser transitions,	$F \to F'$	Frequency command (MHz)	Detuning (MHz)
Master laser,	$1 \to 2$	80	-80
MOT repump,	$1 \to 2$	80	0
Imaging (repump),	$1 \to 2$	80	0
Bragg probe,	$1 \to 0$	200 or -200 (and -400)	-51 or -451
Beat-note cooling laser,	$2 \to 3$	102.875×64	-97
MOT cooling,	$2 \to 3$	80	-17
Imaging (cycling),	$2 \to 3$	97	0
Optical pumping,	$2 \to 2$	80 (beat-note at 104.65×64)	136

driving electronics `SYS DC 110` module to control the current and temperature of the laser diode. This module also features the ability to control the laser frequency within a mode-hop-free tuning range of 20 GHz which is important in its application to laser cooling. The tapered amplifier provides ~ 2 W of power used for the MOT cooling, imaging probe in the cycling transition ($|2,2\rangle \to |3,3\rangle$), and optical pumping to the dark states. In addition, the unused monitor output of the MOT cooling fiber fused couplers provides the main beam for very far-detuned Bragg probe for observations of the stripe-ordered phase.

The frequency shifts for the laser cooling transitions are summarized in Table 3.1. The beat-note locked laser frequency has a factor of $\times 64$ from the phase-locked loop (PLL) frequency divider. The frequency command gives a red-detuned shift of the slave laser with respect to the master laser, a net shift of -97 MHz from the $F = 2 \to F' = 3$ transition in the D_2 line. In practice, for frequency scanning of the cooling beams, we scan the beat-note frequency of the cooling laser where each

AOM's frequency is generally kept constant. For the example is given in Table 3.1, the beat-note frequency is set at a different value to give the optical pumping a detuning frequency of 136 MHz from the $F = 2 \rightarrow F' = 2$ transition.

For the Bragg probe, I used a separate optical setup with double-pass AOM configuration to red-shift the frequency by -400 MHz. The single-pass AOM on the master laser system in Fig. 3.2 can be switched to give either $+200$ MHz or -200 MHz frequency shift with respect to the master laser. This corresponds to a detuning of -51 MHz to -451 MHz from the closed transition $F = 1 \rightarrow F' = 0$ in the D_2 line of ^{87}Rb [124]. Variations of the AOM frequencies then allowed me to do a near-resonant Bragg probe with the detuning range of $\Delta = +10$ MHz to -500 MHz for the $F = 1 \rightarrow F' = 0$ transition. For the purpose of doing very far-detuned Bragg probe of the $F = 1$ state, I used the monitor output port of the MOT cooling fiber fused couplers / combiners. This gives a red-detuning of $\Delta = 6.8$ GHz for the $F = 1 \rightarrow F'$ transition within the elastic Rayleigh scattering regime, where $\Delta/\Gamma = 1.1 \times 10^3$ and Δ is much larger than the energy splitting of the F' excited states.

For frequency-shifting using AOMs with typically low input optical power ~ 1 W, we used acousto-optic products from `IntraAction Corp.`, i.e. the `ATM-A2` series (780 nm optical wavelength). To drive the AOMs with a fixed frequency shift depending on the needs of the laser cooling processes, we used a stand-alone radio-frequency (RF) driver with a built-in RF oscillator (matching the center frequency of the AOMs), i.e. the model `DE series`. However, in most applications, time-varying

frequency ramps of the lasers are required and hence we built a customized RF electronic system to drive the AOMs, as will be described in the next subsection. The tunable frequency reference is supplied by a direct-digital-synthesized (DDS) signal generator `Novatech Model 409B` which is programmable in 0.1 Hz steps from 0.1 Hz to 171 MHz.

The capabilities of frequency shifting in this system are constrained by the AOMs' crystal material. The maximum diffraction efficiency of the AOM at its operating center frequency is $\simeq 70-80\%$. Depending on the AOM specifications, the diffraction efficiency usually drops to $\simeq 40\%$ if the RF driving frequency is off by 20% from the AOM operating center frequency. Frequency-shifted beams are then injected through optical fiber launch systems to the atoms in the main glass "science" cell. In this system, the laser powers are controlled by analog voltage sent to the electronic drivers which drive the AOMs.

Although the acousto-optic devices offer switching capabilities at a timescale less than $1\,\mu$s, they do not provide a 100% transmission extinction ratio. Since pW laser power of near-resonant light is enough to heat the atoms and disrupt the cooling process, additional mechanical shutters must be deployed to block leaking light from the AOMs. To do this, we used computer hard-disk-drive (HDD) shutters [106] placed right before the optical fibers. The switching times of these shutters are typically in the order of $< 100\,\mu$s and they can completely block a beam size of ~ 1 mm. The HDD shutters have a 5 ms delay time before mechanical motions are generated once the driving transitor-transistor logic (TTL) signal is received.

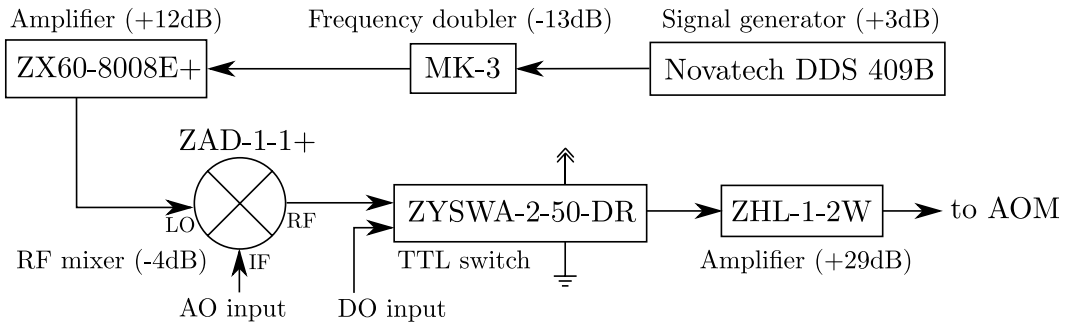

FIGURE 3.4. RF electronics drive of the AOMs.

The HDD shutters have very low cost and are particularly advantageous for high power applications. The shutter flags are easily modifiable, for example a 1/2"⌀ mirror can be glued to the end of the HDD pivot arm to block high power $> 1\,\mathrm{W}$ laser beams. However, the HDD shutters often fail after > 30 thousand cycles (within a year or two). For the latter reason, we opt for commercial shutter systems, such as the `SRS SR474` laser shutter system which has a lifetime of > 10 million cycles. We measured the delay time of the `SR474` shutters to be $3.7(1)\,\mathrm{ms}$ and thus we had to take this delay into account in our experimental sequences when sending digital TTL signals to close or open the shutters.

3.1.2. RF driving electronics. The typical customized RF electronics we used to drive the AOMs are shown in Fig. 3.4. We used a frequency doubler (`MK-3`) after the `Novatech DDS` output to increase the range of the oscillator frequency by a factor of 2. For example, we implemented the doubler to drive AOMs with operating center frequency above $171\,\mathrm{MHz}$. An RF amplifier (`ZX60-8008E+`) was added to compensate attenuation from the frequency doubler. Note these two components were not needed for applications with AOM's operating frequency $< 171\,\mathrm{MHz}$ in

most of our experiments. To be able to control the RF output power via an analog (AO) voltage, we used RF mixer electronics (`ZAD-1-1+`) to combine an oscillating RF source with a programmable analog DC voltage. We then used a TTL switch (`ZYSWA-2-50-DR`) for digital switching of the RF power within 10′s of ns. Lastly, another RF amplifier (`ZHL-1-2W`) was used to raise the RF power to the operating level of the AOMs, which is typically $\sim 1\,\mathrm{W}$.

3.1.3. Laser for red-detuned optical dipole trap. The availability of commercial cw lasers has made evaporative cooling with a 1064 nm red-detuned optical dipole trap a standard practice in the production of ^{87}Rb BECs. In our experiments, we used a single-mode fiber amplifier `IPG YAR-30K-1064-LP-SF` to provide a continuous laser power of $\sim 10 - 20\,\mathrm{W}$ at a wavelength of 1064 nm. The amplifier is seeded by an `NP Photonics FLS-25-1-1064` fiber laser source. The setup for this laser system is shown in Fig. 3.5. It is important to note since this laser falls into the class 4 category (based on the ANSI Z136.1 laser safety standard), appropriate safety precautions must be taken. Hence we used beam dumps in any open-ended paths of the beam.

The 1064 nm laser power is divided into two parts, the main dipole and the weak dipole (see Fig. 3.5). The "main" dipole power is split into two crossed-beam traps in the main experimental chamber to create optical dipole trapping of BECs. Meanwhile, the "weak" dipole power was used in the 1D Bose gases project that was operated by my colleague to provide a weak confinement in the longitudinal axis of a 1D trap.

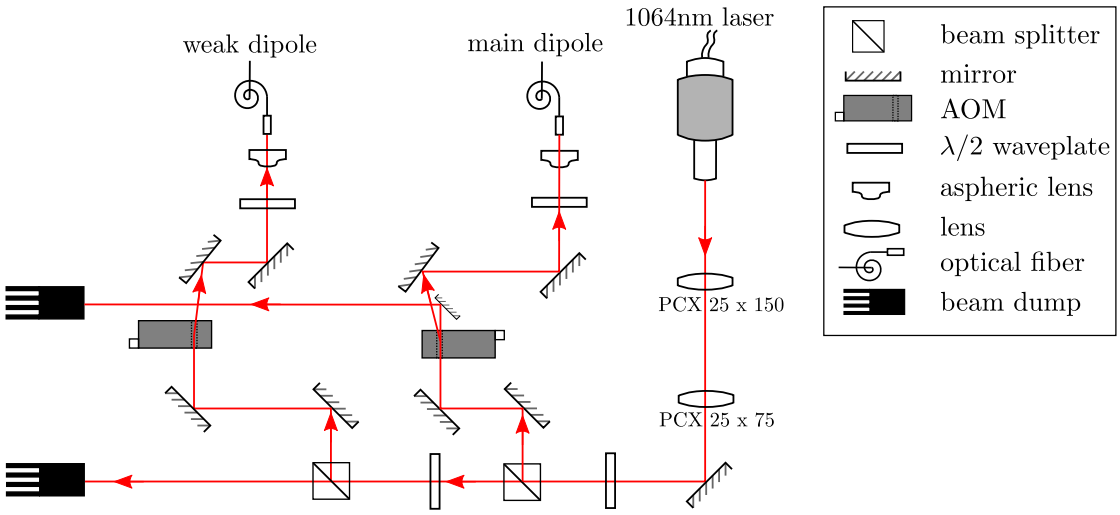

FIGURE 3.5. Laser system for the 1064 nm optical dipole trap.

The 1D trap was created with a 532 nm blue-detuned optical trap with a Laguerre-Gaussian beam [91, 167].

3.2. Green laser and Ti:sapphire laser

The two main research projects going on in the lab as of Summer 2017 involved 1D Bose gases and SOC condensates. A green laser at 532 nm was used to create the 1D blue-detuned optical dipole trap and a Ti:sapphire laser was used to deliver the Raman transitions in SOC condensates. The green laser (25W `Millenia eV`) provides $\sim$ 4W power to the 1D optical dipole fiber injection and $\sim$ 10W pump power to the Ti:sapphire laser `(SolsTiS-SRX-F 4000)`. The optical layout of this laser system is shown in Fig. 3.6. We found the typical warm-up time for these lasers to be about $15-20$ minutes, after which they yielded nominally stable output power within $< 2\%$.

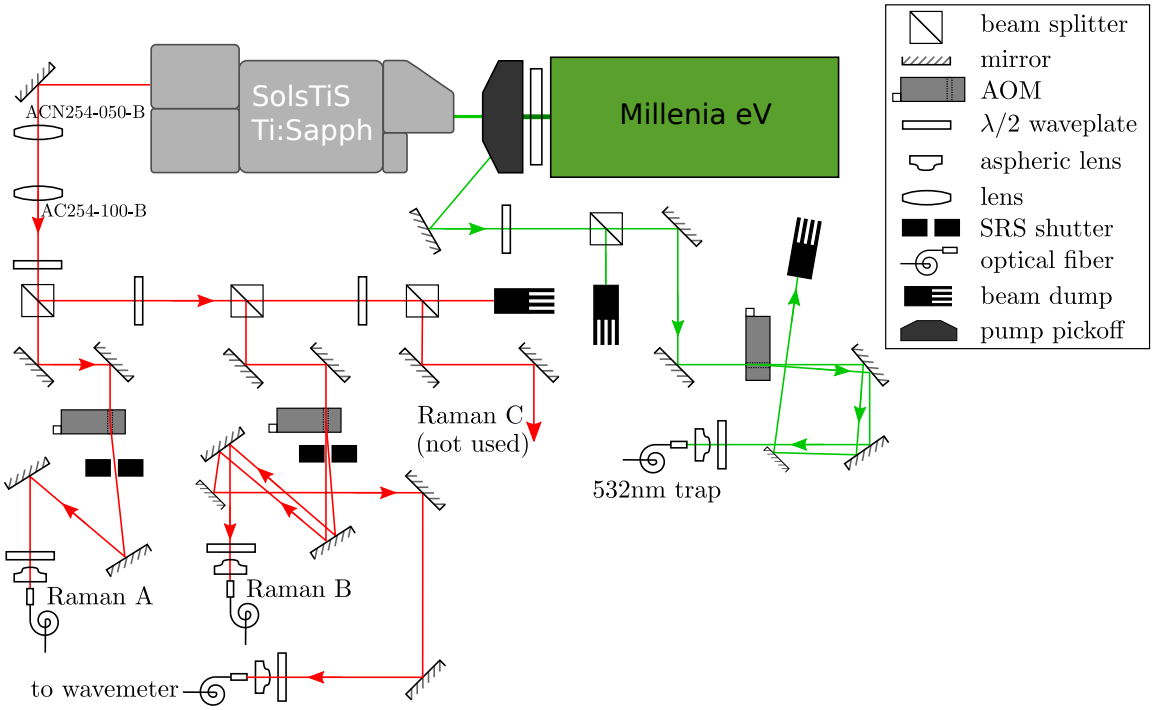

FIGURE 3.6. Optical layout of the Ti:sapphire laser system. A green laser at 532 nm is used to pump the Ti:sapphire laser and to provide blue-detuned optical trap. The Ti:sapphire laser is tunable in near-infrared regime, suitable for Raman applications to create SOC condensates and optical lattice experiments.

The Ti:sapphire laser is tunable in the near-infrared regime $725-875$ nm, suitable to create SOC condensates involving Raman transitions and optical lattices. Tuning of the Ti:sapphire laser is done by first tweaking the intracavity birefringent filter (BRF) via the software user interface of the `SolsTiS` laser. The BRF tuning gives a discrete change for the wavelength of the laser mode, which can take values from 0.15 to 0.80 nm. Next, changing the etalon tuning gives a more precise wavelength in the order of 0.01 nm. The etalon tune control has to be set near the middle of its adjustment range, i.e close to 50%, or else the laser may undergo mode-hopping to the next etalon mode. The single mode operation of the Ti:sapphire laser with etalon

locking gives a spectral linewidth of $\sim 10\,\mathrm{MHz}$, which is sufficient for my experiments. To further reduce the laser linewidth to sub-50kHz, a reference cavity could be used. However, the `SolsTiS SRX` scanning reference cavity was not in operation (in need of repair) at the time of writing this dissertation.

3.3. The main experiment chamber

Figure 3.7 shows our main experiment chamber where BEC is created in an ultra-high vacuum (UHV) environment. The main chamber consists of optical tables, UHV glass cell, vacuum pumps, various electromagnetic sources, and cameras. The atoms are manipulated using various lasers (as described in the previous sections), which are sent through optical fibers and focused to the atoms. Since the original plan for the apparatus was to conduct atom-chip experiments, the main chamber was designed to be composed of the bottom and the upper parts. The bottom part contains cold atoms in a MOT which are transported vertically to the location near the chip in the upper science cell [131], as shown in Fig. 3.7(b). In the upper cell, BEC is achieved and science experiments are performed.

A full explanation on all components of the main experiment chamber requires an extensive description. In this section, my discussion will instead focus on the optical layout on the upper part of the main chamber. Other details on the design of the apparatus can be found in previous dissertation from the group [131].

3.3.1. Optical layout on the upper part of the main experiment chamber. Figure 3.8 shows the optical layout on the upper part of the main experiment

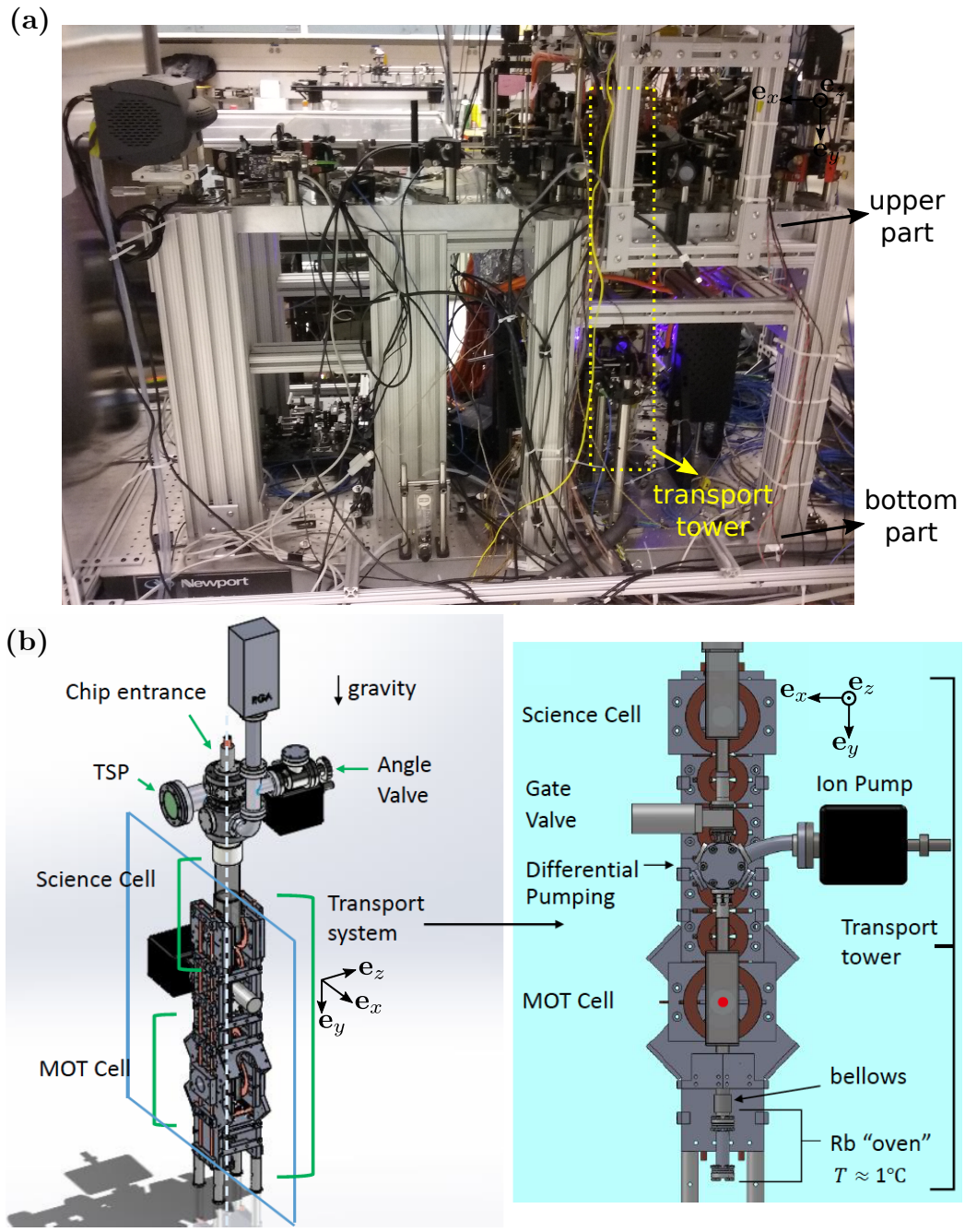

FIGURE 3.7. The main experiment chamber where BEC is created and experiments are performed. (a) Photograph of the `RbChip` main apparatus. (b) An illustration of the vertical magnetic transport system to move the atoms from the bottom cell (MOT) to the upper science cell, as taken from Figure 4.1 of Perry's thesis [131].

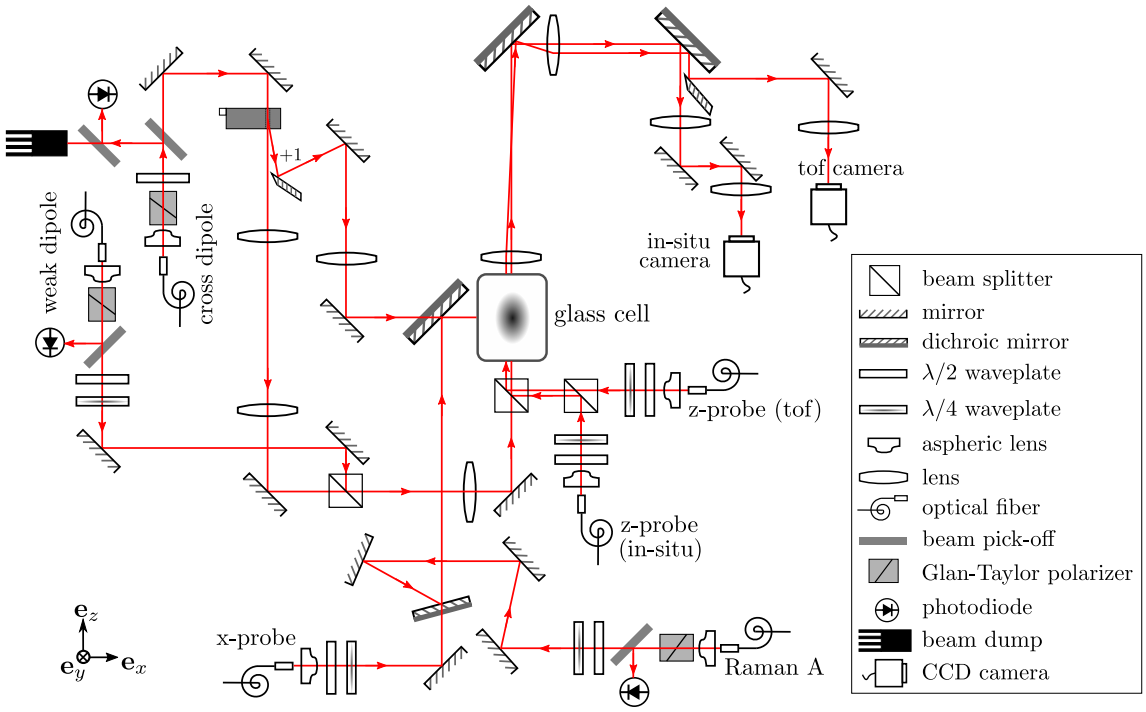

FIGURE 3.8. Optical layout on the upper part of the main experiment chamber. The convention for the Cartesian coordinates used in our lab is as displayed above, with gravity pointing along the $\mathbf{e}_y$ direction. The optical components located on the right side ($+\mathbf{e}_x$ direction) of the glass cell is not shown here (see Fig. 3.9 instead).

chamber. The optical components consist of crossed-beam dipole trap, Raman lasers, absorption imaging systems, and relay assembly for optical Bragg scattering. The relay imaging system is not shown in Fig. 3.8 (see Fig. 3.9 instead) and it will be discussed in the next subsection.

Our optical dipole trap is a crossed-beam setup [61] where one main beam is split into two parts with an AOM. The zeroth order beam with higher power and tighter focus is sent along $\mathbf{e}_z$. This is used to optically trap the atoms after being transferred from the magnetic trap. The +1 order beam with less power and slightly larger beam

waist, is sent along $\mathbf{e}_x$ to serve as the "cross" dipole beam. Evaporative cooling is then performed by exponentially ramping down the overall power of both dipole beams and allowing the highly collisional thermal atoms to be evaporated away.

Typical trap frequencies of our dipole trap are $(\omega_x, \omega_y, \omega_z) = (93, 64, 39)$ Hz. Measurements of the dipole trapping frequencies are done by exciting the sloshing dipole mode [118]. The atoms in the optical dipole trap are given an initial "kick" from a pulsed magnetic gradient force. The frequency of the collective oscillations of the atoms' center of mass is the optical trapping frequency.

Besides using the crossed-dipole beams to make BECs, we also have a weaker 1064 nm optical dipole trap with beam path along $\mathbf{e}_z$. This beam was used to give a lesser trapping frequency (~ 10 Hz) in the $x-$direction for the 1D Bose gases project.

Two counter-propagating Raman lasers are used to create SOC condensates. The Raman A beam along $\mathbf{e}_x$, as shown in Fig. 3.8, provides one of the Raman lasers. Another Raman beam along $-\mathbf{e}_x$, labelled by Raman B, is located on the other side of the glass cell and it will be discussed in the next section (see Fig. 3.9 instead).

Properties of the ultracold atoms are measured using the absorption imaging technique [81]. In our apparatus, we have three absorption imaging systems for different purposes. Two imaging probe beams along $\mathbf{e}_z$ are combined with a beamsplitter to do absorption imaging in situ and at ~ 25 ms time-of-flight (TOF). These imaging systems share the same first telescope pair for the objective and the eyepiece lenses. Since it is important to minimize the aberrations in the in situ image, the optical

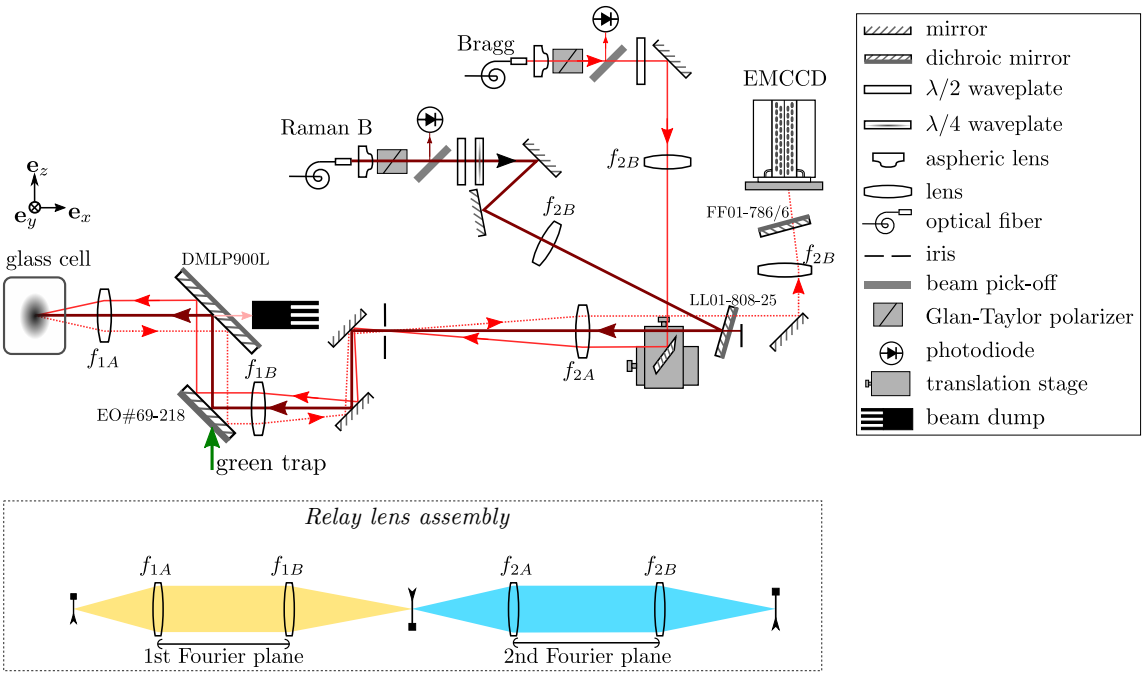

FIGURE 3.9. Relay assembly for optical Bragg scattering experiments. The bottom inset shows schematic of the relay lenses and the two Fourier plane regions as mentioned in the text.

axis of the lens systems is aligned to the in situ location of the atoms. The vertically-spaced in situ and TOF images are then picked up by two separate telescope pairs, giving a total image magnification of 5.22× for the in situ images and 3.11× for the TOF images.

It is important to note the biggest problem we had in our experiment was back reflectance from the glass cell. Each surface of the glass cell gave about 8% reflectance for light at 780 nm wavelength which was unavoidable unless we re-constructed the whole apparatus. For this reason, careful alignment of the optics was crucial to avoid interfering beam from back reflectance.

3.3.2. Relay assembly for optical Bragg scattering. I used an optical Bragg scattering technique to observe the stripe-phase in SOC condensates. Due to limited optical access in our experiment, I had to come up with creative ideas to send our Bragg probe beam in conjunction with the Raman lasers. In addition, I needed to preserve the abilities to do absorption imaging, to combine a 532 nm laser beam, and to dump the 1064 nm red-detuned optical dipole trap within the same optical axis. To satisfy all these requirements, I constructed a relay imaging system consisting of two pairs of $f_1 + f_2$ imaging telescopes (afocal system). The optical setup of the Bragg probe with other laser beams is shown in Fig. 3.9.

The first pair of our relay imaging system was composed of lenses with focal length $f_{1A} = 38\,\text{mm}$ (`EO49-104`) and $f_{2A} = 250\,\text{mm}$ (`AC254-250-B`). The second pair of lenses had focal length $f_{1B} = 250\,\text{mm}$ (`AC254-250-B`) and $f_{2B} = 150\,\text{mm}$ (`AC254-150-B`). In between these two pairs of lenses, I put an iris on the first image focal point to assist with aligning the optics. This relay assembly had a total magnification of 3.9× and it allowed me to have an "arm extension" to send the Bragg beam within the Fourier plane region of the second lens pair.

Similar lenses with focal length of $f_{2B} = 150\,\text{mm}$ (`AC254-150-B`) were used to focus the Bragg probe and the Raman B beam to the atoms. To collimate the Bragg probe fiber output, an aspheric lens `PAF-X-5-B FiberPort` was used to give a 1 mm output waist diameter. A `C220TME-B` collimating lens was used for the Raman beam giving about 2 mm output waist diameter. With 3.9× de-magnification by the relay imaging system, the beam waist diameters seen by the atoms were respectively 250 μm

and 500 μm for the Bragg and Raman beams. To clean up the polarization of the Raman beams and Bragg probe, Glan-Laser `GL10-B` polarizers were used after the collimated fiber output. Photodiodes were used to monitor the power of each Bragg probe and the Raman B beam.

In a well-focused imaging system, a transverse displacement of the Bragg beam automatically turns into a change in the Bragg angle with respect to the optical axis. I used a D-shaped mirror mounted on two linear translation stages to send the Bragg beam at $\lambda = 780.24\,\text{nm}$. To calibrate the Bragg signal, I created periodic modulation to the atomic density distribution by applying an optical lattice potential along $\mathbf{e}_x$ [17, 77]. In my optical lattice system with periodicity of $d = 395.01\,\text{nm}$, the Bragg's angle was $\theta_B = \arccos(\lambda/2d) = 9.02^\circ$ with respect to the optical axis. To satisfy the Bragg's condition, I first aligned the beam's transverse displacement t to be always equal to $t = f_{1A} \cdot \tan(\theta_B) = 6.03\,\text{mm}$ along the Fourier plane region between lenses f_{1A} and f_{2A}. Since the lens pair $f_{2A} - f_{1B}$ formed a 1:1 imaging system, the 1$^{\text{st}}$ Fourier plane in between lenses $f_{1A} - f_{2A}$ mapped directly to the $f_{1B} - f_{2B}$ region.

For alignment purposes, I made sure the Bragg signal was on the same spot with the in situ BEC location, which was easily done with the relay imaging system. I gradually displaced the `Thorlabs PT1` xz-translational stages of the D-shaped mirror using `Newport Model 8302` piezo-controlled motor (Picomotor) actuators. I found the optimum Bragg angle by maximizing the measured in situ Bragg signal. To further optimize and fine tune the Bragg signal, I also rotated the D-shaped mirror with a `Newport Model 8401` Picomotor actuator. I could do a scan of the Bragg angle with

a precision of $\geq 30\,\text{nm}/f_{1A} = 8 \cdot 10^{-7}$ rad limited by the minimum incremental motion of the linear Picomotor actuator. I would like to point out that the Picomotors I used experienced hysteresis and they had no feedback mechanism (open-loop) to measure their exact movements. It was thus important for me to keep track on the scan directions while stepping the translation stages.

The same relay imaging system was used to send the 790 nm Raman B beam and detect the Bragg signal at the wavelength of 780 nm. I used laser clean-up filters to serve as dichroic mirrors for 780/790 nm light. An `LL01-808-25` filter oriented at 33° incident angle acted as an ultra-narrow bandpass filter with 94% transmission at peak wavelength of 780 nm and bandwidth of ±3 nm. The laser line filter was placed at the image focal point of f_{2A} to give the best collimation angle for the Raman beam being sent.

The diffracted Bragg signal was captured using an electron-multiplying charge-coupled device (EMCCD) camera, `iXon Ultra 888`, which has high photon sensitivity. This camera was mounted on custom-made plates to ensure mechanical stability (see Appendix C). The wavelength of the scattered Bragg signal was expected to be 780 nm. To reduce other spurious light making it to the camera, e.g. the Raman laser with 790 nm wavelength, I introduced an additional filter before the camera to block out any unwanted part of the spectrum from the detected light. I used an extra `FF01-786/6` filter which was aligned at 14.5° incident angle to transmit wavelengths of light at 780±6 nm. When performing experiments using the Bragg probe, an easily removable sheet was introduced in the half numerical aperture of the imaging plane

behind the dichroic `LL01-808-25`. The purpose of this was to block most of the high power Raman A beam coming from the opposite side and the atoms' non-interfering fluorescence signal, assuring the light being detected did satisfy the Bragg's condition.

I noted that the dichroic mirrors acted as tilted parallel plates for 780 nm light. They inevitably caused coma and spherical aberrations in our imaging system along $\mathbf{e}_x$. However, since detection of the reflected Bragg signal mostly involved photon counting, these aberrations did not have a significant effect on our optical Bragg scattering measurements.

3.4. Experimental sequences to produce ^{87}Rb BECs

The following is a brief description of the standard experimental sequences we used to produce ^{87}Rb BECs.

- **MOT loading / UV LIAD:** Vapors of ^{87}Rb atoms were first captured in a MOT at the bottom cell for a duration of 1.5 to 3 s. The loading procedure we used was based on the *ultraviolet light-induced atom desorption* (UV LIAD) technique as described in Ref. [85]. An ampule provided the ^{87}Rb metallic source and a custom designed adapter held a thermoelectric cooler (TEC) to control the vapor pressure in the bottom cell. The TEC was usually kept at $< -0.5^\circ$ C. The UV light came from digitally controlled 350 mW light-emitting diode sources (`Mightex SLS-0309-B`, with driver `SLA-1200-2`). The duration of this MOT loading process typically took $2 - 3$ s, depending on the number of atoms we needed to produce.

In daily operations, we turned on the UV source for $15 - 20$ mins to build up enough rubidium vapor pressure before starting our experiments. For a typical experimental cycle with a total duration of 28 s, we found it was best to keep the UV light on for about 8 s, even when we were not loading the MOT. We did this by turning on the UV light in other steps of the experimental cycle, such as during the dipole evaporation stage on the top cell. It was crucial to maintain constant vapor pressure in the bottom cell; since too short a duration of UV light caused the number of atoms in the produced BECs to decrease gradually. On the other hand, too long a duration of UV caused significant heating in the BECs.

- **Compressed MOT :** During this step, the phase-space density of the atoms was increased by compressing the MOT. Magnetic field gradient was produced by a pair of opposing anti-Helmholtz (quadrupole) coils, with quantization axis along the $z-$direction. This was done by ramping up the currents in the quadrupole coils from 8.5 A to 20 A to produce stronger magnetic field gradient within 0.5 s. In our MOT configuration, three extra pairs of Helmholtz coils produced a bias field with adjustable orientation. In this stage, the bias field was also changed to optimize the phase-space density.
- **Optical molasses :** After the compressed MOT stage, the system parameters were adjusted to create optical molasses for a duration of 19 ms. To

do this, the quadrupole field was changed to zero (no magnetic field gradient) and the polarization gradient from interfering counter-propagating lasers cooled the atoms further [37]. The residual bias field was zeroed out in this step because cooling mechanism in optical molasses was very sensitive to stray magnetic field. In this step, the cooling and repump laser powers were kept high enough (several times larger than I_{sat}) to optimize the rate of optical pumping, and the detunings were far enough from the atomic transitions to optimize the cooling process [115].

- **Pre-optical pumping :** In this stage, a small bias field in the $z-$direction was applied by changing the currents on the Helmholtz coils for 1 ms (enough time for the bias field to settle).
- **Optical pumping :** The optical pumping process transferred most of the atoms to the $|F, m_F = 2, 2\rangle$ state within 0.8 ms. A laser beam with σ^+ polarization in resonance to the $F = 2 \rightarrow F' = 2$ transition was shone on the atoms. This eventually pumped most of the atoms to the dark states $|F, m_F = 2, 2\rangle$ via decay by spontaneous emission. We specifically chose the low-field seeking state $|F, m_F = 2, 2\rangle$ due to its highest sensitivity to the magnetic field (the magnetic moment is $|\mu| = h \times 2.1\,\text{MHz/G}$). This allowed us to use smaller currents in our magnetic trap coils to transport the cold atoms vertically.

- **Magnetic trap recapture :** During this step, the quadrupole current was turned on for 0.1 s to recapture atoms in the magnetic trap. We typically ran the quadrupole coil current at 34 A. Next, the magnetic trap was compressed by ramping up the quadrupole current to 90 A in 0.1 ms. This provided a large enough magnetic field gradient of $b' \approx 60\,\mathrm{G/cm}$ (see Eq. 2.36) to hold the atoms agains gravity in the $y-$direction.

- **Vertical magnetic transport :** The $|F, m_F = 2, 2\rangle$ atoms were transported vertically ($y-$direction) in 2.2 s by spatially shifting the magnetic trap center. The transport field was generated using eleven pairs of overlapping coils in anti-Helmholtz configurations with quantization axis along z. The geometries of the coils were fixed and the trap gradient force was kept nominally constant to minimize heating of the atoms during transport. This was achieved by maintaining three constraints during the transport:

$$\frac{\delta B_z}{\delta z} = 120\,\mathrm{G/cm}, \quad \frac{\delta B_z}{\delta y} = 47\,\mathrm{G/cm}, \quad A = \frac{\delta B_z/\delta x}{\delta B_z/\delta y} = 1.28, \tag{3.1}$$

where $\delta B_z/\delta z, \delta B_z/\delta y$, and $\delta B_z/\delta x$ are respectively the magnetic field gradients along the strong (bias field) axis, transport axis, and the non-elongated weak axis. In each step of the transport sequence, three adjacent coil-pairs were energized (except in the very first and last step) sequentially to move the trapped atoms from the bottom MOT cell to the top cell in 2.2 s at an

average speed of 200 mm/sec. Details on the design of the vertical magnetic transport can be found in Perry's thesis [131].

- **RF evaporation :** RF induced evaporation was performed for a duration of 4 s [39]. Forced evaporative cooling was accomplished by linearly ramping the RF frequency from 20 MHz to 3 MHz in a fixed magnetic field with optimum sweep (multiple steps) to keep up with collisional thermalization.

- **Decompression :** The magnetic trap was adiabatically decompressed for a total of 5 s. The decompression of the quadrupole field was done in two stages, each with a duration of 2.5 s. In the first stage, the RF power was kept on at the frequency of 3 MHz and the field gradient was ramped down to a small value below $b' = 15.3\,\mathrm{G/cm}$ (see Subsection 2.2.4) to allow transfer of atoms from the magnetic trap to the optical dipole trap. In the second stage of the decompression, the gradient field was gradually brought to zero to completely load the atoms into the optical dipole trap.

- **Dipole evaporation :** During this step, several stages of evaporative cooling were done successively with exponential ramps of the optical trap power. The atoms were cooled adiabatically via collisional thermalization, reaching a phase density necessary to achieve the phase transition towards quantum degenerate states. In between these evaporation stages, either microwave or RF-dressing could be performed to transfer the atoms from their initial $|F = 2, m_F = 2\rangle$ state to other sub-levels in the $F = 1$ or $F = 2$ manifold.

> In our typical experimental sequences, we performed the first evaporative cooling of the atoms for 3 s to reach the degeneracy temperature and to produce a small fraction of BEC. We transferred the atoms from $|F, m_F = 2, 2\rangle$ state to $|F, m_F = 1, 1\rangle$ state with microwave dressing. BECs in the $F = 1$ electronic ground states of ^{87}Rb were preferable since they have smaller three-body recombination loss rates [21, 157]. We performed a second evaporation stage for 3 s to produce $N \approx 2.2 \times 10^5$ condensed atoms with negligible thermal fractions. We used RF-dressing to transfer the atoms from $|F, m_F = 1, 1\rangle$ state to other m_F states. Finally, we performed a third evaporation stage for 2.5 s to reduce the number of atoms and slightly lower their temperature.

In `RbChip` lab, we used several hardware devices to conduct our experimental sequences. A master hardware device based on a field-programmable gate array (FPGA) card served as the *master clock* to control the timing sequences of other devices. We used a `SpinCore PulseBlaster` to provide TTL pulses with programmable timing sequences. Devices from National Instruments, `NI PCI-6733` and `NI USB-6343`, provide programmable analog voltages and digital signals to our apparatus. Other hardware devices consist of `Novatech 409B` for generating programmable RF frequencies, and `Flea3` charged-coupled device (CCD) cameras for imaging the atoms.

The experimental sequences above were implemented with software interface written in `LabVIEW` or `labscript suite` [161] (an open-source Python based control system). The `LabVIEW` software allowed us to program devices in a serial way and it

was convenient because most of our commercial hardwares came with `LabVIEW`-based libraries. In recent few years, our lab migrated our software control system from `LabVIEW` to `labscript`. This allowed us to use scripted programming on our devices [161]. With `labscript`, a fuller exploration of the parameter spaces was feasible and close-loop optimization of experimental parameters could be done online while running the experiment. However, since it was time-consuming to translate `LabVIEW`-based libraries to Python compatible language, I decided to use the `LabVIEW`-based software for most of my experiments.

3.5. Control of magnetic field

3.5.1. Bias field calibration. We used three pairs of Helmholtz coils to generate DC bias field in our experiments, with the coil quantization axes lie along the x, y, and z directions. The total field B_{tot} near the center of the coil configuration as a function of current I_i of the $i-$th pair is given by

$$B_{\text{tot}}\left[I_i\right] = \sqrt{C^2 \cdot \left(I_i - I_{\text{off}}\right)^2 + B_{\perp}^2}, \qquad i = x, y, z, \tag{3.2}$$

where C is the proportionality constant for the coil strength, $B_{\perp}$ is the field perpendicular to the coil quantization axis, and $C \cdot I_{\text{off}}$ is the offset due to the background DC field along the coil quantization axis.

The calibration of the bias field in the science cell was performed by measuring the total magnetic field experienced by the atoms. To do this we applied an RF-coupling to the atoms and measured the resonance frequency f_{RF} for each value of current

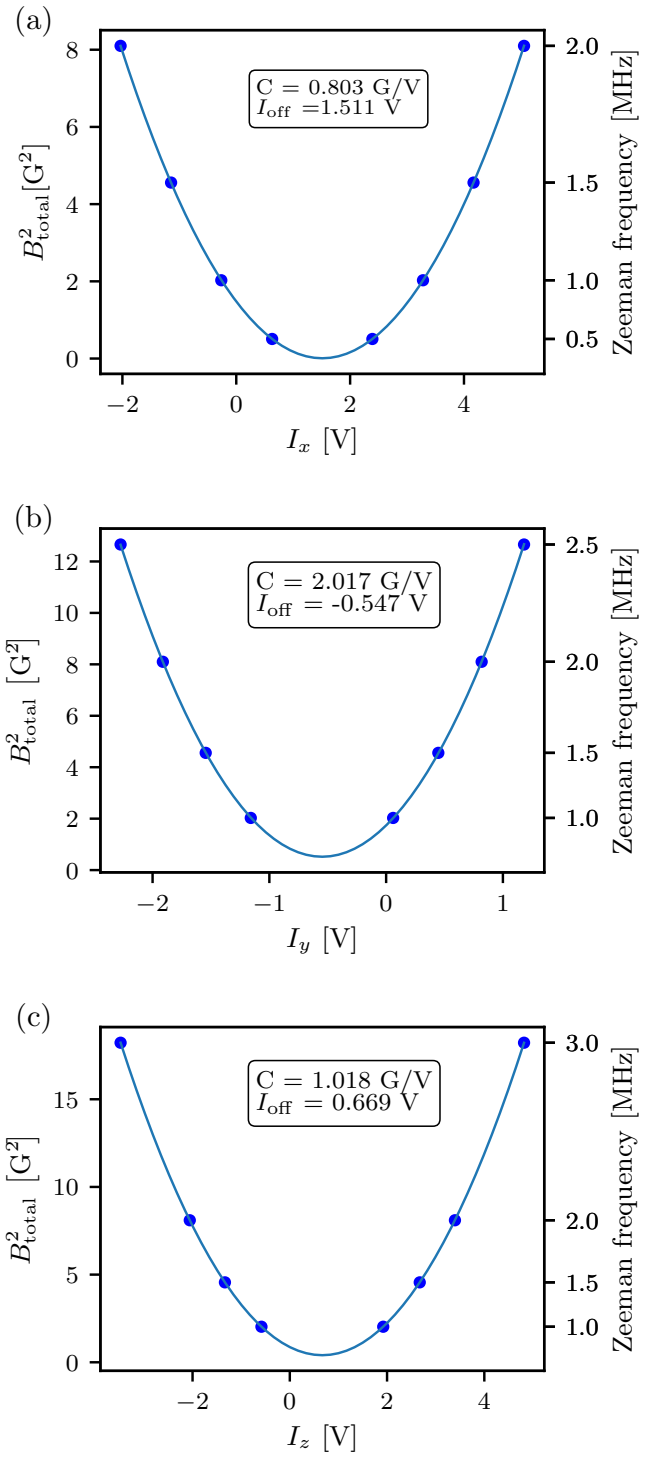

FIGURE 3.10. Bias field calibration for each pair of coils in the Helmholtz configuration. Here the coil current is expressed in terms of the scaled currents I_x, I_y, and I_z.

TABLE 3.2. Calibration parameters for each pair of Helmholtz coils

	x-coil	y-coil	z-coil
C [G/V]	0.803	2.017	1.018
I_{off} [V]	1.511	-0.547	0.669

I_i being sent to the coil. The measured frequency was converted to magnetic field strength by calculating the corresponding Zeeman splitting of the hyperfine structure. For example, RF-coupling between $|F = 1, m_F = -1\rangle$ state and $|F = 1, m_F = 0\rangle$ state within the linear Zeeman regime gives the relation $f_{\text{RF}} = 0.7\,\text{MHz/G} \times B_{\text{tot}}$. We then fit the measurement result to Eq. 3.2 to obtain the coil strength and the offset of the bias field, as shown in Fig. 3.10. In practice, to include all scaling factors from the devices being used, the coil currents were expressed in terms of the applied voltage (V). From these measurements, we found each coil strength C in the units of G/V and each offset current I_{off} to give the zero bias field condition in our experiment cell, as summarized in Table 3.2.

3.5.2. Cancellation of magnetic field gradient. In experiments with spinor BECs, control of the magnetic field gradient is very important. The spatial gradient of a vectorial magnetic field is a tensor quantity with 9 matrix elements. Gauss's law for magnetism $\nabla \cdot \mathbf{B} = 0$ reduces the tensor to 8 independent elements and in current free regions the tensor becomes symmetric with 5 independent components. In practice, we cancelled the gradient for the bias field B_z along the quantization axis

$\mathbf{e}_z$ of the atoms, i.e. $\nabla B_z = 0$. In order to do this, we used three additional pairs of compensation coils, as shown in Fig. 3.11.

The first pair uses anti-Helmholtz coils to cancel $\partial B_z/\partial z$. The other two pairs are arranged in a clover-leaf configuration, as shown in Fig. 3.11(a). These latter pairs of four coils create a dipole-like magnetic field pattern if viewed along x, with zero bias field at the origin. This gave us the ability to compensate the gradient $\partial B_z/\partial x$ (or the gradient $\partial B_z/\partial y$ if the coil setup shown in the right panel of Fig. 3.11(a) is rotated 90° in the $z-$axis).

Due to spatial constraints in the apparatus, we had to modify the setup of the clover-leaf coils. The two clover-leaf pairs, each consisting of four coils, were mounted in such a way they cancel field gradients $\partial B_z/\partial x'$ and $\partial B_z/\partial y$' in $\mathbf{e}_{x'}$ and $\mathbf{e}_{y'}$, where the new Cartesian axes were defined as

$$\mathbf{e}_{x'} = \frac{1}{\sqrt{2}}\left(\mathbf{e}_x + \mathbf{e}_y\right) \qquad \mathbf{e}_{y'} = \frac{1}{\sqrt{2}}\left(\mathbf{e}_y - \mathbf{e}_x\right). \tag{3.3}$$

Further, we had to deform the planar orientation of the clover-leaf coils to make it possible to mount them in our apparatus. The placement of the coils in practice is illustrated in the right panel of Fig. 3.11(b).

To keep things straight, we labelled the currents that go to the coils as: I_A for the set of coils which gave $\partial B_z/\partial x'$, I_B for the set of coils which gave $\partial B_z/\partial y'$, and I_C for the anti-Helmholtz pair which gave $\partial B_z/\partial z'$. In the calibration of the compensation gradient $\partial B_z/\partial x$, we typically scanned I_A or I_B while keeping $I_A + I_B$ constant to

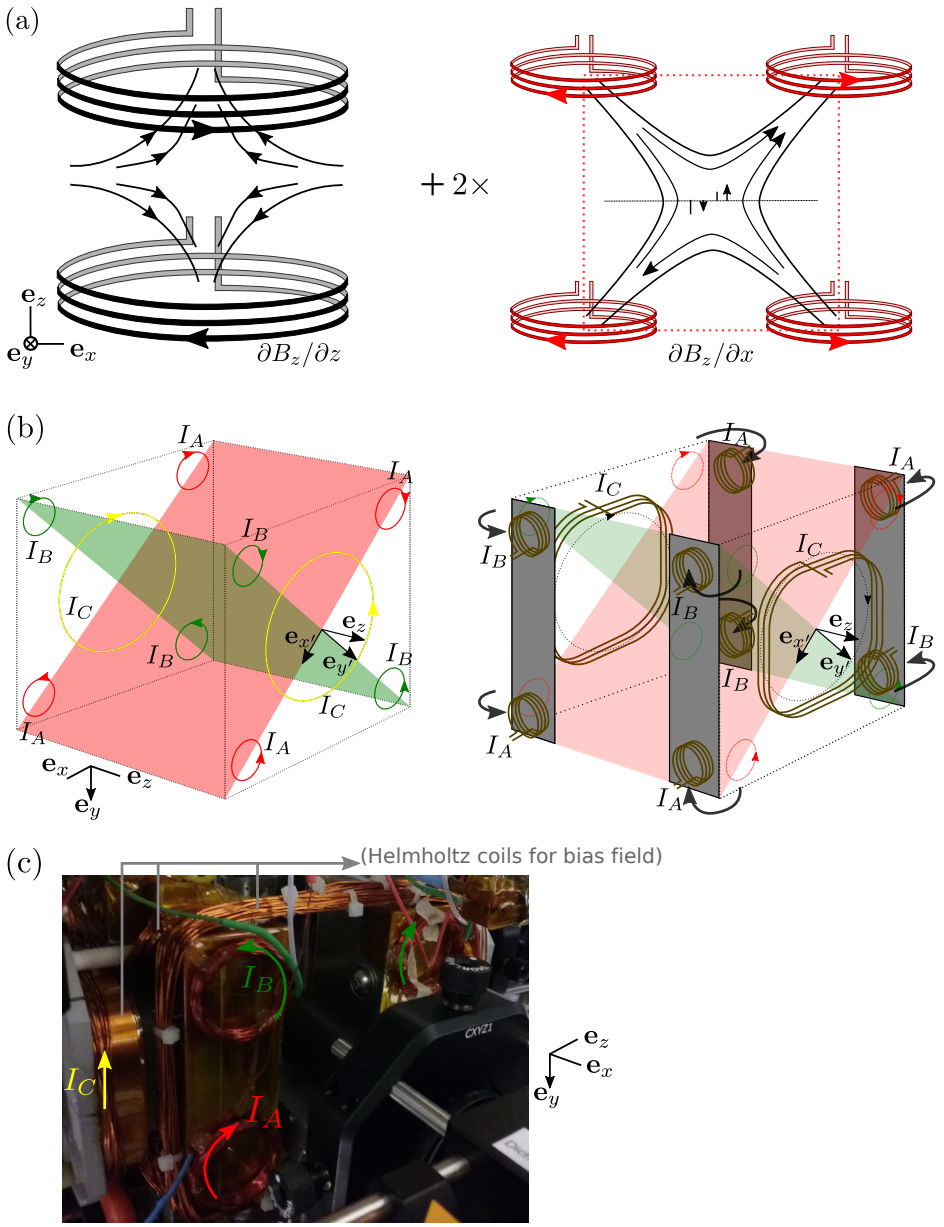

FIGURE 3.11. Configuration of compensation coils used to cancel ambient magnetic field gradient ∇B_z. (a) Conceptual design of the compensation coils. A pair of anti-Helmholtz coils (left) is used to cancel $\partial B_z/\partial z$, while a set of four coils (right) is used to cancel $\partial B_z/\partial x$ or $\partial B_z/\partial y$. (b) In practice, the placement must be adjusted and the coils are deformed to meet the space constraints in the apparatus. I_A, I_B, and I_C are the currents on each set of the coils. (c) Photograph of the gradient compensation coils in our apparatus.

maintain a nominally constant value of $\partial B_z/\partial y$. Similarly, for compensating the gradient $\partial B_z/\partial y$, we scanned I_A or I_B while keeping $I_A - I_B$ constant so $\partial B_z/\partial x$ was not changing. Compensation of the gradient $\partial B_z/\partial z$ was trivially done by scanning the current I_C.

In order to cancel the field gradient, we used the atoms to observe the stray magnetic field gradient near the atoms' location. The simplest method was to use the compensation coils to apply Stern-Gerlach forces to the atoms during TOF imaging (with gravity along y). Atoms with non-zero magnetic moment ($m_F \neq 0$) would have a shifted location after TOF and the strength of the field gradient from the compensation coils could be calculated. The stray field gradient was cancelled if atoms with different spin components fell on the same spot in the TOF camera, independent of their m_F spin state. This method was convenient to measure and compensate the background gradients $\partial B_z/\partial x$ and $\partial B_z/\partial z$, which were present in our system. However, it was not very sensitive to $\partial B_z/\partial y$ along the TOF direction itself, since the atoms had moved in the $y-$direction from their in situ trap location.

A more precise way to cancel the field gradient in situ was to measure the degree of phase mixing in a spinor mixture of Bose gases inside the harmonic trap. For example, the spinor condensates of ^{87}Rb in the $|F = 1, m_F = 0\rangle$ and $|F = 1, m_F = -1\rangle$ states were miscible if there was no field gradient in the system. To quantify the miscibility, I introduce the variables $n_0(\mathbf{r})$ and $n_{-1}(\mathbf{r})$ to represent the spatial density distribution of the $m_F = 0$ and $m_F = -1$ components, respectively. The degree of miscibility is

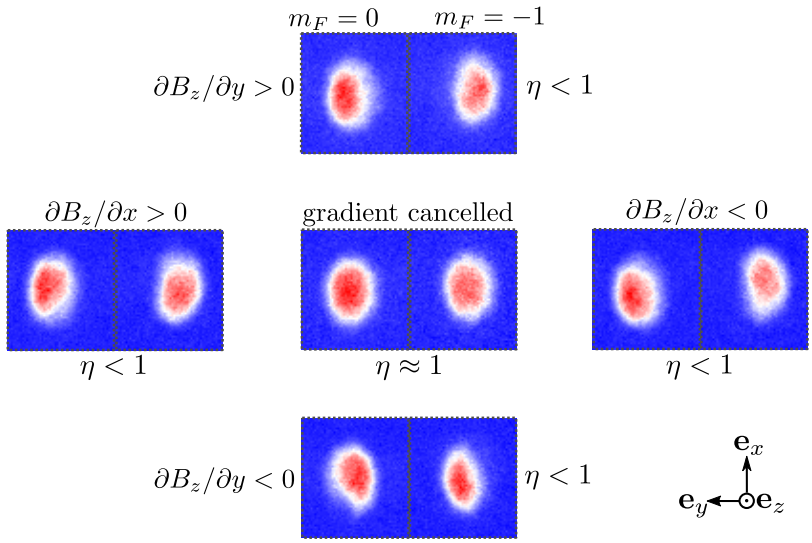

FIGURE 3.12. Images of spinor Bose gases in $|F = 1, m_F = 0\rangle$ and $|F = 1, m_F = -1\rangle$ in the $xy-$plane. The spatial density distributions $n_0(\mathbf{r})$ and $n_{-1}(\mathbf{r})$ are overlapping when the stray field gradient is cancelled. The degree of miscibility is parameterized by a dimensionless metric η as in Eq. 3.4, which has a value $\eta \approx 1$ if the two components are almost perfectly overlapping ($n_0(\mathbf{r}) \propto n_{-1}(\mathbf{r})$).

parametrized by a dimensionless metric

$$\eta = \frac{\langle n_0 n_{-1} \rangle}{\sqrt{\langle n_0^2 n_{-1}^2 \rangle}}, \tag{3.4}$$

where the operator $\langle \ldots \rangle = \int (\ldots)\, \mathrm{d}^3 r$ gives the spatial average over the density products. The metric η takes the value $\eta = 1$ if the two spatial density distributions are perfectly overlapping or $n_0(\mathbf{r}) \propto n_{-1}(\mathbf{r})$, and $\eta = 0$ if the two components are completely phase separated or $n_0(\mathbf{r})\, n_{-1}(\mathbf{r}) = 0$.

Next, I scanned the currents of the compensation coils to optimize the degree of miscibility $\eta \approx 1$. The three-dimensional density distributions of the spin components were obtained from images along two axes, i.e. along $\mathbf{e}_x$ and $\mathbf{e}_z$. Figure 3.12 shows

image examples in the $xy-$plane (image axis along $\mathbf{e}_z$) for spinor Bose gases in $m_F = 0$ and $m_F = -1$ states. If there was a small magnetic field gradient presence, the two spin component were phase separated ($\eta < 1$). This method gave an error for the compensated field gradient on the order of the spin-interaction energy scale over the cloud size, i.e. $\mu_B g_F b' \lesssim 7\,\mathrm{Hz}/10\,\mu\mathrm{m}$ or $b' \lesssim 0.1\,\mathrm{G/cm}$. Calibration of the compensation coils gave me the currents needed to cancel the gradients as $I_A = 0.57(1)\,\mathrm{A}$, $I_B = 0.11(1)\,\mathrm{A}$, and $I_C = -3.18(1)\,\mathrm{A}$.

3.5.3. 60 Hz noise cancellation. The other main source of field noise in our experiment is the power line hum, i.e. 60 Hz field noise and higher order harmonics associated with the alternating current (AC) from the power line. In order to compensate this AC field, we first used a Schmitt trigger [71] to synchronize our experimental sequences with the phase of the 60 Hz power line. This guaranteed our hardware electronics worked at the same phase as the AC power for each cycle of the experimental sequence.

Next, we used the atoms to measure the background 60 Hz noise. Spinor mixtures, e.g. $|F = 1, m_F = 0\rangle$ and $|F = 1, m_F = -1\rangle$, were prepared with RF-sweep through their Zeeman resonance to give nearly 50%/50% equal spin populations [116]. The mixtures were held in their RF-dressed state for a specific duration before being released from the trap and imaged in TOF. Any ambient 60 Hz noise would cause the spin populations to oscillate around their balanced 50%/50% populations.

Lastly, to compensate for the 60 Hz noise, we sent an additional oscillating current to our $z-$bias coil with amplitude $I_{\rm osc}$ and phase ϕ to give a total AC magnetic field

$$B_{\rm ac,tot} = c \cdot I_{\rm osc} \cos\left(\phi + 120\pi t\right) + B_{\rm bg} \cos\left(\phi_{\rm bg} + 120\pi t\right), \tag{3.5}$$

where c is the proportionality constant for the generated field, $B_{\rm bg}$ is the background field amplitude and $\phi_{\rm bg}$ is the phase of the AC magnetic field noise. We then intentionally drove the quantization coil until they were in-phase with the ambient 60 Hz field, $\phi \simeq \phi_{\rm bg}$. We then gradually scanned the amplitude until it was of opposite polarity to the background amplitude, i.e. $c \cdot I_{\rm osc} \simeq -B_{\rm bg}$. This compensated the 60 Hz noise, where $B_{\rm tot} \simeq 0$. Although there are still higher order harmonics (at frequencies of 120 Hz, 180 Hz, etc.), we were nevertheless able to bring the AC noise RMS level down to $\lesssim 100\,\mu$G from typical levels of 1 mG.

3.5.4. Combined feedforward plus feedback control of the magnetic field. A crucial step in conducting our experiments, especially for those requiring hours of experimental cycles, was to counteract drifts in ambient DC magnetic field. To do this we used a combined feedforward plus feedback control system to send correction current to the power supply generating the bias field. The flowchart for this control system is shown in Fig. 3.13.

To measure the ambient DC field, we used a pair of `Stefan-Mayer FL-100` fluxgate magnetometers, which had a sensitivity of 1 V/100 mG and a measurement range of 1 G. Ideally, we would place two magnetometers on opposite sides of the glass

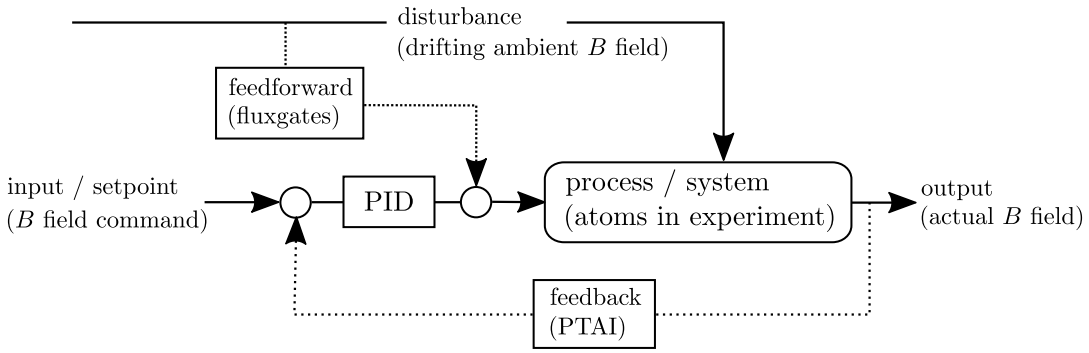

FIGURE 3.13. Flowchart of the combined feedforward plus feedback control system for the DC field.

"science" cell at the same distance from the atoms. The averaged reading of both magnetometers gave the field measurement at the atoms' location. However, due to space constraints in our lab, we only used one magnetometer near the glass cell and assumed the measured field was proportional to the field experienced by the atoms. To reduce radiated noise from the fluxgate electronics and unwanted induced eddy currents, we enclosed the sensors in custom-made aluminum shields.

The fluxgate readings provided measurement of the field disturbance in our system, which was fed forward to the system as a correction to the desired input value. We typically did this reading near the end of each experimental cycle by sending a TTL signal to the fluxgates. Figure 3.14(a) shows how the magnetic field drifted over hundreds of experimental runs, as measured by the magnetometer before the fed forward control system was performed. Each experimental run took about 28 s and the feed-forward signal was updated to the next run after 5 s delay time in programming the next experiment sequence.

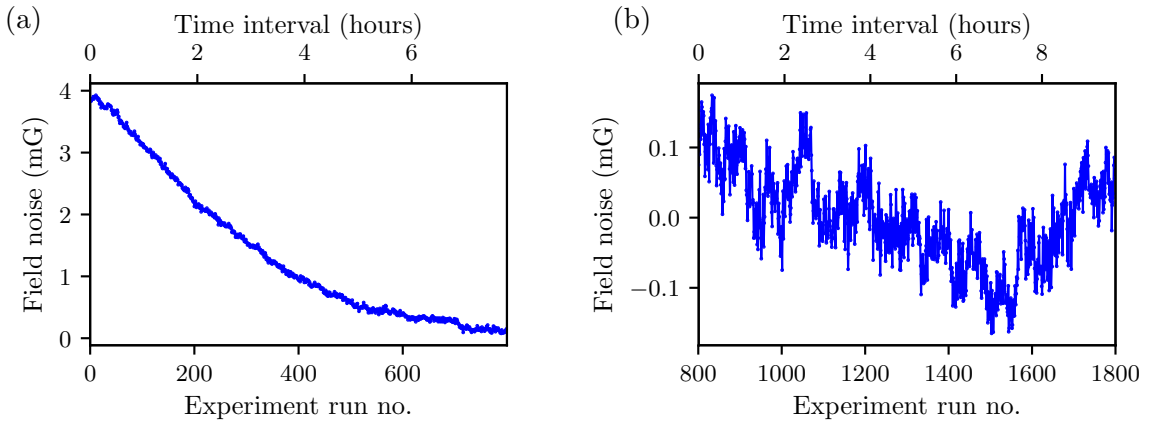

FIGURE 3.14. Magnetic field measured by the magnetometer over hours of experimental runs: (a) before the field control system was in operation, and (b) while the field control system was in operation.

Besides using the magnetometer, we also measured the DC field "output" experienced by the atoms with partial-transfer absorption imaging (PTAI) technique [142]. This technique compared the population of atoms transferred by the red- and blue-detuned microwave pulses, a few ms right before the main sequence of our magnetic field sensitive experiment was performed. The PTAI sensed the "output" field by measuring the population difference of transferred atoms. This measurement took about ~ 10 ms and it was fed back to the field setpoint in the next experimental run.

The fluxgate readings were used to correct for long-term drift of ambient field in the experiment, while the PTAI corrected for short-term errors within each experimental cycle. With both of these "sensors", we thus did a combined feedforward plus feedback control, giving a control of DC magnetic field with a variation of less than $\pm 200\,\mu$G over the course of 10 hours of data taking. Figure 3.14(b) shows the magnetic field variation while the field control system was in operation.

CHAPTER 4

Optimally focused cold atom systems obtained using density-density correlations

In our experiments, properties of ultracold atoms were generally measured with absorption imaging after the atomic cloud was released during time-of-flight (TOF). In this chapter, I discuss a systematic technique to determine the optimal focal plane in absorption imaging of cold atoms, which is a reprint of my previous work published in Ref. [140]. This work was originally initiated as we were studying domain formation and coarsening [40] in spinor Bose gases (see Figs. 2.6-2.7), where we observed spurious noise in the Fourier transform of the images. We eventually found this problem was due to defocus in our imaging system. As the first author of the published work, I developed theoretical models and performed simulations of diffraction-limited wave propagation to quantify the optimal focus. Measurements and analysis of the imaging data (taken by the group) confirmed the models. Accordingly we implemented this technique to identify the optimal focus in our absorption imaging system.

4.1. Abstract

Resonant absorption imaging is a common technique for detecting the two-dimensional column density of ultracold atom systems. In many cases, the system's thickness along the imaging direction greatly exceeds the imaging system's depth of field,

making the identification of the optimally focused configuration difficult. Here we describe a systematic technique for bringing Bose-Einstein condensates (BECs) and other cold-atom systems into an optimal focus even when the ratio of the thickness to the depth of field is large: a factor of 8 in this demonstration with a BEC. This technique relies on defocus-induced artifacts in the Fourier-transformed density-density correlation function (the power spectral density, PSD). The spatial frequency at which these artifacts first appear in the PSD is maximized on focus; the focusing process therefore both identifies and maximizes the range of spatial frequencies over which the PSD is uncontaminated by finite-thickness effects.

4.2. Introduction

Since the most important technique for obtaining properties of ultracold atoms is direct imaging, a well-designed and well-aligned imaging system is crucial for obtaining high quality data which is valid at all length scales. While large scale properties such as the system's width or peak density can be obtained with little effort, significant care must be taken for experiments requiring very good spatial resolution [13, 154], or those studying correlations [47, 73]. It is difficult to bring objects extended along the imaging axis, such as degenerate Fermi gases [56, 146], 3D Mott insulators [58], and Bose-Einstein condensates (BECs) [7, 38], into focus particularly after time-of-flight (TOF) expansion because their spatial thickness often exceeds the imaging system's depth of field. Even for such objects, a high degree of accuracy in focusing is required

to minimize imaging artifacts. Understanding and minimizing these artifacts is particularly important when studying density-density correlations, where the artifacts can be confused with the correlation signal under study [30, 40, 73, 92, 153]. Here we describe a fairly generic technique for focusing on these extended objects which is far more precise than simply optimizing the "sharpness" of imaged atom clouds.

Absorption imaging is a ubiquitous approach for measuring the density distribution of ultracold atom systems [81]. A probe beam illuminates the atomic system, and the resulting shadow is imaged onto a scientific camera, typically a charge-coupled device (CCD) or complementary metal-oxide-semiconductor (CMOS) detector. Ideally, the fraction of light absorbed would be directly related to the two-dimensional column density $\rho_{2\mathrm{D}}(x, y) = \int \mathrm{d}z\ \rho(x, y, z)$ of the atoms along the imaging direction $\mathbf{e}_z$, where $\rho(x, y, z)$ is the density of atoms. If the thickness δz along $\mathbf{e}_z$ exceeds the imaging system's depth of field, then some of the atomic distribution must necessarily be out of focus, invalidating any simple relationship between absorption and column density. Given this, it is a challenge to obtain the optimal focal plane of the extended system that minimizes the artifacts resulting from this defocus, e.g., at the center of a distribution symmetric along $\mathbf{e}_z$.

Typically a system is brought into a focus by minimizing the size or apparent diffraction effects from a compact object such as a trapped BEC; in many cases, no such compact reference at the desired image plane is available. In this paper, we present a technique for determining the optimal focus of absorption-imaged extended objects. Using this technique, we identify the focal plane within an accuracy of

$2\,\mu$m for a $\delta z = 150\,\mu$m thick object. Specifically, given an object with density-density correlations [73] with a spatial correlation length ℓ, we show that observations of correlations in the optical absorption as a function of camera position allow us to bring the object into focus to within a fraction of the depth of field associated with ℓ, even without knowing the details of the correlation function. This optimal focus is the camera position where the imaged auto-correlation function (ACF) most accurately reflects the atomic density-density correlations, minimizing both defocus-induced artifacts and the resolution limiting effect of the system's finite thickness [40, 92].

In this work, we review the basic theoretical formulation required to understand light propagating through an absorbing dielectric medium. We then consider several example images created by different idealized objects, in each case noting how to determine their optimal focus. Lastly, we experimentally apply this technique to images of BECs after TOF.

4.3. Theory

Monochromatic light of free-space wavelength λ and wavenumber $k_0 = 2\pi/\lambda$ propagating through an object with complex relative permittivity $\varepsilon(\mathbf{r}) = \epsilon/\epsilon_0$ and relative susceptibility $\chi(\mathbf{r}) = \varepsilon(\mathbf{r}) - 1$, where ϵ is the permittivity, and ϵ_0 is the electric constant, is described by the vectorial wave equation for the electric field $\mathbf{E}(\mathbf{r})$:

$$\nabla^2\mathbf{E}(\mathbf{r}) + k_0^2\varepsilon(\mathbf{r})\mathbf{E}(\mathbf{r}) = -\nabla\left[\mathbf{E}(\mathbf{r})\cdot\nabla\ln\varepsilon(\mathbf{r})\right]. \tag{4.1}$$

In a medium where $\varepsilon(\mathbf{r})$ is slowly varying, the right-hand side (rhs) of Eq. 4.1 can be neglected, reducing Eq. 4.1 to separate scalar wave equations

$$\nabla^2 E(\mathbf{r}) + k_0^2 \varepsilon(\mathbf{r}) E(\mathbf{r}) = 0, \tag{4.2}$$

for each vector component of $\mathbf{E}(\mathbf{r})$, e.g., we might have $\mathbf{E}(\mathbf{r}) = E(\mathbf{r})\mathbf{e}_x$ for linearly polarized light along $\mathbf{e}_x$.

4.3.1. Wavefield propagation. Here, we cast the above scalar wave equation into the form

$$-\frac{\partial^2 E(\mathbf{r})}{\partial z^2} \;=\; \left[\nabla_\perp^2 + k_0^2\right] E(\mathbf{r}) + k_0^2 \chi(\mathbf{r}) E(\mathbf{r}), \tag{4.3}$$

suitable for light predominantly traveling along $\mathbf{e}_z$. For a known field configuration at $E(\mathbf{r})$ (such as the probe laser before it interacts with the atoms), Eq. 4.3 has the formal solution

$$E\left(\mathbf{r} + \Delta z \mathbf{e}_z\right) \;=\; \exp\left[\pm \mathrm{i}\Delta z \sqrt{\nabla_\perp^2 + k_0^2 + k_0^2 \chi(\mathbf{r})}\right] E\left(\mathbf{r}\right), \tag{4.4}$$

describing the field propagated a distance Δz along $\mathbf{e}_z$.

Wave propagation in free space [i.e., $\chi(\mathbf{r}) = 0$ in Eq. 4.3] is solved exactly in the angular spectrum representation [126]

$$E_{\mathrm{fs}}(\mathbf{r} + \Delta z \mathbf{e}_z) = \mathbf{P}(\Delta z) E(\mathbf{r}) = \int \mathrm{d}^2 \mathbf{k}_{2\mathrm{D}} \left[\tilde{\mathbf{P}}(\mathbf{k}_{2\mathrm{D}}, \Delta z) \tilde{E}(\mathbf{k}_{2\mathrm{D}}, z)\right] \mathrm{e}^{\mathrm{i}\mathbf{k}_{2\mathrm{D}} \cdot \mathbf{r}_{2\mathrm{D}}}, \tag{4.5}$$

for a forward going wave, with the 2D position $\mathbf{r}_{2D} = (x, y)$ and wavevector $\mathbf{k}_{2D} = (k_x, k_y)$; the Fourier-transformed wavefield $\tilde{E}(\mathbf{k}_{2D}, z) = \int \mathrm{d}^2\mathbf{r}_{2D} \exp(-\mathrm{i}\mathbf{k}_{2D} \cdot \mathbf{r}_{2D}) E(\mathbf{r})$; and the transfer function for propagating a distance Δz in free space

$$\tilde{\mathbf{P}}\left(\mathbf{k}_{2D}, \Delta z\right) \;=\; \exp\left[\mathrm{i}\Delta z \left(k_0^2 - k_{2D}^2\right)^{1/2}\right]. \tag{4.6}$$

The transfer function behaves differently in two regions of spatial frequencies: for $k_{2D}^2 < k_0^2$, $\tilde{\mathbf{P}}$ is oscillatory (propagating regime), and for $k_{2D}^2 > k_0^2$, it is exponentially decaying (evanescent regime).

Meanwhile, considering only $\chi(\mathbf{r})$ [neglecting the first term in the rhs of Eq. 4.3], the absorption and refraction of light traveling a distance Δz is described by

$$E_{\mathrm{BL}}(\mathbf{r} + \Delta z \mathbf{e}_z) = \mathbf{Q}(\Delta z) E(\mathbf{r}) = \exp\left[\mathrm{i}k_0 \int_z^{z+\Delta z} \mathrm{d}z \sqrt{\chi(\mathbf{r})}\right] E(\mathbf{r}). \tag{4.7}$$

Unlike the usual Beer-Lambert (BL, discussed in Sec. 4.3.2), this expression alone does not reflect a good approximation to beam propagation for systems of any significant thickness.

4.3.2. Beer-Lambert law and the paraxial approximation . To better understand the independent influence of the beam's propagation and its interaction with matter, we apply the paraxial approximation to Eq. 4.3, allowing us to draw an analogue between the paraxial wave equation and the Schrödinger equation, which can be solved numerically using a split-step Fourier method (SSFM) [76]. To understand the difference between Eq. 4.7 and the usual BL law, we again turn to Eq. 4.3,

now assuming that the electric field can be written as $E(\mathbf{r}) = \exp(\mathrm{i}k_0 z)\, E'(\mathbf{r})$, where $E'(\mathbf{r})$ is a slowly varying envelope along $\mathbf{e}_z$. Inserting this form into Eq. 4.3 gives the paraxial wave equation

$$-2\mathrm{i}k_0 \frac{\partial E'(\mathbf{r})}{\partial z} = \nabla_\perp^2 E'(\mathbf{r}) + k_0^2 \chi(\mathbf{r}) E'(\mathbf{r}), \tag{4.8}$$

where the assumed weak z dependence of $E'(\mathbf{r})$ allowed us to drop $\partial_z^2 E'(\mathbf{r})$. Like above, the spatial evolution of an initial $E'(\mathbf{r})$ can be partitioned into a spectral part $\tilde{\mathbf{P}}'(\mathbf{k}_{2\mathrm{D}}, \Delta z)$ and a coordinate part $\mathbf{Q}'(\Delta z)$, with

$$\tilde{\mathbf{P}}'(\mathbf{k}_{2\mathrm{D}}, \Delta z) = \exp\left(-\mathrm{i}\frac{k_{2\mathrm{D}}^2}{2k_0}\Delta z\right), \tag{4.9}$$

$$\mathbf{Q}'(\Delta z) = \exp\left[\mathrm{i}\frac{k_0}{2}\int_z^{z+\Delta z} \chi(\mathbf{r})\mathrm{d}z\right]. \tag{4.10}$$

For the paraxial approximation to be valid, the condition $|\chi(\mathbf{r})| \ll 1$ must also hold: otherwise the $\mathbf{Q}'(\Delta z)$ evolution would lead $E'(\mathbf{r})$ to depend strongly on z.

We numerically evolve the paraxial wave equation [Eq. 4.8] along $\mathbf{e}_z$ using a split-step Fourier method (SSFM) [46, 87], where the operators in the rhs of Eq. 4.8 are split into two: one operator represents wave propagation in a uniform medium using Eq. 4.9 and the other operator takes into account the effect of refractive index variation using Eq. 4.10. In the SSFM, we alternately apply the two evolution operators with steps of size Δz. For each step, the complex amplitude $E'(\mathbf{r})$ is

propagated first by $\mathbf{P}'(\Delta z/2)$, then by $\mathbf{Q}'(\Delta z)$, and then again by $\mathbf{P}'(\Delta z/2)$. The resulting symmetrized split evolution

$$E'\left(\mathbf{r}+\Delta z\mathbf{e}_z\right)=\mathbf{P}'\left(\Delta z/2\right)\mathbf{Q}'(\Delta z)\mathbf{P}'\left(\Delta z/2\right)E'\left(\mathbf{r}\right), \tag{4.11}$$

has its first correction at order Δz^3.

The paraxial equations allow us to introduce the *depth of field*

$$d_{\mathrm{dof}}=\frac{2k_0}{k_{\mathrm{max}}^2}=\frac{l_{\mathrm{min}}^2}{\pi\lambda}, \tag{4.12}$$

where k_{max}^2 is the largest $k_{2\mathrm{D}}$ of interest and $l_{\mathrm{min}}=2\pi/k_{\mathrm{max}}$ is the corresponding minimum length scale [these might be specified by: the maximum significant wavevector in $\chi(\mathbf{k}_{2\mathrm{D}},z)$; the resolution of the physical imaging system; or at most by k_0].

We obtain the BL law by assuming that the system is thin along $\mathbf{e}_z$, i.e., both $\delta z\ll d_{\mathrm{dof}}$, and $\tilde{\mathbf{P}}'(\mathbf{k}_{2\mathrm{D}},\Delta z)$ may be neglected. For purely absorbing materials where $\chi(\mathbf{r})\propto \mathrm{i}\sigma_0\rho(\mathbf{r})$, this gives the usual BL law

$$I(\mathbf{r}+\delta z\mathbf{e}_z)=\exp\left[-\sigma_0\int_z^{z+\delta z}\rho(\mathbf{r})\mathrm{d}z\right]I(\mathbf{r}) \tag{4.13}$$

describing the attenuation of the free space optical intensity $I(\mathbf{r})=c\epsilon_0\left|E(\mathbf{r})\right|^2/2$ by absorbers of density $\rho(\mathbf{r})$ and scattering cross-section σ_0. This BL result can also be obtained without the paraxial approximation by first neglecting the $\nabla_\perp^2$ term in Eq. 4.3 (valid when $k_{\mathrm{max}}\delta z\ll 1$: a more strict requirement than in the paraxial

approximation where we had $\delta z \ll d_{\rm dof}$) and again assuming $|\chi(\mathbf{r})| \ll 1$, a small relative susceptibility.[1]

In experiment, the BL law is generally applied by comparing the intensities $I(\mathbf{r}_{\rm 2D})$ and $I_0(\mathbf{r}_{\rm 2D})$ measured with and without atoms present, respectively. This relates the optical depth

$$\mathrm{OD}(\mathbf{r}_{\rm 2D}) \equiv -\ln \frac{I(\mathbf{r}_{\rm 2D})}{I_0(\mathbf{r}_{\rm 2D})} = \sigma_0 \rho_{\rm 2D}(\mathbf{r}_{2D}) \tag{4.14}$$

to the 2D column density. In cold atom experiments, this column density is the primary observable in experiment.

4.3.3. Absorption imaging. Here we consider systems of ultracold atoms illuminated by laser light on a cycling transition, where the atom-light interaction is described by a complex relative susceptibility

$$\chi(\mathbf{r}) = \frac{\sigma_0}{k_0} \left[\frac{\mathrm{i} - 2\delta/\Gamma}{1 + I/I_{\rm sat} + (2\delta/\Gamma)^2} \right] \rho(\mathbf{r}). \tag{4.15}$$

$\rho(\mathbf{r})$ is the atomic density; δ is the laser's detuning from atomic resonance; $\sigma_0 = 6\pi/k_0^2$ is the resonant scattering cross-section; Γ is the atomic linewidth; and $I_{\rm sat}$ is the saturation intensity [81]. The standard BL law is valid for dilute ($\rho \ll k_0^3$)[2], spatially thin systems ($k_0 \delta z \ll 1$), illuminated by low intensity ($I_0 \ll I_{\rm sat}$) probe beams.

[1] Moreover, the gradient term $\nabla \ln \varepsilon(\mathbf{r})$ in Eq. 4.1 cannot be safely neglected for systems where $|\chi(\mathbf{r})|$ is large or sufficiently rapidly varying, although this would generally imply a breakdown of the paraxial approximation as well.

[2] A dilute regime, with density $\rho \ll k_0^3$, can be achieved by letting the atomic cloud to ballistically expand.

The $I_0 \ll I_{\text{sat}}$ requirement can be lifted by introducing the intensity-corrected optical depth

$$\text{OD}_{\text{cor}}(\mathbf{r}_{2D}) \equiv -\ln \frac{I(\mathbf{r}_{2D})}{I_0(\mathbf{r}_{2D})} + \frac{I_0(\mathbf{r}_{2D}) - I(\mathbf{r}_{2D})}{I_{\text{sat}}}, \tag{4.16}$$

which is related to the column density

$$\rho_{\text{2D}}(\mathbf{r}_{2D}) = \frac{\text{OD}_{\text{cor}}(\mathbf{r}_{2D})}{\sigma_0}, \tag{4.17}$$

of dilute ($\rho \ll k_0^3$), spatially thin systems ($k_0 \delta z \ll 1$). Due to the limited dynamic range of the camera's pixels [147] and the presence of background light, it is technically difficult to reliably detect uncorrected optical depths, larger than ≈ 4. Thus, we deliberately select $I_0 > I_{\text{sat}}$, saturating the transition with I_0 such that $\text{OD}_{\text{cor}} < 3$.

In addition, the spatial thickness of many cold atom systems exceed the depth of field leaving parts of its distribution along imaging direction inevitably out of focus, thereby invalidating Eq. 4.17. Even for dilute clouds (after sufficient TOF), images taken an equal distance above and below the focal plane can differ. This lack of symmetry makes a straightforward determination of the optimal focus difficult (lensing effects from even slightly off-resonance imaging beams and aberrations in the imaging system can complicate the situation further.)

To illustrate this difficulty, we consider images of BECs with the focal plane displaced a distance $d = -54\,\mu$m, 0 μm, and $54\,\mu$m from the BECs' center (see Fig. 4.1). Because the BEC is thick compared to the depth of field, Eq. 4.17 does not hold; in addition lensing effects cause the cloud's peak OD_{cor} to behave asymmetrically

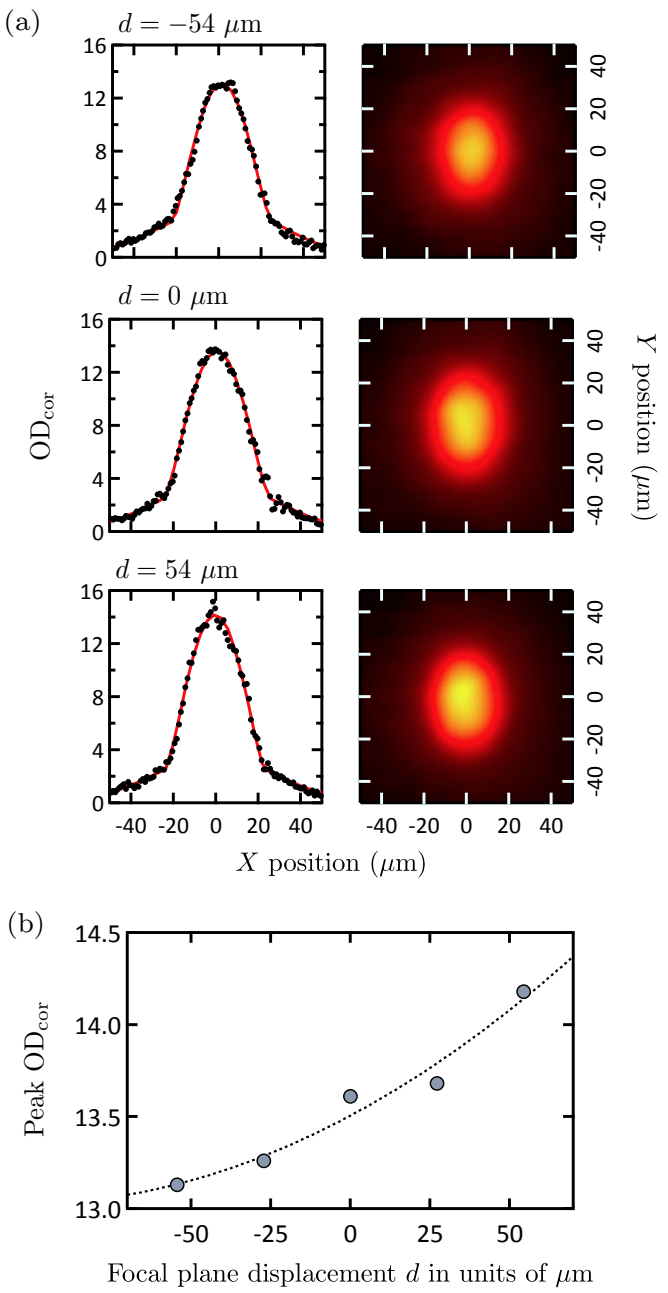

FIGURE 4.1. Dependence of BEC images on image plane position. (a) Intensity corrected optical depth measured $d = -54\,\mu$m, 0 μm, and $54\,\mu$m from the optimal focus: images (right) and line cuts at $y = 0$ (left). (b) The peak optical depth depends only weakly on d; is not maximized at $d = 0$; and has no structure on the $2\,\mu$m scale.

when the focus is behind or in front of the cloud. In these images, there are no sharp features that identify the optimal focus at the micron level. Owing to the weak dependence of large-scale parameters such as peak-height or width on defocus, such precise focusing is not required in many experiments. As we see below, experiments that study correlations within such images are extremely sensitive to defocus and new methods are required. Our technique brings images such as these into focus, identifying an optimal focal plane at the $\approx 2\,\mu$m level.

4.3.4. Modeling. To obtain a basic understanding of our approach, we first consider the defocused image of a $1\,\mu$m thick absorbing medium, inhomogeneous $\mathbf{e}_x$-$\mathbf{e}_y$ plane, bounded above and below by vacuum, with, $\chi(\mathbf{r}) = \mathrm{i}g(x,y)$ for $z \in (-0.5\,\mu\mathrm{m}, 0.5\,\mu\mathrm{m})$, where $g(x,y) \geq 0$ is a Poisson distributed random variable. Like atoms illuminated on resonance, this medium has a purely imaginary susceptibility. The illuminating light is modeled by a plane wave with wavelength $\lambda = 780\,\mathrm{nm}$ suitable for imaging our ^{87}Rb Bose-Einstein condensates.[3] While this object has no visible structure, by virtue of its spectrally flat density-density correlation function, it can be brought into focus.

The imaged intensity pattern $I(x,y)$ from this $1\,\mu$m layer appears random at various distances from focus, but its correlations become oscillatory. To reveal this information, we turn to its spatial power spectral density: the magnitude squared of $I(x,y)$'s Fourier transform.[4] The power spectral density (PSD) is circularly symmetric

[3] In our SSFM simulation of light traversing this medium, we used a $\Delta z = 1\,\mu$m step size.

[4] The Wiener-Khinchin theorem states that the spectral decomposition of the autocorrelation function is equal to the power spectral density.

in the spatial frequency $\mathbf{k}_{2D} = (k_x, k_y)$ plane. Fig. 4.2(a) shows the PSD in this $k = |\mathbf{k}_{2D}|$ "radial" direction as a function of distance from focus d. This PSD has a fringe pattern; the wavevector of the first minimum exceeds the maximum imaged wavevector only near the image's focus at $d = 0\ \mu m$.

The physical origin of this structure can be understood by turning to the paraxial wave equations [Eqs. 4.9 and 4.10], and by first studying a single absorber at $\mathbf{r} = 0$ illuminated by a plane wave $E_0'(\mathbf{r}_{2D}, 0^-) = E_0$. Equation 4.10 shows that a thin absorber simply changes the amplitude of the field, leaving its phase untouched, and for simplicity, we assume this absorber has a Gaussian profile in the $\mathbf{e}_x$-$\mathbf{e}_y$ plane with width w_0. Thus the electric field just following the absorber is changed by $\delta E'(\mathbf{r}_{2D}, 0^+) = -\delta E \exp[-r^2/w_0^2]$, with $r^2 = x^2 + y^2$. The propagation of such a gaussian mode by a distance d along $\mathbf{e}_z$ can be solved exactly in the paraxial approximation, and in the spectral basis this is

$$\delta\tilde{E}'(\mathbf{k}_{2D}, d) = -\pi w_0^2 \delta E \exp\left[-\frac{w_0^2 k_{2D}^2}{4}\left(1 + \frac{2\mathrm{i}}{w_0^2 k_0} d\right)\right]. \tag{4.18}$$

The total field from an absorber located at a different location $\mathbf{r}_0$ in the $\mathbf{e}_x$-$\mathbf{e}_y$ plane simply acquires an overall phase factor $\exp[-\mathrm{i}\mathbf{k}_{2D} \cdot \mathbf{r}_0]$. We now compute the experimentally relevant optical depth by taking the reverse Fourier transform of the full electric field, computing the intensity, then the optical depth, and taking the Fourier

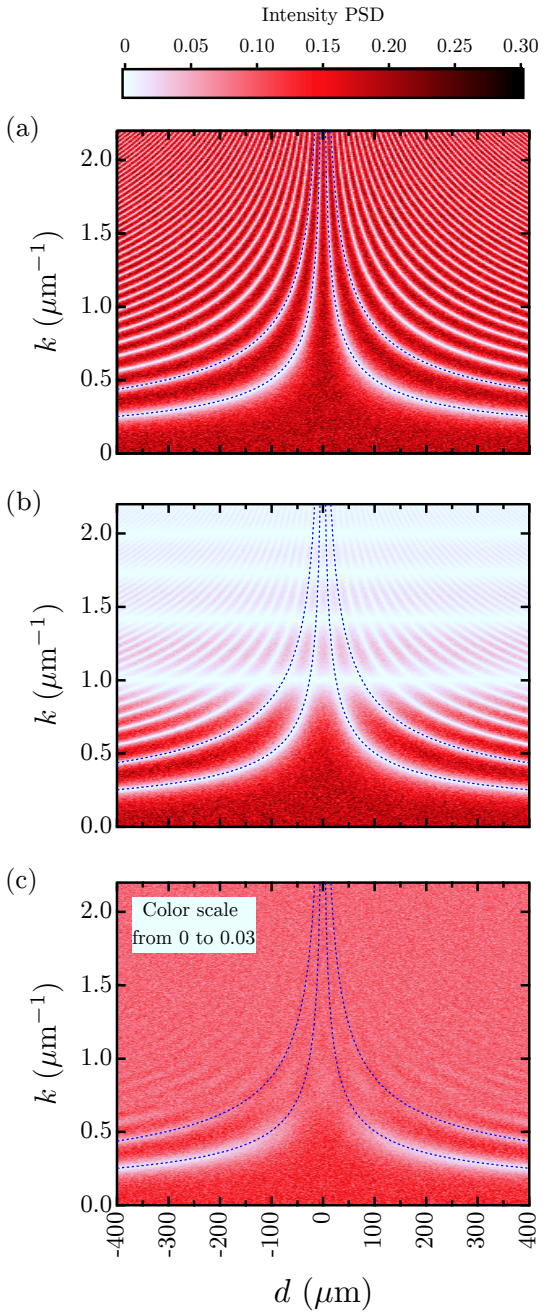

FIGURE 4.2. (a) Spatial PSD of the intensity produced by 1 μm thick layer of randomly distributed scatterers showing that fringes diverge in focus. (b) PSD produced by a 100 μm thick sheet of random columnar scatterers. (c) PSD produced by a 100 μm thick sheet of random scatterers. The dotted lines are functional forms of the lowest curved-fringes, and in each case d is measured from the objects' center.

transform to obtain (retaining terms of order $\delta E/E_0$)

$$\widetilde{\mathrm{OD}} = \frac{2\pi w_0^2 \delta E}{E_0} \exp\left(-\frac{w_0^2 k_{2\mathrm{D}}^2}{4}\right) \cos\left(\frac{k_{2\mathrm{D}}^2 d}{2k_0}\right), \tag{4.19}$$

with the same overall phase factor depending on the initial position. Averaging over N randomly placed absorbers therefore gives an overall signal scaling as $\sqrt{N}$ with a random overall phase. Taking the magnitude squared gives the PSD

$$\mathrm{PSD}_{\mathrm{thin}} = \mathrm{PSD}_0 \times \cos^2\left(\frac{k_{2\mathrm{D}}^2 d}{2k_0}\right), \tag{4.20}$$

with

$$\mathrm{PSD}_0 = N\left(\frac{2\pi w_0^2 \delta E}{E_0}\right)^2 \exp\left(-\frac{w_0^2 k_{2\mathrm{D}}^2}{2}\right). \tag{4.21}$$

This quantity has zeros located at $k_{\mathrm{zero}}[n] = \sqrt{2\pi(n+1/2)k_0/d}$ for integer n. In our numerical simulation, the minima follow the functional form $k_{\mathrm{zero}}[n] = A[n]|d|^{-1/2}$ as shown by the dotted lines in Fig. 4.2, with $A[0] \approx 5.08$ and $A[1] \approx 8.76$ for the first and second zeros: the expected values for $A[n]$. Thus, for this thin apparently structureless system, fringes in the PSD allow us to identify the focal plane.

To demonstrate the technique of finding optimal focus of an extended object, we now consider a second disordered scattering potential with a columnar structure, now $100\,\mu$m thick, i.e., $\chi(\mathbf{r}) = \mathrm{i}g(x,y)$ for $z \in (-50\,\mu\mathrm{m}, 50\,\mu\mathrm{m})$, where again $g(x,y) \geq 0$ is a Poisson distributed random variable. This object's PSD is plotted as a function of distance d from its center in Fig. 4.2(b); in addition to the same fringe pattern as for

the 1 μm thick case, the PSD now vanishes at specific spatial frequencies independent of d. To model this, we note that the absorbers can now be located at a distance z from the symmetry plane, so in Eq. 4.19, we replace $d \to d - z$ and integrate z from $-\delta z/2$ to $\delta z/2$, which ultimately gives the PSD

$$\mathrm{PSD}_{\mathrm{col}} = \mathrm{PSD}_0 \times \cos^2\left(\frac{k_{2\mathrm{D}}^2 d}{2k_0}\right) \mathrm{sinc}^2\left(\frac{k_{2\mathrm{D}}^2 \delta z}{4k_0}\right). \tag{4.22}$$

This predicts the appearance of additional zeros located at $k'_{\mathrm{zero}}[m] = \sqrt{4\pi m k_0/\delta z}$ for non-zero integer m (this is an artifact of the box-like density distribution of atoms, and would be greatly softened in real systems where the density drops smoothly to zero). In our example, the lowest order horizontal fringes is located at $k'_{\mathrm{zero}}[1] = 1.00\,\mu\mathrm{m}^{-1}$. Here again, we easily determine the optimal focus, $d = 0$ μm, from the diverging curved-fringes.

Next, we consider a scattering potential fully disordered in 3D, again with a 100 μm thickness, i.e., $\chi(\mathbf{r}) = \mathrm{i}g(x, y, z)$ for $z \in (-50\,\mu\mathrm{m}, 50\,\mu\mathrm{m})$, where $g(x, y, z) \geq 0$ is a Poisson distributed random variable. In this case, the independent random scatterers along imaging direction causes the PSD to rapidly loose structure with increasing $k_{2\mathrm{D}}$ (see Fig.4.2(c)). Here too, our random scatter model can be applied, giving

$$\mathrm{PSD}_{\mathrm{rnd}} = \mathrm{PSD}_0 \times \left[\frac{\cos\left(k_{2\mathrm{D}}^2 d/k_0\right) \mathrm{sinc}\left(k_{2\mathrm{D}}^2 \delta z/2k_0\right) + 1}{2}\right]. \tag{4.23}$$

This reduces to our earlier result when $\delta z \to 0$ for a thin system and shows that, while the same fringes exist, they are rapidly attenuated for larger spatial frequencies,

where the signal approaches a constant background value. However, in principle the curved-fringes still allow the optimal focus to be identified.

4.4. Optimal focusing of elongated Bose-Einstein condensates

Using on our model, we now consider absorption imaged BECs and implement the technique presented in Sec. 4.3 to find the optimal focus.

We prepared $N = 7\times10^5$ atom ^{87}Rb BECs in the $\left|5\mathcal{S}_{1/2}, f = 1, m_F = 0\right\rangle$ electronic ground state in a crossed-dipole trap with frequencies $\omega_{x,y,z} = 2\pi \times (3.1, 135, 135)$ Hz. In situ, the BECs were javelin shaped owing to the extremely anisotropic confining potential. After a 17 ms to 21 ms TOF, we repumped into the $f = 2$ manifold, and resonantly imaged on the $\left|5\mathcal{S}_{1/2}, f = 2, m_F = 2\right\rangle$ to $\left|5\mathcal{P}_{3/2}, f = 3, m_F = 3\right\rangle$ cycling transition with a $\lambda \approx 780.2\,\text{nm}$ probe laser.

The imaging system consisted of a CCD camera and two pairs of lenses functioning as a compound microscope, magnifying the intensity pattern at the object by a factor of ≈ 6 at the image plane. The first pair of objective lenses, with effective focal length (efl) $\hat{f}_1 = 53.6\,\text{mm}$, collimated the light diffracted by the cloud and were separated by a distance $D = \hat{f}_1 + \hat{f}_2$ from a second pair of lenses with a $\hat{f}_2 = 325\,\text{mm}$ efl. The resulting 0.23 numerical aperture implies that a $10.6\,\mu$m diffraction-limited spot on our CCD sensor is larger than its $5.6\,\mu$m pixel size. The associated $1.7\,\mu$m spot-size on the cloud gives a $d_{\text{dof}} = 18.6\,\mu$m depth of field in our imaging system [74].

Instead of varying the distance from focus by physically moving imaging lenses or the CCD, we changed the time during which the BEC fell along $\mathbf{e}_z$ and obtained

absorption images with TOF times t_{TOF} from 17.0 ms to 21.0 ms. At these TOFs, the condensates' radii were $R_{y,z} \approx 75(5)\,\mu$m and $R_x \approx 210(10)\,\mu$m. Initially, the cloud was elongated in the harmonic trap with aspect ratio 43 to 1. The initial 43 : 1 aspect ratio was reduced to 2.65 : 1 after TOF, and the transverse size of the cloud exceeded the imaging depth of field by a factor of 8.

Figure 4.3(b) shows the 1D PSD of the atoms' corrected optical depths along $\mathbf{e}_z$, which is directly related to the absorption intensity through Eq. 4.16. The fluctuations in the BEC's density distribution behave like the randomly modulated $\chi(\mathbf{r})$ in our example systems, creating a recurring fringe pattern in the PSD spectrum as obtained in Fig. 4.3(c). The fringes are quite pronounced for quasi one-dimensional BECs, where initial phase fluctuations map into pancake-shaped density fluctuations arrayed along the initially long axis after TOF [42]. Despite the decreased contrast at high spatial frequencies due to the BEC extent along $\mathbf{e}_z$, we clearly observe fringes curving as a function of t_{TOF} in Fig. 4.3(c). This allows us to determine the optimal focus of the system.

From the above experimental data, we fit the two lowest order fringes to $k_m \times [(d - z_0)^2/\delta z^2 + 1]^{-1/4}$, a peaked function with the expected $d^{-1/2}$ behavior away from z_0. The fits give an optimal focus location of $z_0[0] = 1836(2)\,\mu$m using the zeroth order fringe or of $z_0[1] = 1837(2)\,\mu$m using the first order fringe. These values correspond to a TOF of 19.36(1) ms. We are thus able to determine the optimal focus within $\approx 2\,\mu$m or equivalently $\approx 10\,\mu s$ in TOF. Comparing the experimental data to the theoretical forms, we notice that the fringes are slightly asymmetrical with their

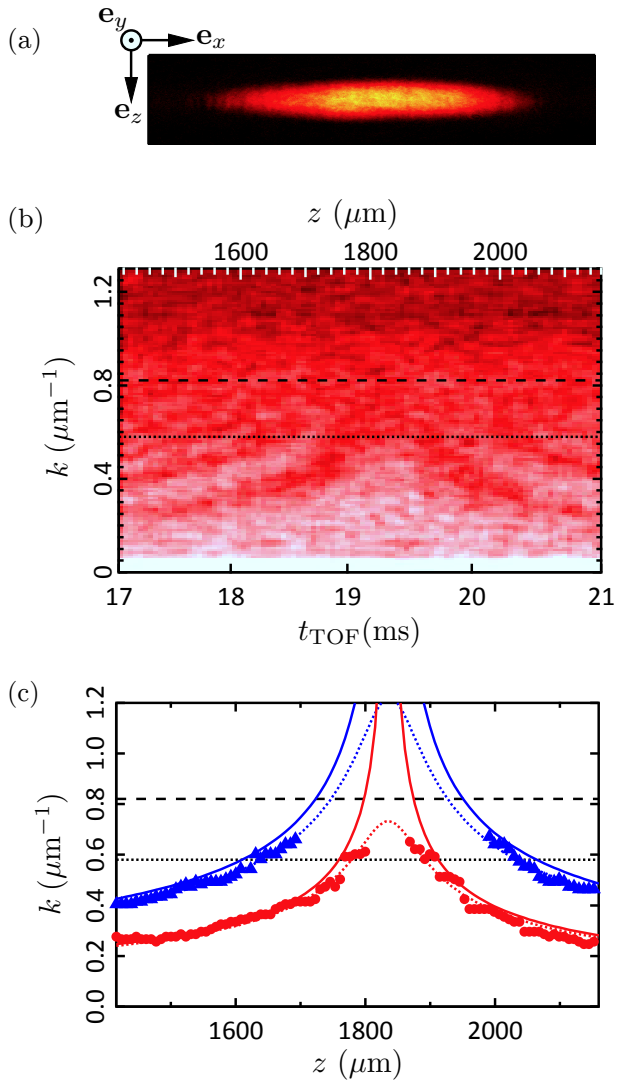

FIGURE 4.3. (a) Absorption imaged elongated BEC with density fluctuations. (b) 1D PSD of column density along weakly trap direction $\mathbf{e}_x$ as a function of t_{TOF}. (c) Values of k where the 1D PSD is minimum. The two lowest such k-fringes are depicted. Symbols denote the fringe locations extracted from (b) plotted along with Lorentzian fits (dotted lines), determining the optimal focus. The solid curves depict theoretical functional forms for the two lowest order fringes. In (b) and (c) the dashed line marks $k = k'_{\mathrm{zero}}[1] = 0.82\,\mu\mathrm{m}^{-1}$ for our condensate thickness of $150\,\mu$m; the dotted line marks $k = k'_{\mathrm{zero}}[1]/\sqrt{2}$, below which the ACF of the focused images reliably reflects the ACF $n_{\mathrm{2D}}(\mathbf{r}_{\mathrm{2D}})$.

locations slightly below theoretical ones for larger TOF. Based on our simulations, this likely results from the z dependent magnification of our imaging system, which changes by about 10% as the atoms fall from 1420 μm to 2150 μm (17 ms to 21 ms TOF).

4.5. Summary

We presented a systematic method to bring clouds of ultracold atoms, particularly initially elongated BECs, into an optimal focus. The density fluctuations in the BECs after TOF acted like random scatterers, creating diffraction pattern which changed predictably as a function of distance from the optimal focus. Using TOF absorption imaging, we demonstrated this method, pinpointing the optimal focus of the BEC to within 2 μm for a 150 μm thick BEC. This robust technique is easily implemented, requires no hardware changes, and uses a minimum of computation.

CHAPTER 5

Coherent manipulation of atoms with electromagnetic fields

Over the past decade, ultracold quantum gases have offered numerous examples of new phases of matter. Control and manipulation have been primarily achieved by coherent interaction between light and matter. Within the semi-classical regime, the classical optical fields perturb the quantized atomic structure where the external electromagnetic waves are treated using Maxwell equations and the atoms are treated quantum mechanically. In this discussion, I consider the electromagnetic waves to be monochromatic (single-frequency) and coherent (having a definite phase relation).[1] Under the influence of light-matter interactions, the atoms behave coherently in a sense that mechanisms which cause dephasing of the atomic wavefunctions can be neglected. For this reason, quantum degenerate gases can have negligible fluctuations in their collective atomic wavefunctions and this makes them potentially useful to simulate various quantum phenomena.

In this chapter, I discuss the coherent manipulation of atoms with electromagnetic waves from the radio-frequency (RF) range to the optical regime. Here, I discuss three different regions of electromagnetic spectrum I used to engineer cold atom systems. First, I used RF waves (with frequency $\sim 1 - 20\,\mathrm{MHz}$) to transfer atoms between

[1]Quantization of the electromagnetic waves leads to the concept of optical "coherence" in quantum optics. Interested readers may find Ref. [52] to be useful.

different m_F states within a specific F manifold. Next, I used microwave radiation (with frequency $\sim 6.8\,\mathrm{GHz}$) to transfer ^{87}Rb atoms among the $F = 1$ and $F = 2$ manifolds of their $5\mathcal{S}_{1/2}$ electronic ground states, enabling me to do minimally destructive partial transfer absorption imaging [142]. Third, I used light from lasers operating in the optical frequency range (with frequency $\sim 380\,\mathrm{THz}$). Exploiting the vectorial light shift of the ac-Stark effect, I used two counter-propagating lasers to create a spin-dependent lattice and spin-orbit coupling to the atomic Zeeman sublevels. This configuration allowed me to engineer various effective Hamiltonians with minimal changes to the experimental setup. Lastly, I will discuss relevant calibration techniques that I used to investigate the effective Hamiltonian under study.

5.1. Adiabatic rapid passage with RF-dressing

RF radiation with MHz frequencies are used to transfer different m_F spin states within the $F = 1$ (or $F = 2$) manifold of the ^{87}Rb atoms electronic ground state. The simplest method to transfer atoms to different states is to do a Rabi oscillation where the atomic states evolve during the pulse duration. However, this approach is very sensitive to detuning and phase noise in the system. A better way to transfer atoms is using the adiabatic rapid passage (ARP) techniques [130, 171] based on the Landau-Zener model [179].

Here, I give an overview of the ARP technique used in our lab to transfer ^{87}Rb atoms among their $5\mathcal{S}_{1/2}$ electronic ground states. Within a two-level system, the

Hamiltonian can be put in the form

$$\hat{H} = \begin{bmatrix} -\frac{\delta(t)}{2} & \Omega \\ \Omega & \frac{\delta(t)}{2} \end{bmatrix} = \begin{bmatrix} -\lambda t & \Omega \\ \Omega & \lambda t \end{bmatrix}, \tag{5.1}$$

where $\delta(t)$ is the detuning between the two states coupled by the RF field with coupling strength Ω. The atoms are brought into RF-dressed states and the time evolution is governed by the dynamics of the detuning. In the Landau-Zener model [179], the detuning is ramped with a linear rate λ. The instantaneous eigenenergies of the Hamiltonian in Eq. 5.1 are given by $\xi(t) = \pm\sqrt{\lambda^2 t^2 + \Omega^2}$. Diagonalization of the Hamiltonian matrix in Eq. 5.1 leads to the adiabatic form

$$\begin{aligned} \mathrm{i}\hbar\frac{\partial}{\partial t}\Psi_A &= \left\{\hat{U}^\dagger H\hat{U} - \mathrm{i}\hbar\hat{U}^\dagger\frac{\partial}{\partial t}\hat{U}\right\}\Psi_A(t) \\ &= \left\{\begin{bmatrix} -\xi(t) & 0 \\ 0 & \xi(t) \end{bmatrix} + \frac{\hbar}{2\left(\lambda^2 t^2 + \Omega^2\right)}\begin{bmatrix} 0 & -\mathrm{i}\lambda\Omega \\ \mathrm{i}\lambda\Omega & 0 \end{bmatrix}\right\}\Psi_A(t) \end{aligned} \tag{5.2}$$

where Ψ_A is the two-component wavefunction in the adiabatic basis. The measure of *adiabaticity* is determined by comparing the off-diagonal coupling to the energy level and requiring that

$$\frac{\hbar\lambda\Omega}{\left[2\left(\lambda^2 t^2 + \Omega^2\right)\right]^{3/2}} \ll 1. \tag{5.3}$$

Equation 5.3 guarantees the atomic states can "follow" the time changing Hamiltonian. The ratio in Eq. 5.3 has its highest value at $t = 0$ and hence the condition $\hbar\lambda/2\Omega^2 \ll 1$ is met by selecting a strong coupling Ω and a low rate of the detuning ramp λ.

Although it is non-trivial, the time-evolving Landau-Zener model in Eq. 5.2 is exactly solvable. In the long time limit (starting from $t \to -\infty$), the probability for the system to remain in its initial eigenstate is given by

$$P_{\text{initial}} = \exp\left(-\pi\Lambda\right), \tag{5.4}$$

where the adiabaticity parameter is $\Lambda = \Omega^2/\hbar\lambda$. A full transfer between the two-atomic states ($P_{\text{initial}} \simeq 0$) thus is easily achievable by selecting large Λ. The adiabaticity of the transfer is easily understood by comparing the bare uncoupled energies $\pm\lambda t$ to the adiabatic energies $\pm\xi(t)$, as shown in Fig. 5.1(a). Although the bare energies have a cross over at $t = 0$, the coupled energies have an avoided crossing and hence a small fractional population $1 - P_{\text{initial}}$ gets transferred to the others states, unless the ramping rate is very slow. Since the process of population transfer must occur in a timescale shorter than the radiative lifetime of the excited state, this technique is often known as "rapid" adiabatic passage as well.

In many practical cases, we would like to partially transfer atomic populations, i.e. $P_{\text{initial}} \sim 0.2$ or $\Lambda \sim 0.5$, while still satisfying the adiabaticity condition $1/\Lambda \ll 1$. To achieve this, we can apply specific sequences for the detuning ramp $\delta(t)$ and the coupling strength Ω. In our experiment, we apply a half-Gaussian ramp to the detuning parameter $\delta(t)$; this involves a slow ramp of $\delta(t)$ in the beginning, followed by a speeding up near the avoided crossing to give enough population transfer, and finally ending with a slow change in $\delta(t)$ to let the atoms follow the adiabatic eigenenergies.

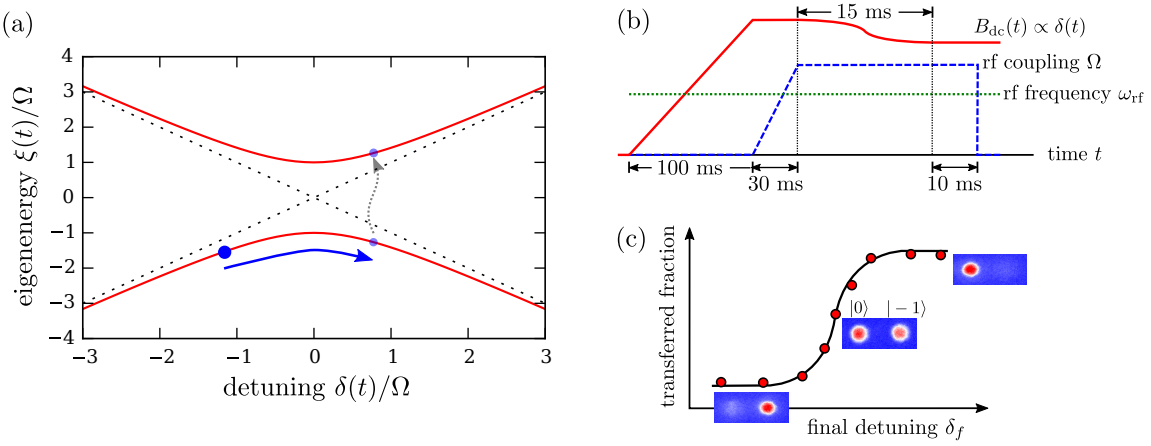

FIGURE 5.1. Transfer of atomic populations between the $|F=1, m_F=-1\rangle$ and $|F=1, m_F=0\rangle$ states with RF-dressing at coupling strength Ω. (a) Avoided crossing in coupled two-level system. (b) Experimental sequence to ramp the detuning $\delta(t)$ in time. (c) Transferred population of the coupled two-level system.

For example, I consider ARP between the $|F=1, m_F=-1\rangle$ and $|F=1, m_F=0\rangle$ states with RF-dressing at coupling strength Ω. The time sequence of the ARP is shown in Fig. 5.1(b). To change the detuning $\delta(t) = \mu B_{\rm dc}(t)/\hbar - \omega_{\rm rf}$, we ramp the bias field $B_{\rm dc}(t)$ instead of the RF frequency $\omega_{\rm rf}(t)$. We operate at low field $B_{\rm dc} \lesssim 20\,\text{G}$ in the linear Zeeman regime where the magnetic moment of the state under consideration is $\mu = 0.7\,\text{MHz/G}$. The sigmoid functional ramp in $B_{\rm dc}(t)$ to its final value takes a duration of 15 ms; we hold the system in the RF-dressed state for 10 ms; and we finally turn off the RF-coupling and project the atoms to their bare spin states. A "controlled" population transfer between the two states is then achieved by controlling the final value in the detuning ramp $\delta(t \to \infty) = \delta_f$ as displayed in Fig. 5.1(c). I note this approach can be extended to three-level system as well [116], such as coupling between the $m_F = -1, 0$ and $+1$ states of the $F = 1$ manifold.

5.2. Microwave-assisted partial-transfer absorption imaging

Electromagnetic radiation at $\sim 6.8\,\mathrm{GHz}$ can be used to transfer ^{87}Rb atoms among the $F = 1$ and $F = 2$ manifolds of their $5\mathcal{S}_{1/2}$ electronic ground states, as shown in Fig. 5.2(a). This radiation is in the *microwave* band. In our experiments, microwave radiation is broadcast by an antenna horn. For details on the experimental setup of the microwave source, see Ref. [131].

In this section, I discuss the application of microwave-assisted partial-transfer absorption imaging (PTAI) to provide feedback in our dc magnetic field control. A small fraction of atoms in the $F = 1$ manifold is transferred to the $F = 2$ manifold, and the atoms are imaged in the cycling transition $F = 2 \rightarrow F' = 3$ using absorption imaging. This technique is non-destructive to the atoms in the initial $F = 1$ state as they are unaffected by the imaging light [142]. If there is any detuning present between the two successive microwave pulses being applied, there is imbalance in the transferred populations of the atoms. Within an experimental cycle, we then use two successive PTAIs to provide a real-time feedback of magnetic field error from the setpoint.

To control the magnetic field to be better than mG precision, I transfer a small fraction of ^{87}Rb atoms from the ground state $|1, -1\rangle$ to the excited state $|2, -2\rangle$. I use this transition since it has the highest sensitivity to the magnetic field.[2] Pulsing the microwave for a duration τ, I partially transfer the atoms to the $m_{F'} = -2$

[2]The difference in the magnetic moment is maximum for either $|1, -1\rangle \rightarrow |2, -2\rangle$ or $|1, +1\rangle \rightarrow |2, +2\rangle$ transition with $\Delta\mu_F/h = 2.1\,\mathrm{MHz/G}$ in the linear Zeeman regime.

state. The coupling strength of the pulse was chosen to be $\Omega_0 \ll 1/\tau$ to guarantee the Rabi evolution is less than a $\pi/2$ rotation on the Bloch sphere. I used two subsequent microwave pulses with specific red- and blue-detuned frequencies $\mp\delta_0$ from the transition resonance (see Fig. 5.2(a)). The Rabi pulse between the two-level system yields the fractional population being transferred as:[3]

$$\begin{aligned} P(\Delta_\pm) &= \frac{\Omega_0^2}{\Omega_0^2+\Delta_\pm^2}\sin^2\left(\frac{\sqrt{\Omega_0^2+\Delta_\pm^2}\tau}{2}\right) \\ &= \left(\frac{\Omega_0\tau}{2}\right)^2 \mathrm{sinc}^2\left(\frac{1}{2\pi}\sqrt{\Omega_0^2+\Delta_\pm^2}\tau\right) \end{aligned} \tag{5.5}$$

where $\Delta_\pm = 2\pi(\delta_{\mathrm{DC}} \pm \delta_0)$ is the combined detuning due to the magnetic field drift δ_{DC} and intentionally chosen microwave detuning δ_0. Figure 5.2(b) shows the fractional population transfer for blue- and red-detuned pulses as a function of δ_{DC}. I then measured the normalized population imbalance between the two successive microwave-assisted PTAIs:

$$N_{\mathrm{imb}} = \frac{P(\Delta_+) - P(\Delta_-)}{P(\Delta_+) + P(\Delta_-)}, \tag{5.6}$$

which was converted to provide feedback correction to the bias field detuning δ_{DC}.

In my experiments, I used $\tau = 400\,\mu$s and $\delta_0 = 1.25\,$kHz (the combined blue- and red-detunings are $\Delta_\pm/2\pi = \delta_{\mathrm{DC}} \pm \delta_0$). Figure 5.2(c) shows experimental measurements of $P(\Delta_\pm)$ and N_{imb} as a function of intentionally introduced field detuning

[3]The cardinal sine function has two definitions, the unnormalized sinc function $\mathrm{sinc}(x) = \sin(x)/x$ and the normalized sinc function $\mathrm{sinc}(x) = \sin(\pi x)/\pi x$. Here I use the latter definition as commonly used in information theory [164].

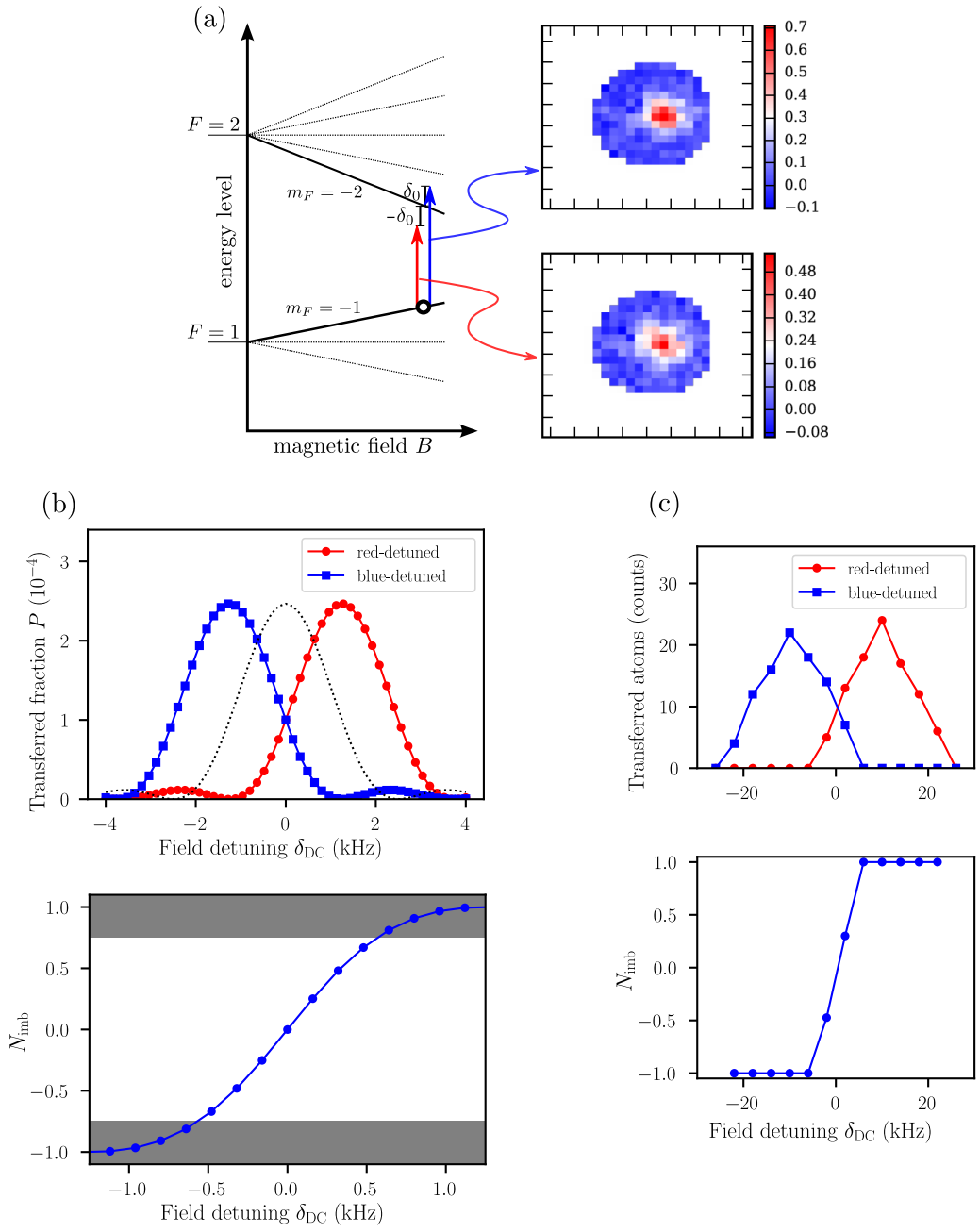

FIGURE 5.2. Illustration of microwave-assisted PTAI to provide feedback correction to the field drift δ_{DC}. (a) Atoms are transferred with red- and blue-detuned microwave pulses to the $|2,-2\rangle$ state and the numbers are counted in absorption imaging. (b) Fractional population transfer $P(\Delta_{\pm})$ as given by Eq. 5.5 (top) and the normalized population imbalance N_{imb} as given by Eq. 5.6 (bottom). (c) Experimental measurements of $P(\Delta_{\pm})$ and N_{imb}.

δ_{DC}. With PTAIs, the measured population imbalance was fedback to the field control system to keep N_{imb} in the range of $-0.75 < N_{\mathrm{imb}} < 0.75$. This gave corrections to the drifting magnetic field in the range corresponding to $-500\,\mathrm{Hz}$ to $500\,\mathrm{Hz}$. I note that the sensitivity to the field drift δ_{DC} is only determined by δ_0, if $\delta_0 \sim 1/\tau$ and $\Omega_0\tau \ll 1$ are satisfied. In practice this gave me a field control within the range of $\pm 200\,\mu\mathrm{G}$ from the setpoint of the resonant field condition at $20\,\mathrm{G}$ (as previously mentioned in Subsection 3.5.4).

5.3. The ac-Stark effect

The interaction between laser-light and atoms within the dipole approximation is described by the ac Stark shift [163]. A coherent electromagnetic field $\mathbf{E}(\mathbf{r},t)$ with frequency ω can be written as

$$\mathbf{E}(\mathbf{r},t) := \tilde{\mathbf{E}}(\mathbf{r};\omega)\,\mathrm{e}^{-\mathrm{i}\omega t} + \tilde{\mathbf{E}}^{*}(\mathbf{r};\omega)\,\mathrm{e}^{+\mathrm{i}\omega t}, \tag{5.7}$$

where $\tilde{\mathbf{E}}(\mathbf{r};\omega)$ and $\tilde{\mathbf{E}}^{*}(\mathbf{r};\omega)$ are the negative and positive frequency components of the Fourier transform of $\mathbf{E}(\mathbf{r},t)$. Since the electric field is a real physical quantity, $\tilde{\mathbf{E}}(\mathbf{r};\omega)$ is the complex conjugate of $\tilde{\mathbf{E}}^{*}(\mathbf{r};\omega)$ and vice versa. In this representation, the intensity of light is given by $I = \epsilon_0 c \left\langle |\mathbf{E}(\mathbf{r},t)|^2 \right\rangle_t = 2\epsilon_0 c \left|\tilde{\mathbf{E}}\right|^2$. The effective Hamiltonian for the ac Stark shift is given by

$$\hat{H}_{\mathrm{Stark}}(F;\omega) = -\hat{\alpha}_{\mu\nu}(F;\omega)\,\tilde{E}^{*}_{0\mu}\tilde{E}_{0\nu}, \tag{5.8}$$

where the spherical tensor polarizability operator $\hat{\alpha}_{\mu\nu}$ is commonly written in its irreducible components [163]

$$\begin{aligned}\hat{\alpha}_{\mu\nu}(F;\omega) &= \hat{\alpha}^{(0)}(F;\omega)\,\delta_{\mu\nu} + \hat{\alpha}^{(1)}(F;\omega)\,\mathrm{i}\epsilon_{\sigma\mu\nu}\frac{F_\sigma}{F} \\ &\quad + \hat{\alpha}^{(2)}(F;\omega)\,\frac{3}{F(2F-1)}\left[\frac{1}{2}(F_\mu F_\nu + F_\nu F_\mu) - \frac{1}{3}\mathbf{F}^2\delta_{\mu\nu}\right], \quad (5.9)\end{aligned}$$

where μ, ν are the indices for the chosen basis vectors and summation over the repeated indices is implied; $\mathbf{F}$ is the total angular momentum operator for the F hyperfine level; and σ is the quantization axis for the good quantum number m_F. The polarizabilities have scalar, vector, and tensor reduced components, which are respectively $\hat{\alpha}^{(0)}(F;\omega)$, $\hat{\alpha}^{(1)}(F;\omega)$, and $\hat{\alpha}^{(2)}(F;\omega)$. In my work, the term $\hat{\alpha}^{(2)}(F;\omega)$ is generally very small compared to the other terms and hence it can be neglected. The scalar and vector components are discussed in the following subsections, where I concentrate on the $F = 1$ manifold of the ^{87}Rb $5\mathcal{S}_{1/2}$ electronic ground states.

5.3.1. Scalar light shift. For most laser frequencies, the largest contribution to the $F = 1$ hyperfine level is from the D_1 and D_2 transitions. For large laser detunings compared to the hyperfine splittings, I can express $\alpha^{(0)}(F;\omega)$ in terms of the fine-structure dipole matrix elements $|\langle J \|\mathbf{d}\| J'\rangle|^2$:

$$\alpha^{(0)}(F;\omega) \approx \sum_{J'} \frac{|\langle J \|\mathbf{d}\| J'\rangle|^2}{3\hbar}\left(\frac{1}{\omega + \omega_{J'J}} - \frac{1}{\omega - \omega_{J'J}}\right), \quad (5.10)$$

where ω is the laser frequency, and $\omega_{J'J}$ are transition frequencies between the atomic ground state J and the multiple excited states J'. Replacing the reduced dipole matrix element with the spontaneous decay rate $\Gamma_{JJ'}$, I can write:

$$\frac{|\langle J \|\mathbf{d}\| J'\rangle|^2}{3\hbar} = \frac{2J'+1}{2J+1}\frac{\pi\epsilon_0 c^3}{\omega_{JJ'}^3}\Gamma_{JJ'}. \tag{5.11}$$

Equations 5.8-5.11 then give the scalar light shift for the $F = 1$ manifold as

$$\Delta E^{(0)}(\omega) = -\frac{\pi c^2 I}{2}\left[\frac{2\Gamma_{\mathrm{D2}}}{\omega_{\mathrm{D2}}^3}\left(\frac{1}{\omega+\omega_{\mathrm{D2}}} - \frac{1}{\omega-\omega_{\mathrm{D2}}}\right) + \frac{\Gamma_{\mathrm{D1}}}{\omega_{\mathrm{D1}}^3}\left(\frac{1}{\omega+\omega_{\mathrm{D1}}} - \frac{1}{\omega-\omega_{\mathrm{D1}}}\right)\right], \tag{5.12}$$

where I is the laser intensity; ω_{D1} and ω_{D2} are the D_1 and D_2 transition frequencies; Γ_{D1} and Γ_{D2} are the D_1 and D_2 transition linewidths.

In this calculation of the scalar light shift, I implicitly assumed $\alpha^{(0)}(F;\omega)$ to be real in Eq. 5.10. To include heating due to spontaneous decay, I can make a substitution $\omega_{\mathrm{D}} \rightarrow \omega_{\mathrm{D}} + \mathrm{i}\Gamma_{\mathrm{D}}\omega^3/\omega_{\mathrm{D}}^3$ to the D_1 and D_2 transition frequencies which then gives the imaginary part of the polarizability [61]. Assuming there is no heating due to the induced dipole fluctuations from gradients in the electric field, I obtain the scattering rate (heating rate) as [54]

$$\Gamma(\omega) = \frac{\pi c^2 I}{2\hbar}\left[\frac{2\Gamma_{\mathrm{D2}}^2\omega^3}{\omega_{\mathrm{D2}}^6}\left(\frac{1}{\omega+\omega_{\mathrm{D2}}} - \frac{1}{\omega-\omega_{\mathrm{D2}}}\right)^2 + \frac{\Gamma_{\mathrm{D1}}^2\omega^3}{\omega_{\mathrm{D1}}^6}\left(\frac{1}{\omega+\omega_{\mathrm{D1}}} - \frac{1}{\omega-\omega_{\mathrm{D1}}}\right)^2\right]. \tag{5.13}$$

By tuning the laser frequency ω to be between the ω_{D1} and ω_{D2} transitions, I can cancel the scalar light shift in Eq. 5.12. The scalar light shift plotted as a function of

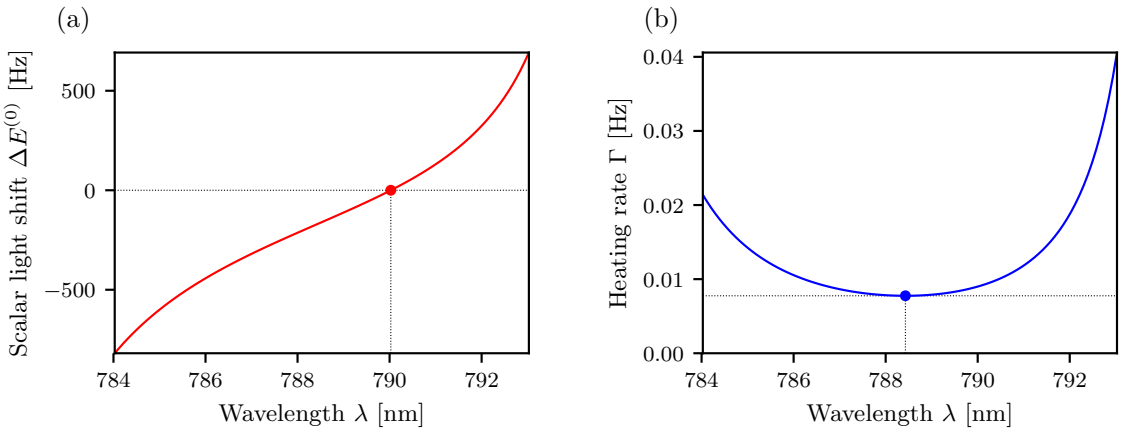

FIGURE 5.3. (a) Scalar light shift $\Delta E^{(0)}$ and (b) scattering rate Γ for wavelengths in between the D_1 and D_2 transitions of ^{87}Rb atoms. The scalar light shift is zeroed out at $\lambda_{\text{zero}} = 790.027\,\text{nm}$ and the heating rate has a local minimum at $\lambda = 788.43\,\text{nm}$. I use λ_{zero} to create our engineered Hamiltonians with minimal heating.

$\lambda = 2\pi c/\omega$ is shown in Fig. 5.3(a). The wavelength λ_{zero} where $\Delta E^{(0)} \to 0$ is called the *magic* wavelength (or *tune-out* wavelength in some references [9]). Substituting the relevant parameters for the D_1 and D_2 transitions (i.e. $\lambda_{D1} = 794.979\,\text{nm}$ and $\lambda_{D2} = 780.241\,\text{nm}$) into Eq. 5.12 gives $\lambda_{\text{zero}} = 790.027\,\text{nm}$. In engineering the Hamiltonians, tuning to λ_{zero} is beneficial since then the atomic internal energy-level spacing is not affected by the light intensity. Furthermore, the heating rate at the magic wavelength is minimal (see Fig. 5.3(b)), allowing me to manipulate the atoms at the magic wavelength for a few seconds before significant loss occurs.

In above, I discussed the scalar polarizability due to the induced dipole moment by taking into account atom-light interaction with just the valence electron. However, there are correction terms due to the contribution from the core electrons (in the inner shell) and a core modification by the valence electron when the atoms are interacting

with an ac electric field. Including these corrections give a more precise value for the magic wavelength, $\lambda_{\text{zero}} = 790.034(7)\,\text{nm}$ [9]. For this reason, I generally used $\lambda_{\text{zero}} = 790.034(4)\,\text{nm}$ in my experiments.

5.3.2. Light-induced effective magnetic field. I next consider the vectorial light shift from the ac Stark effect to the $F = 1$ manifold. Recall that the hyperfine Hamiltonian in the presence of an external magnetic field $\mathbf{B}_{\text{dc}}$ is given by

$$\hat{H}_{\text{hfs,B}} = A_{\text{hfs}} \frac{\mathbf{I} \cdot \mathbf{J}}{\hbar^2} + \frac{\mu_B}{\hbar} \left(g_J \mathbf{J} + g_I \mathbf{I} \right) \cdot \mathbf{B}_{\text{dc}}, \tag{5.14}$$

where A_{hfs} is the magnetic-dipole hyperfine constant, $\mathbf{I}$ is the nuclear spin operator, $\mathbf{J}$ is the electron total angular momentum operator, g_I and g_J are the $g-$factors of the nuclear spin and the electron total angular momentum. The main idea of the vectorial light shift is to treat the effect of the vectorial light polarizability $\hat{\alpha}^{(1)}(F;\omega)$ as an effective magnetic field [53, 64]

$$\mathbf{B}_{\text{eff}} = -\frac{\hbar}{\mu_B g_J} \text{i}\hat{\alpha}^{(1)}(J;\omega) \left(\tilde{\mathbf{E}}^* \times \tilde{\mathbf{E}} \right), \tag{5.15}$$

in the linear Zeeman regime. In this regime, the vectorial light shift is very small compared to the Zeeman splitting (around 10's of kHz compared to 10's of MHz). I can then treat the vectorial ac Stark shift as an effective perturbing Hamiltonian

$$\hat{H}_{\text{eff}} = \frac{\mu_B g_F}{\hbar} \mathbf{B}_{\text{eff}} \cdot \mathbf{F} \tag{5.16}$$

to the hyperfine structure governed by $\hat{H}_{\mathrm{hfs,B}}$. This effective Hamiltonian allowed me to engineer various potentials in spinor condensates as described in the next section.

5.4. Engineered Hamiltonians in ^{87}Rb Bose gases

I used different coupling schemes to create three specific engineered Hamiltonians. Each scheme utilized two counter-propagating lasers at the magic wavelength λ_{zero} in the cross-polarized (lin $\perp$ lin) configuration, as depicted in Fig. 5.4. The vectorial light shift from the two-photon Raman processes enabled me to generate an effective magnetic field that perturbed the Zeeman structure in the $F = 1$ manifold of the spinor Bose gases. I realized three different effective Hamiltonians by changing the orientation of the quantizing bias field and adjusting the "colors" of the counter-propagating lasers, as described below.

5.4.1. Spin-dependent lattice. The first case is shown in Fig. 5.4(a). In this case there is a bias magnetic field $\mathbf{B}_{\mathrm{dc}} = B_x\hat{x}$ that is parallel to the propagation direction of the laser along x. The two lasers have the same frequency ω which is tuned to the magic wavelength $\omega = \omega_{\mathrm{zero}}$ with zero scalar light shift. The laser propagating along $\hat{\mathbf{e}}_x$ is linearly polarized in the $y-$direction with field amplitude E_A and the laser propagating along $-\hat{\mathbf{e}}_x$ is linearly polarized in the $z-$direction with field amplitude E_B. The total electric field at the location of the atoms has the form

$$\mathbf{E}(\mathbf{r},t) = \hat{\mathbf{e}}_y E_A \mathrm{e}^{\mathrm{i}k_R x}\mathrm{e}^{-\mathrm{i}\omega t} + \hat{\mathbf{e}}_z \mathrm{i}E_B \mathrm{e}^{-\mathrm{i}(k_R x+\phi)}\mathrm{e}^{-\mathrm{i}\omega t} + \mathrm{c.c.}, \tag{5.17}$$

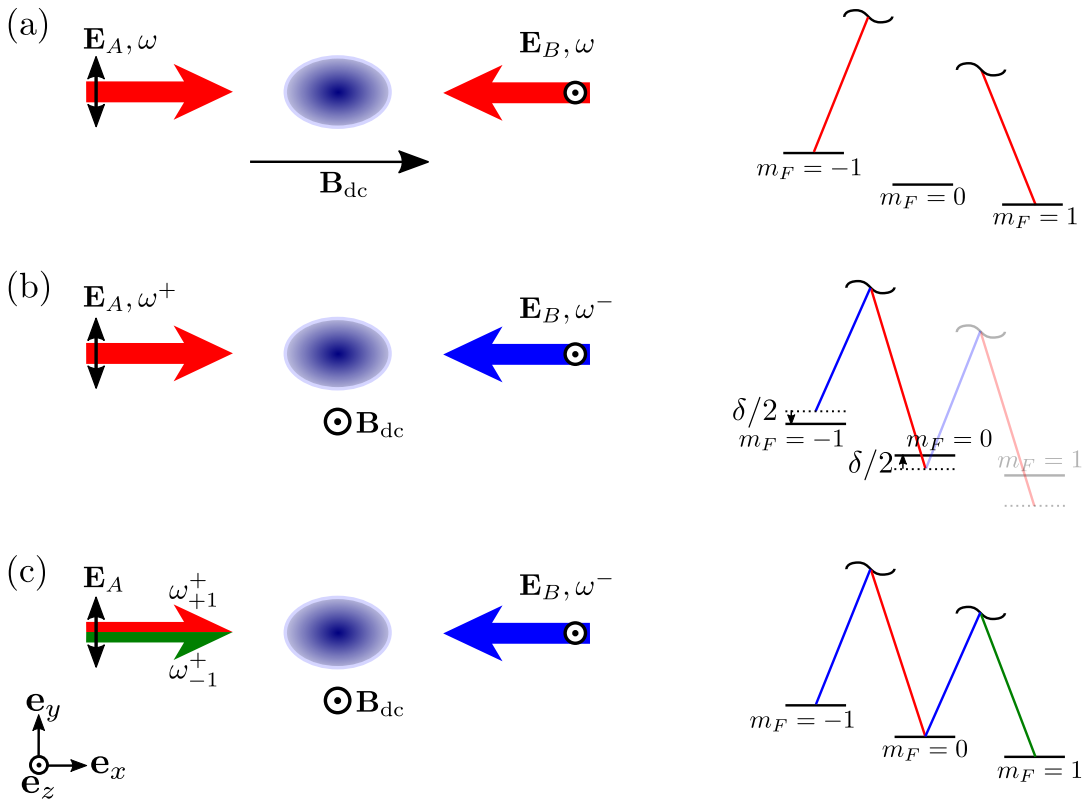

FIGURE 5.4. Three cases of engineered Hamiltonians: (a) spin-dependent lattice, (b) spin-1/2 SOC, and (c) spin-1 SOC.

where $k_R = \omega/c$ is the wavenumber of the laser and the phase difference between the two lasers is chosen to be $\phi + \pi/2$. The cross product of the two mutually conjugate Fourier components of the total field is

$$\tilde{\mathbf{E}}^* \times \tilde{\mathbf{E}} = E_B E_A \left[\mathrm{e}^{-\mathrm{i}(2k_R x+\phi)} + \mathrm{e}^{\mathrm{i}(2k_R x+\phi)}\right] \hat{\mathbf{e}}_x = 2\mathrm{i}\cos(2k_R x + \phi) E_B E_A \hat{\mathbf{e}}_x. \tag{5.18}$$

This produces an effective magnetic field of the form

$$\mathbf{B}_{\rm eff} = \frac{2\hbar\hat{\alpha}^{(1)}(J;\omega)\, E_B E_A}{\mu_B g_J} \cos(2k_R x)\hat{\mathbf{e}}_x. \tag{5.19}$$

Without loss of generality, I have omitted the relative phase ϕ in Eq. 5.18 by appropriate choice of coordinate origin.

In this configuration, the spin quantization axis is along $\mathbf{e}_x$ (defined by the bias field $B_x\hat{x}$) and the effective Hamiltonian can be written as

$$\hat{H}_{\text{eff}} = \frac{V_0}{2}\begin{pmatrix} \cos(2k_R x) & 0 & 0 \\ 0 & 0 & 0 \\ 0 & 0 & -\cos(2k_R x) \end{pmatrix}, \tag{5.20}$$

where $V_0 = -4\alpha^{(1)}(g_F/g_J)E_B E_A$ is the depth of the spin-dependent lattice. The lattice depth V_0 can be tuned by changing the geometric mean of the laser intensity since $V_0 \propto \sqrt{I_A I_B}$. The lattice potential only affects the spin components $m_F = -1$ and $m_F = +1$ (with anti-phase relation between them), while the spin state $m_F = 0$ is unaffected by the coupling light. This scheme provides a way to create a spin-dependent lattice in the $F = 1$ manifold.

5.4.2. Spin-1/2 spin-orbit coupling . In the second configuration, the two Raman lasers have different frequencies ω^+ and ω^- (or different wavenumbers $k^+ = \omega^+/c$ and $k^- = \omega^-/c$), as shown in Fig. 5.4(b). Each laser frequency is tuned close to the magic wavelength $\omega^+, \omega^- \simeq \omega_{\text{zero}}$ with a small frequency difference $|\omega^+ - \omega^-| \ll \omega_{\text{zero}}$. The value of $\delta\omega = \omega^+ - \omega^-$ is adjusted to be close to the Zeeman split ω_Z introduced by the bias magnetic field $\mathbf{B}_{\text{dc}} = B_z\hat{z}$. In my experiments, the typical bias field strength is $B_z \lesssim 20\,\text{G}$ which corresponds to a linear Zeeman split of $\omega_Z \lesssim$

$2\pi \cdot 14\,\mathrm{MHz}$. A careful choice of $\delta\omega \simeq \omega_z$ ($\delta\omega/\omega_{\mathrm{zero}} \sim 10^{-8}$) allows me to couple two specific Zeeman sublevels to create a spin-1/2 spin-orbit-coupled (SOC) Hamiltonian, as described in more details below.

For this case, I can write the total electric field experienced by the atoms as

$$\mathbf{E}\left(\mathbf{r},t\right) = \mathbf{e}_y E_A \exp[\mathrm{i}(k^+ x - \omega^+ t)] + \mathbf{e}_z \mathrm{i} E_B \exp[-\mathrm{i}(k^- x + \omega^- t + \phi)] + \mathrm{c.c.}, \quad (5.21)$$

and consequently

$$\begin{aligned}\tilde{\mathbf{E}}^* \times \tilde{\mathbf{E}} &= \mathrm{i} E_A E_B \left\{\mathrm{e}^{\mathrm{i}(2k_R x - \delta\omega\, t + \phi)} + \mathrm{c.c}\right\} \mathbf{e}_x \\ &= 2\mathrm{i} E_A E_B \cos(2k_R x - \delta\omega\, t + \phi)\mathbf{e}_x, \end{aligned} \quad (5.22)$$

where the single-photon recoil momentum is defined as $k_R = \left(k^+ + k^-\right)/2$.

The effective Hamiltonian in our system then becomes

$$H_{\mathrm{eff}} = \sqrt{2}\Omega \cos(2k_R x - \delta\omega\, t) F_x, \quad (5.23)$$

where the spin-1 matrices are

$$F_x = \frac{\hbar}{\sqrt{2}} \begin{pmatrix} 0 & 1 & 0 \\ 1 & 0 & 1 \\ 0 & 1 & 0 \end{pmatrix}, \quad F_y = \frac{\hbar}{\sqrt{2}} \begin{pmatrix} 0 & -\mathrm{i} & 0 \\ \mathrm{i} & 0 & -\mathrm{i} \\ 0 & \mathrm{i} & 0 \end{pmatrix}, \quad F_z = \hbar \begin{pmatrix} 1 & 0 & 0 \\ 0 & 0 & 0 \\ 0 & 0 & -1 \end{pmatrix}, \quad (5.24)$$

and the Rabi coupling strength is $\Omega = \hat{\alpha}^{(1)} \left(\sqrt{2} g_F / g_J\right) E_B E_A \propto \sqrt{I_A I_B}$.

To get rid of the time dependence in the effective Hamiltonian (Eq. 5.23), I can apply a unitary transformation $\hat{U}_t = \mathrm{e}^{-\mathrm{i}\delta\omega\, tF_z/\hbar}$ and make the rotating-wave approximation (RWA), where the term oscillating with frequency $2\delta\omega$ is omitted, to obtain

$$\hat{U}_t^\dagger H_{\mathrm{eff}} \hat{U}_t \simeq \frac{\Omega}{\sqrt{2}} \cos(2k_R x) F_x - \frac{\Omega}{\sqrt{2}} \sin(2k_R x) F_y. \tag{5.25}$$

The effective Hamiltonian in the rotating frame of the spin space, written in the matrix representation of the $F = 1$ spin states, becomes [69]

$$\begin{aligned} \hat{h}_{\mathrm{eff}} &= \hat{U}_t^\dagger H_{\mathrm{eff}} \hat{U}_t - \mathrm{i}\hbar \hat{U}_t^\dagger \frac{\partial \hat{U}_t}{\partial t} \\ &= \hbar \begin{bmatrix} \delta\omega & \frac{\Omega}{2}\exp(\mathrm{i}2k_R x) & 0 \\ \frac{\Omega}{2}\exp(-\mathrm{i}2k_R x) & 0 & \frac{\Omega}{2}\exp(\mathrm{i}2k_R x) \\ 0 & \frac{\Omega}{2}\exp(-\mathrm{i}2k_R x) & -\delta\omega \end{bmatrix}. \end{aligned} \tag{5.26}$$

This effective Hamiltonian can be treated as a perturbation to the bare hyperfine spin states, with the Zeeman eigenenergies are defined by the diagonal matrix

$$\hat{h}_{\mathrm{hfs,B}} = \hat{U}_t^\dagger H_{\mathrm{hfs,B}} \hat{U}_t = \hbar \begin{bmatrix} -\omega_Z + \epsilon/2 & 0 & 0 \\ 0 & 0 & 0 \\ 0 & 0 & \omega_Z + \epsilon/2 \end{bmatrix} + \hbar\frac{\delta}{2}\hat{\mathbf{I}}. \tag{5.27}$$

Here I have introduced the quadratic shift ϵ to take into account the slight asymmetry between the linear Zeeman split ω_Z and the zero energy reference, which is shifted by $\delta/2$. In other words, the energy levels of the $m_F = +1, 0$, and $m_F = -1$ states are

chosen to be $\hbar\left(-\omega_Z+\epsilon/2+\delta/2\right), \hbar\delta/2$, and $\hbar\left(\omega_Z+\epsilon/2+\delta/2\right)$, respectively. Choosing the laser frequency difference to be $\delta\omega=\omega_Z+\delta+\epsilon/2$, the combined single particle Hamiltonian becomes [103]

$$\hat{h}_{\mathrm{hfs,B}}+\hat{h}_{\mathrm{eff}}=\hbar\begin{bmatrix}\epsilon+3\delta/2 & \frac{\Omega}{2}\exp(\mathrm{i}2k_Rx) & 0\\ \frac{\Omega}{2}\exp(-\mathrm{i}2k_Rx) & \delta/2 & \frac{\Omega}{2}\exp(\mathrm{i}2k_Rx)\\ 0 & \frac{\Omega}{2}\exp(-\mathrm{i}2k_Rx) & -\delta/2\end{bmatrix}. \tag{5.28}$$

The two spin states $|\uparrow\rangle=|F=1,m_F=0\rangle$ and $|\downarrow\rangle=|F=1,m_F=-1\rangle$ can be coupled together by tuning δ, e.g. $\delta=0$ will bring the two spin states into resonance. In the case of $\epsilon\gg\delta$ and $\epsilon\gg\Omega$, coupling to the $|F=1,m_F=1\rangle$ state can be neglected and I obtain the Raman coupled spin-1/2 Hamiltonian

$$\hat{h}_{\mathrm{hfs,B}}+\hat{h}_{\mathrm{eff}}=\hbar\begin{bmatrix}\delta/2 & \frac{\Omega}{2}\exp(\mathrm{i}2k_Rx)\\ \frac{\Omega}{2}\exp(-\mathrm{i}2k_Rx) & -\delta/2\end{bmatrix}. \tag{5.29}$$

The off-diagonal terms in Eq. 5.29 are responsible for the "spin-momentum locking" in this Raman coupling scheme, where any change in the spin state $\Delta m_F=\pm1$ is accompanied by a change in the momentum $\Delta k=\pm2k_R$. In typical experiments, the coupling strength Ω and detuning δ are on the order of a few kHz while the linear Zeeman splitting is on the order of a few MHz. This justifies both the RWA and the treatment of $\hat{h}_{\mathrm{eff}}$ as a perturbation to the spinor hyperfine structure.

I now include the kinetic energy of the atoms and consider only the motion along x. I apply another unitary transform $\hat{U}_k=\mathrm{e}^{\mathrm{i}k_Rx\sigma_z}$ to the Hamiltonian in Eq. 5.29, which

acts as a momentum translation operator to the spin states in the initial lab frame $\vec{\chi}_{\rm lab}$. In the new frame, the spin states become $\vec{\chi}^{1/2}_{\rm SO} = \hat{U}_k \hat{U}_t \vec{\chi}_{\rm lab} = e^{{\rm i}(k_R x - \delta\omega\, t)\sigma_z}\vec{\chi}_{\rm lab}$. Finally, I arrive at the spin-1/2 SOC Hamiltonian

$$\hat{h}^{1/2}_{\rm SO} = \frac{\hbar^2}{2m}\left(q_x - k_R\sigma_z\right)^2 + \hbar\frac{\delta}{2}\sigma_z + \hbar\frac{\Omega}{2}\sigma_x \tag{5.30}$$

where $\sigma_{x,y,z}$ are the Pauli matrices for spin-1/2 system:

$$\sigma_x = \begin{pmatrix} 0 & 1 \\ 1 & 0 \end{pmatrix}, \quad \sigma_y = \begin{pmatrix} 0 & -{\rm i} \\ {\rm i} & 0 \end{pmatrix}, \quad \sigma_z = \begin{pmatrix} 1 & 0 \\ 0 & -1 \end{pmatrix}. \tag{5.31}$$

This configuration couples the bare atomic states $|\uparrow, k_x = q_x - k_R\rangle$ and $|\downarrow, k_x = q_x + k_R\rangle$, realizing an SOC Hamiltonian in the quasi-momentum space q_x [158].

5.4.3. Spin-1 spin-orbit coupling. In the third scenario, as shown in Fig. 5.4(c), I introduce bi-chromatic frequencies ω^+_{-1} and ω^+_{+1} to the laser beam propagating in the $+x$ direction. This laser beam has wavenumbers $k^+_{-1} = \omega^+_{-1}/c$, $k^+_{+1} = \omega^+_{+1}/c$, and field amplitude E_A . The other Raman laser propagating in the $-x$ direction has a single frequency ω^-. This laser beam has wavenumber $k^- = \omega^-/c$ and field amplitude E_B. In order to characterize the beat-note frequency of the bi-chromatic laser, I define new quantitites: the average wavenumber $k^+ = \left(k^+_{-1} + k^+_{+1}\right)/2$, the wavenumber difference $\Delta k^+ = \left(k^+_{+1} - k^+_{-1}\right)/2$, the average frequency $\omega^+ = \left(\omega^+_{+1} + \omega^+_{-1}\right)/2$, and the frequency difference $\Delta\omega^+ = \left(\omega^+_{+1} - \omega^+_{-1}\right)/2$.

The total electric field for the counter-propagating laser geometry is given by

$$\begin{aligned}\mathbf{E} =&\mathbf{e}_y E_A \cos\left(\Delta k^+ x - \Delta\omega^+ t\right)\ \exp[\mathrm{i}(k^+ x - \omega^+ t)]\\ &+ \mathbf{e}_z \mathrm{i} E_B \exp[-\mathrm{i}(k^- x + \omega^- t + \phi)] + \mathrm{c.c.},\end{aligned} \tag{5.32}$$

which gives rise to the time-dependent effective Zeeman coupling term

$$\begin{aligned}\tilde{\mathbf{E}}^* \times \tilde{\mathbf{E}} &= \mathrm{i} E_A E_B \cos\left(\Delta k^+ x - \Delta\omega^+ t\right)\left\{\mathrm{e}^{\mathrm{i}(2k_R x - \delta\omega\, t + \phi)} + \mathrm{c.c}\right\}\mathbf{e}_x\\ &= 2\mathrm{i} E_A E_B \cos\left(\Delta k^+ x - \Delta\omega^+ t\right)\cos(2k_R x - \delta\omega\, t + \phi)\mathbf{e}_x,\end{aligned} \tag{5.33}$$

where $\delta\omega = \omega^+ - \omega^-$ and $k_R = (k^+ + k^-)/2$. This gives an effective Hamiltonian

$$\hat{H}_{\text{eff}} = 2\Omega_1 \cos\left(\Delta k^+ x - \Delta\omega^+ t\right)\cos(2k_R x - \delta\omega\, t)\hat{F}_x. \tag{5.34}$$

To bring the three independent m_F state into resonance to realize a spin-1 SOC system, I choose the bi-chromatic laser frequencies to be $\omega_{+1}^+ = \omega_- + \omega_Z + \epsilon/2$ and $\omega_{-1}^+ = \omega_- + \omega_Z - \epsilon/2$. The linear and quadratic Zeeman shifts, Ω_Z and ϵ, are defined as before in Eq. 5.27. For a typical bias field strength of $B_z \lesssim 20\,\mathrm{G}$, the quadratic shift is $\epsilon \lesssim 2\pi\cdot 100\,\mathrm{kHz}$, which gives $\Delta\omega^+/2\pi \sim 50\,\mathrm{kHz}$ and $\Delta k^+/2\pi \sim 10^{-4}\,\mathrm{m}^{-1}$. Since the size of the atoms is typically in the order of $10\,\mu\mathrm{m}$ (and I am not interested in the short-time dynamics of the Hamiltonian with time scale of $\lesssim 10^{-13}\,\mathrm{s}$), I could safely neglect the term $\Delta k^+ x$ inside the cosine function, where $\cos\left(\Delta k^+ x - \Delta\omega^+ t\right) \simeq \cos\left(\Delta\omega^+ t\right)$. The effective Hamiltonian in Eq. 5.34 then becomes

$$\hat{H}_{\text{eff}} = 2\Omega_1 \cos\left(\Delta\omega^+ t\right) \cos(2k_R x - \delta\omega\, t)\hat{F}_x. \tag{5.35}$$

I apply a unitary transformation $\hat{U}_t = \mathrm{e}^{-\mathrm{i}\delta\omega\, t F_z/\hbar}$ (where $\delta\omega = \omega_Z$) to the Hamiltonian in Eq. 5.35 and make the RWA to obtain a time-harmonic Hamiltonian

$$\hat{h}_{\text{hfs,B}} + \hat{h}_{\text{eff}} = \Omega_1 \cos\left(\Delta\omega^+ t\right) \left[\cos\left(2k_R x\right) \hat{F}_x - \sin\left(2k_R x\right) \hat{F}_y\right] + \frac{\epsilon}{2}\frac{\hat{F}_z^2}{\hbar}. \tag{5.36}$$

with $\Delta\omega^+ = \epsilon/2$. The Hamiltonian in Eq. 5.36 is a periodic function of time and can be solved using Floquet theory, as discussed in Appendix D. Similar to the application of Bloch's theorem in position-momentum space, the Floquet theory leads to the concept of "quasi-energy" $\epsilon_{\text{Floquet}}$ periodically defined within the first Brillouin zone of the frequency space, i.e. $0 < \epsilon_{\text{Floquet}} < \hbar\Delta\omega$. This allows the Hamiltonian in Eq. 5.36 to be cast into the same form as a spin-1 SOC system [22]

$$\hat{h}^1_{\text{SO}} = \frac{\hbar^2\mathbf{k}^2}{2m} + \Omega_1 \left[\cos\left(2k_R x\right) \hat{\mathbf{e}}_x - \sin\left(2k_R x\right) \hat{\mathbf{e}}_y\right] \cdot \mathbf{F} + \Omega_2 \hat{F}^{(2)}_{zz}, \tag{5.37}$$

where the quadrupole tensor operator is given by $\hat{F}^{(2)}_{zz}/\hbar = \hat{F}_z^2/\hbar^2 - 2/3$ and there is an additional Zeeman-like tensor coupling with strength Ω_2. Here Ω_2 includes the quadratic energy shift of the bare Zeeman sublevels and energy correction to the lowest band of the Floquet quasi-energy spectrum. The Hamiltonian in Eq. 5.37 allows us to realize magnetic phases of spin-1 SOC Bose gases 5.36. This Hamiltonian has a rich phase diagram as will be discussed in Chapter 6.

In the above SOC systems, it is important to note the offset $\pm k_R$ from the recoil momentum in quasi-momentum space is equivalent to the presence of an artificial gauge field. As in the quantization of electromagnetic field, the gauge field $\mathbf{A}$ is responsible for the presence of magnetic and electric fields, for example $\mathbf{B} = \nabla \times \mathbf{A}$ and $\mathbf{E} = -\partial \mathbf{A}/\partial t$ [100, 101]. Up to this point, I have treated the detuning δ in the SOC Hamiltonian to be spatially uniform. Introducing a spatially dependent detuning to the system $\delta(y)$, i.e. by applying a magnetic field gradient $B_z \hat{\mathbf{e}}_z \rightarrow (B_z + b'y)\,\hat{\mathbf{e}}_z$, a synthetic magnetic field can be realized. Different spin states of the "neutral" atoms act like charged particles moving in the synthetic magnetic field. In this scenario, we could create vortices in the condensate and the vortex nucleation exhibits a structural phase transition above a threshold artificial field strength. [93, 101, 138]. Detailed discussions on the research work to explore vortex nucleation in a non-uniform synthetic magnetic field can be found in my previous colleague's (Ryan Price) thesis [139] and his published work in Ref. [138].

5.5. Calibration techniques

5.5.1. Minimizing circular polarization of the optical light. The engineered Hamiltonian schemes, as mentioned in the previous section, are realized using the vectorial light shift governed by the term $\tilde{\mathbf{E}}^* \times \tilde{\mathbf{E}}$. It is thus important to make certain on the degree of linear polarization of the light to produce the desired effective magnetic field configuration.

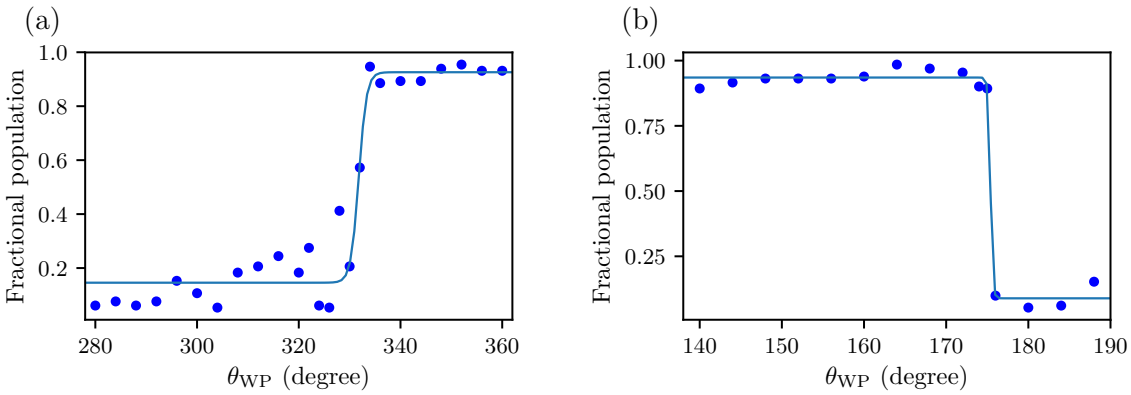

FIGURE 5.5. Alignment of the Raman quarter-wave plate angle θ_{WP} for (a) Raman A and (b) Raman B laser beams. Vectorial light shift from circularly polarized light causes a shift in the resonance condition of the RF-dressed states with 0.5 fractional population. Observed data (circles) are fitted to the logistic functions (solid curves) to determine θ_{WP} which does not affect the resonance condition.

In order to minimize the circular polarization of the counter-propagating Raman lasers, I make use of the vectorial light shift and measure the shift in the atomic resonance condition in an RF-dressed state. I utilize a combination of half- and quarter-wave plates to realize polarization in the lin $\perp$ lin configuration for the aforementioned engineered Hamiltonians. The orientation of the linear polarization is easily aligned by using the half-wave plate to maximize the coupling strength experienced by the atoms. To minimize any circularity in the laser polarization, the quarter-wave plate is used to compensate any unwanted elliptical polarization introduced by the optical components.

To align the quarter-wave plates, I prepared an equal 50%/50% population of $|F = 1, m_F = -1\rangle$ and $|F = 1, m_F = 0\rangle$ atoms in the RF-dressed states. Any light shift alters the resonance condition of the RF-dressed states. With bias field oriented

along the laser propagation direction $\mathbf{e}_x$, I adiabatically turned on a single Raman beam with its wavelength tuned to $\lambda_{\text{zero}} = 790.034(4)\,\text{nm}$. Next, I gradually tweaked the quarter-wave plate angle θ_{WP} and monitored the shift in resonance due to the vectorial light shift from circularly polarized light, as shown in Fig. 5.5. The circular polarization was minimized when the atoms remained at resonance in the RF-dressed state (with 0.5 fractional population) without being affected by the Raman beam. This gave an accuracy within 1° on the quarter-wave plate reading.

5.5.2. Lattice depth calibration. To calibrate the lattice depth V_0, I applied a square pulse of standing-wave light with variable duration τ. The optical lattice diffracts the condensate into multiple momentum orders $\pm 2nk_R$, where n are integers and $k_R = 2\pi/\lambda$ is the wavenumber of a single laser beam. The energy scale in this system is set by the (single-photon) recoil energy $E_R = \hbar k_R^2/2m$. In pulsing the lattice, I used a short interaction time $\tau \ll 1/E_R$ to observe the Kapitza-Dirac effect in the scattering of atoms by the standing-wave light [48, 55].

Time evolution of the condensate in the lattice can be modeled by solving the single-particle Hamiltonian (neglecting mean-field interactions)

$$-\mathrm{i}\hbar\frac{\partial}{\partial t}\psi\left(x,t\right) = \left[-\frac{\hbar^2}{2m}\frac{\partial^2}{\partial x^2} + V_0\cos^2\left(k_R x\right)\right]\psi\left(x,t\right), \tag{5.38}$$

using the plane-wave basis $\psi\left(x,t\right) = \sum_n c_n\left(t\right)\exp\left(\mathrm{i}2nk_R x\right)$. The highest momentum order which can be populated is determined by the cutoff value $n_{\max} \lesssim \sqrt{V_0/4E_R}$. For a short pulsing duration $\tau \ll \hbar/\sqrt{4V_0E_R}$ [72], the fractional population P_n of the

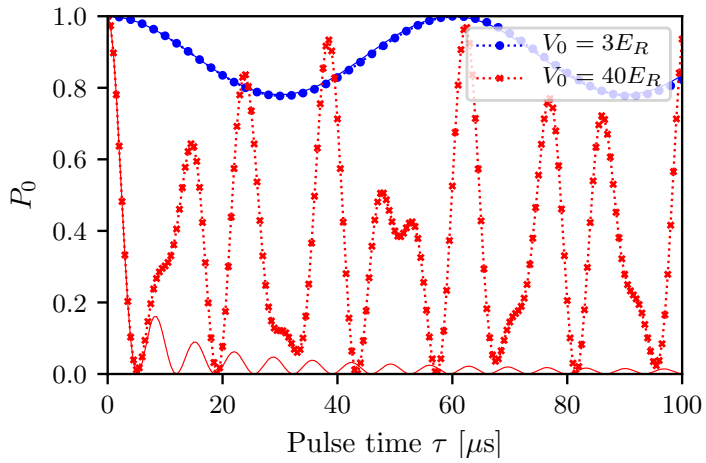

FIGURE 5.6. Time evolution of the 0-th momentum order P_0 for lattice depth $V_0 = 3E_R$ (circles) and $V_0 = 40E_R$ (crosses). Markers with dotted lines are numerical solutions of Eq. 5.38. Solid lines are approximate solutions based on Eqs. 5.39-5.40.

n-th diffracted order has the form [48]

$$P_n = |c_n(\tau)|^2 \simeq J_n^2\left(\frac{V_0}{2\hbar}\tau\right), \tag{5.39}$$

where J_n is the Bessel function of the first kind for an integer n. This approximation is known as the Raman-Nath regime [48]. For shallow potentials $V_0 \lesssim 4E_R$, the time evolution of the $n = \pm 1$ diffraction order has a sinusoidal form, similar to that of Rabi oscillation in a two-level system. The Rabi-like solution of $P_{\pm 1}$ is given by

$$P_{\pm 1} = \frac{1}{4}\left(\frac{V_0}{\hbar\Omega}\right)^2 \sin^2\left(\frac{\Omega}{2}\tau\right), \tag{5.40}$$

where $\hbar\Omega = \sqrt{V_0^2/2 + 16E_R^2}$, and the 0-th order fractional population satisfies $P_0 = 1 - 2P_{\pm 1}$.

The time evolution of the 0-th momentum order is shown in Fig. 5.6. I determined the lattice depth V_0 by fitting the population in different n-th diffracted orders with the numerical solution of Eq. 5.38.

5.5.3. Coupling strength and degenerate minima in an SOC system. To calibrate the coupling strength for SOC cases, I applied a square pulse of the Raman beams. The atoms then exhibit Rabi oscillation between the different coupled spin states. For simplicity, I consider a spin-1/2 system in the following discussion. Since a change in spin is always accompanied by a recoil momentum kick $2k_R$, I have to include a factor of $4E_R$ in the SOC energy dispersion during the Rabi pulsing, as shown in Fig. 5.7(a). For an initial state $|\downarrow\rangle = |m_F = -1\rangle$ prepared at rest, corresponding to the quasi-momentum $q_x = -k_R$, this couples the bare atomic states $|\downarrow, q_x + k_R\rangle = |m_F = -1, k_x = 0\rangle$ and $|\uparrow, q_x - k_R\rangle = |m_F = 0, k_x = -2k_R\rangle$. It is then trivial to obtain the Raman coupling strength Ω by fitting the Rabi evolution of the two coupled states to the relation $P_\uparrow(t) = \sin^2(\Omega t/2)$.

Another important observation in the SOC system is the doubly-degenerate energy minima. The energy dispersion in the quasi-momentum space q_x (for zero detuning $\delta = 0$) has two local minima, as illustrated in Fig. 5.7(a). For coupling strength $\Omega < 4E_R$, the energy dispersion consists of two degenerate minima located at

$$q_0 = \pm k_R \sqrt{1 - \left(\frac{\Omega}{4E_R}\right)^2}. \tag{5.41}$$

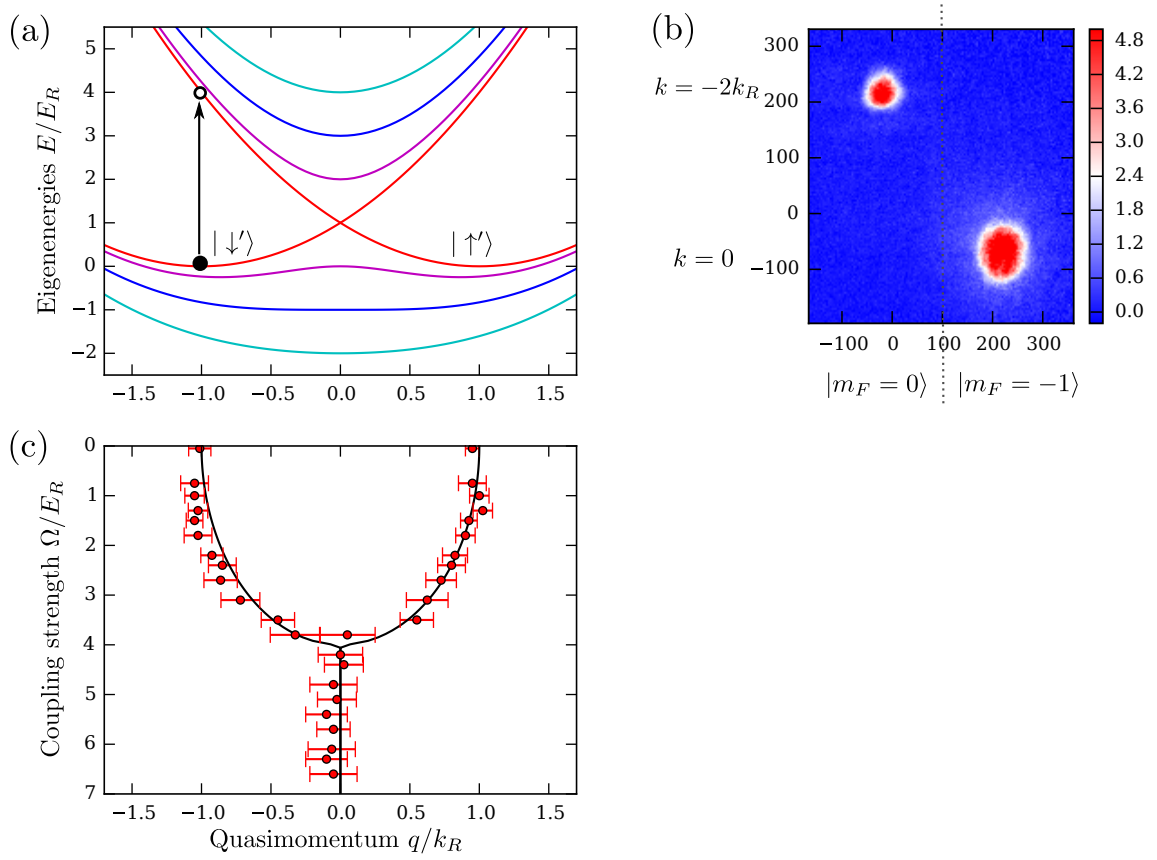

FIGURE 5.7. (a) Energy dispersion of spin-1/2 SOC condensates for $\Omega/E_R = 0, 2, 4$, and 6 (as indicated by the red, magenta, blue, and cyan curves, respectively). (b) Example of absorption imaging where the bare momentum and spin states are distinguished after TOF release while applying Stern-Gerlach gradient force. (c) Tracking the two degenerate minima q_0 of the Raman dressed states.

As Ω increases, the two dressed spin states merge into a single minimum at $q_0 = 0$. To observe the degenerate minima, I prepared atoms in the dressed state by adiabatically increasing the coupling strength to a final value Ω (i.e. by ramping it up linearly within 10's of ms). I then abruptly ($t < 1\,\mu$s) turned off both the Raman lasers and the dipole trap to project the cloud into the bare spin and momentum states. After a few ms of time of flight (TOF), I did absorption imaging of the clouds to determine

their locations and the corresponding minima location q_0. The different spin states are separated by applying Stern-Gerlach force during TOF, as shown in Fig. 5.7(b). I note that the agreement between the imaging data and the expected minima location, as depicted in Fig. 5.7(c), is consistent with the existence of SOC produced by the Raman lasers.

CHAPTER 6

Magnetic phases of spin-1 spin-orbit-coupled Bose gases

In this chapter, I present our observation of magnetic phases of spin-1 spin-orbit-coupled Bose gases. This chapter is a reprint of our work published in Ref. [140]. As one of the authors, I was involved with the data collection, analysis, and writing of the manuscript. My particular role was to collect the data on the quenching dynamics through the first-order transition from the unmagnetized phase to the magnetized phase (shown in Fig 6.3 below). While analyzing the data for the measured phase diagram, we found a mismatch between our theoretical prediction and experimental results. It turned out that there was a mistake in our theoretical model. We forgot to take into account the laser beat-note frequency which we used to realize the spin-1 spin-orbit coupling system. My other contribution was then to include this correction and apply Floquet formalism to our model Hamiltonian. Our group effort eventually obtained measurement and data analysis that were accurate and consistent.

6.1. Abstract

Phases of matter are characterized by order parameters describing the type and degree of order in a system. Here we experimentally explore the magnetic phases present in a near-zero temperature spin-1 spin-orbit-coupled atomic Bose gas and the

quantum phase transitions between these phases. We observe ferromagnetic and unpolarized phases which are stabilized by spin-orbit coupling's explicit locking between spin and motion. These phases are separated by a critical curve containing both first- and second-order transitions joined at a tricritical point. The first-order transition, with observed width as small as $h \times 4$ Hz, gives rise to long-lived metastable states. These measurements are all in agreement with theory.

6.2. Introduction

Most magnetic systems are composed of localized particles such as electrons [3], atomic nuclei [1], and ultracold atoms in optical lattices [57, 65, 89, 155], each with a magnetic moment $\boldsymbol{\mu}$. By contrast, itinerant magnetism [133, 149] describes systems where the magnetic particles, here ultracold neutral atoms, can themselves move freely, and for which magnetism is generally weak. Our spin-orbit-coupled Bose-Einstein condensates [66, 90, 103, 141] (BECs) constitute a magnetically ordered itinerant system in which – unlike more conventional spinor BECs [159] – the atoms' kinetic energy explicitly drives a phase transition between two different ordered phases [90]. While the coupling between spin and momentum afforded by spin-orbit coupling (SOC) is insufficient to stabilize ferromagnetism in itinerant fermionic systems [181], in bosonic systems it leads to magnetic phases that are not present in spinor BECs without SOC [66, 141].

Phase transitions can generally be described in terms of a free energy $G(M_z)$ – including the total internal energy along with thermodynamic contributions that are

negligible for our nearly zero temperature $T = 0$ system – that is minimized for an equilibrium system. Here the magnetization $M_z = \langle \hat{S}_z \rangle / \hbar$ is an order parameter, associated with the spin $\hat{\mathbf{S}}$, which changes abruptly as our system undergoes a phase transition. Figure 6.1(c) shows typical $T = 0$ free energies: a first-order phase transition (top panel) occurs when the number of local minima in $G(M_z)$ stays fixed, but the identity of the global minima changes; and a second-order phase transition (bottom panel) occurs when degenerate global minima merge or separate. These defining features are true both for $T > 0$ thermal and $T = 0$ quantum phase transitions.

For spin-1/2 systems (i.e, total angular momentum, $f = 1/2$) like electrons, ferromagnetic order can be represented in terms of a magnetization vector $\mathbf{M} = \langle \hat{\mathbf{S}} \rangle / \hbar$. This is rooted in the fact that the three components of the spin operator $\hat{\mathbf{S}}$ transform vectorially under rotation. More specifically, any Hamiltonian describing a two level system may be expressed as $H = \hbar\Omega_0 + \mathbf{\Omega}_1 \cdot \hat{\mathbf{S}}$, the sum of a scalar (rank-0 tensor) and a vector (rank-1 tensor) contribution. The former, described by Ω_0 gives an overall energy shift, and the latter takes the form of the linear Zeeman effect from an effective magnetic field proportional to $\mathbf{\Omega}_1$. Going beyond this, fully representing a spin-1 (total angular momentum $f = 1$ with three m_F sublevels: $|-1\rangle$, $|0\rangle$, and $|+1\rangle$) Hamiltonian with angular momentum $\hat{\mathbf{F}}$ requires an additional five-component rank-2 tensor operator – the quadrupole tensor – and therefore there exist "magnetization" order parameters that are not simply associated with any spatial direction[16, 159, 165].

Pioneering studies in GaAs quantum wells [86, 160] showed that material systems with equal contributions of Rashba and Dresselhaus SOC described by the term

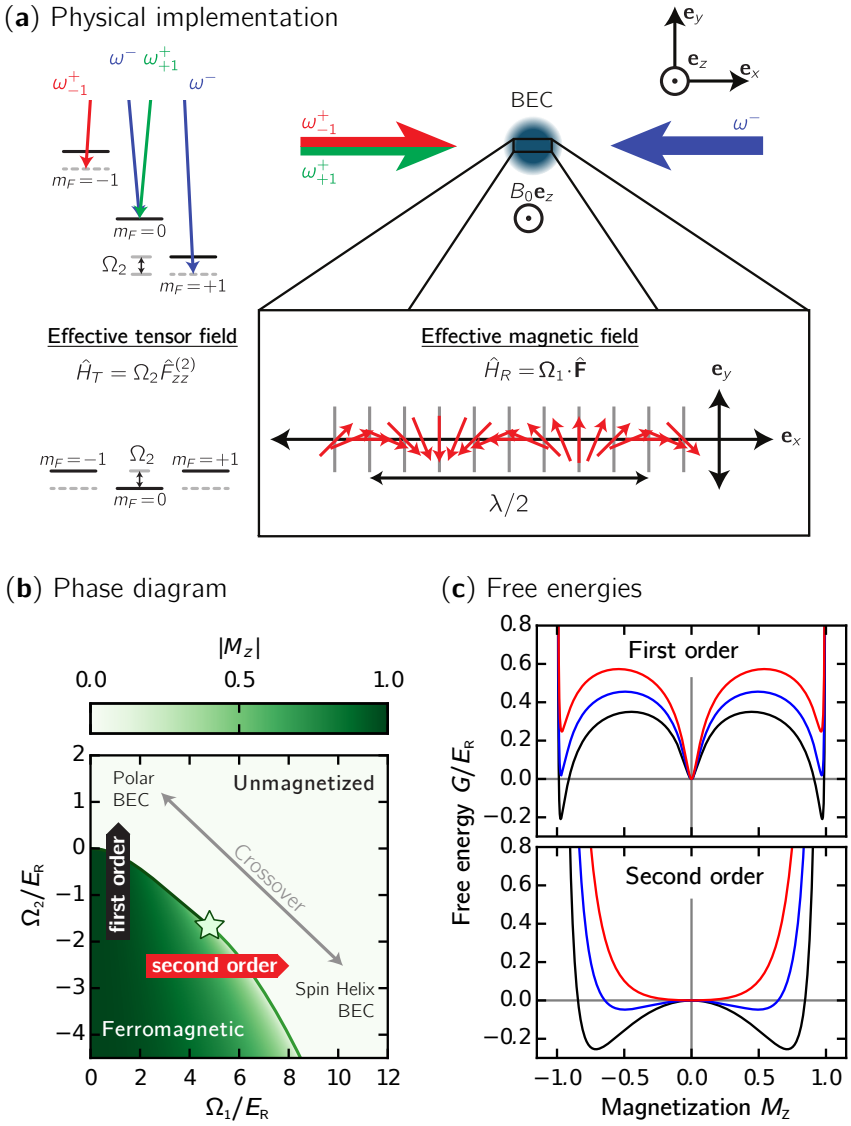

FIGURE 6.1. **Experimental system** (a) Schematic and level diagram. The $|-1\rangle \leftrightarrow |0\rangle$ and $|0\rangle \leftrightarrow |+1\rangle$ transitions of the $f = 1$ ground state manifold of ^{87}Rb were independently Raman coupled, giving experimental control of Ω_1 and Ω_2. (b) Phase diagram. The ferromagnetic order parameter $|M_z|$ is plotted against Ω_2 and Ω_1. The solid (dashed) red curve denotes the first-order (second-order) transition from the magnetized phase. (c) Free energies. Top: near the first-order phase transition at $\Omega_1/E_R = 1$ for $\Omega_2/E_R = -0.35, -0.1$ and 0.15 for the black, blue and red traces respectively, as marked by the red flags in (b). Bottom: near the second-order phase transition at $\Omega_2/E_R = -2.5$ for $\Omega_1/E_R = 4.5, 5.5$, and 6.5 for the black, blue and red traces respectively.

$\alpha k_x \hat{F}_z$, subject to a transverse magnetic field with Zeeman term $\Omega_1 \hat{F}_x$, can equivalently be described as a spatially periodic effective magnetic field. Our experiments with spin-1 atomic systems use "Raman" lasers with wavelength λ to induce SOC of this form [29, 49, 69, 103, 172, 173, 180] with strength $\alpha = 2\hbar k_R/m$, where the single-photon recoil energy and momentum are $E_R = \hbar^2 k_R^2/2m$ and $\hbar k_R = 2\pi\hbar/\lambda$. This atomic system can therefore be described by the magnetic Hamiltonian

$$\hat{H} = \frac{\hbar^2 \mathbf{k}^2}{2m} + \mathbf{\Omega}_1(x)\cdot\hat{\mathbf{F}} + \Omega_2 \hat{F}_{zz}^{(2)}, \tag{6.1}$$

describing atoms with mass m and momentum $\hbar\mathbf{k}$ interacting with an effective Zeeman magnetic field $\mathbf{\Omega}_1(x)/\Omega_1 = \cos(2k_R x)\mathbf{e}_x - \sin(2k_R x)\mathbf{e}_y$ helically precessing in the $\mathbf{e}_x$-$\mathbf{e}_y$; and an additional Zeeman-like tensor coupling with strength Ω_2. Here, $\hat{F}_{zz}^{(2)}/\hbar = \hat{F}_z^2/\hbar^2 - 2/3$ is an element of the quadrupole tensor operator. The competing contributions between kinetic and magnetic ordering energies (interactions select between different nearly degenerate ground states, but only weakly perturb the location of the phase transitions, see Methods) make ours an archetype system for studying exotic magnetic order and understanding the associated quantum phase transitions, of which both first- and second-order are present in our experiments (Fig.6.1(b)).

We can easily understand the first-order transition in the limit of infinitesimal Ω_1 where the tensor field favors either: a polar BEC for $\Omega_2 > 0$ ($m_F = 0$: unmagnetized, $M_z = 0$), or a ferromagnetic BEC for $\Omega_2 < 0$ ($m_F = +1$ or -1: magnetized, $|M_z| = 1$). As with spinor BECs [148], these phases are separated by a first-order phase

transition at $\Omega_2 = 0$. The ferromagnetic phase spontaneously breaks the Z_2 symmetry associated with the Hamiltonian's invariance under the exchange $|-1\rangle \leftrightarrow |+1\rangle$. The second-order transition can be intuitively understood by considering the large Ω_1 limit where the system forms a spin helix BEC (with local magnetization antiparallel to $\mathbf{\Omega}_1$: unmagnetized, $M_z = 0$). This order increases the system's kinetic energy, leading to the second-order phase transition into the ferromagnetic phase shown in Fig.6.1(b) as Ω_1 decreases. Analogues to this second-order phase transition are present in other systems with effective spin-degrees of freedom such as double-leg ladders [11] or engineered optical lattices [128, 166].

These two extreme limits continuously connect at the point (Ω_1^*, Ω_2^*), the green star in Fig. 6.1(b), where the small-Ω_1 first-order phase transition gives way to the large-Ω_1 second-order transition, and together these regions constitute a curve of critical points $\{(\Omega_1^C, \Omega_2^C)\}$. Here we realized spin-1 spin-orbit-coupled BECs and varied the magnetic coupling fields using externally applied fields. By directly measuring the system's magnetization, we studied the associated quantum phase transitions present in the phase diagram, all in quantitative agreement with theory.

6.3. Results

As shown in Fig. 6.1(a), we realized this magnetic system by illuminating ^{87}Rb BECs in the $f = 1$ ground state manifold with a pair of counter propagating and orthogonally polarized Raman lasers that coherently coupled the manifold's m_F states. Physically, the spatial interference of the orthogonally polarized laser beams give rise

to the helical effective magnetic field (see Methods) with period $\lambda/2$. As we first showed [103] using effective $f = 1/2$ systems, this introduces both a spin-orbit and a Zeeman term into the BEC's Hamiltonian, equivalent to Eq. 6.1. Here the quadratic Zeeman shift from a large bias magnetic field $B_0\mathbf{e}_z$ split the low-field degeneracy of the $|-1\rangle \leftrightarrow |0\rangle$ and $|0\rangle \leftrightarrow |+1\rangle$ transitions, and we independently Raman coupled these state-pairs with equal strength Ω_1. We dynamically tuned the quadrupole tensor field strength Ω_2 by simultaneously adjusting the Raman frequency differences; as shown in Fig. 6.1 we selected frequencies differences where the detuning from the $|+1\rangle$ to $|0\rangle$ and $|-1\rangle$ to $|0\rangle$ were both equal to Ω_2 (see Methods). Without this technique, only the upper half-plane of the phase diagram (Fig. 6.1(b)) would be accessible: containing only an unmagnetized phase, therefore lacking any phase transitions.

In each experiment, we first prepared BECs at a desired point in the phase diagram, possibly having crossed the phase transition during preparation. A combination of trap dynamics [100, 102] collisions, and evaporation [78] kept the system in or near (local) thermal equilibrium. We then made magnetization measurements directly from the Bose-condensed atoms measured in the spin resolved momentum distribution obtained using the time-of-flight (TOF) techniques described in Ref. [100].

6.3.1. Critical line of phase transitions. Our experiment first focused on thermodynamic phase transitions. We made vertical (horizontal) scans through the phase diagram by initializing the system in the unmagnetized phase at a desired value of Ω_1 (Ω_2) with $\Omega_2 \gtrsim 0$ ($\Omega_1 \lesssim 10E_R$), and then ramping Ω_2 (Ω_1) through the transition

region. (As discussed in the methods our nominally horizontal scans of Ω_1 followed slightly curved trajectories through the phase diagram, such as the red dashed curve in Fig. 6.2(c)). Following such ramps, domains with both $\pm M_z$ can rapidly form, and we therefore focus on the tensor magnetization $M_{zz} = \langle \hat{F}_{zz}^{(2)} \rangle / \hbar + 2/3$ which is sensitive to this local magnetic order.

Using horizontal scans, we crossed through the second-order phase transition ($\Omega_2 < \Omega_2^*$) where the free energy evolves continuously from having one minimum (with $M_{zz} = 0$, for large Ω_1) to having two degenerate minima (with $M_{zz} > 0$, for smaller Ω_1). As shown in Fig. 6.2(a), M_{zz} continuously increases with decreasing Ω_1, reaching its saturation value as $\Omega_1 \to 0$. Repeating these processes for $\Omega_2^* < \Omega_2 < 0$, we found a sharp first-order transition. In each case, data is plotted along with theory with no adjustable parameters. Using data of this type for a range of Ω_2 and fitting to numeric solutions of Eq. 6.1, we obtained the critical points plotted in Fig. 6.2(c). Because horizontal cuts through the phase diagram are nearly tangent to the transition curve for small Ω_2, this produced large uncertainties in Ω_1^C for the first-order phase transition.

We studied the first-order phase transition with greater precision by ramping Ω_2 through the transition at fixed Ω_1 (Fig. 6.2(b)) and found near perfect agreement with theory. For all the experimentally measured critical points, see Fig. 6.2(c) top, separating the unmagnetized and ferromagnetic phase, we also measured the corresponding transition width defined as the required interval for the curve to fall from 50% to 20% of its full range. This width Δ decreases sharply at Ω_1^*, marking the

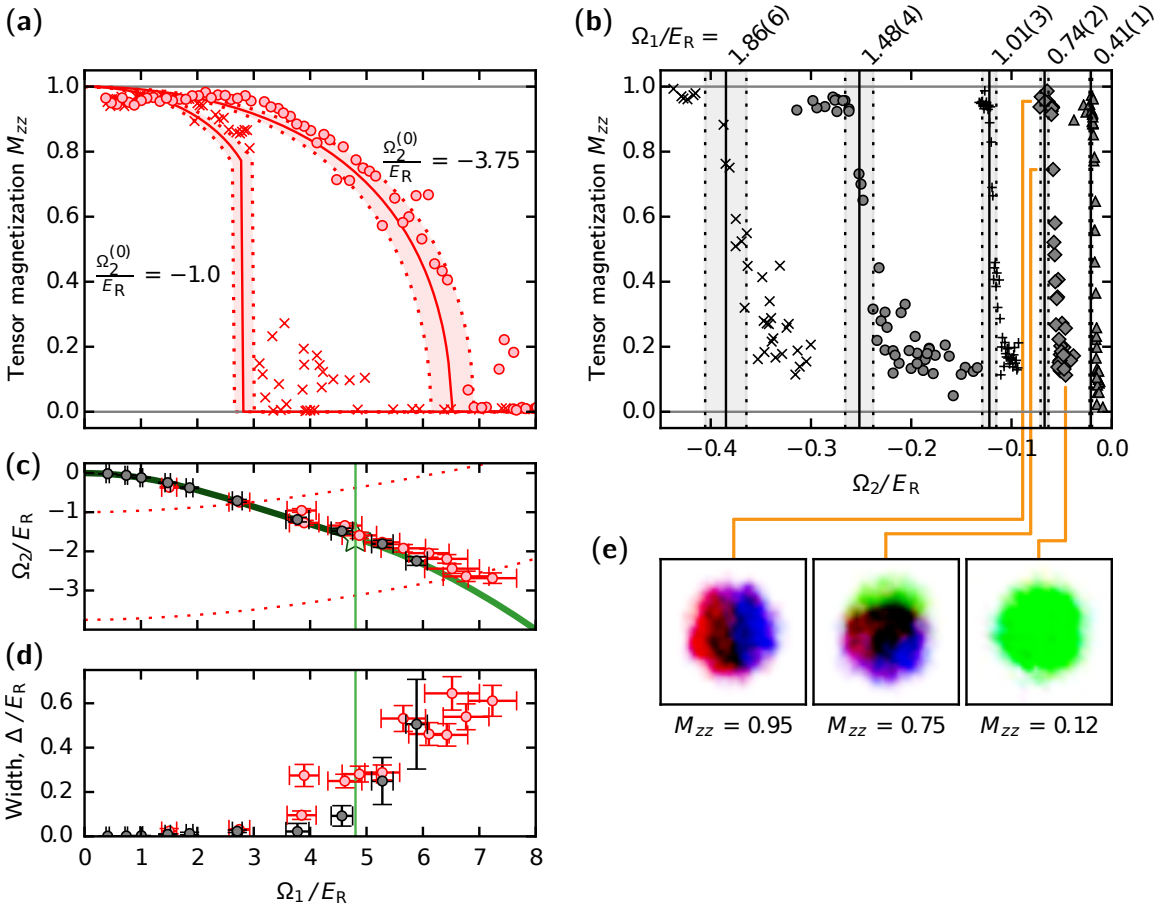

FIGURE 6.2. **Measured phase transition** (a) Tensor magnetization M_{zz} measured as a function of Ω_1, showing both second-order $[\Omega_2(\Omega_1 = 0) = -3.7500(3)E_R]$ and first-order $[\Omega_2(\Omega_1 = 0) = -1.0E_R]$ phase transitions in comparison with theory. These curves followed the nominally horizontal trajectories (see Methods) marked by red dashed curves in (c). (b) Tensor magnetization measured as a function of Ω_2 at $\Omega_1/E_R = 1.86(6)$, 1.48(4), 1.01(3), 0.74(2), and 0.41(1), plotted along with the predicted critical Ω_2. In (a) and (b) the light-colored region reflects the uncertainty in theory resulting from our $\approx 5\%$ systematic uncertainty in Ω_1. (c), (d) Phase transition. Black (red) symbols depict data obtained using vertical (nominally horizontal) cuts through the phase diagram. (c) measured phase transitions plotted along with theory: solid (phase transition), and green vertical line (tricritical point, Ω_1^*) Horizontal error bars correspond to one standard deviation on Ω_1 and vertical error bars are the 95% confidence intervals from the fitting function that determines the critical point.

FIGURE 6.2. (Continued) (d) 20% to 50% transition width showing the clear shift from first- to second-order with increasing Ω_1. (e) Domain formation for $\Omega_1 = 0.74(2)$ showing interaction-driven spin structure near the first-order phase transition. In all images, red corresponds to spatial regions with local $M_z \approx -1$, the green regions correspond to $M_z \approx 0$ and the blue regions correspond to $M_z \approx +1$. In the polar regime at $M_{zz} = 0.12$ only the $m_F = 0$ cloud is visible; near the first-order phase transition at $M_{zz} = 0.75$ all three $m_F = 0$ clouds are visible and have partially phase separated; and in the ferromagnetic regime at $M_{zz} = 0.95$ only $m_F \pm 1$ clouds are visible and they have completely phase separated.

crossover between second- and first-order phase transitions (see Fig. 6.2(c) bottom). In these data, the width of the first-order transition becomes astonishingly narrow: as small as $0.0011(3)E_R = h \times 4(1)$Hz at $\Omega_1 = 0.41(1)$. This narrowness results from the energetic penalty associated with condensation into multiple modes for repulsively interacting bosons. In addition we find that ramps through the 1st order transition are hysteretic, and very slow ramps (See Methods) for the system to equilibrate.

During the long equilibration times required to study this transition, spin-domains formed in our system, shown in Fig. 6.2(e). For Bose-condensed atoms, our TOF procedure expanded the initial spin-distribution allowing us to reconstruct any in-situ spin structure. Figure 6.2(e) shows that domains form as the systems enters into the magnetized phase; these domains mark the role of interactions in spontaneously breaking the Hamiltonian's Z_2 symmetry (see Methods for a comparison with sodium where the sign of the spin-dependent interactions is reversed, and the Z_2 symmetry remains unbroken for a wide range of parameters). Figure 6.2(b) shows that additional tripartite spin structure is present very near the first-order phase transition, which

was not anticipated in our initial single-particle description. This tripartite mixture, predicted in Ref. [125] is an in-plane ferromagnetic phase with no analogue in spinor BECs or effective spin-1/2 SOC BECs.

6.3.2. Metastable states. We observed that scans crossing the second-order transition typically required 50 ms to equilibrate, while for scans crossing the first-order transitions we allowed as long as 1.5 s for equilibration. Systems taken through a first-order phase transition can remain in long-lived metastable states. Here a metastable state with $M_z = 0$ persists in the ferromagnetic phase, and a pair of metastable states with $M_z \neq 0$ persists in the unmagnetized phase. We began our study of this metastability by quenching through the first-order transition at $\Omega_1 = 0.74(8)E_R$ with differing rates from -0.5 to -0.2 $E_R\mathrm{s}^{-1}$, as shown in Fig. 6.3. We observed the transition width continuously decreases with decreasing absolute value ramp rate (inset to Fig. 6.3), consistent with slow relaxation from a metastable initial state.

We explored the full regime of metastability by initializing BECs in each of the m_F states, at fixed Ω_2, then rapidly ramping $\Omega_1(t)$ from zero to its final value fast enough that the system did not adiabatically follow into the true ground state, yet slow enough that the quasi-equilibrium metastable state was left near its local equilibrium. We found that the rate $\lesssim 200E_Rs^{-1}$ was a good compromise between these two requirements. For points near the first-order phase transition three metastable states

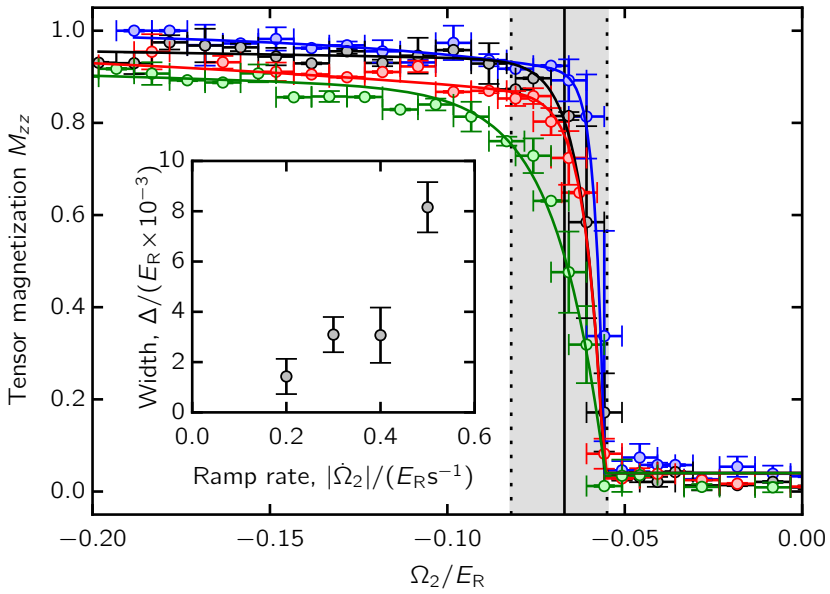

FIGURE 6.3. **Quenching dynamics** The system was prepared in the unmagnetized phase with $\Omega_1 = 0.74(8)E_R$ and Ω_2 was ramped through the phase transition at ramp-rates $d\Omega_2/dt = -0.2, -0.3, -0.4$, and $-0.5E_R s^{-1}$ (blue, black, red, and green symbols, respectively). The curves are guides to the eye. The inset shows the decreasing width, defined as the required interval for the curve to fall from 50% to 20% of its full range, of the first-order transition as the ramp-rate decreases. Vertical error bars correspond to one standard deviation of up to 10 measurements, and horizontal error bars correspond to a systematic error of $0.005E_R$ from fluctuations in the bias field. Error bars on the inset panel correspond to the 95% confidence interval on the fitting function of the quenching data.

exist (Fig. 6.4); near the second-order transition this count decreases, giving two local minima which merge to a single minimum beyond the second-order transition.

We experimentally identified the number of metastable states by using M_z and its higher moments, having started in each of the three m_F initial states. A small variance in M_z, less than 0.25, indicates the final states are clustered together – associated with a single global minimum in the free energy $G(M_z)$ – and it increases

when metastable or degenerate ground states are present. We distinguished systems with two degenerate magnetization states ($M_z \approx \pm 1$) from those with three states by the same method, since when $M_z \approx \pm 1$, the variance of $|M_z|$ is smaller than 0.25, and it distinguishably increases beyond 0.25 as a third metastable state appears with $M_z = 0$. In this way we fully mapped the system's metastable states in agreement with theory, as shown in Fig. 6.4

6.4. Discussion

We accurately measured the two-parameter phase diagram of a spin-1 BEC, containing a ferromagnetic phase and an unmagnetized phase, continuously connecting a polar spinor BEC to a spin-helix BEC. The ferromagnetic phase in this itinerant system is stabilized by SOC, and vanishes as the SOC strength $\hbar k_R$ goes to zero. Our observation of controlled quench dynamics through a first-order phase transition opens the door for realizing Kibble-Zurek physics [84, 182] in this system, where the relevant parameters can be controlled at the individual Hz level. The quadrupole tensor field $\propto \hat{F}^{(2)}_{zz}$ studied here is the $q = 0$ component of the rank-2 spherical tensor operator $\hat{F}^{(2)}_q$, with $q \in \{\pm 2, \pm 1, 0\}$. The physics of this system would be further enriched by the addition of the remaining four tensor fields. The $q = 0$ term we included is the most simple of the tensor fields to deploy, as it only required control over frequencies. The $q = \pm 1$ components are relatively simple to incorporate by rf-coupling the $|m_F = -1\rangle$ to $|m_F = 0\rangle$ and $|m_F = +1\rangle$ to $|m_F = 0\rangle$ transitions with different phases. The $q = \pm 2$ components require direct coupling between $|m_F = +1\rangle$

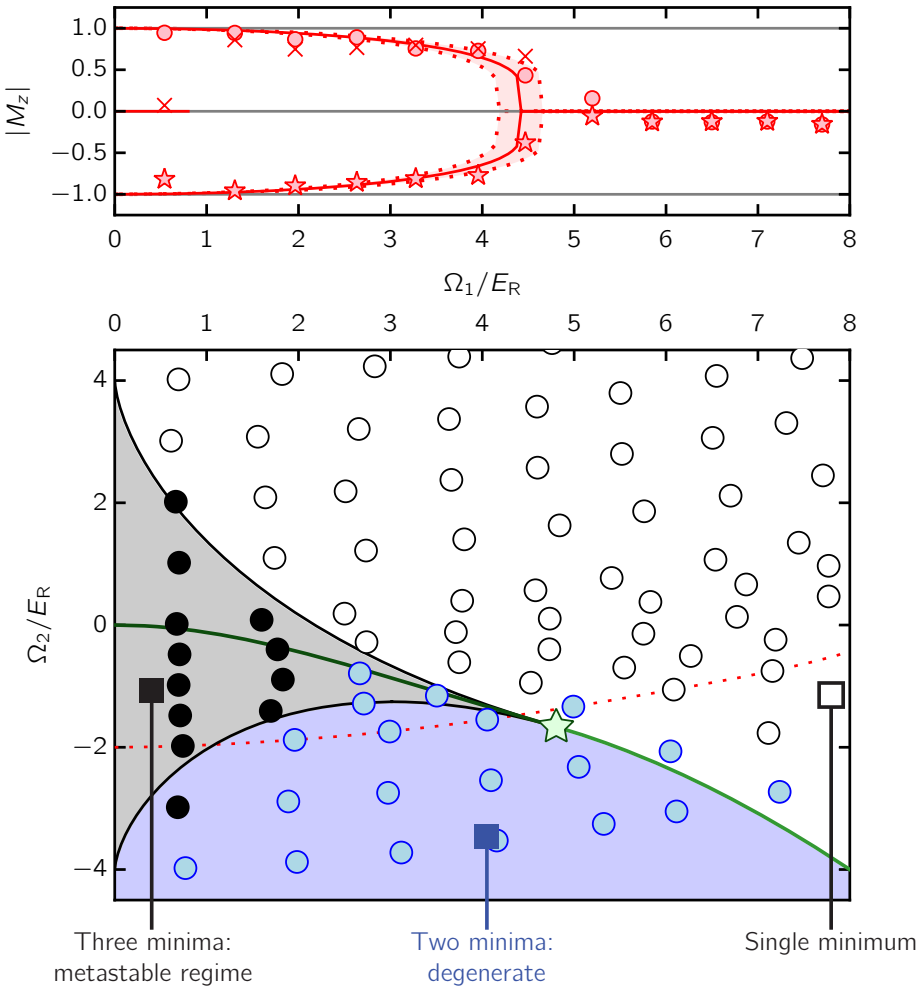

FIGURE 6.4. **Metastable states** Top, Measured magnetization plotted along with theory. The system was prepared at the desired $\Omega_2 = -2E_R$; $\Omega_1(t)$ was then increased to its displayed final value; during this ramp Ω_2 also changed, and the system followed the curved trajectory in the bottom panel. Each displayed data point is an average of up to 10 measurements, and the colored region reflects the uncertainty in theory resulting from our $\approx 5\%$ systematic uncertainty in Ω_1. Circles/crosses/stars represent data starting in $m_F = +1$, 0, and -1 respectively. Bottom, state diagram: theory and experiment. Blue: two states; black: three states; white: one state. Colored areas denote calculated regions where the color-coded number of stable/metastable states are expected. Symbols are the outcome of experiment. Each displayed data point is an average of up to 20 measurements.

and $|m_F = -1\rangle$ which is straightforward using two-photon microwave transitions, but is challenging to include with significant strength.

6.5. Methods

6.5.1. System Preparation. We created $N \approx 4 \times 10^5$ atoms ^{87}Rb BECs in the ground electronic state $|f = 1\rangle$ manifold [104], confined in the locally harmonic trapping potential formed at the intersection of two $1,064$ nm laser beams propagating along $\mathbf{e}_x$ and $\mathbf{e}_y$ giving trap frequencies of $(\omega_x, \omega_y, \omega_z)/2\pi = (33(2), 33(2), 145(5))$ Hz. The quadratic contribution to the $B_0 = 35.468(1)$ G magnetic field's $\approx h \times 25$ MHz Zeeman shift lifts the degeneracy between the $|f = 1, m_F = -1\rangle \leftrightarrow |f = 1, m_F = 0\rangle$ and $|f = 1, m_F = 0\rangle \leftrightarrow |f = 1, m_F = 1\rangle$ transitions, by $\epsilon = h \times 90.417(1)$ kHz. We denote the energy differences between these states as $\hbar\delta\omega_{-1,0}$, $\hbar\delta\omega_{0,+1}$, and $\hbar\delta\omega_{-1,+1}$.

6.5.2. Frequency selective Raman coupling. We Raman-coupled the three m_F states using a pair of $\lambda = 790.024(5)$ nm laser beams counter-propagating along $\mathbf{e}_x$. The beam traveling along $+\mathbf{e}_x$ had frequency components ω^+_{-1} and ω^+_{+1}, while the beam traveling along $-\mathbf{e}_x$ contained the single frequency ω^-. These beams were linearly polarized along $\mathbf{e}_z$ and $\mathbf{e}_y$ respectively. The frequencies were chosen such that the differences $\delta\omega_{-1,0} \approx \omega^- - \omega^+_{-1}$ and $\delta\omega_{0,+1} \approx \omega^- - \omega^+_{+1}$ independently Raman coupled the $|m_F = -1, 0\rangle$ and $|m_F = 0, +1\rangle$ state-pairs, respectively. Furthermore we selected $2\omega^- - (\omega^+_{-1} + \omega^+_{+1}) = \delta\omega_{-1,+1}$ such that, after making the rotating wave approximation (RWA) the $|m_F = \pm 1\rangle$ states were energetically shifted by the same $\Omega_2^{(0)} = [(\delta\omega_{-1,0} - \delta\omega_{0,+1}) + (\omega^+_{-1} - \omega^+_{+1})]/2$ energy from $|m_F = 0\rangle$, thereby yielding

the frequency-tuned tensor energy shift depicted in Fig. **6.1**(a). In addition, Ω_2 in Eq. 6.1 differs from $\Omega_2^{(0)}$ by a small shift $\propto \Omega_1^2/\epsilon$ resulting from off-resonant coupling to transitions detuned by 2ϵ, which we computed directly using Floquet theory (see Eq. 6.6 in Methods). This tensor contribution $\Omega_2 \hat{F}_{zz}^{(2)}$ to the Hamiltonian might equivalently be introduced by a quadratic Zeeman shift alone, giving $\Omega_2 \propto B_0^2 > 0$.

6.5.3. The physical basis for SOC using Raman lasers. As explained in Ref. [80], the spin-dependent (vector) part of the light-matter interaction can be written in terms of an effective Zeeman field

$$\mathbf{\Omega} = \mathrm{i}u_v(\mathbf{E}^* \times \mathbf{E}) \tag{6.2}$$

with overall strength given by u_v as defined in Ref. [80], where $\mathbf{E}$ is the total optical electric field from the Raman lasers. This field then enters into the Hamiltonian as an effective magnetic field

$$H_v = \mathbf{\Omega} \cdot \hat{\mathbf{F}}. \tag{6.3}$$

The electric field for the laser geometry depicted in Fig. 6.1(a) is $\mathbf{E} = E^+ \mathbf{e}_z \exp[\mathrm{i}(k_R x - \omega_{-1}^+ t)] + E^+ \mathbf{e}_z \exp[\mathrm{i}(k_R x - \omega_{+1}^+ t)] + \mathrm{i}E^- \mathbf{e}_y \exp[\mathrm{i}(-k_R x - \omega^- t)]$, giving rise to the time-dependent effective Zeeman coupling term

$$\mathbf{\Omega} = u_v E^+ E^- \mathbf{e}_x \left\{ \mathrm{e}^{2\mathrm{i}k_R x} \left[\mathrm{e}^{-\mathrm{i}\delta\omega_{-1} t} + \mathrm{e}^{-\mathrm{i}\delta\omega_{+1} t} \right] + \mathrm{c.c} \right\} \tag{6.4}$$

$$= 2\Omega_1 \left[\cos(2k_R x - \delta\omega_{-1} t) + \cos(2k_R x - \delta\omega_{+1} t) \right] \mathbf{e}_x \tag{6.5}$$

where we defined $\delta\omega_{\pm 1} = \omega^- - \omega^+_{\pm 1}$.

This gives the Hamiltonian term

$$H_v = 2\Omega_1 \left[\cos(2k_R x - \delta\omega_{-1} t) + \cos(2k_R x - \delta\omega_{+1} t)\right] \hat{F}_x. \tag{6.6}$$

In our experiment the $\omega_Z/2\pi \approx 25\,\mathrm{MHz}$ linear Zeeman shift is large compared to all other energy scales, so we make the rotating wave approximation (RWA) to arrive at the low-frequency Hamiltonian

$$\begin{aligned} H_{\mathrm{RWA}} = {} & \Omega_1 \left\{\cos[2k_R x - (\delta\omega_{-1} - \omega_Z)t] + \cos[2k_R x - (\delta\omega_{+1} - \omega_Z)t]\right\} \hat{F}_x \\ & - \Omega_1 \left\{\sin[2k_R x - (\delta\omega_{-1} - \omega_Z)t] + \sin[2k_R x - (\delta\omega_{+1} - \omega_Z)t]\right\} \hat{F}_y. \end{aligned} \tag{6.7}$$

We selected our frequencies to be in four-photon resonance with the $|-1\rangle$ to $|+1\rangle$ transition, giving $(\delta\omega_{-1} - \omega_Z) = -(\delta\omega_{+1} - \omega_Z)$, in which case the Hamiltonian is time-periodic. Equation 6.1 in the manuscript is obtained by making independent RWAs on the $|-1\rangle \to |0\rangle$ and $|0\rangle \to |+1\rangle$ transitions separately, giving the helically precessing coupling described in the manuscript.

6.5.4. Floquet and polynomial shift. The frequency differences $\delta\omega_{-1,0} \approx \omega^- - \omega^+_{-1}$ and $\delta\omega_{0,+1} \approx \omega^- - \omega^+_{+1}$ nominally Raman dress both $|-1, 0\rangle$ and $|0, +1\rangle$ state pairs independently. In practice, the cross coupling may be substantial and the adjusted eigenenergies may be computed exactly from Floquet theory. For our $\epsilon + \Omega_2^0 = (\delta\omega_{-1,0} - \delta\omega_{0,+1})/2$ separation between Floquet bands [in our experiment

$\epsilon = h\times 90.417(1)$ kHz] we find the relationship between Ω_1, Ω_2 and Ω_2^0 is well described by the polynomial

$$\frac{\Omega_2}{E_R} = \frac{\Omega_2^0}{E_R} + \left(\frac{\Omega_1}{E_R}\right)^2 \Bigg[-4.90\times 10^{-2} + 1.56\times 10^{-2}\left(\frac{\Omega_1}{E_R}\right) - 4.41\times 10^{-3}\left(\frac{\Omega_1}{E_R}\right)^2 + 5.80\times 10^{-4}\left(\frac{\Omega_1}{E_R}\right)^3 - 2.76\times 10^{-5}\left(\frac{\Omega_1}{E_R}\right)^4 \Bigg]. \tag{6.8}$$

6.5.5. Measurement details. In the horizontal scans in Fig. 6.1 of the manuscript, we ramped Ω_1 at a rate of $\approx -40E_{\mathrm{R}}/\mathrm{s}$, allowing the system to adiabatically track the ground state, and allowed 50 ms for equilibration before the measurement process. In contrast, for our vertical scans we found the system required between 0.2 ms and 2 s to equilibrate.

We studied the metastable states by performing three separate experiments for each raw data point: one each for a system initially prepared in $m_F = 0, \pm 1$ state at the desired value of Ω_2. We then adiabatically ramped Ω_1 from zero to its final value. For each resulting (Ω_1, Ω_2) pair, we obtained the magnetization M_z for each initial state. In all of the described procedures Ω_1 was turned off immediately, at the start of our 28 ms time-of-flight imaging process which included a Stern-Gerlach gradient to separate the spin components.

6.5.6. Operators. The total angular momentum $f = 1$ spin operators in Eq. 6.1 of the main manuscript take the explicit form

$$\hat{F}_x = \frac{\hbar}{\sqrt{2}} \begin{pmatrix} 0 & 1 & 0 \\ 1 & 0 & 1 \\ 0 & 1 & 0 \end{pmatrix}, \; \hat{F}_y = \frac{\hbar}{\sqrt{2}} \begin{pmatrix} 0 & -\mathrm{i} & 0 \\ \mathrm{i} & 0 & -\mathrm{i} \\ 0 & \mathrm{i} & 0 \end{pmatrix}, \text{ and } \hat{F}_z = \hbar \begin{pmatrix} 1 & 0 & 0 \\ 0 & 0 & 0 \\ 0 & 0 & -1 \end{pmatrix} \tag{6.9}$$

in the basis of the magnetic sublevels $|-1\rangle$, $|0\rangle$, and $|+1\rangle$; together these comprise the vector operator $\hat{\mathbf{F}} = \hat{F}_x \mathbf{e_x} + \hat{F}_y \mathbf{e_y} + \hat{F}_z \mathbf{e_z}$. Likewise the quadrupole tensor operator is expressed as

$$\hat{F}_{zz} = \hbar \begin{pmatrix} 1/3 & 0 & 0 \\ 0 & -2/3 & 0 \\ 0 & 0 & 1/3 \end{pmatrix}. \tag{6.10}$$

In terms of these operators it is clear than any Hamiltonian involving only $\hat{1}$, $\hat{F}_x$, $\hat{F}_y$ and $\hat{F}_{zz}$ is invariant under the transformation that swaps $|+1\rangle$ and $|-1\rangle$: a discrete Z_2 symmetry.

6.5.7. Wavefunctions. The wavefunctions in the polarized and unpolarized regimes are qualitatively different. In the unpolarized regime the wavefunction takes the general form $|\psi\rangle = A \exp(2\mathrm{i}k_R x) |+1\rangle - \sqrt{1-2A^2}\,|0\rangle + A \exp(-2\mathrm{i}k_R x) |-1\rangle$. The value of A depends in detail on Ω_1 and Ω_2, but two limits are clear. Firstly, when $\Omega_1 = 0$ and $\Omega_2 > 0$ the system forms a spinor BEC in the polar phase, with $A = 0$: a BEC in $m_F = 0$. Secondly, for $\Omega_1 \to \infty$ the local spin follows $\mathbf{\Omega}$ giving $A = \sqrt{2/5}$.

In the polarized regime the wavefunction has the general form

$$|\psi\rangle = A_{+1}\exp[\mathrm{i}(k_0+2k_R)x]\,|{+1}\rangle - \sqrt{1-A_{+1}^2-A_{-1}^2}\exp[\mathrm{i}k_0x]\,|0\rangle + A_{-1}\exp[\mathrm{i}(k_0-2k_R)x]\,|{-1}\rangle\,, \tag{6.11}$$

but with constraints: firstly $M_z = A_{+1}^2 - A_{-1}^2$ (the definition of magnetization), and secondly $M_z = -k_0/2k_R$ (ensuring zero center-of-mass motion, see Ref. [100]). In our experiment $m_F = \pm 1$ are coupled at second order inΩ_1, and for $|M_z| \lesssim 1$, these states are $\approx 16E_R$ detuned. Thus for $M_z \lesssim +1$, we have $A_{-1} \approx 0$ with corrections at order Ω_1^2, giving the wavefunction $|\psi\rangle \approx \mathrm{e}^{-\mathrm{i}2k_RM_zx}\left\{\sqrt{M_z}\mathrm{e}^{\mathrm{i}2k_Rx}\,|{+1}\rangle - \sqrt{1-M_z}\,|0\rangle\right\}$ in terms of the magnetization.

6.5.8. Free energy and phase diagram. We obtained the free energy $G(M_z)$ as a function of the magnetization M_z by first numerically solving the system's Hamiltonian given by Eq. 6.1, obtaining the eigenenergies $E_\sigma(\mathbf{k})$ and state $\psi_\sigma(\mathbf{k})$, each identified by a momentum $\hbar\mathbf{k}$ and a "band" index $\sigma \in \{-1, 0, +1\}$. We then computed M_z for each of these states (dependent on k_x, but independent of k_y and k_z), thereby obtaining the internal energy $E(M_z)$ in the lowest band ($\sigma = -1$).

As our BEC is very near the ground state the free energy $G(M_z) = E(M_z) - TS$, where T is the temperature and S is the entropy is well approximated by $G(M_z) \approx E(M_z)$, and it is this free energy which is plotted in Fig. 6.1(c). We then obtained the phase diagram in Fig. 6.1(b) by numerically computing the free energy for each pair Ω_1, Ω_2 and identifying its equilibrium magnetization.

For non-interacting systems, we found that the curves defining the phase transitions and also those bounding the region containing metastable states could all be computed in closed form. Firstly, the critical point at which the first- and second-order phase transitions meet is at

$$\frac{\Omega_1^*}{E_R} = 8\sqrt{10\sqrt{5}-22}, \text{ and } \frac{\Omega_2^*}{E_R} = 52 - 24\sqrt{5}. \tag{6.12}$$

The curve defining the first-order phase transition (for $0 \geq \Omega_2 \geq \Omega_2^*$) is given by

$$\frac{\Omega_1^C(\Omega_2)}{E_R} = 2\sqrt{2}\sqrt{72 + 10\frac{\Omega_2}{E_R} - \sqrt{\left(\frac{\Omega_2}{E_R}+36\right)^2\left(\frac{\Omega_2}{E_R}+4\right)}}, \tag{6.13}$$

and the curve defining the second-order phase transition (for $\Omega_2^* \geq \Omega_2$) is given by

$$\frac{\Omega_1^C(\Omega_2)}{E_R} = \frac{1}{2\sqrt{2}}\sqrt{-16 - \left(\frac{\Omega_2}{E_R}\right)^2 - 72\frac{\Omega_2}{E_R} - \left(\frac{\Omega_2}{E_R}-12\right)\sqrt{\frac{\Omega_2}{E_R}\left(\frac{\Omega_2}{E_R}-88\right)-112.}}. \tag{6.14}$$

The upper boundary of the metastable regime (in the unmagnetized phase) is given by

$$\frac{\Omega_1^+(\Omega_2)}{E_R} = \left(\frac{2}{3}\right)^{3/2}\sqrt{\frac{(4-\Omega_2/E_R)^3}{4+\Omega_2/E_R}}. \tag{6.15}$$

and the lower boundary of the metastable regime (in the ferromagnetic phase) is given by

$$\frac{\Omega_1^-(\Omega_2)}{E_R} = \frac{1}{2\sqrt{2}}\sqrt{-16 - \left(\frac{\Omega_2}{E_R}\right)^2 - 72\frac{\Omega_2}{E_R} \pm \left(\frac{\Omega_2}{E_R}-12\right)\sqrt{\frac{\Omega_2}{E_R}\left(\frac{\Omega_2}{E_R}-88\right)-112.}}. \tag{6.16}$$

This is the same equation defining the second-order phase transition with an added $\pm$, the full curve defining the boundary of the metastable regime crosses over between the + and − solutions at $\Omega_2/E_R = 4(11 - 8\sqrt{2})$.

6.5.9. Magnetic Fields. Because the free energy $G(M_z)$ is sensitive to unwanted detuning δ from the four-photon resonance near the phase transitions which contributes an added symmetry breaking field $\delta\hat{F}_z$ to the Hamiltonian, controlling the bias magnetic field and nulling its gradients is critical. A pair of flux-gate sensors measuring the ambient magnetic field along $\mathbf{e}_z$, allowed us to compensate for long-term field drifts. We compensated any field gradients using four pairs of anti-Helmholtz coils in a clover leaf configuration [117], and a conventional anti-Helmholtz pair, all aligned along $\mathbf{e}_z$.

6.5.10. Interactions. We studied the impact of interactions at the level of mean field theory using a variational approach, assuming an infinite homogenous system. For each point in the phase diagram labeled by (Ω_1, Ω_2), we first located the local minima in the single-particle free energy described by the Hamiltonian $\hat{H}$ of Eq. 6.1 in the manuscript. The free energy had from one to three minima, with energies E_j and eigenstates $|\psi_j\rangle$.

We then considered an infinite system and minimized the mean field energy density

$$\mathcal{E} = \frac{1}{V}\int \mathrm{d}^3\mathbf{x}\psi^\dagger(\mathbf{x})\hat{H}(\mathbf{x})\psi(\mathbf{x}) + \frac{1}{2V}\int \mathrm{d}^3\mathbf{x}\left[(c_0 + c_2)n_T^2 - c_2 n_0^2 - 4c_2 n_{+1}n_{-1}\right] \quad (6.17)$$

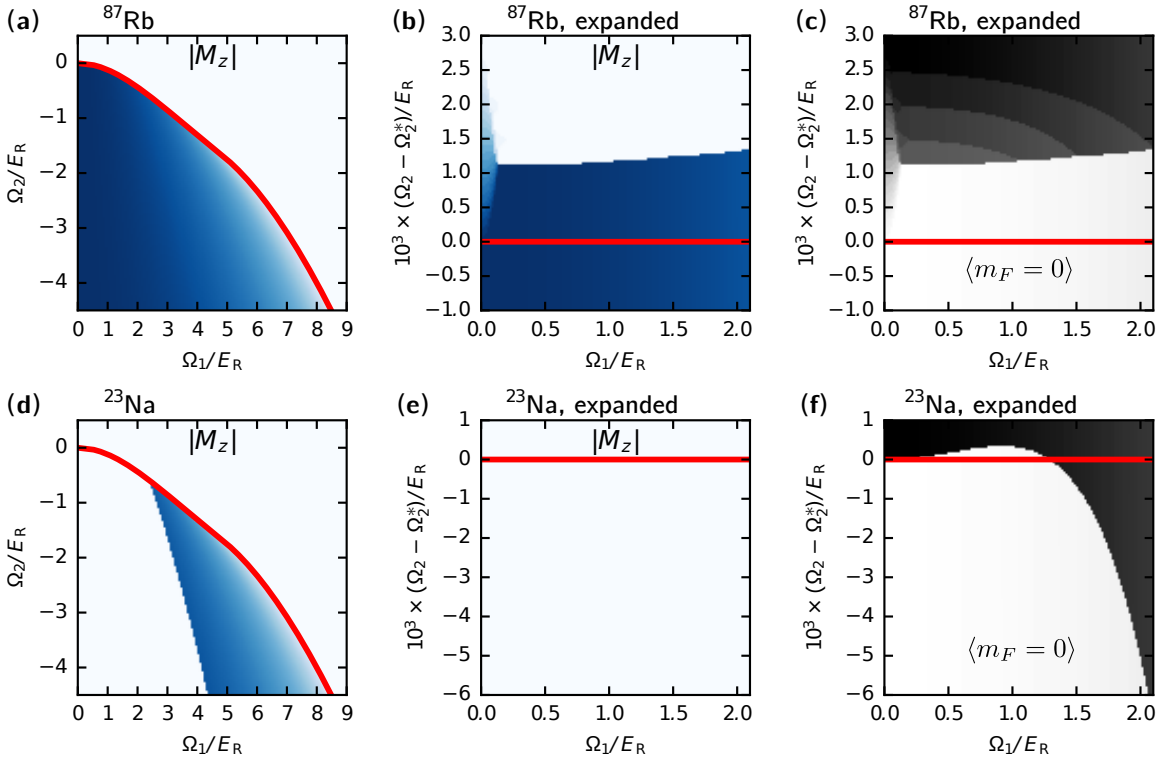

FIGURE 6.5. **Mean field phase diagram** (a)-(c) Rubidium. (d)-(f) Sodium. In each panel, the red curve marks the location of the phase transition as computed excluding interactions. Panels (b), (c), (e), and (f) are all expanded views of the region around the critical curve. Panels (a), (b), (d), and (e) plot the $|M_z|$ order parameter: the plot is dark blue when $|M_z| = 1$ and there is a continuous gradation to white when $|M_z| = 0$. Panels (c) and (f) plot the fraction of the wavefunction in $m_F = 0$: similarly, black color indicates when all the atoms are in $m_F = 0$ and white when none of the atoms are in $m_F = 0$.

for an arbitrary linear combination of these single particle states with amplitudes α_j, where $n_\sigma(\mathbf{x})$ is the local density in a given spin state σ; $n_T(\mathbf{x})$ is the total local density; and c_0 and c_2 are the spin-independent and spin-dependent interactions respectively. For ^{87}Rb these have the ratio $c_2/c_0 \approx -0.005$ and for ^{23}Na they are $c_2/c_0 \approx +0.05$. In our minimization, we modeled our systems with a typical mean-field energy of $(c_0 + c_2)n_T \approx 1\,\text{kHz}$ per particle.

Figure 6.5 shows the result of this calculation both for rubidium and sodium. In both cases the overall phase diagram (Fig. 6.5 (a),(d)) is shaped by the single-particle Hamiltonian; at this coarse level the rubidium phase diagram is hardly different from that predicted from single particle physics, but in the case of sodium a large swath of the expected ferromagnetic phase remains symmetry unbroken. This phase continuously connects to an equal superposition of $|-1\rangle$ and $|+1\rangle$ as $\Omega_1 \to 0$.

The situation becomes more complex as we focus on M_z near the curve defining the first-order phase transition (Fig. 6.5(b),(e)), for the case of rubidium a new mixed phase appears at low Ω_1 analogous to the striped phase in spin-1/2 systems, but nothing new is apparent for sodium.

Lastly we consider the same region, but looking at the fraction of the variational wavefunction in the $m_F = 0$ spin state. For rubidium, this allows us to identify a new state which is a three-way mixture of all three components considered in the variational calculation (with no analogue in the $\Omega_1 = 0$ spinor limit), and we can see the abrupt transition in sodium from a state connecting to the polar phase ($\Omega_2 > 0$) and to the uniaxial nematic phase ($\Omega_2 < 0$). Each of these phases are as described in Ref. [125].

CHAPTER 7

Probing atomic structure with optical Bragg scattering

Bragg scattering is a useful method to probe crystal structure and magnetic (spin) structure in many solid state systems. In atomic physics, optical Bragg diffraction has provided crucial insights into the localization of atomic wavefunction arranged in an optical lattice [17, 174]. Interference of coherent light scattered by spatially periodic atoms enhances the angular distribution of the diffracted light in the direction satisfying Bragg's law. Recently, this method has been extended to probe quantum phase transitions in various engineered quantum systems, including the superfluid transition to the Mott-insulator regime in a three-dimensional optical lattice [120], and antiferromagnetic correlations in the Hubbard model realized with a two-spin component Fermi gas in an optical lattice [65].

Motivated by this work, I used optical Bragg scattering to map out the stripe ordered phase in spin-orbit-coupled (SOC) Bose-Einstein condensates (BECs) realized with two-photon Raman coupling scheme. Complementary to this work, Jun-Ru Li *et al.* has also observed the stripe phase in SOC BECs realized with optical superlattices [96], as published in Ref. [95]. Before presenting my observations of the stripe-ordered phase in Chapter 8, I first give a physical explanation of optical Bragg scattering. In this chapter, I review the theory of optical Bragg scattering and discuss

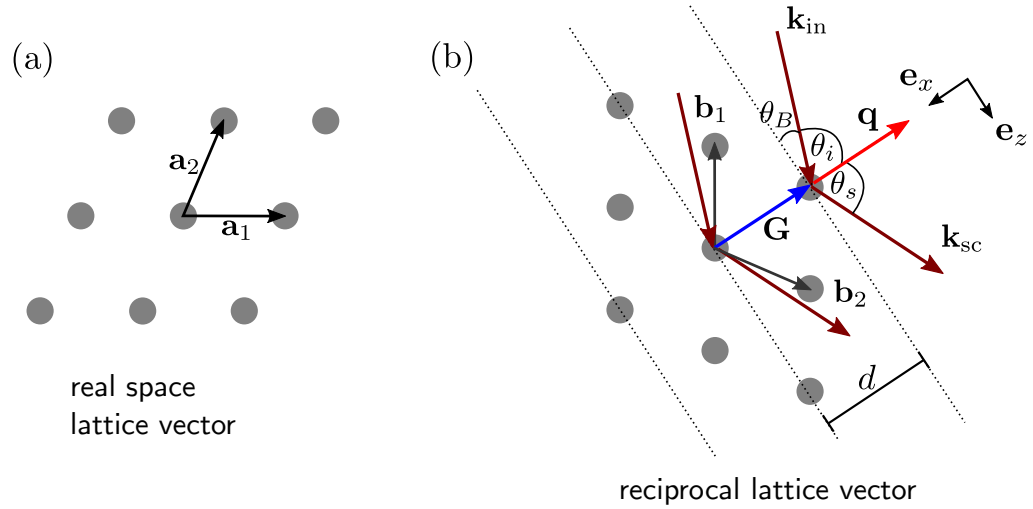

FIGURE 7.1. Two-dimensional illustration of (a) real space lattice and (b) reciprocal space scattering from periodic scatterers with direct lattice vector $\mathbf{R}_n = n_1\mathbf{a}_1 + n_2\mathbf{a}_2$. Bragg's law is satisfied when the scattering wavevector $\mathbf{q} = \mathbf{k}_{\text{sc}} - \mathbf{k}_{\text{in}}$ follows the von Laue equation $\mathbf{q} = \mathbf{G}_m$ in the reciprocal space, where $\mathbf{G}_m = m_1\mathbf{b}_1 + m_2\mathbf{b}_2$ is the reciprocal lattice vector.

the characterization of the Bragg signal, with a focus on its geometrical properties. In addition, I also present my observations of various atomic structures probed with optical Bragg scattering.

7.1. Theory of optical Bragg scattering

Consider a system of scatterers arranged periodically with lattice vector $\mathbf{R}_n$, where the density distribution is a periodic function satisfying $\rho(\mathbf{r}) = \rho(\mathbf{r} + \mathbf{R}_n)$, as shown in Fig. 7.1. The lattice vector describes the translational symmetry in the system:

$$\mathbf{R}_n = n_1\mathbf{a}_1 + n_2\mathbf{a}_2 + n_3\mathbf{a}_3, \tag{7.1}$$

where $\mathbf{a}_1, \mathbf{a}_2$, and $\mathbf{a}_3$ are the primitive translation vectors, which span the smallest volume of the lattice cell, and (n_1, n_2, n_3) are integers. The corresponding reciprocal lattice vectors $\mathbf{G}_m$ are defined by the relation $\mathbf{G}_m \cdot \mathbf{R}_n = 2\pi m$ where m are non-zero integers. For an incoming wave with wavevector $\mathbf{k}_{\text{in}}$, the maximum intensity of the scattered wave with wavevector $\mathbf{k}_{\text{sc}}$ in the far-field limit occurs when the scattering wavevector $\mathbf{q} = \mathbf{k}_{\text{sc}} - \mathbf{k}_{\text{in}}$ satisfies the von Laue equation $\mathbf{q} = \mathbf{G}_m$ [10]. The Bragg's law is equivalent to the von Laue equation in the case of elastic scattering where $|\mathbf{k}_{\text{sc}}|^2 = |\mathbf{k}_{\text{in}}|^2$, specifically

$$2\mathbf{k}_{\text{in}} \cdot \mathbf{G}_m = G_m^2 \tag{7.2}$$

$$2d \sin\theta_B = m\lambda, \tag{7.3}$$

where d is the lattice spacing and θ_B is the angle between the incoming wavevector and the lattice plane, as displayed in Fig. 7.1.

Needless to say, this textbook explanation of Bragg's law assumes the scatterers are arranged in a regular lattice. In this simple picture, the atomic distribution within a lattice site is typically assumed to be a $\delta-$function and there are an infinite number of lattice sites. The resulting scattered Bragg signal has a very sharp angular distribution and Eq. 7.3 determines the peak locations of the scattered signal. However, in real atomic experiments, the finite size of the samples must be taken into account and this broadens the angular spectrum of the observed Bragg signal. Moreover, the nature of the atom-light interaction affecting the scattering properties has to be

considered as well. In crystallography, one needs to include the interaction between the crystalline matter with the scattered particles. This leads to the concept of the atomic form factor [10].

To study Bragg scattering in more detail, I present an overview of the relevant theory in the following subsections. I consider the Maxwell-Bloch equations [25] which give a complete description of the atom-light interaction within the semi-classical approach. With suitable approximations, I then derive a differential cross-section, as commonly used in the scattering theory. Next, I discuss the quantized nature of the light and how this affects the scattered Bragg signal.

7.1.1. The semi-classical approach. In the semi-classical treatment of light scattering by atoms [119], the electric field $\mathbf{E}(\mathbf{r},t)$ is treated classically and governed by Maxwell equations. For a system without free charges and free currents, Maxwell equations lead to the general wave equation [25]:

$$\left[\nabla^2 - \frac{1}{c^2}\partial_t^2\right]\mathbf{E}(\mathbf{r},t) = \frac{1}{\epsilon_0}\left[-\nabla\left(\nabla\cdot\right) + \frac{1}{c^2}\partial_t^2\right]\mathbf{P}(\mathbf{r},t), \tag{7.4}$$

where the polarization density $\mathbf{P}(\mathbf{r},t)$ describes the "induced" density of charge and current in the medium.

Here I assume the quantum mechanical model of an ensemble of identical atoms and their behavior is governed by the master equation [12]:

$$\frac{\mathrm{d}}{\mathrm{d}t}\rho(t) = \mathcal{L}[\rho(t)] - \frac{\mathrm{i}}{\hbar}\left[-\mathbf{d}\cdot\mathbf{E}(\mathbf{R},t),\ \rho(t)\right], \tag{7.5}$$

where $\rho(t)$ is the atomic density matrix, and $\mathcal{L}[\rho(t)]$ is the Liouville operator which incorporates the atomic kinetic energy, internal energy, and radiative decays due to spontaneous emission and/or collisions. The equations of motions derived from the master equation is also known as the optical Bloch equations. In Eq. 7.5, I have made the usual electric dipole approximation. The interaction between light and atoms is described by the dipole interaction $-\mathbf{d}\cdot\mathbf{E}$, where $\mathbf{E}(\mathbf{R},t)$ is the electric field at the center of mass location of an individual atom and the field induces a dipole moment $\mathbf{d}$ in the atom.

As a counterpart to Eq. 7.5, the induced dipole moment creates polarization vector field which is governed by the relation

$$\mathbf{P}(\mathbf{r},t) = N\ \mathrm{Tr}\left[\rho(t)\,\delta(\mathbf{r}-\mathbf{R})\,\mathbf{d}\right] = N\ \mathrm{Tr}_{\mathrm{int}}\left[\langle\mathbf{r}|\,\rho(t)\,|\mathbf{r}\rangle\,\mathbf{d}\right], \tag{7.6}$$

where N is the total number of atoms and the trace in Eq 7.6 is taken over the atomic internal degrees of freedom.

The Eqs. 7.4-7.6 are the Maxwell-Bloch equations [25]. These coupled equations can be solved in a self-consistent manner and the solution gives a comprehensive picture of propagation of light through matter within the semi-classical approach.

For a physical understanding of Bragg's law, I now consider a simplified version of the Maxwell-Bloch equations. I assume the atomic system is illuminated by a weak laser beam with a time-harmonic field of the form $\vec{E}(\mathbf{r},t) = \Re\left[\hat{\epsilon}E(\mathbf{r})\exp(\mathrm{i}k_0 r - \mathrm{i}\omega t)\right]$.

The wave equation then reduces to the scalar Helmholtz equation

$$\nabla^2 E(\mathbf{r}) + k_0^2 E(\mathbf{r}) = -U(\mathbf{r}) E(\mathbf{r}), \tag{7.7}$$

which describes wave propagation in a medium characterized by relative permittivity $\varepsilon(\mathbf{r})$. Here I have introduced the "scattering potential" $U(\mathbf{r}) = k_0^2 [\varepsilon(\mathbf{r}) - 1]$. In the limit of weak scattering, the scattered field in the far-field region behaves as

$$E_{\mathrm{sc}}(\mathbf{r}) = F(\mathbf{q}) \frac{\exp(\mathrm{i}k_0 r)}{r}, \tag{7.8}$$

where the scattering wavevector is $\mathbf{q} = \mathbf{k}_{\mathrm{sc}} - \mathbf{k}_{\mathrm{in}}$ and the *scattering amplitude* $F(\mathbf{q})$ in the first Born approximation [34] is given by:

$$F(\mathbf{q}) = \frac{1}{4\pi} \int U(\mathbf{r}') \, \mathrm{e}^{-\mathrm{i}\mathbf{q}\cdot\mathbf{r}'} d^3\mathbf{r}'. \tag{7.9}$$

In this approximation, the scattering is assumed to be elastic, where $|\mathbf{k}_{\mathrm{sc}}| \simeq |\mathbf{k}_{\mathrm{in}}| = k_0$.

To find the scattering of light by a periodic array of atoms, I use the definition of susceptibility $\chi(\mathbf{r}) = \varepsilon(\mathbf{r}) - 1$ and write the scattering amplitude as $F(\mathbf{q}) = (k_0^2/4\pi) \int \chi(\mathbf{r}') \, \mathrm{e}^{-\mathrm{i}\mathbf{q}\cdot\mathbf{r}'} \mathrm{d}^3\mathbf{r}'$. At the detection point along the direction of the diffracted wave vector $\hat{\mathbf{k}}_{\mathrm{sc}}$, the differential cross-section of the scattered light intensity is given by [34]:

$$\frac{\mathrm{d}P}{\mathrm{d}\Omega} = |F(\mathbf{q})|^2 = \left| \frac{\pi}{\lambda_0^2} \int \mathrm{d}^3\mathbf{r}' \, \chi(\mathbf{r}') \, \mathrm{e}^{-\mathrm{i}\mathbf{q}\cdot\mathbf{r}'} \right|^2. \tag{7.10}$$

Without loss of generality, I can express $\chi(\mathbf{r}')$ as a summation over each single lattice site local distribution $\chi_j\left(\mathbf{r}'_j\right)$

$$\chi(\mathbf{r}') = \sum_{j=1}^{N_S} \chi_j\left(\mathbf{r}'_j\right), \tag{7.11}$$

where the local coordinates of each j-th lattice site are $\mathbf{r}'_j = \mathbf{r}' - \mathbf{R}_j$, the periodicity of the system is described by the lattice vector $\mathbf{R}_j$, and the atoms are spread over N_s sites of the lattice within a finite size. I then write the scattering amplitude as

$$F\left(\mathbf{q}\right) = \frac{\pi}{\lambda_0^2} \sum_{j=1}^{N_S} \mathrm{e}^{-\mathrm{i}\mathbf{q}\cdot\mathbf{R}_j} \tilde{\chi}_j, \tag{7.12}$$

where the Fourier transform of $\chi_j\left(\mathbf{r}'_j\right)$ is given by $\tilde{\chi}_j = \int d^3\mathbf{r}'_j\ \chi_j\left(\mathbf{r}'_j\right) \exp\left(-\mathrm{i}\mathbf{q}\cdot\mathbf{r}'_j\right)$.

Based on the Heisenberg uncertainty principle, the atom's location can be thought of as having some fluctuations, i.e. $\mathbf{r}'_j \rightarrow \mathbf{r}'_j\left(t\right) = \mathbf{r}'_j + \mathbf{u}\left(t\right)$. This effect can be incorporated by including the time displacement $\mathbf{u}(t)$ with respect to the lattice site into the exponential term

$$\mathrm{e}^{-\mathrm{i}\mathbf{q}\cdot\mathbf{R}_j} \rightarrow \mathrm{e}^{-\mathrm{i}\mathbf{q}\cdot\mathbf{R}_j} \left\langle \mathrm{e}^{\mathrm{i}\mathbf{q}\cdot\mathbf{u}(t)} \right\rangle_\tau, \tag{7.13}$$

and using the Taylor expansion for the exponential of an operator, I obtain:

$$\left\langle \mathrm{e}^{\mathrm{i}\mathbf{q}\cdot\mathbf{u}(t)} \right\rangle_\tau = \exp\left[-\frac{1}{2}\sum_{i=x,y,z} q_i^2 \left\langle u_i^2 \right\rangle_\tau\right] = \prod_{i=x,y,z} \exp\left[-\frac{1}{2} q_i^2 \left\langle u_i^2 \right\rangle_\tau\right]. \tag{7.14}$$

Taking into account the spatial fluctuations, the elastic scattered intensity $I_{\mathrm{d}\Omega} \propto \mathrm{d}P/\mathrm{d}\Omega$ of a finite-sized medium then becomes

$$I_{\mathrm{d}\Omega} \propto \mathrm{e}^{-2W_q(\tau)} \sum_{j,k}^{N_S} \tilde{\chi}_j \tilde{\chi}_k^* \mathrm{e}^{-\mathrm{i}\mathbf{q}\cdot(\mathbf{R}_j - \mathbf{R}_k)}, \tag{7.15}$$

where the Debye-Waller factor is defined by:

$$\mathrm{e}^{-W_q(\tau)} = \prod_{i=x,y,z} \exp\left[-\frac{1}{2} q_i^2 \left\langle u_i^2 \right\rangle_\tau\right]. \tag{7.16}$$

In the semi-classical treatment of Bragg scattering, the atomic structure is treated with the quantum master equation and this leads to the optical Bloch equations [163]. For a two-level system in the steady-state, the susceptibility is proportional to the atomic density $\rho_{\mathrm{at}}(\mathbf{r})$ and it can be written in the form [81]

$$\chi(\mathbf{r}) = \frac{\sigma_0}{k_0}\left[\frac{\mathrm{i} - 2\Delta}{1 + s_0 + 4\Delta^2}\right] \rho_{\mathrm{at}}(\mathbf{r}), \tag{7.17}$$

where $\rho_{\mathrm{at}}(\mathbf{r})$ is the atomic density, δ is the laser's detuning from atomic resonance, $\sigma_0 = 6\pi/k_0^2$ is the resonant scattering cross-section, Γ is the atomic linewidth, and s_0 is the saturation parameter (as discussed previously in Chapter 4). Similar to Bragg scattering in solid-state physics, I can now define the *atomic form factor*:

$$f_j = \int d^3\mathbf{r}'_j \; \rho_l\left(\mathbf{r}'_j\right) \mathrm{e}^{-\mathrm{i}\mathbf{q}\cdot\mathbf{r}'_j}, \tag{7.18}$$

where $\rho_l\left(\mathbf{r}'_j\right)$ is the local density distribution of the atomic electron cloud about its center of mass located at the $j-$th lattice site. Substituting Eq. 7.17 for the susceptibility into Eq. 7.15 gives

$$I_{\mathrm{d}\Omega} \propto \mathrm{e}^{-2W_Q(\tau)} \frac{4\Delta^2+1}{\left(1+s_0+4\Delta^2\right)^2} \sum_{j,k}^{N_S} f_j f_k^* \mathrm{e}^{-\mathrm{i}\mathbf{q}\cdot\left(\mathbf{R}_j-\mathbf{R}_k\right)}. \tag{7.19}$$

The properties of the scattered Bragg signal are governed by Eq. 7.19. It is useful to define the *static structure factor* as

$$S\left(\mathbf{q}\right) = \frac{1}{\sum_{j=1}^{N_S}\left|f_j\right|^2} \sum_{j,k}^{N_S} f_j f_k^* \mathrm{e}^{-\mathrm{i}\mathbf{q}\cdot\left(\mathbf{R}_j-\mathbf{R}_k\right)} = \frac{1}{N_{\mathrm{atom}}} \sum_{j,k}^{N_S} f_j f_k^* \mathrm{e}^{-\mathrm{i}\mathbf{q}\cdot\left(\mathbf{R}_j-\mathbf{R}_k\right)}. \tag{7.20}$$

For a Dirac-delta function in the atomic local density $\rho_l\left(\mathbf{r}'_j\right) = \delta\left(\mathbf{r}'_j\right)$, the location of the peak in the static structure factor coincides with that given by Bragg's law (Eq. 7.3) for an infinite number of scattering sites $N_S \gg 1$. This is known as the Kronig-Penney model [10].

In summary, Eqs. 7.19-7.20 describe the scattering from a periodic finite system for a very-far detuned probe in the elastic Rayleigh scattering regime.[1] The results in this subsection are limited to two-level systems where the structure factor is only sensitive to the periodic density modulation (crystal structure). For a multi-level system with two-ground states $|\uparrow\rangle$ and $|\downarrow\rangle$, periodic spin structure could exist where

[1]Historically, *Rayleigh* scattering is named after the British physicist Lord Rayleigh, which is an elastic scattering of light by particles much smaller than the wavelength of light (equivalent to the dipole approximation) [169].

the internal structure of the atoms alternate between each lattice site, for example due to the presence of a precessing magnetic field. Although there would be no spatial modulation in the total atomic density, the spin structure or magnetic ordering could lead to interference effects in the scattered signal [45].

7.1.2. Quantization of the electric field. In previous derivation of the Maxwell-Bloch equations using a semi-classical treatment, the electric field was treated as an expectation value of its corresponding quantum operator and any incoherent component of the field due to radiative spontaneous decay was neglected. Although the semi-classical approach has been successful in explaining many physical phenomena, it does not account for radiative spontaneous emission due to atoms interacting with electromagnetic vacuum fluctuations. To understand incoherent scattering due to spontaneous emission processes, one must treat the field in a quantized manner [119]. Here, I review the calculation of Bragg scattering from atoms acting as independent scatterers, where the electric field is quantized and treated as an operator. The theory presented in this subsection is based on Refs. [45, 65].[2]

Consider an ensemble of two-level atoms with ground state $|g\rangle$, excited state $|e\rangle$, dipole transition matrix element $\mathbf{d}_{ge} = \langle g|\,\mathbf{d}\,|e\rangle$, and transition linewidth Γ. When being illuminated with a probe light at frequency ω_0 and incoming wavevector $\mathbf{k}_{\text{in}}$,

[2]Correlations between the bosonic particles and multiple scattering in the atoms lead to a whole new series of phenomena, such as superradiant effect and non-linear four wave mixing. However, this treatment is beyond the scope of my work. Interested readers could consult the review article in Ref. [82] and references therein.

the electric dipole radiation emitted by an atom at a distance r is given by [35]

$$\hat{\mathbf{E}}_j^+(\mathbf{r}) = \frac{1}{\sqrt{2\epsilon_0 c}}\left[\frac{3}{8\pi}\frac{\hbar c k\Gamma}{r^2}\right]^{1/2}\mathbf{\Lambda}\exp\left[\mathrm{i}\mathbf{q}\cdot\hat{\mathbf{r}}_j\right]\hat{\sigma}_j^-, \tag{7.21}$$

where $\hat{\mathbf{E}}_j^+(\mathbf{r})$ is the positive frequency component of the electric field, $\mathbf{q} = \mathbf{k}_{\mathrm{sc}} - \mathbf{k}_{\mathrm{in}}$ is the scattering wavevector, $\hat{\mathbf{r}}_j$ is the position operator of the $j-$th atom, $\mathbf{\Lambda} = \mathbf{k}_{\mathrm{sc}} \times (\mathbf{k}_{\mathrm{sc}} \times \mathbf{d}_{ge})/k_{\mathrm{sc}}^2 |\mathbf{d}_{ge}|$ is the polarization vector of the scattered field, and $\hat{\sigma}_j^- = \exp(\mathrm{i}\omega_0 t)|g\rangle\langle e|$ is the off-diagonal matrix element of the atomic density matrix operator.

To obtain the total scattered intensity, I sum the field contributions from each of the individual atoms and square the total field to get

$$\begin{aligned} I(\mathbf{q}) &= 2\epsilon_0 c\langle\Psi|\sum_j \hat{\mathbf{E}}_j^- \cdot \sum_k \hat{\mathbf{E}}_k^+ |\Psi\rangle \\ &= \frac{3}{8\pi}\frac{\hbar c k\Gamma}{r^2}|\mathbf{\Lambda}|^2\left[\sum_{j,k;j\neq k}\rho_j^{eg}\rho_k^{ge}\langle u|\,\mathrm{e}^{-\mathrm{i}\mathbf{q}\cdot\hat{\mathbf{r}}_j}|u\rangle_j\langle u|\,\mathrm{e}^{\mathrm{i}\mathbf{q}\cdot\hat{\mathbf{r}}_k}|u\rangle_k + \sum_j \rho_j^{ee}\right]. \end{aligned} \tag{7.22}$$

Here I have used the product state $|\Psi\rangle = \prod_j |u\rangle_j |\psi\rangle_j$ to describe the wavefunction of the array of atoms, with $|u\rangle_j$ represents the center of mass state of the $j-$th atom and $|\psi\rangle_j = c_g^{(j)}|g\rangle + c_e^{(j)}|e\rangle$ is the electronic states of the $j-$th atom. The density matrix elements are represented by $\rho^{ee}, \rho^{gg}, \rho^{eg}$ and ρ^{ge}.

I now define the translation vector $\mathbf{R}_j$ for each of the individual atom to describe its center of mass, where the position operator satisfies $\langle\hat{\mathbf{r}}_j\rangle = 0$. The Debye-Waller

factor is:

$$\langle u|\, \mathrm{e}^{-\mathrm{i}\mathbf{q}\cdot\hat{\mathbf{r}}_j}\, |u\rangle_j = \mathrm{e}^{-\mathrm{i}\mathbf{q}\cdot\mathbf{R}_j} \prod_{i=x,y,z} \exp\left[-\frac{1}{2}q_i^2 \left\langle u_i^2\right\rangle_\tau\right] = \mathrm{e}^{-\mathrm{i}\mathbf{q}\cdot\mathbf{R}_j}\mathrm{e}^{-W_q(\tau)}. \tag{7.23}$$

Solving for the steady-state solutions of the density matrix elements governed by the optical Bloch equations, I obtain the scattered intensity as [45]:

$$\frac{I\left(\mathbf{q}\right)}{A} = \mathrm{e}^{-2W_q} \sum_{j,k;j\neq k} \frac{s_0}{2} \frac{(2\Delta_j + \mathrm{i})}{\left(1+s_0+4\Delta_j^2\right)} \frac{(2\Delta_k - \mathrm{i})}{(1+s_0+4\Delta_k^2)} \mathrm{e}^{-\mathrm{i}\mathbf{q}\cdot(\mathbf{R}_j-\mathbf{R}_k)} + \sum_j \frac{s_0/2}{1+s_0+4\Delta_j^2} \tag{7.24}$$

where $A = 3\hbar ck\Gamma\left|\mathbf{\Lambda}\right|^2/8\pi r^2$, s_0 is the on-resonance saturation parameter, and Δ is the probe detuning normalized to the linewidth Γ.

In light of the above derivation, it is helpful to make some comments on the scattered intensity in Eq. 7.24.

- The last term in Eq. 7.24 captures the non-interfering parts of the intensity. This term originates from radiative spontaneous emission and it becomes the dominant term if the saturation parameter satisfies $s_0 \gg |\Delta|$.[3] I obtain the same limit if the atomic sample has no correlation or no periodic behavior in its spatial arrangement, i.e. the first term is negligible.
- The first term on the right-hand side of Eq. 7.24 captures the interference from spatial ordering of the atoms. For atoms with multi-level ground states,

[3]Here, I have implicitly assumed the frequency spectrum of the radiative spontaneous decay is dominated by that of the driving frequency ω_0 (the coherent part). This subtlety originates from the solutions of the optical Bloch equations where periodic harmonic functions with frequency ω_0 are imposed on all of the time-dependent variables.

the interfering part also includes "magnetic ordering" of the system – where the atomic ground states are alternating in a spatially periodic way. For a very large detuning $\Delta \gg s_0$ and $\Delta_j \simeq \Delta_k = \Delta$, this term reduces to that of Eq. 7.19 if I replace the individual atoms with a continuum model for the atomic density.

- The non-interfering term scales as N_{atom}, which describes the fluorescence from spontaneous emission of the excited state. Meanwhile, the interfering term scales as N_{atom}^2, which can be interpreted as stimulated emission with definite phase relations between the scattered photons.
- When using optical Bragg scattering to probe periodic structure of ^{87}Rb atoms, I typically used the D_2 transition, which has a transition linewidth of $\Gamma = 6\,\text{MHz}$. For a far-detuned probe and weak enough probe intensity, or specifically $\delta \gg \Gamma\sqrt{1+s_0}$, the integrated scattered intensity depends linearly on the probe pulse time τ. I observed the detected Bragg signal did not saturate up to $\tau < 400\,\mu\text{s}$ for the parameter values $\delta/\Gamma \sim -10^3$ and $s_0 \sim 10$, and this was before the atoms heated up to the point where they were not trapped anymore. The detected Bragg signal also had a linear dependence on incoming probe intensity s_0, and there was no saturation effect for typical values of $s_0 < 100$. Meanwhile, for near-resonant beam with detuning $\delta < \Gamma\sqrt{1+s_0}$, the Bragg signal started to saturate pretty quickly, on a timescale of $\tau > 5\,\mu\text{s}$ for $s_0 \sim 10$.

7.2. Geometrical properties of optical Bragg scattering

7.2.1. The static structure factor. The simplest optical lattice can be made by retro-reflecting a single laser beam or interfering two counter-propagating lasers at wavenumber $k_d = 2\pi/\lambda_d$, forming a standing wave with periodicity of $d = \lambda_d/2$. In this one-dimensional (1D) lattice, let the $x-$axis lie along the laser propagation direction $\mathbf{k}_d$ and the $xz-$plane be the observation plane for the Bragg scattering (see Fig. 7.1). For an incoming Bragg probe with wavelength λ_0, I write the incoming wavevector $\mathbf{k}_{\rm in}$ and scattered wavevector $\mathbf{k}_{\rm sc}$ as

$$\mathbf{k}_{\rm in} = k_0\ \cos\theta_i \mathbf{e}_x + k_0\ \sin\theta_i \mathbf{e}_z, \quad \text{and} \qquad \mathbf{k}_{\rm sc} = -k_0\ \cos\theta_s \mathbf{e}_x + k_0\ \sin\theta_s \mathbf{e}_z, \quad (7.25)$$

where θ_i and θ_s are the incident and scattered angle with respect to the lattice axis $\mathbf{e}_x$, and $k_0 = 2\pi/\lambda_0$ is the wavenumber of the Bragg probe. Here, I consider the probe to be far-detuned with respect to the atomic transition and hence I am in the elastic Rayleigh scattering regime where $|\mathbf{k}_{\rm sc}| \simeq |\mathbf{k}_{\rm in}| = k_0$.

I now calculate the static structure factor of the finite-size 1D lattice. Assuming the atomic form factor to be identical for each lattice site j located at $\mathbf{R}_j = jd\mathbf{e}_x$, the structure factor has the form [156]

$$S(\mathbf{q}) = \frac{1}{N_{\rm atom}} \sum_{j=1}^{N_S} \sum_{k=1}^{N_S} f_j f_k^* e^{-i\mathbf{q}\cdot(\mathbf{R}_j - \mathbf{R}_k)} = \frac{1}{N_{\rm atom}} \left| \sum_{j=1}^{N_S} e^{-\mathrm{i}\mathbf{q}\cdot\mathbf{R}_j} \right|^2 |f_j|^2 . \quad (7.26)$$

The summation term in Eq. 7.26 gives [175]

$$\begin{aligned}|A|^2 =& \frac{1}{N_{\text{atom}}}\left|\sum_{j=1}^{N_S} \mathrm{e}^{-\mathrm{i}jq_xd}\right|^2 \\ =& \frac{1}{N_{\text{atom}}}\frac{\sin^2\left(q_xN_sd/2\right)}{\sin^2\left(q_xd/2\right)} = \frac{1}{N_{\text{atom}}}\frac{\sin^2\left[k_0\left(\cos\theta_s+\cos\theta_i\right)N_sd/2\right]}{\sin^2\left[k_0\left(\cos\theta_s+\cos\theta_i\right)d/2\right]}.\end{aligned} \tag{7.27}$$

I next assume the atomic density at each lattice site to have a Gaussian distribution with identical sizes in y and z, i.e.:

$$\rho_l\left(\mathbf{r}'_j\right) = n_0\exp\left(-\frac{x^2}{\sigma_x^2}\right)\exp\left(-\frac{y^2+z^2}{\sigma_r^2}\right), \tag{7.28}$$

where n_0 is the peak density, σ_x is the axial RMS width along x, and $\sigma_r = \sigma_y = \sigma_z$ is the radial RMS width along y and z. In the harmonic approximation of the trapping potential with radial beam waist w_d, the thermal RMS size of the atomic layers can be related to the potential depth U_0 and the temperature T, i.e. $\sigma_x \approx \lambda_d/2\pi\cdot\sqrt{k_BT/2U_0}$ and $\sigma_r \approx w_d/2\cdot\sqrt{k_BT/2U_0}$. Consequently, the magnitude squared of the atomic form factor becomes

$$\begin{aligned}|f_j|^2 &= n_0^2\exp\left[-\left(q_z^2\sigma_r^2+q_y^2\sigma_r^2+q_x^2\sigma_x^2\right)\right] \\ &= n_0^2\exp\left[-k_0^2\left(\sin\theta_s-\sin\theta_i\right)^2\sigma_r^2 - k_0^2\left(\cos\theta_s+\cos\theta_i\right)^2\sigma_x^2\right],\end{aligned} \tag{7.29}$$

where $q_y = 0$ with above choice of the plane of incidence ($xz-$plane). Note the definition of the static structure factor $S = |A|^2\,|f_j|^2$ in Eq. 7.26 is normalized to the total number atoms N_{atom}, and hence S scales as $S \propto n_0^2N_s^2/N_{\text{atom}} \approx N_{\text{atom}}$. This also

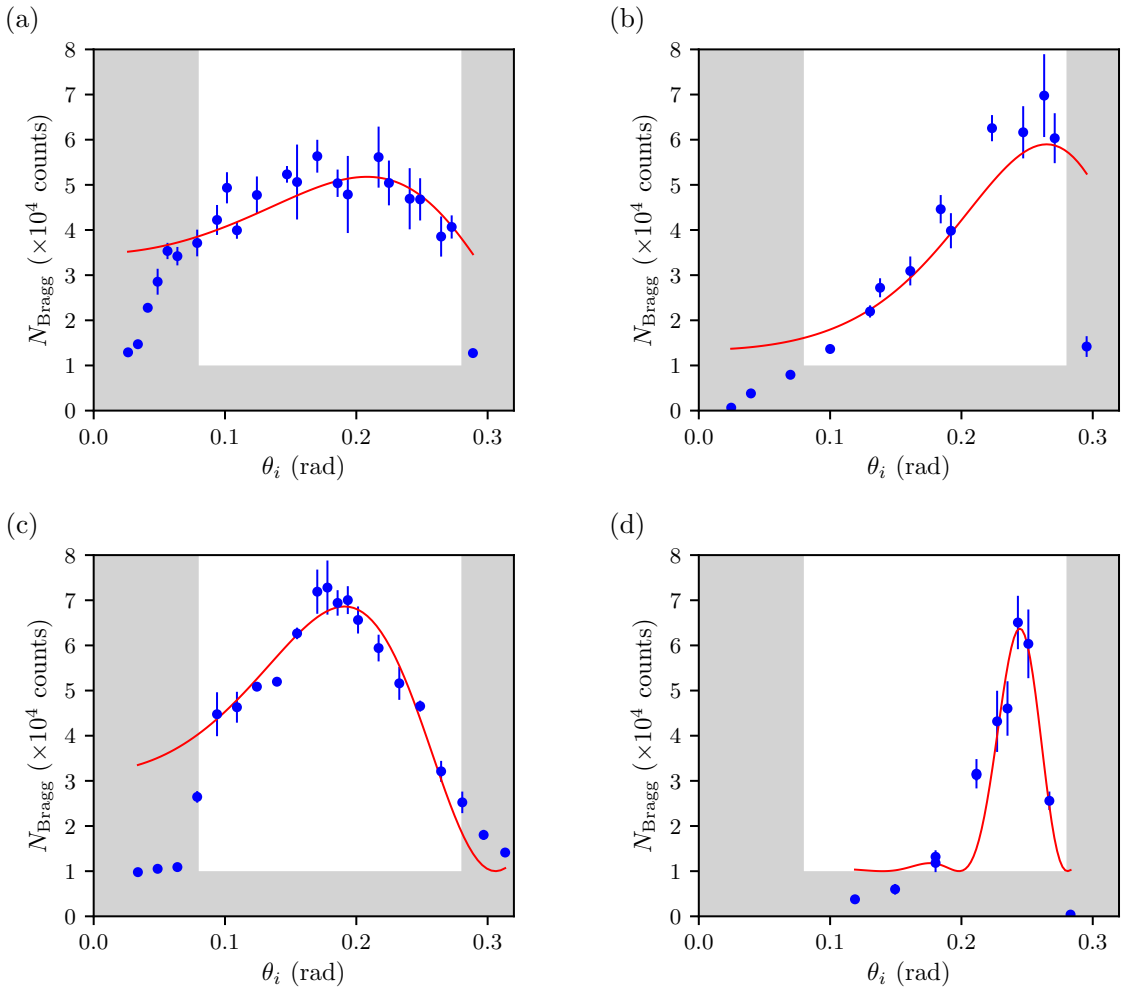

FIGURE 7.2. Bragg signal as a function of the incident probe angle θ_i. Here I show four different cases of ultracold atoms being loaded into 1D optical lattices and probed with optical Bragg scattering. (a) BEC in a lattice with $d = 395\,\mathrm{nm}$, (b) BEC in a lattice with $d = 405\,\mathrm{nm}$, (c) thermal clouds in a lattice with $d = 395\,\mathrm{nm}$, and (d) thermal clouds in a lattice with $d = 405\,\mathrm{nm}$.

means that the Bragg intensity has a quadratic proportionality to either the number of atoms N_{atom}^2 or the number of periodic layers N_s^2.

Based on this model for the structure factor, I can now discuss my observations of the scattered Bragg signal N_{Bragg} from atoms in 1D lattice. An example of the

scattered Bragg signal (integrated over the numerical aperture of our imaging system) as a function of the incoming angle θ_i is shown in Fig. 7.2. Here I consider the cases of a thermal cloud above the transition temperature T_C and of Bose-Einstein condensed atoms below T_C. I also compare the results for two different lattice periodicities, $d = 395\,\text{nm}$ [see Figs. 7.2(a) and (c)] and $d = 405\,\text{nm}$ [see Figs. 7.2(b) and (d)] .

Our collection optics had a capture angle $\alpha \sim \arctan(25/40) = 0.56\,\text{rad}$, centered on the optical axis (along the lattice direction). This allowed me to scan the incoming angle to a maximum value of 0.28 rad. For comparison, the Bragg probe had a beam waist diameter of 0.25 mm or 5.6×10^{-3} rad, two order of magnitude smaller than the capture angle. Meanwhile, the lower limit of the incoming angle scan was set by the edge of the D-shaped mirror which I used to send the Bragg probe. In Fig. 7.2, notice there is a sudden drop in the Bragg signal at the start and end of the plots ($\theta_i < 0.08\,\text{rad}$ and $\theta_i > 0.28\,\text{rad}$). This was due to the probe being clipped by the optics, indicated by the gray shaded area. In this region, the incoming angle was outside the limit of my scanning ability.

I fit the observation results in Fig. 7.2 with the structure factor as given by Eq. 7.26, as shown by the red curves in Fig. 7.2.[4] The peak Bragg signal for the particular case of infinite lattice is theoretically $\theta_B = \arccos(\lambda_0/2d)$. This gives peak Bragg angle at $\theta_B = 0.16\,\text{rad}$ and 0.27 rad for $d = 395\,\text{nm}$ and 405 nm, respectively. However, due to the finite size of the atomic cloud I observed small shifts in the peak

[4]In the fitting, I have used $\theta_s = \theta_i$ for the sake of simplicity. A more precise model is to integrate θ_s within the capture angle of the collection optics and including the Gaussian spread of the Bragg probe in θ_i.

value of θ_B. My observations are consistent to the structure factor model in Eqs. 7.26-7.29, where lattices with larger periodicity d have a larger peak Bragg angle. In the fit, I also find that the parameter $\sigma_x \lesssim d$ strongly affects the asymmetrical shape of the Bragg profile.

In the BEC regime with $T < T_C$, the diffracted signal has a broader spread in the angular distribution than that of the thermal atoms, as shown by Fig. 7.2. The reason is because the BEC is more confined spatially, and consequently the diffracted signal becomes broader in reciprocal $k-$space [156]. In contrast, the hotter thermal clouds have larger spatial size, and the atoms occupy more lattice sites N_s. The Bragg signal has a sharper angular spread with larger $Q-$factor for thermal clouds and it approaches that of the infinite lattice case. For this reason, I typically used thermal clouds loaded into the 1D lattice to optimize the alignment of the Bragg probe.

7.2.2. Beam waist of the Bragg probe. In the Bragg setup (see Section 3.3.2), I designed the beam waist diameter of the Bragg probe to be about $2w_0 = 250\,\mu$m. To verify the actual waist diameter, I measured the Bragg probe beam waist using scattered light by the atoms. I first trapped Bose-condensed ^{87}Rb atoms in the 1064 nm optical dipole trap and adiabatically turned on the 1D lattice to a lattice depth $V_0 \gtrsim 20E_R$. I then suddenly turned off the dipole trap to let the atoms fall due to gravity and move through the lattice standing wave created by the two counter-propagating lasers. I then pulsed the Bragg probe and measured the signal N_{Bragg} as a function of the vertical displacement d_{TOF} during the time-of-flight (TOF).

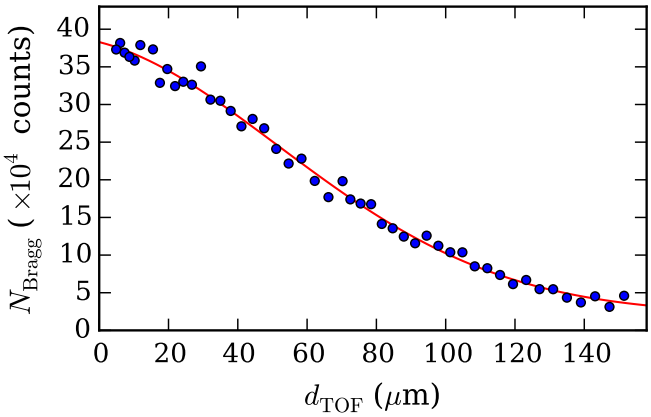

FIGURE 7.3. Beam waist of the Bragg probe measured by releasing ^{87}Rb atoms from the dipole trap while the lattice potential is kept on.

My observations are shown in Fig. 7.3, for d_{TOF} up to 160 μm (TOF duration up to 5.6 ms). Since the atoms' size ($\sim 10\,\mu$m) was small compared to the designed Bragg probe beam waist ($\sim 250\,\mu$m), a change in the scattered Bragg signal N_{Bragg} by the displaced atoms resembled a change in the intensity profile of the Bragg probe $I_{\mathrm{probe}} \propto \exp(-2r^2/w_0^2)$. This was within the assumption the atomic spatial distribution and coherence did not change as the atoms slide through the lattice potential. Fitting the measured data to a Gaussian profile (red curve in Fig. 7.3) $N_{\mathrm{Bragg}} = N_0 \exp(-d_{\mathrm{TOF}}^2/2\sigma_{\mathrm{TOF}}^2)$, I find that the width of the observed scattered intensity is $\sigma_{\mathrm{TOF}} \simeq 65\,\mu$m. Assuming that $N_{\mathrm{Bragg}} \propto I_{\mathrm{probe}}$, this implies a beam waist diameter of $2w_0 = 4\sigma_{\mathrm{TOF}} \simeq 260\,\mu$m which is close to the designed value.

Note this measurement is only an estimate in a sense that I did not include the Gaussian profile of the lattice depth confinement from the interfering laser intensity. In my estimate, I assume the atoms' spatial size and density modulation stay the same during TOF; where the amount of scattered Bragg signal determines the intensity

profile of the Bragg probe. However, as the atoms slide through the lattice during a few ms, the atomic spatial distribution and coherence might change as the lattice depth gets weaker. For example, the product of the Bragg probe intensity with beam waist w_0 and the lattice laser intensity with beam waist w_l gives a combined intensity I_{tot} with beam waist $w_{\text{tot}}^2 = w_0^2 w_l^2 / (w_B^2 + w_l^2)$. If the atoms follow the lattice depth adiabatically $N_{\text{Bragg}} \propto I_{\text{tot}}$, I would then expect the observed Bragg signal in TOF to have a smaller Gaussian RMS width since $w_{\text{tot}} < w_0$.

7.2.3. Angular width of the scattered Bragg signal. To measure the angular extent of the scattered Bragg signal, I used an adjustable mechanical slit placed at a distance of $L \sim 9.5\,\text{cm}$ in front of the EMCCD camera (see Fig 3.9) which counted the number of scattered photons. The adjustable slit was a `Thorlabs VA100` which gave 0.025" slit width adjustment per revolution of the micrometer drive. I intentionally clipped the Bragg signal by closing the slit gradually, i.e. similar to the knife-edge measurement to determine the beam waist of a laser beam. Figure 7.4 shows the measured Bragg signal N_{Bragg} as a function of the slit traveling distance d. The data points (red markers) are fitted to a logistic function (blue curve)

$$f(d) = \frac{A}{1 + \exp\left[-r\left(d - d_0\right)\right]} + c, \tag{7.30}$$

where the fitting parameters are the function's growth amplitude A, the offset c, the steepness of the curve r, and the midpoint of the growth d_0.

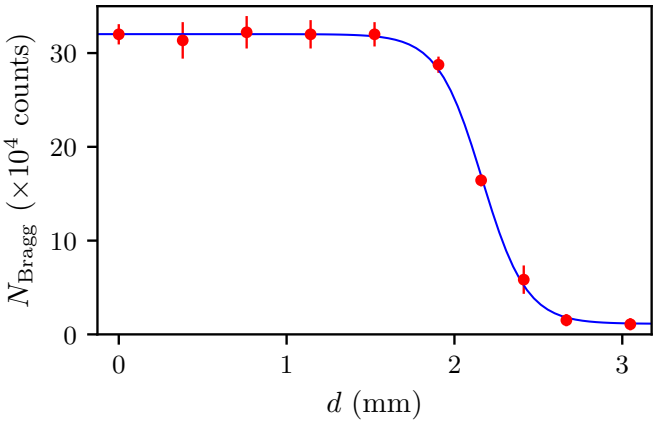

FIGURE 7.4. Scattered Bragg signal as a function of the traveling distance of a slit placed in front of the EMCCD camera.

The observations gave a traveling distance of $d_m \sim 1\,\mathrm{mm}$ at the image plane region (with $M = 3.9\times$ magnification) before the Bragg signal was completely blocked. This corresponded to an angular width of about $\theta_{\mathrm{meas}} = M \cdot d_m/L = 0.04\,\mathrm{rad}$. For comparison, the radial in situ cloud size was about $D = 10\,\mu\mathrm{m}$ and the Bragg probe wavelength was $\lambda = 780\,\mathrm{nm}$. This gave a predicted value for the angular extent of the scattered signal to be $\theta \sim \lambda/2D = 0.04\,\mathrm{rad}$.

7.3. Observations of optical Bragg scattering in engineered Hamiltonians

In this section, I present my measurements of optical Bragg scattering in 1D lattice and spin-orbit-coupled (SOC) condensates. I created an optical lattice potential for either $|F = 1, m_F = -1\rangle$ or $|F = 1, m_F = +1\rangle$ state using counter-propagating lasers at the magic wavelength $\lambda_{\mathrm{zero}} = 790.034\,\mathrm{nm}$ with zero scalar light shift [9]. This gave a periodicity of $d = 395\,\mathrm{nm}$ in the atomic density distribution. I also examined

spin-1/2 SOC condensates where I coupled the two states $|F = 1, m_F = -1\rangle$ and $|F = 1, m_F = 0\rangle$ with Raman transitions.

For the data presented below, I chose the frequency of the Bragg probe to be nearly resonant with the atomic transition $5\mathcal{S}_{1/2}, F = 1 \rightarrow 5\mathcal{P}_{3/2}, F' = 0$ where the detuning was $\delta \simeq -13\Gamma$ and the saturation parameter was $s_0 \simeq 10$. The Bragg scattering from the optical lattice served as a calibration reference and the main measurements were observations of the spin-helix phase [22, 53] in SOC condensates at high coupling strength $\Omega \sim 1 - 10E_R$. The near-resonant Bragg probe is spin-sensitive and it allows me to measure the precessing effective magnetic field in the SOC condensates.

7.3.1. Probing atoms in a one-dimensional lattice. Condensed atoms loaded into an optical lattice will exhibit periodic modulation in their density distribution. I prepared Bose-condensed atoms in an optical dipole trap (at 1064 nm) and adiabatically loaded them into the 1D lattice potential with lattice depth V_0. In the case of a 1D optical lattice, the atoms retain their long-range phase coherence (a characteristic of superfluidity) between different lattice sites even for large lattice depth $V_0 > 20E_R$ and there does not exist phase transition from the superfluid to the Mott-insulator phase [77, 88]. Figure 7.5 shows the observed scattered Bragg signal N_{Bragg} counted by the EMCCD camera. The signal increased monotonically for lattice depth $V_0 < 10E_R$ before it started to saturate at higher lattice depth confinement.

Based on Eq. 7.29 for the atomic form factor, I assumed the spatial extent of the atomic wavefunction in a single lattice site scaled as $\sigma_x \propto 1/\sqrt{V_0}$. I fit the observed

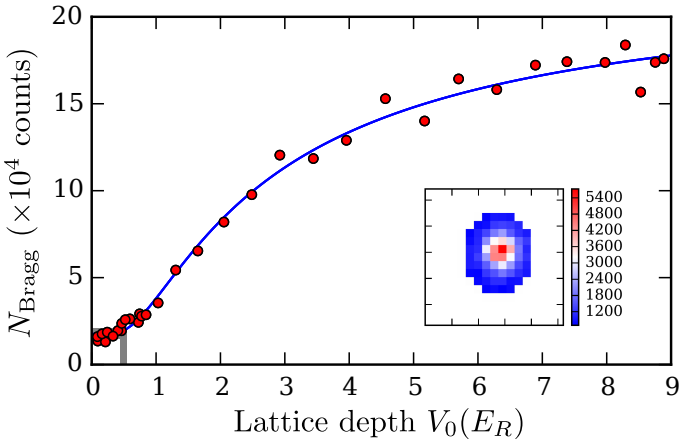

FIGURE 7.5. Bragg signal N_{Bragg} as a function of lattice depth V_0. Inset shows the 68 pixels ROI for the Bragg signal imaged by the EMCCD camera. Solid blue curve is a fit to Eq. 7.31, and the shaded gray line shows the chosen threshold for a detectable Bragg signal (15% above the offset value c obtained from the fitting).

Bragg signal with the function

$$N_{\mathrm{Bragg}}(V_0) = a\exp(-b/V_0) + c, \tag{7.31}$$

where a, b, and c are the fitting parameters. The fit gave an offset value of $c = 17.6 \times 10^3$ for a total of 68 pixels region-of-interest (ROI) in the imaged Bragg signal. Accordingly, I set the lowest limit for a detectable Bragg signal to be 15% above the offset (background) value c obtained from the fitting, as shown by the gray line in Fig. 7.5. This gave a detection threshold $V_0 \geq 0.48(2)E_R$ for the lattice depth. Based on numerical simulations of the Gross-Pitaveskii equation [14, 15], this threshold corresponded to $\sim 8\%$ contrast in the density modulation for our typical ^{87}Rb BEC with 2.2×10^5 atoms prepared in a harmonic trap with frequencies $(\omega_x, \omega_y, \omega_z) =$

$2\pi\,(93, 64, 39)$ Hz. For comparison, my BEC had a chemical potential of $\mu_{\mathrm{TF}}/h \approx 1.3\,\mathrm{kHz}$ and the lattice potential threshold in frequency unit was $V_0/h \geq 1.8\,\mathrm{kHz}$.

In order to probe the coherence properties of the atoms, I initially prepared the atoms in an optical lattice with depth V_0, turned off the lattice suddenly and let the atoms expand for a duration of τ inside the harmonic dipole trap. I then used an optical Bragg probe for a pulse time of $\sim 20\,\mu\mathrm{s}$. The expanding atomic wavefunction from each lattice site interfered with each other and after a certain expansion time, "rephasing" of the wavefunction yielded a maximum interference, similar to that of the Talbot effect in optics [150, 168].

Figure 7.6 shows my observations of the atomic Talbot effect in a 1D lattice using optical Bragg scattering [120]. The atoms were initially prepared in a 1D lattice with $V_0 = 5E_R$, where $E_R = h^2/2m\lambda_d^2$ is the single photon recoil energy at wavelength $\lambda_d = 790.034\,\mathrm{nm}$. The coherence revival was expected to occur once the width of the atomic wavefunction expanded for a distance of $d/2 = \lambda_d/4$, or half of the lattice spacing. Assuming the atoms expanded freely after being released from the lattice potential, the revival period T_{rev} was predicted to be [120, 150] [5]

$$T_{\mathrm{rev}} = \frac{md^2}{h} = \frac{1}{2} \cdot \left(\frac{h}{4E_R}\right) = 33.99\,\mu\mathrm{s}. \tag{7.32}$$

[5]The initial periodic density modulation d is recovered in the same spatial coordinates after $2T_{\mathrm{rev}}$. Meanwhile, maximum interference occurs after T_{rev} to yield similar periodic structures which are shifted by $d/2$. The Talbot time is defined as $T_{\mathrm{Talbot}} = 2T_{\mathrm{rev}}$ [150].

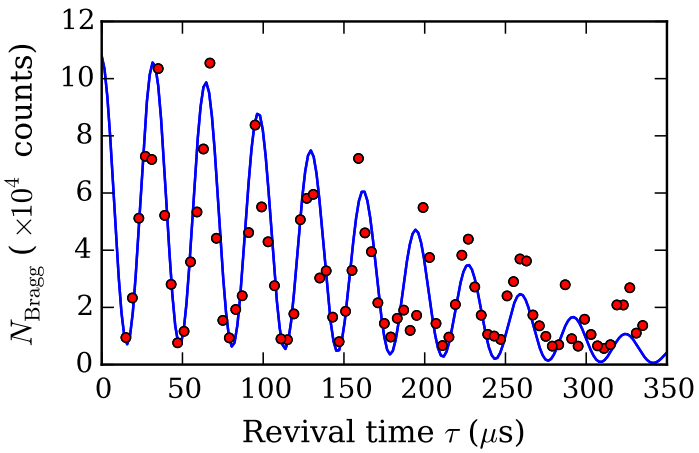

FIGURE 7.6. Coherence revival after the condensates are released from the lattice potential at $V_0 = 5E_R$.

To obtain the revival period from the measurements displayed in Fig. 7.6, I fit these data to the function

$$f(\tau) = A \exp(-\lambda\tau) \left[\sin^2(2\pi\tau/T_{\mathrm{rev}} + \phi) + c\right], \tag{7.33}$$

where the term $\exp(-\lambda\tau)$ was introduced to include the Debye-Waller factor.

My observations yielded a revival period of $T_{\mathrm{rev}} = 32.9(4)$ μs, slightly shorter than the predicted value. I attributed the smaller measured T_{rev} to the presence of the harmonic trap potential. This caused the collapse and revival dynamics of the wavefunction to deviate from the predicted value in Eq. 7.32 [2]. In addition, due to the interaction between particles, the collective atomic wavefunction has smaller effective mass. The energy dispersion $\epsilon(q)$ for repulsively interacting particles with $g > 0$ has smaller curvature (larger second derivative) compared to that of free particles with no interaction $g = 0$. The effective mass is defined as $1/m^* = (1/\hbar^2)\left[\partial^2\epsilon(q)/\partial q^2\right]$.

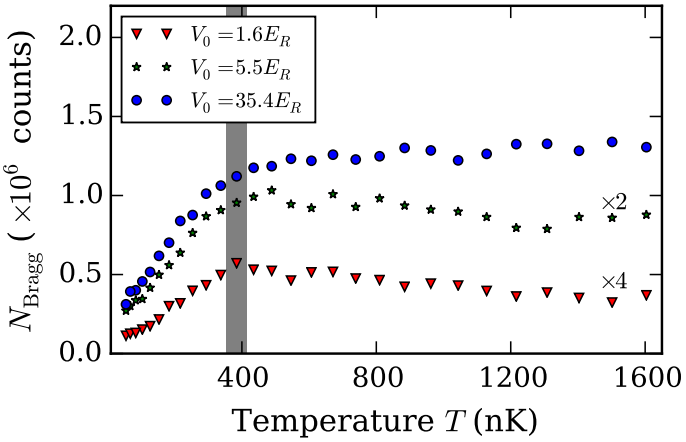

FIGURE 7.7. Optical Bragg scattering of atoms loaded into the 1D optical lattice as a function of temperature. The temperature T was measured using TOF release from the corresponding dipole trap without the lattice potential. The shaded area corresponds to the transition temperature $T_C = 381\,(30)$ nK when the BEC starts to appear.

Consequently, the effective mass became smaller $m^* \approx 0.97m$ and the measured T_{rev} was shorter than its predicted value for free particles [88, 132].

I next observed the dependence of the Bragg signal on the temperature of the atoms, as displayed in Fig. 7.7. I prepared the atoms at temperature T by adjusting the final power of the optical dipole trap (trap depth) after the evaporation stage. The temperature T was measured using TOF release from the dipole trap (without lattice). I then loaded the atoms adiabatically into the optical lattice with potential V_0 and probed them with the Bragg beam. For a small lattice depth $V_0 = 1.6E_R$, I observed a distinct kink where the Bragg signal was maximum at the transition temperature T_C (see Fig. 7.7). This kink gradually disappeared as I increased the lattice depth confinement.

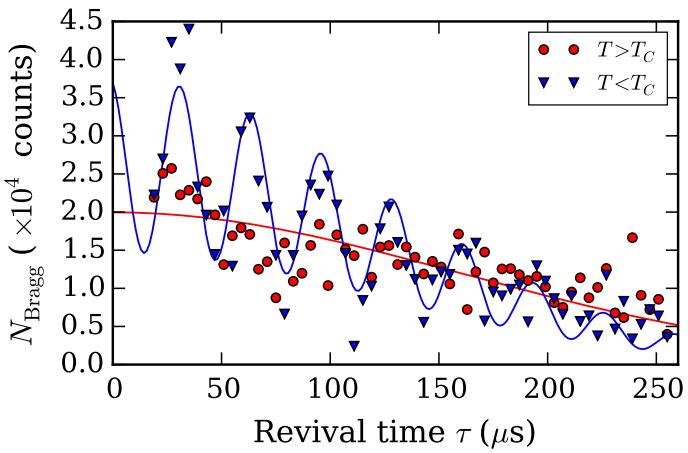

FIGURE 7.8. Coherence revival of atoms in optical lattice below and above the transition temperature $T_C \approx 380\,\mathrm{nK}$. The atoms, initially confined in a 1D lattice potential with $V_0 = 3.43E_R$, are released from the lattice and let expand in the harmonic trap to exhibit the atomic Talbot effect.

I attributed the decreasing Bragg signal for $T < T_C$ to the decreasing number of atoms N_{atom} and smaller size of the BEC cloud (fewer lattice sites N_s are occupied) as they become colder. On the other hand, thermal atoms have relatively larger fluctuations in the atomic wavefunction at temperature $T > T_C$, and I still observed a significant amount of Bragg signal. This was expected since N_{atom} was bigger and more lattice sites N_s were occupied, compared to the BEC case.

I also studied the coherence revival of the atomic wavefunction for $T < T_C$ and for $T > T_C$ (see Fig. 7.8). The atoms were loaded into an optical lattice with $V_0 = 3.43E_R$ after being prepared at temperatures of $T \sim 340\,\mathrm{nK}$ and $T \sim 420\,\mathrm{nK}$ (for the condensed and thermal phases, respectively). As before, I observed the atomic Talbot effect for condensed atoms at $T < T_C$, as shown by the blue triangles in Fig. 7.8. I fit the data to Eq. 7.33, as shown by the solid blue curve in Fig. 7.8. In

contrast to the condensed case, the observed Bragg signal for the thermal clouds (red circles in Fig. 7.8) decayed rapidly once the lattice potential V_0 was turned off and the atoms expanded in the dipole trap. This indicated that the thermal clouds had strong fluctuations causing any initial phase coherence to decay rapidly.

Finally, I would like to make a few minor comments on some experimental details. As described previously, I applied a bias field $B_{\rm dc}$ to create the spin-dependent lattice. There were always transient eddy currents in the system when I turned off the biasing field, and it took about $10-100\,$ms before the bias field $B_{\rm dc}$ settled to a stable value. For this reason, I chose to keep $B_{\rm dc}$ constant while performing Bragg scattering. The bias field affected the resonance condition for the optimum Bragg signal and I have found this to be spin-dependent as well. I measured a detuning value of $\delta \simeq -80\,$MHz to give the maximum Bragg signal, for a bias field of $B_{\rm dc} \sim 5\,$G along $\mathbf{e}_x$ and saturation parameter $s_0 \simeq 10$. I did not observe any dependence on the polarization of the Bragg probe. This was expected since I chose the near-resonant transition to be $5\mathcal{S}_{1/2}, F=1 \rightarrow 5\mathcal{P}_{3/2}, F'=0$ (which has the same transition matrix elements between the different sublevels $m_F = \pm 1, 0 \rightarrow m_{F'} = 0$). To find the optimum parameters for the detuning δ and s_0 in a multi-level system theoretically, I needed to solve the Maxwell-Bloch equations numerically. Instead, I chose the parameter values which gave the optimum Bragg signal experimentally.

7.3.2. Precessing magnetic field in SOC condensates. In this subsection, I discuss my observations of near-resonant optical Bragg scattering off of spin-1/2

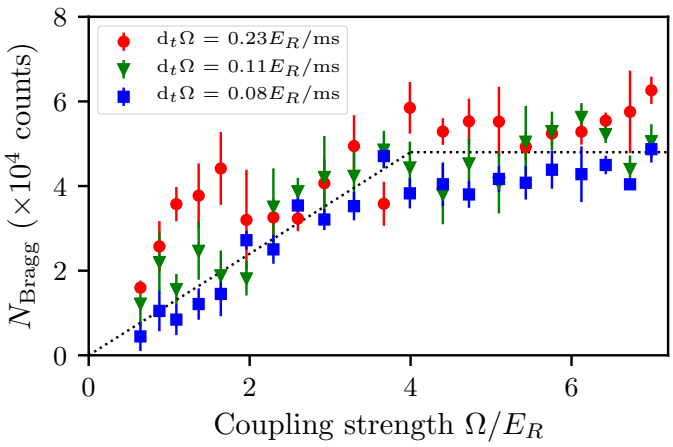

FIGURE 7.9. Bragg signal N_{Bragg} as a function of the Raman coupling strength Ω_f for loading rates of $0.23E_R/\mathrm{ms}$, $0.11E_R/\mathrm{ms}$ and $0.08E_R/\mathrm{ms}$. The dotted line shows N_{Bragg} is proportional to the transverse spin polarization $|\langle\sigma_x\rangle|$ of the SOC system.

spin-orbit-coupling (SOC) condensates. I prepared ^{87}Rb atoms in equal population mixtures of spin-down $|\downarrow\rangle = |F = 1, m_F = -1\rangle$ and spin-up $|\uparrow\rangle = |F = 1, m_F = 0\rangle$ states. I dressed the SOC Hamiltonian by ramping up the Raman coupling strength Ω gradually from 0 to its final value Ω_f with a linear rate of $\mathrm{d}_t\Omega$. For adiabatic dressing of the atoms with $\mathrm{d}_t\Omega = 0.08E_R/\mathrm{ms}$, I observed an increase of the Bragg signal as a function of coupling strength, up to $\Omega_f < 4E_R$. Beyond this point, the Bragg signal started to saturate, as depicted in Fig. 7.9. I found the adiabaticity condition was satisfied when the atoms were dressed with a rate below $\mathrm{d}_t\Omega \lesssim 0.1E_R/\mathrm{ms}$.

In this engineered SOC Hamiltonian, the bias field $\mathbf{B}_{\mathrm{dc}} = B_z\mathbf{e}_z$ and the counter-propagating lin $\perp$ lin Raman lasers create an effective magnetic field of $\mathbf{B}_{\mathrm{eff}} \propto \Omega\cos(2k_Rx - \delta\omega\, t)\,\mathbf{e}_x$, where k_R is the single-photon recoil momentum and $\delta\omega$ is the detuning between the Raman lasers (see Chapter 5). For coupling strength $\Omega < 4E_R$,

the system has two degenerate minima located at $q_0 = \pm k_R\sqrt{1-(\Omega/4E_R)^2}$ and the dressed eigenstates are [69, 98]

$$\tilde{\chi}_+ = \begin{pmatrix} \cos\theta \\ -\sin\theta \end{pmatrix} \exp\left(\mathrm{i}q_0 x\right) \quad \text{and} \quad \tilde{\chi}_- = \begin{pmatrix} \sin\theta \\ -\cos\theta \end{pmatrix} \exp\left(-\mathrm{i}q_0 x\right). \tag{7.34}$$

The spinor wavefunction of the system then becomes $\Psi(x) = n\left(C_1\tilde{\chi}_+ + C_2\tilde{\chi}_-\right)$ which has non-zero transverse spin polarization

$$\langle\sigma_x\rangle = -\frac{\sqrt{k_R^2 - q_0^2}}{k_R} = -\frac{\Omega}{4E_R}, \quad \text{for } \Omega < 4E_R. \tag{7.35}$$

Near-resonant optical Bragg scattering, which is spin-sensitive, probes the precessing spin polarization. The precessing spin has a periodicity of $d_{\mathrm{spin}} = \pi/k_R = \lambda_{\mathrm{zero}}/2$, identical to the density modulation in a periodic lattice case. For coupling strength $\Omega \geq 4E_R$, the minima merges at $q_0 = 0$ and the spinor wavefunction is fully polarized with $\langle\sigma_x\rangle = -1$, causing the Bragg signal to saturate. I attributed the observed dependency of N_{Bragg} as a function of Ω_f to the existence of the transverse spin polarization $\langle\sigma_x\rangle$. For an adiabatic ramp, the measured N_{Bragg} is proportional to the transverse spin polarization $|\langle\sigma_x\rangle|$, as shown by the dotted line in Fig. 7.9. I noted that the spin-sensitive Bragg signal ceased to exist as I detuned the Bragg probe further away from the atomic transitions.

Figure 7.9 shows how the Bragg signal behaves as I shortened the loading duration to be non-adiabatic, i.e. $\mathrm{d}_t\Omega = 0.11E_R/\mathrm{ms}$ and $\mathrm{d}_t\Omega = 0.23E_R/\mathrm{ms}$. As I increased the

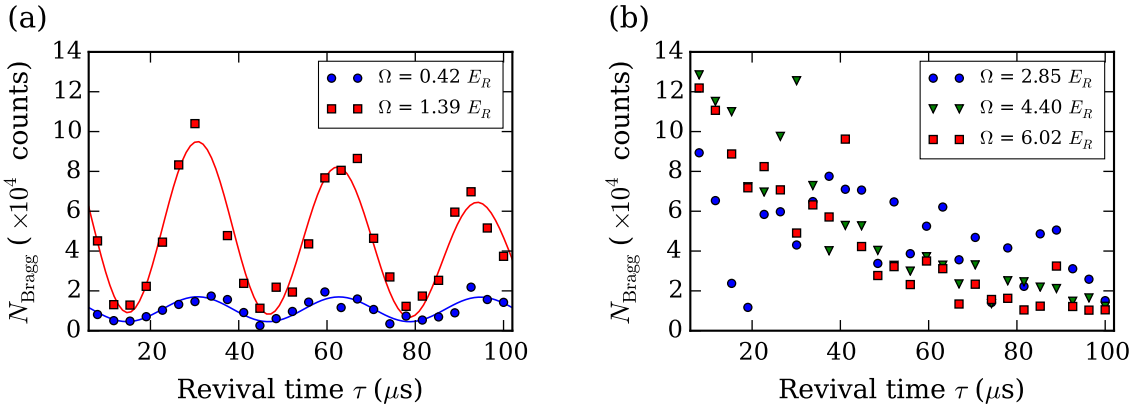

FIGURE 7.10. Bragg signal N_{Bragg} from SOC condensates as a function of revival time τ. (a) I observed the atomic Talbot effect for initial dressing at coupling strength of $\Omega = 0.42E_R$ and $\Omega = 1.39E_R$. (b) The periodic coherence revival ceases for higher coupling strength at $\Omega = 2.85E_R$, $\Omega = 4.40E_R$, and $\Omega = 6.02E_R$.

loading rate, the atoms did not have enough time to evolve and follow the minima condition q_0 adiabatically. This led to more dynamics in the Bragg signal.

I next measured the coherence revival in this Raman dressed system (see Fig. 7.10). After I loaded the atoms into the Raman dressed states, I quickly turned off the Raman lasers and let the atoms expand in the harmonic dipole trap. I then used the Bragg probe to observe the atomic Talbot effect for low coupling strength $\Omega = 0.42E_R$ and $\Omega = 1.39E_R$. In contrast to the previous case, I did not observe a clear signature of periodic coherence revival for $\Omega = 2.85E_R$, $\Omega = 4.40E_R$, and $\Omega = 6.02E_R$. At higher SOC coupling strengths, the dynamics of the different dressed spin states in the harmonic dipole trap might cause degradation in the coherence properties of the atoms. Although, the behavior shown in Fig. 7.10 was interesting, I did not make further investigations of this effect.

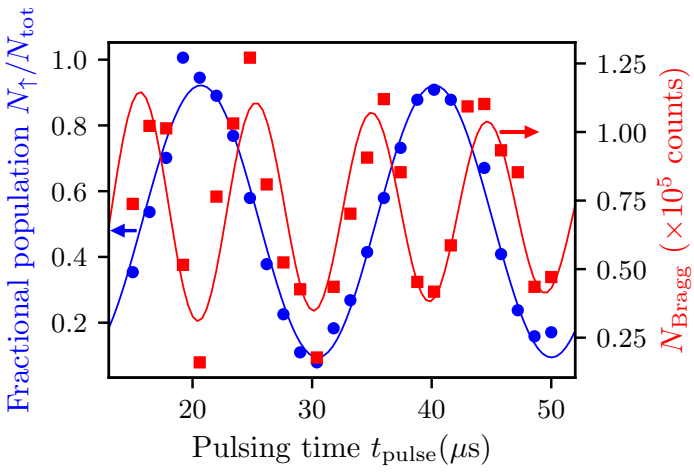

FIGURE 7.11. Bragg signal $N_{\rm Bragg}$ as a function of Rabi pulsing time $t_{\rm pulse}$ of the Raman lasers. I observe the Bragg signal (red, right y-axis) to oscillate with twice the frequency of the Rabi oscillation (blue, left y-axis) in the coupled atomic states.

On the other hand, I further confirmed the origin of the scattered Bragg signal was due to the (precessing) magnetic field by performing Bragg scattering after doing a Rabi pulse of the Raman coupling. Figure 7.11 shows Rabi oscillations of the SOC states (indicated by circles) due to a square pulse with duration $t_{\rm pulse}$. The Bragg signal (indicated by squares) oscillates with twice the frequency of the Rabi oscillation between the coupled $|\uparrow\rangle$ and $|\downarrow\rangle$ states. Here I measured an optimum Bragg signal for nearly equal mixtures of the $|\uparrow\rangle$ and $|\downarrow\rangle$ populations after Rabi pulsing. This indicated the Bragg signal was related to the spin structure factor.

It is important to note here the angular alignment of the Bragg probe was optimized with respect to the corresponding spin-dependent optical lattice at the same laser wavelength $\lambda_{\rm zero}$. I expected the spin structure in the SOC dressed system to have the same periodicity $d = \lambda_{\rm zero}/2$ to the spin-dependent lattice case. I did not

find any spatially periodic structure corresponding to the minima in the SOC energy dispersion, namely $q_0 = \pm k_R\sqrt{1-(\Omega/4E_R)^2}$. In other words, the atoms might have a modulation with different periodicity of

$$d' = \frac{\pi}{2q_0} = \frac{\lambda_{\text{zero}}}{2}\left[1-\left(\frac{\Omega}{4E_R}\right)^2\right]^{-1/2}. \tag{7.36}$$

However, within the range accessible to the the Bragg probe angle, I did not observe any significant enhancement of the Bragg signal corresponding to the increasing periodicity d' as a function of Ω. Based on my observations in the optical lattice potential with a fix periodicity $d = \lambda_{\text{zero}}/2$, the density-modulated BEC atoms had a variation of less than $< 20\%$ in the detected Bragg signal within the scan range of the probe angle. In practice, I optimize the incoming Bragg probe angle with thermal clouds in the corresponding lattice at periodicity $d = \lambda_{\text{zero}}/2$ and fix the Bragg angle in all of the conducted measurements.

7.4. Summary

In this chapter, I present my measurements of various atomic structure using optical Bragg scattering. I discuss the static structure factor to describe geometrical properties of scattered Bragg signal due to periodic distribution of atoms. Measurements of the Bragg counts as a function of the probe incident angle for different periodicities ($d = 395\,\text{nm}$ and $d = 405\,\text{nm}$) are in agreement with the model. Condensed atoms, which have less number of spatially periodic atoms, give broader angular distribution

in the scattered Bragg signal (more spread in the reciprocal k-space) compared to hotter atoms, which occupy more space and have more number of periodic layers (less spread in the reciprocal k-space). I also measured the beam diameter of the Bragg probe $2w_0 \simeq 260\,\mu$m and angular width of the scattered Bragg signal $\theta \simeq 0.04\,$rad.

To calibrate the Bragg signal, I created spatial density ordering in the atoms by loading them adiabatically into a 1D optical lattice potential. Based on the atomic form factor, I observed the Bragg signal to scale as $N_{\text{Bragg}}(V_0) \propto \exp(-b/V_0)$ with respect to the lattice depth V_0. To probe the phase coherence of the condensed atoms, I demonstrated the atomic Talbot effect where the initial density modulation of the atoms was recovered after a certain Talbot time.

I observed a peak in the scattered Bragg signal at the BEC transition temperature T_C. Unfortunately, I did not conduct further investigations on this behavior. I would speculate this might be caused by increasing spatial correlation between the atomic wavefunction as the atoms reached the BEC phase [122]. However, a more careful calibration of the atoms' number and their spatial distribution would need to be performed before I could convincingly argue for the cause of this peculiar peak at T_C. Measurements of the atomic Talbot revival did confirm the atoms lost their coherence properties as the temperature increased above T_C.

The results being discussed here are for condensates in the $m_F = -1$ state affected by the spin-dependent lattice potential. For a mixture of spinor Bose gases in the $F = 1$ manifold, the $m_F = \pm 1$ states are bounded to the lattice potential while $m_F = 0$ atoms are free. With optical Bragg scattering, I could measure how the energy

exchange between atoms confined in a lattice potential coupled to an external bath of lattice-free atom might affect the spatial density ordering of the atoms. Unfortunately, I did not conduct such experiment due to my time constraints. The optical Bragg scattering is promising to study thermalization between a lattice and free Bose gases, complementary to the work done by McKay *et al.* [110, 111, 113].

With near-resonant Bragg scattering, I probed the precessing magnetic field that exist in the SOC condensates as the atoms were loaded adiabatically into the SOC dressed states. I showed the Bragg signal was proportional to the transverse magnetization of the SOC system. The Bragg signal was optimized when 50%/50% mixture of the atoms existed in the two degenerate energy levels of the SOC system. As the Raman coupling strength Ω was increased, the two degenerate minima of the SOC energy dispersion merge to form a single minimum. Consequently, the interference of the two opposite momenta vanished and the observed Talbot revival became weaker. The spin-structure ordering lost its coherence at high Raman coupling strength $\Omega > 2.85E_R$, as confirmed by the Talbot revival data.

Besides loading the atoms adiabatically into the SOC dressed states, I also did a short (Rabi) pulse of the Raman coupling strength and probed the atoms with near-resonant Bragg scattering. The frequency of the observed Bragg signal was twice the frequency of the Rabi oscillation since the Bragg signal was maximized at 50%/50% mixture of the atoms, confirmed the origin of the scattered Bragg signal was due to the precessing magnetic field in the SOC system.

CHAPTER 8

Stripe-ordered phase in spin-orbit coupled condensates

Spinor Bose gases favoring the antiferromagnetic configuration (miscibility) [165] in the presence of spin-orbit coupling exhibit three phases: the stripe-ordered phase, the magnetized plane-wave phase and the zero-momentum phase [69, 98]. The stripe phase occurs when each spin component, with two opposing momentum components $\pm q_1$, are interacting with each other due to the interatomic collisions. This results in the formation of a spatial interference pattern with a period of π/q_1.

The stripe-ordered phase has properties that are analogous to supersolidity, first described by G. Martone and Y. Li et al. [97, 109] for atomic spin-orbit-coupled (SOC) systems. Within the Bogoliubov theory [59], the excitation spectrum of the mean-field energy in the stripe phase exhibit two gapless bands [97]. This gives a divergent structure factor and static response function for wave vectors near the boundary of the Brillouin zone. In addition, in the plane-wave phase of the SOC system, the excitation spectrum is not symmetric and exhibits roton-maxon like structure where the gap of the rotonic structure becomes smaller as one approaches transition to the stripe phase [109]. The roton-mode softening is a precursor of a phase transition which spontaneously breaks the continuous translational symmetry. This gives rise to

a crystalline long-range phase order in a superfluid with weak short-range interaction. This characteristic is a signature of "supersolid" phase of matter [136].

Most recently, Ji et al. [79] have observed roton-mode softening in the excitation spectrum as the SOC Bose gas crosses the phase transition towards the stripe phase. The roton-maxon excitation spectrum in the plane-wave phase was measured using Bragg spectroscopy, and they found good agreement with theoretical predictions [109]. Besides in SOC Bose gases, the roton-maxon spectrum has also been observed in other engineered ultracold atoms, such as in the shaken lattice [62], in BEC-cavity systems [94, 123], and recently in dipolar quantum gases [31].

Another predicted feature of the stripe phase is the existence of spatial density modulation. This is challenging to measure because the expected density contrast is very low and the modulation periodicity is on the order of $0.4\,\mu$m (or less). In the initial work by Lin et al. [103], a signature of the stripe phase region was observed indirectly using time-of-flight (TOF) imaging. Atoms in the dressed states were projected into their bare spin and momentum states; the degree of phase-mixing characterizes the region where stripe-ordered phase occurs.

Here I describe how I used optical Bragg scattering to detect the density modulation. Recently, similar technique was used by Jun-Ru Li et al. [95] to detect the stripe phase in SOC system realized in a superlattice potential [96]. So far, this has been the only experimental work to directly observe the density modulation of the stripe phase. Unfortunately, in the work of Jun-Ru Li et al., the existence of the density modulation was only demonstrated as a function of detuning δ between the two

SOC states in a limited region of coupling strength Ω. It was unclear if the observed density modulation appeared within the predicted two-dimensional (2D) parameter space of the SOC system [108].

In this chapter, I report my observation of the full phase diagram of the stripe-ordered phase. I realized an SOC system using two-photon Raman transitions for a range of coupling strength Ω [67, 102, 103]. My measurements of the stripe-ordered phase in (Ω, δ) phase space were in agreement with theoretical predictions [69, 98]. I also investigated the metastable windows where the density modulation exists [103] and observed the atomic Talbot effect in the time-evolution of the density modulation [120, 150]. Finally, I explored the stripe-ordered phase in the finite temperature parameter space of (Ω, T) and my results were consistent with previous works [28, 78, 178].

8.1. Theory of the stripe-ordered phase

The single-particle Hamiltonian of an SOC Bose-Einstein condensate realized with counter-propagating Raman lasers is given by [69, 103]:

$$h_0^{\mathrm{SO}} = \frac{\hbar^2}{2m}\left[(q_x - k_R\sigma_z)^2 + k_\perp^2\right] + \hbar\frac{\delta}{2}\sigma_z + \hbar\frac{\Omega}{2}\sigma_x + V_{\mathrm{ext}}, \tag{8.1}$$

where m is the atomic mass, k_R is the single photon recoil momentum, $k_\perp$ is the linear momentum perpendicular to the SOC direction, δ is the effective detuning, Ω is the Raman coupling strength, and V_{ext} is the external potential. The term $-2q_xk_R\sigma_z$ is analogous to Rashba and Dresselhaus spin-orbit couplings (with equal

linear contributions) in condensed matter physics [44, 103, 144]. The spin-1/2 system is described by the Pauli matrices σ_x, σ_y, and σ_z, and the coupling between the two different spin states are locked to the linear momentum in the quasi-momentum space q_x. The single photon recoil energy $E_R = \hbar^2 k_R^2/2m$ of the Raman coupling sets the energy scale of this Hamiltonian.

I now include many-body interactions in the $s-$wave channels of the atoms and describe the mean-field energy functional of the system as

$$E\left[\Psi\right] = \int \mathrm{d}\mathbf{r} \left[\Psi^\dagger h_0^{\mathrm{SO}} \Psi + \frac{1}{2}\sum_{\alpha,\beta} g_{\alpha,\beta} \left(\Psi^\dagger P_\alpha \Psi\right)\left(\Psi^\dagger P_\beta \Psi\right)\right], \tag{8.2}$$

where $\Psi = \left(\psi_\uparrow \, \psi_\downarrow\right)^T$ is a two-component wavefunction representing the spin-1/2 system; α, β are spin indices with projection operators to the two spin states given by $P_\uparrow = \left(1+\sigma_z\right)/2$ and $P_\downarrow = \left(1-\sigma_z\right)/2$; and $g_{\alpha\beta} = 4\pi\hbar^2 a_{\alpha\beta}/m$ are the two-body interaction terms corresponding to the $s-$wave scattering lengths $a_{\alpha\beta}$.

To determine the ground states of the mean-field energy, I used the variational method as described in Ref. [98, 108]. I chose the ansatz for the spinor wavefunction as [69, 98, 108]:

$$\Psi\left(\mathbf{r}\right) = \begin{pmatrix} \psi_\uparrow \\ \\ \psi_\downarrow \end{pmatrix} = \sqrt{\bar{n}} \left[C_+ \begin{pmatrix} \cos\theta_+ \\ \\ -\sin\theta_+ \end{pmatrix} \mathrm{e}^{\mathrm{i}k_+ x} + C_- \begin{pmatrix} \sin\theta_- \\ \\ -\cos\theta_- \end{pmatrix} \mathrm{e}^{-\mathrm{i}k_- x} \right]. \tag{8.3}$$

Here the variational parameters are $C_+, C_-, k_+, k_-, \theta_+$ and θ_- , with $\bar{n}$ is the atomic density distribution. The parameter values for the lowest energy eigenstates were

determined by minimizing the energy functional in Eq. 8.2 subject to the constraint $\int \mathrm{d}^3\mathbf{r}\ \Psi^\dagger\Psi = N$ (or $|C_+|^2 + |C_-|^2 = 1$) where N is the total number of atoms.

I first consider a uniform system with zero trapping potential $V_{\mathrm{ext}} = 0$ and neglect the perpendicular kinetic energy $k_\perp = 0$. In the variational method, minimization of $E[\Psi]$ with respect to $\theta_\pm$ yields the relation $2\theta_\pm = \arccos(k_\pm/k_R)$. Next, I consider the special case of spin symmetric interaction $g_{\uparrow\uparrow} = g_{\downarrow\downarrow} = g$ and zero detuning $\delta = 0$, which leads to the relation $k_+ = k_- = q_1$. For miscible condensates ($g > g_{\uparrow\downarrow}$) in the low density limit $g_{\alpha\beta}\bar{n} \ll E_R$, the variational approach yields lowest energy eigenstates which are compatible with the three following phases [98, 108]:

(1) The stripe-ordered or spin-mixed phase.

For small values of Raman coupling Ω, the ground state is a linear combination of the plane-wave states $\mathrm{e}^{\pm \mathrm{i}q_1 x}$ with equal weights $|C_+| = |C_-| = 1/\sqrt{2}$. The magnetization of the system or the difference between the spin population is given by $\langle\sigma_z\rangle = |\psi_\uparrow|^2 - |\psi_\downarrow|^2 = 0$. The most striking feature of this phase is the appearance of density modulations in the form of stripes:

$$n(\mathbf{r}) = \bar{n}\left[1 + \frac{\hbar\Omega}{(4E_R + G_1)}\cos(2q_1 x + \phi)\right], \tag{8.4}$$

where ϕ is the relative phase between the complex variables C_+ and C_-. The periodicity of the fringes π/q_1 is determined by the wave vector

$$q_1 = k_R\sqrt{1 - \frac{\hbar^2\Omega^2}{(4E_R + G_1)^2}}, \tag{8.5}$$

with interaction parameter $G_1 = \bar{n}\left(g + g_{\uparrow\downarrow}\right)/2$.

(2) The plane-wave or magnetized phase.

For larger values of Raman coupling, the atoms condense into a single plane-wave or magnetized state in either the momentum state q_1 ($C_- = 0$) or $-q_1$ ($C_+ = 0$) where

$$q_1 = k_R \sqrt{1 - \frac{\hbar^2 \Omega^2}{\left(4E_R - 2G_2\right)^2}}, \tag{8.6}$$

with the interaction parameter $G_2 = \bar{n}\left(g - g_{\uparrow\downarrow}\right)/2$. In this phase, the density is uniform $n\left(\mathbf{r}\right) = \bar{n}$ and the spin polarization is given by $\langle \sigma_z \rangle = \pm q_1/k_R$. The ground state of the system is doubly degenerate, where the choice between the two eigenstates at $q_x = \pm q_1$ is determined by spontaneous spin symmetry breaking (if $\delta = 0$). However, any non-zero detuning δ breaks the degeneracy of this magnetized phase.

In the low density limit $G_1, G_2 \ll E_R$, the transition between the stripe- and plane-wave phases occurs at

$$\Omega_c^{1\to 2} = \frac{4E_R}{\hbar}\sqrt{\frac{2G_2}{G_1 + 2G_2}}. \tag{8.7}$$

(3) The single momentum or "zero momentum" phase.

At sufficiently large values of Ω, the two-degenerate minima at $\pm q_1$ merge and the system enters the single-minimum phase where $q_x = 0$ and $\langle \sigma_z \rangle = 0$. In this phase the gas is fully polarized along the $x-$direction, i.e. $\langle \sigma_x \rangle = -1$.

The transition between the plane-wave and the single-minimum phases is second-order and it takes place at a critical value of Raman coupling:

$$\Omega_c^{2\to 3} = \frac{1}{\hbar}\left(4E_R - 2G_2\right). \tag{8.8}$$

In Chapters 5 and 6, I discussed the transition between the plane-wave and single momentum phases within the single-particle Hamiltonian h_0^{SO}. In this chapter, I focus on the stripe-ordered phase. The existence of spin exchange due to the two-body collisions gives rise to the stripe-ordered phase in the SOC system if the interaction parameter G_2 is positive or the miscibility condition $g_{\uparrow\uparrow}g_{\downarrow\downarrow} > g_{\uparrow\downarrow}^2$ is satisfied [98].

Now consider the two spin states $|\uparrow\rangle = |m_F = 0\rangle$ and $|\downarrow\rangle = |m_F = -1\rangle$ in the $F = 1$ manifold of the ^{87}Rb atoms' $5\mathcal{S}_{1/2}$ electronic ground states. The s-wave scattering lengths between the different spin states are $a_{\uparrow\uparrow} = 101.41a_B$ and $a_{\downarrow\downarrow} = a_{\uparrow\downarrow} = 100.94a_B$ where a_B is the Bohr radius. In the presence of spin-asymmetric interactions and non-zero detuning δ, I can extend the variational approach I used above to include energy corrections from first order perturbation theory. For small values of $0 < (g_{\uparrow\uparrow} - g_{\downarrow\downarrow}) \ll g_{\uparrow\uparrow}$, the asymmetry in the intra-atomic interactions can be compensated by the choice of detuning shift $\hbar\delta_{\mathrm{corr}} = -\bar{n}\left(g_{\uparrow\uparrow} - g_{\downarrow\downarrow}\right)/2$ [108].

Figure 8.1 shows theoretical prediction for the phase diagram of the stripe-ordered phase in the (Ω, δ) parameter space. Here I consider ^{87}Rb atoms with chemical potential of $\mu \approx g_{\uparrow\uparrow}\bar{n} = 0.2E_R$. This corresponds to a uniform atomic density of

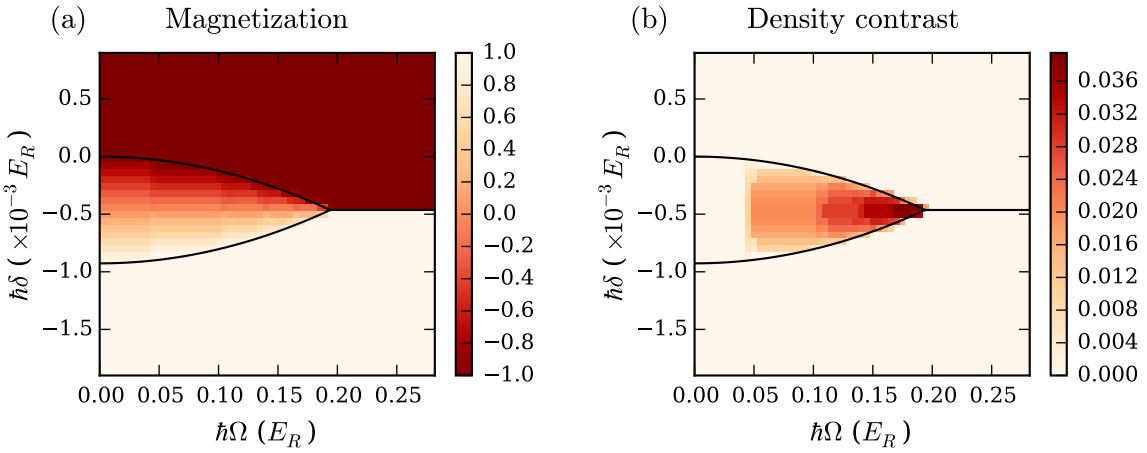

FIGURE 8.1. Theoretical prediction of stripe-ordered phase in (Ω, δ) parameter space for an SOC ^{87}Rb Bose gas ($V_{\text{ext}} = 0$) with chemical potential of $\mu = 0.2E_R$. Using variational method to solve the many-body ground state, I obtain the phase diagram of (a) magnetization and (b) density contrast of the stripe phase versus detuning $\hbar\delta$ and coupling strength $\hbar\Omega$. The stripe-ordered phase has non-polarized magnetization and non-zero density contrast within the area bounded by the solid curves.

$\bar{n} = 0.94 \times 10^{14}\,\text{cm}^{-3}$, a typical value for ^{87}Rb condensates produced in our laboratory. Figure 8.1(a) shows mixing of the spin states in the stripe-ordered phase. This leads to non-polarized magnetization $-1 < \langle\sigma_z\rangle < 1$ within the detuning window $\bar{n}\,|g_{\uparrow\uparrow} - g_{\downarrow\downarrow}|\,/h \lesssim 3.45\,\text{Hz}$ for transition coupling strength $\Omega < \Omega_c^{1\to 2}$. At the detuning value $\delta = \delta_{\text{corr}}$, the critical transition from stripe-ordered phase to plane-wave phase occurs at the Raman coupling strength $\hbar\Omega_c^{1\to 2} \simeq 4E_R\sqrt{(g_{\uparrow\uparrow} - g_{\uparrow\downarrow})\,/2g_{\uparrow\uparrow}} = 0.19E_R$. Figure 8.1(b) displays the density contrast of the stripe modulation, which scales as $\propto \hbar\Omega/\,(4E_R + \mu)$. The maximum density modulation of the stripe phase near the critical transition point is then given by $\sim 0.19E_R/\,(4E_R + \mu) \simeq 0.045$ or 4.5%.

8.2. Experimental setup

I realized a spin-1/2 SOC system by applying two counter-propagating lasers in lin $\perp$ lin configuration, as shown in Fig 8.2. The lasers induced two-photon Raman transitions between the hyperfine states in the $F = 1$ manifold of $5\mathcal{S}_{1/2}$ electronic ground states of ^{87}Rb atoms. I tuned the Raman lasers' wavelength to cancel the scalar light shift at $\lambda_{\text{zero}} = 790.034\,\text{nm}$ [9], which gave a single photon recoil energy of $E_R = h \times 3.678\,\text{kHz}$. For this coupling scheme, I applied a bias field of $B_{\text{dc}} = 19.8595(4)\,\text{G}$. Following Subsection 5.4.2, this gave a linear Zeeman split of $\omega_Z/2\pi = 13.948\,\text{MHz}$ and a quadratic shift of $\epsilon/2\pi = 56.7\,\text{kHz}$. Coupling to the other state $|F = 1, m_F = 1\rangle$ was neglected, as it was detuned by $56.7\,\text{kHz} \gg E_R/h$. This setup realized the single-particle Hamiltonian h_0^{SO} between the two states $|{\downarrow}\rangle = |F = 1, m_F = -1\rangle$ and $|{\uparrow}\rangle = |F = 1, m_F = 0\rangle$ as in Eq. 8.1. The Raman laser frequencies were adjusted to control the detuning δ of the spin-1/2 SOC system and the external potential V_{ext} was the harmonic trapping potential.

The total mean-field energy of the system was given by

$$E\left[\Psi\right] = \int \mathrm{d}\mathbf{r} \left[\Psi^\dagger h_0^{\text{SO}} \Psi + \frac{1}{2} c_0 n_\uparrow^2 + \frac{1}{2}\left(c_0 + c_2\right) n_\downarrow^2 + \left(c_0 + c_2\right) n_\uparrow n_\downarrow\right]. \tag{8.9}$$

Here $n_\uparrow$ and $n_\downarrow$ are respectively the atomic densities of the spin-up and spin-down states, and the interaction parameters are $c_0/h = 7.79 \times 10^{-12}\,\text{Hz}\cdot\text{cm}^3$ and $c_2/h = -3.61 \times 10^{-14}\,\text{Hz}\cdot\text{cm}^3$. To allow comparison with the mean-field energy functional in Eq. 8.2, I defined the interaction terms in Eq. 8.9 as $g_{\uparrow\downarrow} = g_{\downarrow\downarrow} = c_0 + c_2$ and $g_{\uparrow\uparrow} = c_0$.

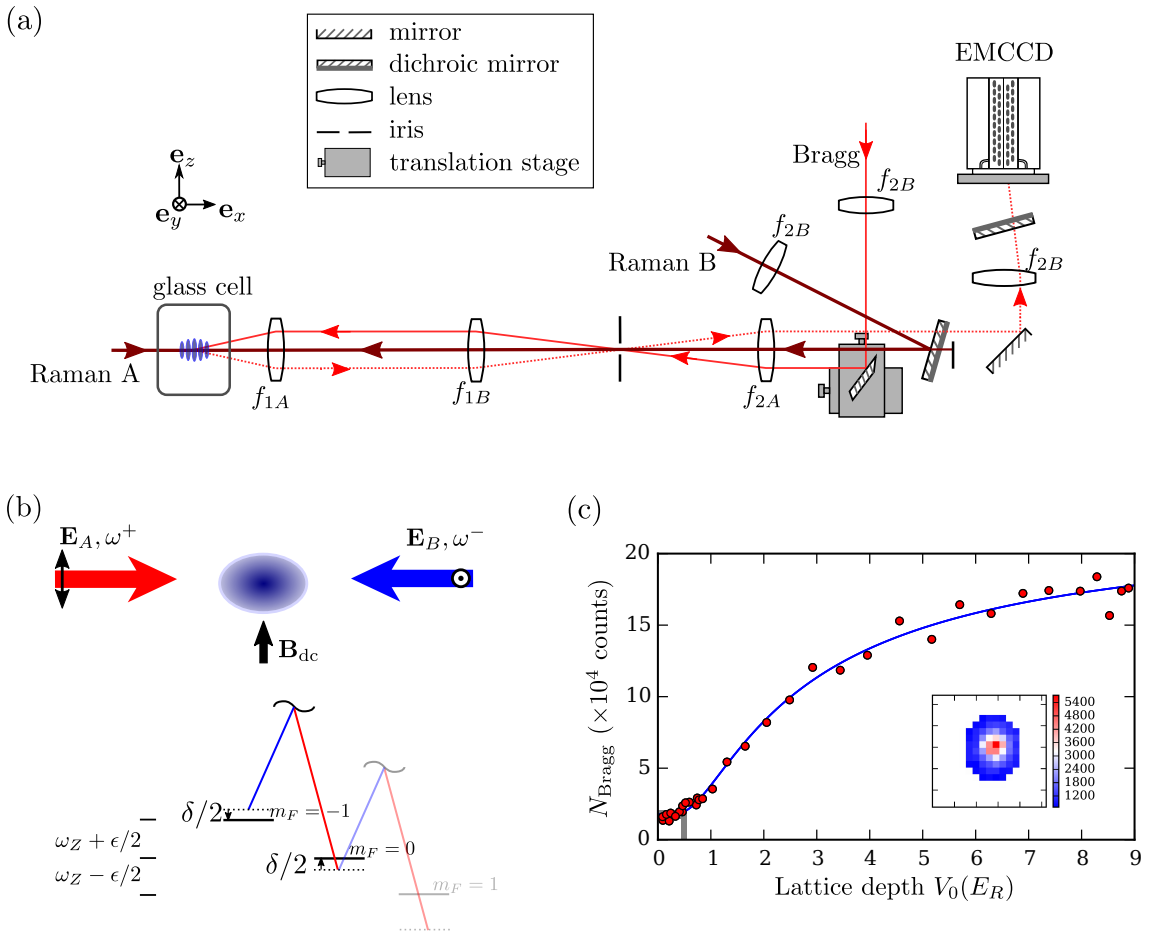

FIGURE 8.2. (a) Experimental setup to detect scattered Bragg signal from the stripe phase, showing counter-propagating Raman lasers, optical Bragg probe, and a highly-sensitive camera. (b) Schematic to realize the spin-1/2 SOC system with two-photon Raman transition. (c) Calibration of the Bragg signal using a spin-dependent optical lattice. Inset shows the region of interest for the Bragg signal imaged by the camera.

In my experiments, I typically produced $N \simeq 2.2 \times 10^5 \pm 15\%$ condensed ^{87}Rb atoms in a harmonic trap with trapping frequencies $(\omega_x, \omega_y, \omega_z) = 2\pi \cdot (105, 67, 40)$ Hz. This corresponded to a chemical potential $\mu \simeq 1.45\,\text{kHz}$ and a peak density $n_0 = 1.86 \times 10^{14}\,\text{cm}^3$. The stripe phase is predicted to exist within the detuning width

of $\delta/2\pi \lesssim |c_2 n_0|/h \simeq 7\,\mathrm{Hz}$ for coupling strength values below $\hbar\Omega < 0.19 E_R$. This requires the ambient magnetic field to be controlled within $< 10\,\mu$G precision. Besides the small detuning window, the stripe phase also has a very low density contrast, on the order of $\lesssim \Omega/(4E_R + \mu)$. In other words, a maximum of only 4.3% of the atoms are expected to be contributing to the periodic density modulation.

In my measurements, I used fluxgate magnetometers to measure drifts in the ambient magnetic field and used partial-transfer absorption imaging (PTAI) in each experimental cycle to correct for magnetic field drifts in the system (as described in Chapter 5). The combined feedforward plus PID feedback control system allowed me to compensate field drift within $< 400\,\mu$G over hours of data taking. The PTAI also served as a sensor of the bias field value and gave an accuracy of $\sim 40\,\mu$G in the field measurement. In terms of the Zeeman frequency detuning, this limited my resolution to $\delta \approx 30\,\mathrm{Hz}$. To calibrate the coupling strength Ω, I applied a square pulse of the Raman beams and obtained Ω from sinusoidal fit to the Rabi oscillation between the different coupled spin states. I used highly sensitive and low-noise photodiodes to measure the laser intensities in each experimental cycle. This gave a precision of $\sim 0.02 E_R$ in the determination of Ω.

As I have noted several times already, the predicted stripe phase exists within a very small window of (Ω, δ) parameter space. In fact, the precision of the equipment I used was barely sufficient. To overcome the aforementioned obstacles, I specifically prepared the SOC dressed states to increase the detectable region of the stripe phase. Based on our knowledge that the stripe-ordering is intertwined with the physics of

spin-mixing, I first prepared the atoms in an equal population of spin $|\uparrow\rangle$ and $|\downarrow\rangle$ states. I then adiabatically loaded the phase-mixed spinor Bose gases into the SOC Hamiltonian by increasing Ω linearly for 50 ms. Next, I held the system at constant Ω for 1 s to reach a metastable equilibrium. Finally, I quickly ramped Ω up to $> 6E_R$ within 200 μs to map the dressed states of the system into well-defined momentum states at $\pm k_R$. The resulting density modulations in the spatial coordinates were amplified as the wave packet of the atoms were enhanced in the corresponding momentum states.

To probe density modulations in the stripe phase region, I used far-detuned optical Bragg scattering in the elastic Rayleigh scattering regime. The experimental setup is depicted in Fig. 8.2(a)-(b). Here, the Bragg beam with wavelength $\lambda_B = 790.2$ nm was red-detuned by 6.34 GHz from the $F = 1 \rightarrow F' = 0$ transition in the D_2 line. The atoms was polarization insensitive to the Bragg probe since its detuning is way larger than the transition linewidth, 6.34 GHz $\gg$ 6.06 MHz. In addition, I chose the $F = 1 \rightarrow F' = 0$ transition for a specific reason that the different magnetic sub-levels $m_F = -1, 0$, and 1 in the $F = 1$ ground state have the same transition strength to the $m_{F'} = 0$ excited state [124] (see Fig. 2.3).

In order to calibrate the Bragg signal, I modified my setup to create a 1D spin-dependent lattice [110, 112] for spin $|\downarrow\rangle$ state. To do this, I flipped the bias magnetic field orientation to be along the laser propagation direction in $\mathbf{e}_x$ and changed the Raman laser frequencies to be identical $\omega^+ = \omega^-$. This allowed me to create density modulation with periodicity $\lambda_{\text{zero}}/2$, similar to the stripe-ordered phase and on the

same axis with the spin-orbit coupling direction, as mentioned previously in Section 5.4. Fig. 8.2(c) shows a typical Bragg signal from the 1D lattice system detected by the electron-multiplying charge-coupled device (EMCCD) camera acting as photon sensor in the relay imaging system. Empirical calibration using a 1D spin-dependent lattice with similar parameters for the atoms gave a limit of 8% on the minimum observable density modulation contrast.

For an infinite crystal structure, the lowest order Bragg's condition is met at an angle of $\theta_B = 0.16\,\text{rad}$ with respect to the lattice axis. However, due to the finite transverse size of the atoms and wide acceptance angle of our imaging setup (numerical aperture of 0.3), the Bragg's condition for the incoming angle was slightly different and not very sharp. I observed a peak Bragg signal at an incoming angle of $\theta_B \simeq 0.2\,\text{rad}$ with a full-width at half maximum (FWHM) of 0.07 rad [156]. I could not detect variations as small as 0.1% in the periodicity of the stripe-ordered phase density modulation $d = \pi/q_1$ as a function of Ω. Further, the Bragg scattering measurements of the SOC states were limited to be within coupling strength of $\Omega < 0.65E_R$. I did not observe significant deviations in the Bragg signal corresponding to spatial structures with periodicities other than $d \approx \pi/k_R$.

During data collection, I pulsed the optical Bragg probe for a duration of $100\,\mu$s; the atoms were greatly disturbed for pulsing duration of $> 250\,\mu$s. I chose this value because I did not observe any significant increase in the signal-to-noise ratio for a longer pulsing duration. Further, the $100\,\mu$s Bragg probe duration allowed me to image the remaining atoms using TOF in the same experimental cycle. The TOF

images gave me an additional observation on the magnetization $\langle\sigma_z\rangle$ of the prepared SOC dressed states. This gave a benchmark for comparison to the Bragg signal as a function of the detuning δ.

8.3. Observations of stripe-ordered phase in the full phase diagram

Figure 8.3 shows the observed Bragg counts N_{Bragg} in (Ω, δ) parameter space. For this data, I initially prepared the atoms in an equal population of the two miscible spin states. I then loaded the atoms into the Raman dressed states with frequency detuning δ as discussed in the previous section. I found that the detection of the stripes was possible for larger detuning window compared to the theoretically predicted value because the population relaxation between the two miscible spin states is very slow. The timescale for the initially phase-mixed spin states to eventually phase separate in the magnetized state is estimated to be on the order of $\sim |\delta/2\pi - c_2 n_0/h|^{-1}$.

The scattered Bragg signal from the stripe phase region in the full-phase diagram is shown in Fig. 8.3(a). Figure 8.3(b) shows a cut through Fig. 8.3(a) that displays N_{Bragg} as a function of detuning δ for four different values of Ω. The Bragg signal shows a distinct double-peak structure with a dip in the center at high coupling strength $\Omega \geq 0.3E_R$. The observed double-peak structure is consistent with Jun-Ru Li et al.'s measurements in Ref. [95]. In their work, the inter-spin interaction strength $g_{\uparrow\downarrow}$ was engineered to yield a larger detuning region and they observed an additional peak in the Bragg signal near $\delta \approx 0\,\text{Hz}$. However, in my data, this feature was not resolvable due to the limitation in our ability to scan $\delta/2\pi$ to better than

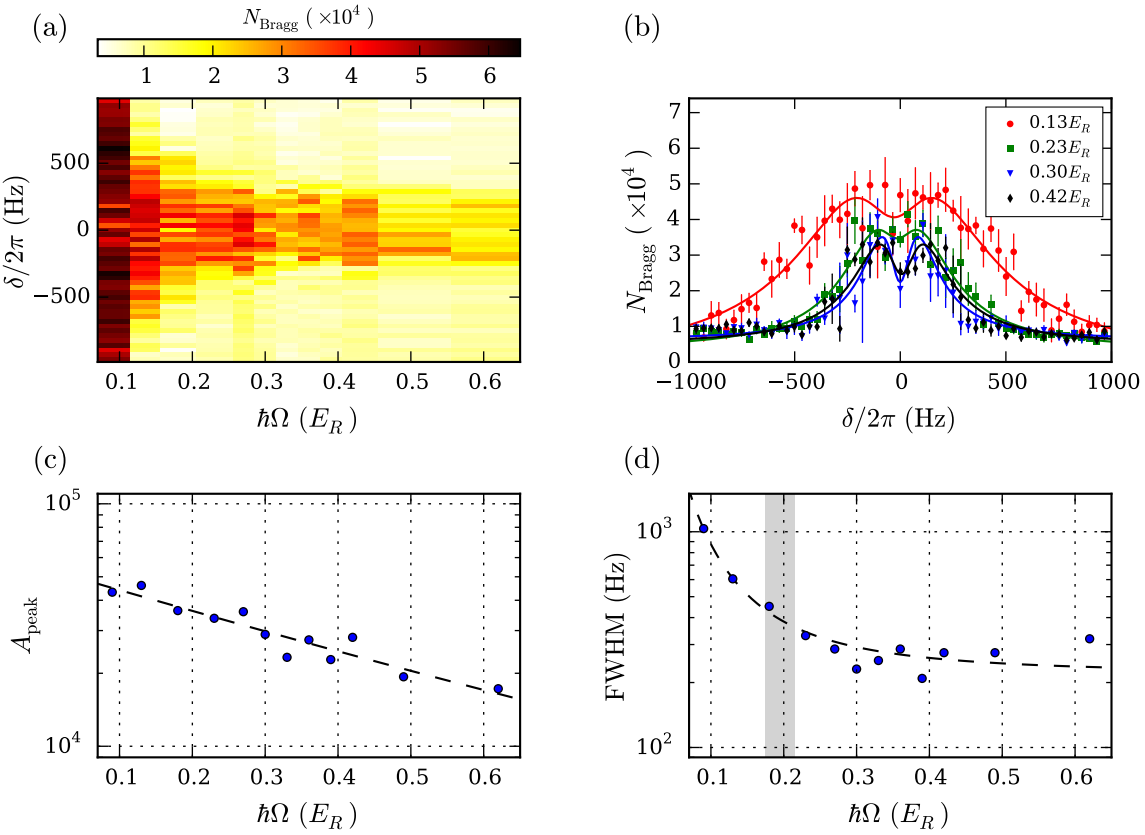

FIGURE 8.3. Stripe-ordered phase in (Ω, δ) parameter space. (a) Phase diagram of the stripe phase region in (Ω, δ) space, as observed by optical Bragg scattering. (b) Bragg counts N_{Bragg} as a function of detuning δ for various coupling strength Ω. Solid lines are fitting to the difference of two Lorentzian distributions as in Eq. 8.10. (c) Fitted amplitude of the Bragg signal as a function of coupling strength Ω. (d) The FWHM obtained from fitting as a function of coupling strength Ω. The gray area shows the predicted transition coupling strength $\Omega_c = 0.19E_R \pm 15\%$ from stripe-ordered phase to magnetized plane-wave phase.

30 Hz precision. The data in Fig 8.3(a)-(b) were taken with a step size of 35.8 Hz for the detuning parameter $\delta/2\pi$. Error bars in Fig. 8.3(b) represent 1σ standard error of the mean with a sample size of 3 to 4 images. I note that the double-peak structure might be blurred out for some values of Ω due to the noise in δ.

I fit the observed signal $N_{\mathrm{Bragg}}(\delta)$ at some constant value of Ω with the difference of two Cauchy-Lorentz distributions (Lorentzian profiles)

$$f(\delta) = \frac{A_0}{1 + \left[(\delta - \delta_0)/\sigma_0\right]^2} - \frac{A_1}{1 + \left[(\delta - \delta_0)/\sigma_1\right]^2} + c, \tag{8.10}$$

with 6 fitting parameters: A_0, A_1, δ_0, σ_0, σ_1 and c. The fitting function $f(\delta)$ is depicted by the solid lines in Fig 8.3(b). The peak amplitude of the Bragg signal A_{peak} was obtained from the maximum value of the fitting function. Figure 8.3(c) shows A_{peak} to decay exponentially as a function of Ω. The fitted detuning FWHM of the combined Lorentzian profiles as a function of Ω is shown in Fig. 8.3(d). I observed a rapid decrease in the FWHM as a function of Ω below the critical transition coupling strength $\hbar\Omega_c \simeq 0.19E_R$. I note that there could be a case of overfitting $N_{\mathrm{Bragg}}(\delta)$ to the function $f(\delta)$ in Eq. 8.10; e.g. if there were only a few data points showing the dip between two peaks centered around δ_0. In this case, the observed data were closer to a single Lorentzian distribution ($A_1 = 0$). I attributed the double-peak structure in the observed $N_{\mathrm{Bragg}}(\delta)$ might be caused by the presence of a harmonic noise in δ. Although I did not investigate this further, it would be interesting to develop a numerical model to calculate $N_{\mathrm{Bragg}}(\delta)$ and see how the density modulation in the stripe phase was affected by the presence of a small ac component in δ during the system preparation.

In an ideal scenario, the presence of detuning $\delta \neq 0$ breaks the symmetry of the two degenerate states in the plane-wave region for $\Omega > \Omega_c$, where the clouds are

spatially separated and exhibit no density modulation. However, due to the finite spin healing length [27] of the condensates (even for $\delta \neq 0$), there always exists a region where the atoms occupy both spin states of the two local minima and they are being phase mixed. The FWHM is largest for $\Omega < \Omega_c$ in the stripe phase region, decreases as Ω approaches Ω_c and it reaches an asymptotic value for $\Omega \gg \Omega_c$. In Fig. 8.3(d), I fit the FWHM to the function $\mathrm{FWHM}(\Omega) = A/\Omega^2 + \mathrm{c}$, and I obtained the best fit values $A = 6.32\,\mathrm{Hz}/E_R^2$ and $c = 215.99\,\mathrm{Hz}$. I note that the results shown in Fig. 8.3 demonstrate that my observations of the stripe phase using optical Bragg scattering were consistent with previous measurements conducted in Ref. [103]. In Ref. [103], the stripe phase region was characterized by the degree of phase separation of the two-component condensates in the SOC dressed states.

The density modulation in the stripe phase existed if there was a mixing of the two spin components. Any detuning noise would alter the population of the two spin components and their degree of mixing. Instead of having δ as a parameter space, I could choose the magnetization or population imbalance between the two spins $\langle \sigma_z \rangle = |\psi_\uparrow|^2 - |\psi_\downarrow|^2$ as an equivalent parameter space. The magnetization $\langle \sigma_z \rangle$ was obtained from TOF imaging of the remaining atoms after a $100\,\mu$s Bragg pulse in the same experimental cycle. Since the Bragg pulse induced transfer between the SOC states, I corrected this by also measuring $\langle \sigma_z \rangle$ in identical SOC system without the Bragg pulse being applied.

Figure 8.4(a) shows the corresponding magnetization $\langle \sigma_z \rangle$ in (Ω, δ) parameter space. The Bragg counts N_{Bragg} as a function of $\langle \sigma_z \rangle$ for four different values of

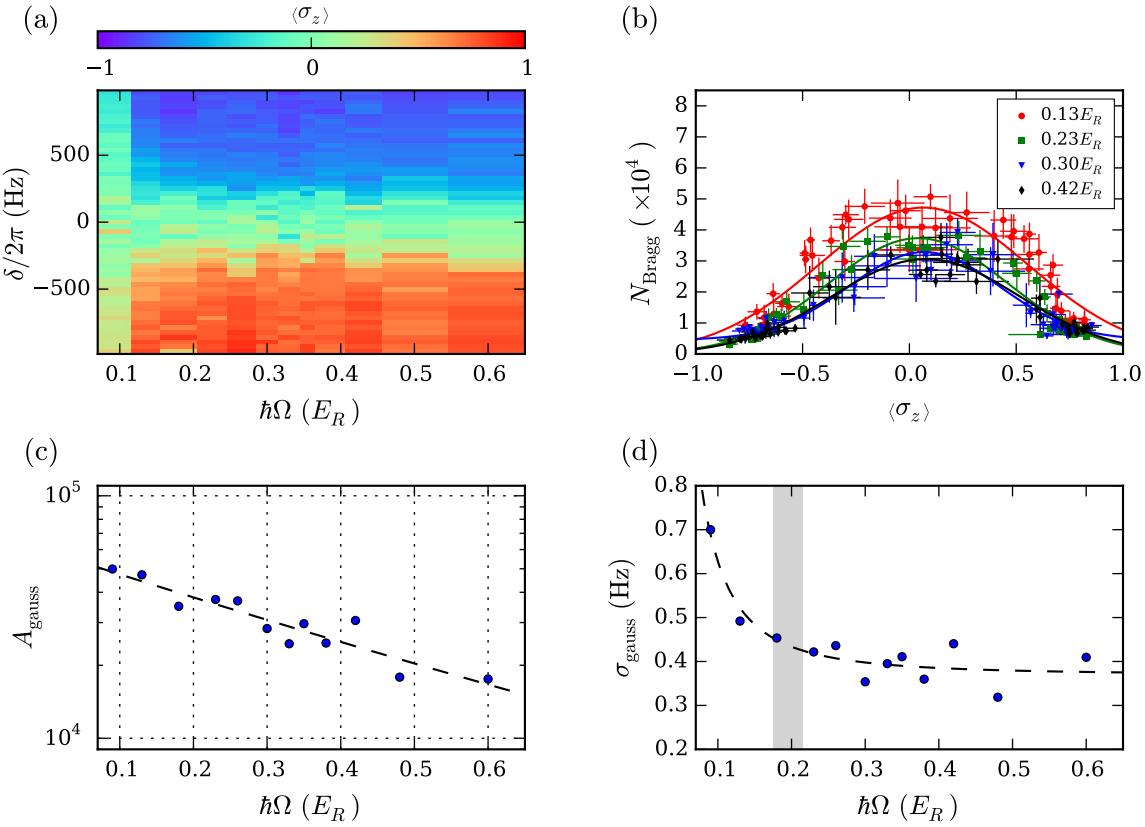

FIGURE 8.4. Stripe-ordered phase as functions of magnetization $\langle\sigma_z\rangle$ and coupling strength Ω. (a) Phase diagram of magnetization $\langle\sigma_z\rangle$ in (Ω, δ) space obtained from TOF imaging, complementary to Fig. 8.3(a). (b) Bragg counts N_{Bragg} as a function of $\langle\sigma_z\rangle$ for various coupling strength Ω. Solid lines are fitting to a Gaussian distribution. (c) Fitted amplitude of the Bragg signal as a function of coupling strength Ω. (d) The gaussian width obtained from fitting as a function of coupling strength Ω. The gray area shows the predicted transition coupling strength $\Omega_c = 0.19E_R \pm 15\%$ from stripe-ordered phase to magnetized plane-wave phase.

Ω is displayed in Fig. 8.4(b). I fit the observed N_{Bragg} as a function of $\langle\sigma_z\rangle$ with a Gaussian distribution, as indicated by the solid lines in Fig. 8.4(b). Similar to previous case where I analyzed the dependency of A_{peak} to the detuning δ (see Fig 8.3(c)), the Gaussian peak of the Bragg signal A_{gauss} also decayed exponentially as

a function of $\langle\sigma_z\rangle$ as shown in Fig. 8.4(c). Figure 8.4(d) shows the σ-width for the Gaussian fitting σ_{gauss} as a function of Ω. Here, again, I observed σ_{gauss} to scale as $\sigma_{\text{gauss}}(\Omega) = A/\Omega^2 + \text{c}$ as shown by the solid line in Fig, 8.4(d). These measurements supported the argument that the stripe phase strongly favors phase-mixing between the spinor components in the SOC system.

8.3.1. Metastability of the stripe-ordered phase. I next investigated the metastability of the stripe-ordered phase. I adiabatically loaded the system into the Raman dressed states by linearly increasing Ω for 50 ms (with $\delta \approx 0$). I held the atoms for various hold times t_{hold} in the dressed states, and finally ramped up the coupling strength $\Omega > 6E_R$ in 200 μs before doing the optical Bragg probing. Figure 8.5(a) shows N_{Bragg} in the $(\Omega, t_{\text{hold}})$ parameter space, where each grid represents more than 3 averaged data points. Figure 8.5(b) shows that the Bragg signal decays as a function of hold time t_{hold}. I fit the data in Fig. 8.5(b) with an exponential function $N_{\text{Bragg}} = A\exp\left(-t_{\text{hold}}/\tau\right) + c$, and plot the lifetime τ in Fig. 8.5(c).

In the data shown in Fig. 8.5(c), I observed a lifetime of $\tau \gtrsim 180\,\text{ms}$ for the initially phase-mixed spin states in the stripe phase region $\Omega < \Omega_c$, and a lifetime of $\tau \lesssim 180\,\text{ms}$ in the magnetized plane-wave states $\Omega > \Omega_c$. The rate of change of τ with respect to Ω changed significantly at the critical point $\Omega = \Omega_c$. I characterized this behavior by fitting the measurements of $\tau\left(\Omega\right)$ to the function

$$\tau\left(\Omega\right) = \begin{cases} A\exp\left(-b_1\Omega\right), & \text{for } \Omega \leq 0.19E_R, \\ A\exp\left(-b_1\cdot 0.19E_R\right)\exp\left\{-b_2\left(\Omega - 0.19E_R\right)\right\}, & \text{for } \Omega > 0.19E_R, \end{cases} \tag{8.11}$$

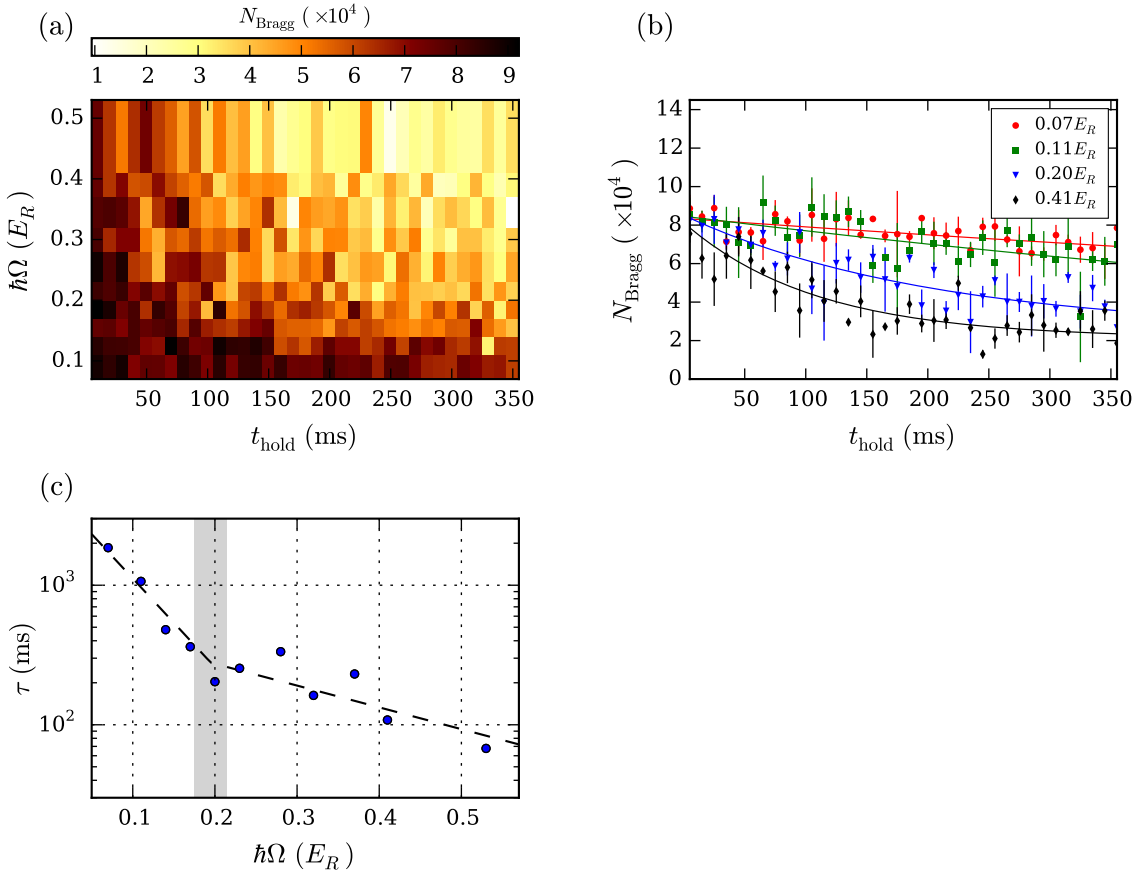

FIGURE 8.5. Metastability of the stripe-ordered phase. (a) Bragg signal as functions of coupling strength Ω and hold time t_{hold}. (b) Bragg counts N_{Bragg} as a function of hold time t_{hold} for various coupling strength Ω. (c) Lifetime τ of the metastable stripe-ordered phase as a function of Ω. The gray area shows the predicted transition coupling strength $\Omega_c = 0.19E_R \pm 15\%$ from stripe-ordered phase to magnetized plane-wave phase.

as indicated by the dashed line in Fig. 8.5(c). I obtained the best fit values $A = 4.83 \times 10^3\,\mathrm{ms}$, $b_1 = 14.6E_R^{-1}$, and $b_2 = 3.6E_R^{-1}$. The lifetime rapidly decayed as Ω approached the critical transition value Ω_c, and it eventually settled to smaller values for $\Omega \gg \Omega_c$. Again, these measurements were consistent with Ref. [103] and showed

that the metastable state of the stripe phase was a result of competing energy scale between the SOC Hamiltonian and the spin-dependent interaction.

8.3.2. Coherence revival of the stripe-ordered phase. In order to confirm the phase coherence of the stripe phase, I did a time revival scan of the observed Bragg signal using Talbot interferometry, as in Refs. [120, 150]. After loading the atoms (see Section 8.2), I turned off the Raman lasers, let the atoms expand in the harmonic dipole trap potential for a duration of $t_{\rm rev}$, and then probed the structure with optical Bragg scattering. I expected the expanding coherent matter wave, which initially had a periodic spatial pattern d, to interfere and exhibit the atomic Talbot effect with a coherence revival period of $T_{\rm rev} = md^2/h$.[1]

Figure 8.6 shows my measurements on the atomic Talbot effect. The observed Bragg counts $N_{\rm Bragg}$ as functions of $(\Omega, t_{\rm rev})$ are displayed in Fig. 8.6(a), where each data mesh element is an average of more than 5 realizations. Figure 8.6(b) shows a horizontal cut through the phase diagram in Fig. 8.6(a); i.e. $N_{\rm Bragg}$ as a function of $t_{\rm rev}$. The plot shows a coherence revival of the detected signal. The maximum interfering signal eventually decayed due to the Debye-Waller factor as the atoms heated up and had more spatial fluctuations.

[1]The initial periodic density modulation d is recovered in the same spatial coordinates after $2T_{\rm rev}$. Meanwhile, maximum interference occurs every time period of $T_{\rm rev}$ to yield similar periodic structures which are shifted by $d/2$.

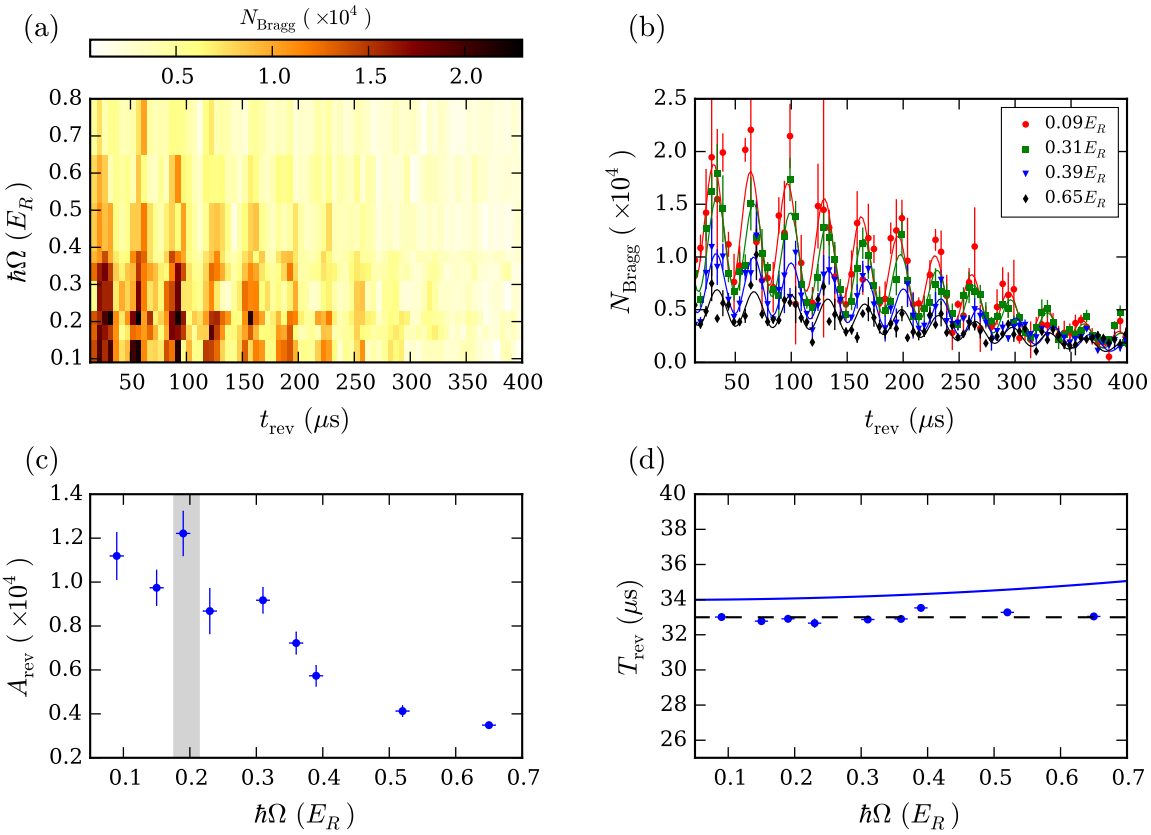

FIGURE 8.6. Periodic revival of the scattered Bragg signal from the stripe phase. (a) Observed Bragg signal as functions of $(\Omega, t_{\mathrm{rev}})$. (b) Coherence revival of the Bragg signal for various coupling strength Ω as a result of the atomic Talbot effect. (c) Revival amplitude A of the Bragg signal as a function of Ω (as obtained from a fit to Eq. 8.12). The gray area shows the predicted transition coupling strength $\Omega_c = 0.19E_R \pm 15\%$ from stripe-ordered phase to magnetized plane-wave phase. (d) Period of coherence revival T_{rev} as a function of Ω (as obtained from a fit to Eq. 8.12). The dashed line shows the average value of observed T_{rev}, while the solid line shows the theoretical prediction of T_{th} (see Eq. 8.13).

I fit the time evolution of the Bragg counts to an exponentially decaying function times the square of a sine:

$$f\left(t_{\mathrm{rev}}\right) = A\exp\left(-\lambda t_{\mathrm{rev}}^2\right)\left[\sin^2\left(2\pi t_{\mathrm{rev}}/T_{\mathrm{rev}}+\phi\right)+c\right], \tag{8.12}$$

where A is the revival amplitude and T_{rev} is the revival period. Figure 8.6(c) shows the revival amplitude A of the Bragg signal as a function of Ω. The revival amplitude decayed rapidly once the coupling strength crosses the transition at $\hbar\Omega_c = 0.19E_R$. Figure 8.6(d) shows that the observed revival period $T_{\text{rev}} = 33.0(3)\,\mu$s does not depend on the coupling strength Ω. This disagreed with the theoretically predicted value (based on a single-particle model) which was given by

$$T_{\text{th}} = \frac{m}{h}\left(\frac{\pi}{q_1}\right)^2 \simeq \frac{m\lambda_{\text{zero}}^2}{4h}\left(1 - \frac{\hbar^2\Omega^2}{16E_R^2}\right)^{-1} \tag{8.13}$$

The predicted revival period T_{th} was dependent on the coupling strength Ω, where its values varied from $T_{\text{th}} = 34.0\,\mu$s to $35.1\,\mu$s for $\hbar\Omega = 0E_R$ to $0.7E_R$ (see solid line in Fig. 8.6(d)). I attributed this discrepancy due to the specific procedure I used to create and measure the stripe phase. At the end of loading the atoms in the SOC dressed states, I ramped Ω up to $> 6E_R$ to map the dressed states of the system into well-defined momentum states at $\pm k_R$. Thus, I did not observe an increasing trend in T_{rev} as the period of the density modulation $d = \pi/q_1$ increases for higher coupling strength Ω. Moreover, the collapse and revival dynamics were affected by the presence of harmonic potential and the spinor condensate interaction energy.

8.3.3. Stripe-ordered phase as functions of coupling strength Ω and temperature T. In this subsection, I investigated the stripe-ordered phase as functions of coupling strength Ω and temperature T. The atoms were first prepared in an equal population of spin $|\uparrow\rangle$ and $|\downarrow\rangle$ states. I varied the initial temperature of the cold

atoms by changing the final optical trap power in the evaporation stage. Next, the phase-mixed spinor Bose gases were loaded into the SOC Hamiltonian by increasing Ω linearly for 50 ms and the atoms were held at constant Ω for 1 s to reach a metastable equilibrium. Finally, I ramped Ω up to $> 6E_R$ within 200 μs and performed the Bragg scattering measurements. The presence of the SOC energy dispersion affected the momentum distribution of the atom, and hence the temperature T was determined for the SOC dressed system in the metastable equilibrium. For each Bragg scattering measurement, I repeated identical experimental run without pulsing the Bragg probe and measured T as described by Ref. [78][2].

The 2D density distribution of the atoms $\rho_{2\mathrm{D}}$ in the bare states was measured using absorption imaging after TOF expansion time τ. A Stern-Gerlach gradient force was applied to separate the two spin components with a distance $\pm d/2$ along the $z-$direction. The temperature T of the system was obtained by fitting the 2D density distribution to the function [78]

$$\rho_{2\mathrm{D}}\left(x,z,T,\tau\right)=\rho_{2\mathrm{D},\uparrow}\left(x,z,T,\tau\right)+\rho_{2\mathrm{D},\downarrow}\left(x,z,T,\tau\right), \tag{8.14}$$

where

$$\begin{aligned}\rho_{2\mathrm{D},\uparrow}\left(x,z,T,\tau\right)=&\rho_{\mathrm{SOC}}^{(+)}\left(x-v_R\tau,z-\frac{d}{2},T,\tau\right)\ a_{(+)}^2\left(\frac{mx}{\hbar\tau}-k_R\right)\\&+\rho_{\mathrm{SOC}}^{(-)}\left(x-v_R\tau,z-\frac{d}{2},T,\tau\right)\ a_{(-)}^2\left(\frac{mx}{\hbar\tau}-k_R\right),\end{aligned} \tag{8.15}$$

[2]See Eqs. S.1-S.7 in the supplementary information of Ref. [78]

$$\rho_{2\mathrm{D},\downarrow}(x,z,T,\tau) = \rho_{\mathrm{SOC}}^{(+)}\left(x+v_R\tau, z+\frac{d}{2}, T, \tau\right)\ b_{(+)}^2\left(\frac{mx}{\hbar\tau}+k_R\right) + \rho_{\mathrm{SOC}}^{(-)}\left(x+v_R\tau, z+\frac{d}{2}, T, \tau\right)\ b_{(-)}^2\left(\frac{mx}{\hbar\tau}+k_R\right). \tag{8.16}$$

Here m is the atomic mass, k_R is the single photon recoil momentum, and $v_R = k_R/m$ is the recoil velocity. The density distribution in the upper and lower branches of the dressed state with quasi-momentum q_x is given by

$$\rho_{\mathrm{SOC}}^{(\pm)}(x',z',T,\tau) = \mathcal{C}\ g_2\left\{\exp\left[\frac{\mu - \frac{m\left(x'^2+z'^2\right)}{2\tau^2} \mp \sqrt{\frac{m^2v_R^2x'^2}{\tau^2}+\frac{\hbar^2\Omega^2}{4}}}{k_BT}\right]\right\}, \tag{8.17}$$

and the coefficients are given by

$$a_{(\pm)}^2(q_x) = \frac{\Omega}{8\sqrt{\left(\frac{\hbar k_R q_x}{m}\right)^2+\frac{\Omega^2}{4}}}\frac{\Omega}{\left(\sqrt{\left(\frac{\hbar k_R q_x}{m}\right)^2+\frac{\Omega^2}{4}} \mp \frac{\hbar k_R q_x}{m}\right)}, \tag{8.18}$$

$$b_{(\pm)}^2(q_x) = \frac{\sqrt{\left(\frac{\hbar k_R q_x}{m}\right)^2+\frac{\Omega^2}{4}} \mp \frac{\hbar k_R q_x}{m}}{2\sqrt{\left(\frac{\hbar k_R q_x}{m}\right)^2+\frac{\Omega^2}{4}}}. \tag{8.19}$$

Figure 8.7(a) shows my measurements of the Bragg counts N_{Bragg} in the finite-temperature phase diagram. Each data mesh element is an average of at least 4 data points. Figure 8.7(b) shows slices of the Bragg counts as a function of Ω for various temperature T. For the data presented in Fig. 8.7, the temperature T was varied with a step size of 60 nK and the standard error of estimate from fitting was 30 nK.

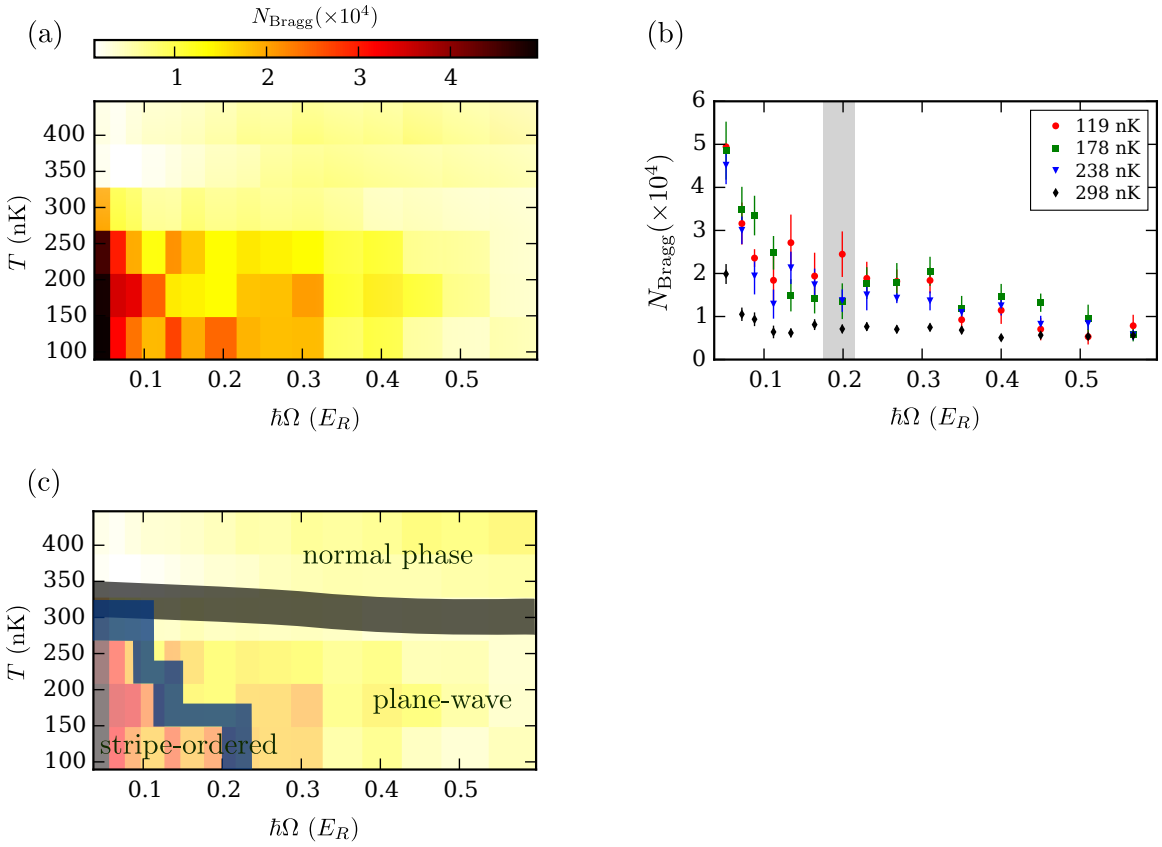

FIGURE 8.7. Stripe-ordered phase in (Ω, T) parameter space. (a) Phase diagram of observed scattered Bragg signal in the parameter space of coupling strength and temperature (Ω, T). (b) Bragg counts as a function of Ω for various temperature T of the system. (c) Estimated phase boundaries for the BEC transition temperature T_C (shaded gray area), and the critical coupling strength Ω_c (shaded blue area) below which I observed an enhancement in the Bragg signal associated with the stripe-ordered phase.

The BEC transition temperature T_C was determined from the data when a condensed fraction of the Bose gas started to appear, as shown by the shaded gray area in Fig. 8.7(c). Despite the phase diagram measurements had a low resolution, I estimated the phase boundary of the stripe phase as the critical coupling strength Ω_c below which I observed a monotonic increase in the Bragg signal as Ω became smaller, shown by

the shaded blue area in Fig. 8.7(c). In this data, I observed the critical coupling strength Ω_c to be decreasing for higher temperature T of the SOC system. This is in agreement with previous experimental and theoretical work [28, 78, 178].

In addition, I also observed an increase in the Bragg signal in a small transient region in the (Ω, T) phase space beyond $\Omega > 0.19E_R$ (see Fig. 8.7(c)). I attributed this increase in the Bragg signal as being due to the metastable nature of the phase-mixed Bose gases, where thermal fluctuations at higher Raman coupling had a significant role. Meanwhile, in the normal phase above the BEC transition temperature T_C, I observed a small increase in the Bragg signal for higher coupling strength Ω. I associated this increase to the substantially larger spatial correlations of the atomic wavefunction. It might be of particular interest to study the observed Bragg signal associated with the density correlations from quantum and thermal fluctuations in the phase space of (Ω, T). Nevertheless, careful calibrations of the Bragg signal are important since, as I have noted previously, the thermal clouds in general have more atoms and larger size compared to those of the BECs.

CHAPTER 9

Conclusions and Outlook

9.1. Conclusions

The central thesis of my Ph.D. research work was to observe the stripe-ordered phase in a spin-orbit coupled (SOC) Bose-Einstein condensate (BEC). A signature of the stripe phase is the existence of density modulation. I prepared atoms in metastable states to enhance the stripe phase region and probed the density modulation using optical Bragg scattering. I was able to explore the full phase diagram of the stripe phase, and my measurements of the phase boundaries were in good agreement with theoretical predictions and previous experimental results [69, 78, 98, 103].

In Chapter 4, I demonstrated a systematic method to bring ultracold atoms into optimal focus [140]. This technique relied on the behavior of the power spectral density of the optical depth to eliminate defocus-induced artifacts. The density fluctuations in BECs, are mapped from the phase fluctuations after time-of-flight release. They act like random scatterers to create diffraction pattern which change as a function of distance from the optimal focus. Using this approach, I was able to pinpoint the optimal focus of the BEC to within $2\,\mu$m for a $150\,\mu$m thick BEC cloud.

In Chapter 5, I showed the techniques I used to manipulated ultracold atoms with electromagnetic waves, ranging from radio frequency (a few MHz's) to the optical

band (hundreds of THz). I explained the preparation methods for different mixtures of the spinor $F = 1$ Bose gases and how I used microwave-assisted partial-transfer absorption imaging to provide feedback for our DC magnetic field control. Further, I exploited the vectorial light shift of the ac-Stark effect and used it to demonstrate various engineered Hamiltonians [53]. This enabled me to realize spin-orbit coupling using a two-photon transition Raman coupling scheme. With a few hardware changes, I also created spin-dependent lattice [110] and used it to calibrate the optical Bragg signal in later experiments.

In Chapter 6, I presented our measurements of the phase diagram of a spin-1 BEC, containing a ferromagnetic phase and an unmagnetized phase [22]. We characterized the first- and second-order phase transition from the ferromagnetic phase to the polar spinor BEC and spin-helix BEC and our results were in agreement with theory. Our observation of controlled quench dynamics through a first-order phase transition opens the door for realizing Kibble-Zurek physics [84, 182] in this system.

In Chapter 7, I discussed my study of the optical Bragg scattering from ultracold atom systems. I gave detailed explanations of the various contributions to the scattered Bragg signal, which capture the non-interfering and interfering parts of the atomic distribution [45]. I demonstrated a new experimental technique to characterize the scattered Bragg signal, focusing on its geometrical properties [156]. Optical Bragg scattering from one-dimensional lattice was displayed as a function of lattice depth and I investigated the atomic Talbot revival [120, 150] in this system. Finally, I studied many physical phenomena using the Bragg scattering technique, including:

- the Bragg counts show a peak near the BEC transition temperature T_C at low lattice depth,
- there is no atomic Talbot revival for temperature above T_C, consistent with the thermal clouds having no phase coherence on the length scale of the lattice periodicity,
- for a near-resonant Bragg probe, the scattered Bragg signal was observed from the spin-helix BEC in the SOC dressed states prepared both diabatically and adiabatically,
- a Rabi pulse of the Raman coupling was applied to create an SOC system and the following Bragg scattering showed similar oscillating behavior with twice the Rabi frequency, which confirmed the presence of precessing spin polarization in the SOC system.

These findings open up new prospects to study the behavior of quantum degenerate gases which possess spatial density modulations.

Finally, I studied the long-sought stripe-ordered phase in SOC condensates. As described in Chapter 8, I explored the parameter space of Raman coupling strength Ω and detuning δ between the two coupled spin components. My observation of the Bragg signal showed a double-peak structure with a dip in the center as a function of detuning δ within the stripe phase region. The δ-width of the stripe phase decreases as a function of Ω and it eventually reaches an asymptote above the critical transition coupling strength $\hbar\Omega_c \simeq 0.19E_R$. I examined the metastability condition of the stripe

phase and confirmed previous work [69, 98, 103]. The stripe phase is claimed to have a crystalline order with long-range phase order and exhibits roton-maxon like structure analogous to supersolidity [97, 109]. Our measurements of atomic Talbot revival in the stripe phase do indeed show the expected coherence behavior. Last but not least, I studied the finite-temperature T phase diagram of the stripe-ordered phase. My results in (Ω, T) parameter space based on the scattered Bragg signal support recent theoretical work [28, 178] and they are in agreement with previous measurements [78].

9.2. Outlook

In the process of conducting this research, I would like to mention two things which can cause unnecessary problems. First, the definition of frequency and angular frequency are often overlooked by atomic physicists where energy is often expressed in terms of "frequency" (either the energy being divided by h or $\hbar$). I often found this to be an unnecessary source of errors, which were time-consuming to hunt down. In terms of technical issue in the laboratory, I found that the back-reflectance from the vacuum glass cell is very annoying. The glass cell acted as a plane-parallel plate which introduced coma (or comatic) aberration for an off-axis beam propagating through it. It is often desired to send laser beams to the atoms in a normal direction since spherical aberration by glass plate can be conveniently corrected with lenses, and it eases optical alignment. However, undesired back-reflectance from the glass cell, especially for near-resonant beams, causes an optical lattice potential from a normal

angle beam. It is thus important to have a well-designed and well-coated glass cell to reduce the back-reflectance as much as possible.

Regarding future outlook, optical Bragg scattering has proven to be useful to investigate density modulation present in quantum degenerate gases, particularly the spatial correlations of the atomic collective wavefunction. The temperature dependence shows a peculiar behavior near the threshold transition temperature of BEC for low lattice depth. One question is whether it is possible to observe quantum statistical effects from the many-body atomic correlations as the atoms condense into the degenerate energy level [122].

In the limit of weak elastic scattering, the optical Bragg probe maps the spatial atomic distribution into Fourier space as the static structure factor. Hypothetically, if we can scan the incoming Bragg angle and detect the scattered signal in all directions, we could determine the atomic density in real space (extending the technique used in X-ray crystallography to atomic physics).

In addition to the work presented in this dissertation, several other important projects were going on in our laboratory. One project involved the production of one-dimensional (1D) Bose gases using a tightly focused Laguerre-Gauss beam. The realization of 1D Bose gases opens up new possibilities to study more elaborate engineered many-body problems, such as 1D spin-orbit coupling in 1D Bose gases, using optical Bragg scattering to study the 1D density-density correlations, and investigating the stripe phase in a (quasi) 1D system. In (quasi) 1D condensates, where the spin healing length is larger than the transverse size of the clouds, magnetic domains only

from in the longitudinal axis of the condensate. This should be readily observable in absorption imaging. Another interesting topic is the formation of stripe-ordered phase and its time-evolution in (quasi) 1D SOC condensates. One could use both optical Bragg scattering and absorption imaging techniques to obtain information on the density modulation and magnetic domains of such system simultaneously.

APPENDIX A

Matrix elements of the hyperfine Hamiltonian in the presence of a magnetic field

In cold atom experiments, it is common to modify the atomic structure with an external dc bias field. Here I discuss the matrix elements of the hyperfine Hamiltonian operator, where diagonalization of the matrix operator gives eigenenergies of the atomic structure.

The atomic interaction with an external static magnetic field, where the bias field quantization axis is chosen along $\mathbf{e}_z$, is given by [163]

$$H_B = \frac{\mu_B}{\hbar}\left(g_S S_z + g_L L_z + g_I I_z\right) B_z, \tag{A.1}$$

where g_S, g_L, and g_I are respectively the electon spin, electron orbital, and nuclear $g-$factors. In alkali atoms, the energy shift due to the magnetic field is commonly small compared to the fine-structure splitting. This allows me to describe the interaction Hamiltonian with the quantum number J of the electron's total angular momentum, namely

$$H_B = \frac{\mu_B}{\hbar}\left(g_J J_z + g_I I_z\right) B_z, \tag{A.2}$$

where the fine structure Lande g-factor is given by

$$g_J = g_L \frac{J\left(J+1\right) - S\left(S+1\right) + L\left(L+1\right)}{2J\left(J+1\right)} + g_S \frac{J\left(J+1\right) + S\left(S+1\right) - L\left(L+1\right)}{2J\left(J+1\right)}. \tag{A.3}$$

TABLE A.1. Magnetic interaction parameters for the D line transitions of ^{87}Rb.

Physical constants	Values	
Magnetic dipole constant, $A_{\rm hf}$	$5\mathcal{S}_{1/2}$	$h \cdot 3417.34130545215(5)$ MHz
	$5\mathcal{P}_{1/2}$	$h \cdot 407.25(63)$ MHz
	$5\mathcal{P}_{3/2}$	$h \cdot 84.7185(20)$MHz
Electric quadrupole constant, $B_{\rm hf}$	$5\mathcal{P}_{3/2}$	$h \cdot 12.4965\,(37)$MHz
Fine structure Lande g-factor, g_J	$5\mathcal{S}_{1/2}$	2.00233113(20)
	$5\mathcal{P}_{1/2}$	0.666
	$5\mathcal{P}_{3/2}$	1.3362 (13)
Nuclear g-factor, g_I	$-0.0009951414(10)$	
Electron spin g-factor, g_S	2.0023193043622 (15)	
Electron orbital g-factor, g_L	0.99999369	
^{87}Rb nuclear spin, I	3/2	
Bohr magneton, μ_B	$h \cdot 1.399624604\,(35)$MHz/G	

The hyperfine Hamiltonian in the presence of an external magnetic field becomes

$$H_{\rm tot} = A_{\rm hf}\frac{\mathbf{I}\cdot\mathbf{J}}{\hbar^2} + B_{\rm hf}\frac{\frac{3}{\hbar^4}\left(\mathbf{I}\cdot\mathbf{J}\right)^2 + \frac{3}{2\hbar^2}\mathbf{I}\cdot\mathbf{J} - I\left(I+1\right)J\left(J+1\right)}{2I\left(2I-1\right)J\left(2J-1\right)} + \frac{\mu_B}{\hbar}\left(g_J m_J + g_I m_I\right)B_z. \tag{A.4}$$

Experimental values of $A_{\rm hf}$, $B_{\rm hf}$, and the g-factors for ^{87}Rb atoms are given in Table A.1.

In order to solve the eigenenergies of the Hamiltonian in Eq. A.4, it is natural to choose the basis states as $|J, m_J, I, m_I\rangle$ where the quantum numbers describe the atomic total angular momentum consisting of nuclear spin and electron orbital angular momentum. To simplify the notation in the remaining of this appendix, the basis states $|J, m_J, I, m_I\rangle$ are represented by $|m_J, m_I\rangle$. The Hamiltonian operator becomes a square matrix with dimension $(2I+1)(2J+1)$. The expressions for the matrix elements can be calculated using properties of the angular momentum operators. I

recall the angular momentum ladder operators are defined by

$$\mathbf{J}_+ = \mathbf{J}_x + \mathrm{i}\mathbf{J}_y \quad \text{and} \quad \mathbf{J}_- = \mathbf{J}_x - \mathrm{i}\mathbf{J}_y, \tag{A.5}$$

which operations on a given angular momentum state $|J, m_J\rangle$ satisfy the relations

$$\mathbf{J}_+ |J, m_J\rangle = \hbar\sqrt{(J - m_J)(J + m_J + 1)}\,|J, m_J + 1\rangle\,, \tag{A.6}$$

$$\mathbf{J}_- |J, m_J\rangle = \hbar\sqrt{(J + m_J)(J - m_J + 1)}\,|J, m_J - 1\rangle\,, \tag{A.7}$$

for bounded values of $-J \leq m_J \leq J$.

With the definition of the ladder operators, I can express the magnetic dipole term as

$$\mathbf{M} := \frac{\mathbf{I}\cdot\mathbf{J}}{\hbar^2} = \frac{1}{\hbar^2}\mathbf{I}_z\mathbf{J}_z + \frac{1}{2\hbar^2}\left(\mathbf{I}_+\mathbf{J}_- + \mathbf{I}_-\mathbf{J}_+\right). \tag{A.8}$$

The relevant matrix elements for the first term on the right-hand side of Eq. A.4 are consequently given by:

$$\langle m_J, m_I\,|\mathbf{M}|\,m_J, m_I\rangle = m_J m_I, \tag{A.9}$$

$$\langle m_J, m_I\,|\mathbf{M}|\,m_J + 1, m_I - 1\rangle = \frac{1}{2}\sqrt{(J - m_J)(J + m_J + 1)(I + m_I)(I - m_I + 1)}, \tag{A.10}$$

$$\langle m_J, m_I\,|\mathbf{M}|\,m_J - 1, m_I + 1\rangle = \frac{1}{2}\sqrt{(J + m_J)(J - m_J + 1)(I - m_I)(I + m_I + 1)}. \tag{A.11}$$

In a similar manner, I express the electric quadrupole term in Eq. A.4 as [143]

$$\mathbf{Q} = \frac{3}{\hbar^4}(\mathbf{I}\cdot\mathbf{J})^2 + \frac{3}{2\hbar^2}\mathbf{I}\cdot\mathbf{J} - I(I+1)J(J+1)\,, \tag{A.12}$$

and obtain the following relevant matrix elements (non-zero for $I \neq 1/2$ or $J \neq 1/2$):

$$\langle m_J, m_I \left|\mathbf{Q}\right| m_J, m_I\rangle = \frac{1}{2}\left[3m_I^2 - I\left(I+1\right)\right]\left[3m_J^2 - J\left(J+1\right)\right], \tag{A.13}$$

$$\langle m_J, m_I \left|\mathbf{Q}\right| m_J - 1, m_I + 1\rangle = \frac{3}{4}\left(2m_J - 1\right)\left(2m_I + 1\right) \sqrt{\left(J + m_J\right)\left(J - m_J + 1\right)\left(I - m_I\right)\left(I + m_I + 1\right)}, \tag{A.14}$$

$$\langle m_J, m_I \left|\mathbf{Q}\right| m_J + 1, m_I - 1\rangle = \frac{3}{4}\left(2m_J + 1\right)\left(2m_I - 1\right) \sqrt{\left(J - m_J\right)\left(J + m_J + 1\right)\left(I + m_I\right)\left(I - m_I + 1\right)}, \tag{A.15}$$

$$\langle m_J, m_I \left|\mathbf{Q}\right| m_J - 2, m_I + 2\rangle = \frac{3}{4}\sqrt{\left(J + m_J\right)\left(J + m_J - 1\right)\left(J - m_J + 1\right)\left(J - m_J + 2\right)} \sqrt{\left(I - m_I\right)\left(I - m_I - 1\right)\left(I + m_I + 1\right)\left(I + m_I + 2\right)}, \tag{A.16}$$

$$\langle m_J, m_I \left|\mathbf{Q}\right| m_J + 2, m_I - 2\rangle = \frac{3}{4}\sqrt{\left(J - m_J\right)\left(J - m_J - 1\right)\left(J + m_J + 1\right)\left(J + m_J + 2\right)} \sqrt{\left(I + m_I\right)\left(I + m_I - 1\right)\left(I - m_I + 1\right)\left(I - m_I + 2\right)}. \tag{A.17}$$

A special case exists for $J = 1/2$ where the Hamiltonian in Eq. A.4 can be solved analytically. The eigenenergies in this case are given by

$$E_{1/2,\pm 1/2,I,m_I} = -\frac{\Delta E_{\mathrm{hf}}}{2\left(2I+1\right)} + \frac{\Delta E_{\mathrm{hf}} g_I \left(m_I \pm \frac{1}{2}\right) x}{\left(g_J - g_I\right)} \pm \frac{\Delta E_{\mathrm{hf}}}{2}\sqrt{1 + \frac{4\left(m_I \pm \frac{1}{2}\right)x}{2I+1} + x^2}, \tag{A.18}$$

where $\Delta E_{\mathrm{hf}} = A_{\mathrm{hf}}\left(J + 1/2\right)$ and $x = (g_J - g_I)\mu_B B_z / \Delta E_{\mathrm{hf}}$. The solution in Eq. A.18 is also known as the Breit-Rabi formula which is particularly useful to describe the hyperfine splitting of electronic structures in alkali atoms with $J = 1/2$ (i.e. the $5\mathcal{S}_{1/2}$ electronic ground state and $5\mathcal{P}_{1/2}$ excited state in the D_1 line of ^{87}Rb atoms).

APPENDIX B

Gross-Pitaevskii equations for $F = 1$ spinor Bose-Einstein condensates

I consider $F = 1$ spinor Bose-Einstein condensates (BECs) within s-wave scattering limit between the two-body collisions. In the following treatment, I assume the atomic interactions do not change the rotational symmetry of the system, implying a conservation of total angular momentum of the colliding pair of atoms. In the $s-$wave channel, the relative center-of-mass orbital angular momentum of the two colliding atoms (labelled by index i and j) is zero, and the total angular momentum of the incoming state is simply the sum of the two atomic hyperfine spins $\mathbf{F}_{ij} = \mathbf{F}_i + \mathbf{F}_j$. Exchange symmetry of the colliding two identical bosons then restricts the quantum number F_{ij} to be an even integer, or it can only take the values $F_{ij} \in \{0, 2, \ldots, 2F\}$ [159].

Within these assumptions, the two-body interaction is only applicable when the outgoing state has the same total angular momentum with the incoming state, and hence the collisional interaction can be described by the potential operator

$$\hat{\mathbf{V}}_{\text{int}} = \frac{1}{2}\sum_{i,j}\delta^3(\mathbf{r}_i - \mathbf{r}_j)\sum_{F_{ij}}\frac{4\pi\hbar^2 a_{F_{ij}}}{m}\hat{\mathbf{P}}_{F_{ij}}, \tag{B.1}$$

where the first summation term is taken over all colliding particle pairs; $a_{F_{ij}}$ are the scattering lengths for collisions between the pair (i, j) with total spin F_{ij}; and $\hat{\mathbf{P}}_{F_{ij}}$ are the projection operators which project the two-atom wave function into the subspace with total angular momentum F_{ij}. To eliminate the summation over the possible collisional channels, I consider the outer product of identity operators for the two

spin-1 particles

$$\hat{I}_i \otimes \hat{I}_j = \sum_{F_{ij}=0,2} \hat{\mathbf{P}}_{F_{ij}} = \hat{\mathbf{P}}_0 + \hat{\mathbf{P}}_2, \tag{B.2}$$

and the composition of the $F = 1$ spin operators

$$\frac{\mathbf{F}_i \cdot \mathbf{F}_j}{\hbar^2} = \frac{\mathbf{F}_{ij}^2 - \mathbf{F}_i^2 - \mathbf{F}_j^2}{2\hbar^2} = \sum_{F_{ij}=0,2} \left[\frac{F_{ij}}{2} \left(F_{ij} + 1 \right) - F(F+1) \right] \hat{\mathbf{P}}_{F_{ij}} = \hat{\mathbf{P}}_2 - 2\hat{\mathbf{P}}_0. \tag{B.3}$$

This allows me to rewrite the interaction potential as

$$\hat{\mathbf{V}}_{\text{int}} = \frac{1}{2} \sum_{i,j} \delta^3(\mathbf{r}_i - \mathbf{r}_j) \left\{ c_0 \hat{I}_i \otimes \hat{I}_j + c_2 \frac{\mathbf{F}_i \cdot \mathbf{F}_j}{\hbar^2} \right\}, \tag{B.4}$$

where the interactions are separated into the spin-independent part $c_0 \hat{I}_i \otimes \hat{I}_j$ and spin-dependent part $c_2 \mathbf{F}_i \cdot \mathbf{F}_j / \hbar^2$. The coefficients c_0 and c_2 are related to the scattering lengths a_0 and a_2 (for collision channels with total spin 0 and 2) via the equations

$$c_0 = \frac{4\pi\hbar^2}{m} \frac{a_0 + 2a_2}{3}, \qquad c_2 = \frac{4\pi\hbar^2}{m} \frac{a_2 - a_0}{3}. \tag{B.5}$$

In the formalism of second quantization, the many-body Hamiltonian within the $s-$wave interactions for $F = 1$ spinor BEC becomes

$$\begin{aligned} \hat{H} \;=\; & \int \mathrm{d}^3\mathbf{r} \left\{ \hat{\Psi}_\alpha^\dagger \left(-\frac{\hbar^2 \nabla^2}{2m} + V_{\text{ext}}(\mathbf{r}) \right) \hat{\Psi}_\alpha + \frac{1}{2} c_0 \hat{\Psi}_\alpha^\dagger \hat{\Psi}_{\alpha'}^\dagger \hat{\Psi}_{\alpha'} \hat{\Psi}_\alpha \right. \\ & \left. + \frac{1}{2} c_2 \left(\hat{\Psi}_\alpha^\dagger \mathbf{F}_{\alpha\beta} \hat{\Psi}_\beta \right) \cdot \left(\hat{\Psi}_{\alpha'}^\dagger \mathbf{F}_{\alpha'\beta'} \hat{\Psi}_{\beta'} \right) \right\}, \end{aligned} \tag{B.6}$$

where $V_{\text{ext}}(\mathbf{r})$ is an external scalar potential, the indices $\alpha, \beta, \alpha', \beta'$ correspond to the $m_F = -1, 0, +1$ components of the $F = 1$ manifold, and repeated indices are implicitly summed over. In Eq. B.6, I have simplified our notations by omitting the

position and time dependence of the field operators $\hat{\Psi}_\alpha(\mathbf{r},t)$ in the writing.[1] The bosonic field operators satisfy the commutation relations

$$\left[\hat{\Psi}_\alpha(\mathbf{r},t),\hat{\Psi}^\dagger_\beta(\mathbf{r}',t)\right] = \delta_{\alpha\beta}\delta(\mathbf{r}-\mathbf{r}'), \tag{B.7}$$

$$\left[\hat{\Psi}_\alpha(\mathbf{r},t),\hat{\Psi}_\beta(\mathbf{r}',t)\right] = \left[\hat{\Psi}^\dagger_\alpha(\mathbf{r},t),\hat{\Psi}^\dagger_\beta(\mathbf{r}',t)\right] = 0, \tag{B.8}$$

and the spin-1 matrix operators are given by

$$F_x = \frac{\hbar}{\sqrt{2}}\begin{bmatrix} 0 & 1 & 0 \\ 1 & 0 & 1 \\ 0 & 1 & 0 \end{bmatrix}, \quad F_y = \frac{\hbar}{\sqrt{2}}\begin{bmatrix} 0 & -\mathrm{i} & 0 \\ \mathrm{i} & 0 & -\mathrm{i} \\ 0 & \mathrm{i} & 0 \end{bmatrix}, \quad F_z = \hbar\begin{bmatrix} 1 & 0 & 0 \\ 0 & 0 & 0 \\ 0 & 0 & -1 \end{bmatrix}. \tag{B.9}$$

The explicit form of the total Hamiltonian in second-quantized form becomes

$$\begin{aligned}\hat{H} &= \int \mathrm{d}^3\mathbf{r}\Bigg\{ \left(\frac{\hbar^2}{2m}\nabla\hat{\Psi}^\dagger_\alpha\cdot\nabla\hat{\Psi}_\alpha + V(\mathbf{r})\hat{\Psi}^\dagger_\alpha\hat{\Psi}_\alpha\right) \\ &+ \left(\frac{c_0+c_2}{2}\right)\left[\hat{\Psi}^\dagger_1\hat{\Psi}^\dagger_1\hat{\Psi}_1\hat{\Psi}_1 + \hat{\Psi}^\dagger_{-1}\hat{\Psi}^\dagger_{-1}\hat{\Psi}_{-1}\hat{\Psi}_{-1} + 2\hat{\Psi}^\dagger_0\hat{\Psi}_0\left(\hat{\Psi}^\dagger_1\hat{\Psi}_1 + \hat{\Psi}^\dagger_{-1}\hat{\Psi}_{-1}\right)\right] \\ &+ \frac{c_0}{2}\hat{\Psi}^\dagger_0\hat{\Psi}^\dagger_0\hat{\Psi}_0\hat{\Psi}_0 + (c_0-c_2)\,\hat{\Psi}^\dagger_1\hat{\Psi}^\dagger_{-1}\hat{\Psi}_{-1}\hat{\Psi}_1 + c_2\left[\hat{\Psi}^\dagger_1\hat{\Psi}^\dagger_{-1}\hat{\Psi}_0\hat{\Psi}_0 + \text{c.c.}\right]. \end{aligned} \tag{B.10}$$

In the mean-field approximation, I then replace the field operators by the complex wave functions to describe the three-component spinor condensates:

$$\hat{\Psi}(\mathbf{r},t) = \begin{pmatrix} \hat{\Psi}_1(\mathbf{r},t) \\ \hat{\Psi}_0(\mathbf{r},t) \\ \hat{\Psi}_{-1}(\mathbf{r},t) \end{pmatrix} \to \Psi(\mathbf{r},t) = \begin{pmatrix} \psi_1(\mathbf{r},t) \\ \psi_0(\mathbf{r},t) \\ \psi_{-1}(\mathbf{r},t) \end{pmatrix}, \tag{B.11}$$

[1] For a single (spin) component of interacting particles in the $s-$wave approximation, the many-body Hamiltonian becomes $\hat{H} = \int \mathrm{d}^3\mathbf{r}\left[\hat{\Psi}^\dagger\left\{-\hbar^2\nabla^2/2m + V_{\text{ext}}(\mathbf{r})\right\}\hat{\Psi} + \frac{1}{2}\int d^3\mathbf{r}'\hat{\Psi}^\dagger\hat{\Psi}'^\dagger g\delta^3(\mathbf{r}'-\mathbf{r})\hat{\Psi}'\hat{\Psi}\right]$ since $a = a_0 = a_2$ and $g = 4\pi\hbar^2 a/m$.

with the normalization to the total number of atoms N is given by

$$\int \mathrm{d}^3\mathbf{r}\ \Psi^\dagger(\mathbf{r},t)\cdot\Psi(\mathbf{r},t) = N. \tag{B.12}$$

I obtain the Gross-Pitaevskii mean-field energy for $F=1$ spinor BEC as

$$\begin{aligned} E_{\mathrm{GP}} = \int \mathrm{d}^3\mathbf{r}\ \varepsilon \ &= \int \mathrm{d}^3\mathbf{r}\Bigg\{ \left(\frac{\hbar^2}{2m}\nabla\psi_\alpha^*\cdot\nabla\psi_\alpha + V(\mathbf{r})\left|\psi_\alpha\right|^2\right) \\ &+ \left(\frac{c_0+c_2}{2}\right)\left[\left|\psi_1\right|^4+\left|\psi_{-1}\right|^4\right] + \frac{c_0}{2}\left|\psi_0\right|^4 \\ &+ (c_0-c_2)\left|\psi_1\right|^2\left|\psi_{-1}\right|^2 + (c_0+c_2)\left|\psi_0\right|^2\left[\left|\psi_1\right|^2+\left|\psi_{-1}\right|^2\right] \\ &+ c_2\left[\psi_1^*\psi_{-1}^*\psi_0^2 + \mathrm{c.c.}\right]\Bigg\}, \end{aligned} \tag{B.13}$$

where ε is defined as the energy density functional . The right-hand side terms on the first line of Eq. B.13 describe the single-particle physics of the system; the terms on the second line describe the self-interaction or intra-state collisions between particles of the same spin; the remaining terms describe the spin-exchange mechanism with the third line representing the inter-state collisions between particles with different spins, and the last term on the fourth line representing coherent spin mixing which is responsible for the relaxation to the spinor ground state energy.

Next, I derive the time-evolution of the wave function $\Psi(\mathbf{r},t)$ from the principle of least action[2]. I define the action of the system as [132]

$$S\left[\Psi(\mathbf{r},t)\right] = \int \mathrm{d}t\ \int \mathrm{d}^3\mathbf{r}\ \mathcal{L}\left(\psi_\alpha,\psi_\alpha^*,\dot{\psi_\alpha},\dot{\psi_\alpha^*},\nabla\psi_\alpha,\nabla\psi_\alpha^*\right), \tag{B.14}$$

and the Lagrangian is given by

$$\mathcal{L} = \frac{\mathrm{i}\hbar}{2}\left[\psi_\alpha^*\dot{\psi_\alpha} - \dot{\psi_\alpha^*}\psi_\alpha\right] - \varepsilon. \tag{B.15}$$

[2]Other derivation method is to use the Heisenberg representation $\mathrm{i}\hbar\partial\hat{\Psi}(\mathbf{r},t)/\partial t = \left[\hat{\Psi}(\mathbf{r},t),\hat{H}\right]$

Using the variational principle method to find the extremum value of S, I obtain the equation of motion:

$$-\frac{\partial}{\partial t}\frac{\partial \mathcal{L}}{\partial \dot{\psi}_\alpha^*}+\frac{\partial \mathcal{L}}{\partial \psi_\alpha^*}-\nabla\cdot\left(\frac{\partial \mathcal{L}}{\partial \nabla\psi_\alpha^*}\right)=0, \tag{B.16}$$

which can be expressed in terms of ε as

$$\mathrm{i}\hbar\frac{\partial \psi_\alpha}{\partial t}=\frac{\delta\varepsilon}{\delta\psi_\alpha^*}=\frac{\partial\varepsilon}{\partial\psi_\alpha^*}-\nabla\cdot\left(\frac{\partial\varepsilon}{\partial\nabla\psi_\alpha^*}\right). \tag{B.17}$$

Finally, I arrive at the time-dependent Gross-Pitaevskii equations (GPEs) describing the $F=1$ spinor condensate wave functions:

$$\begin{aligned}
\mathrm{i}\hbar\partial_t\psi_1 &= \left\{-\frac{\hbar^2}{2m}\nabla^2+V_{\mathrm{ext}}+(c_0+c_2)\left[|\psi_1|^2+|\psi_0|^2\right]+(c_0-c_2)|\psi_{-1}|^2\right\}\psi_1 \\
&\quad +c_2\psi_{-1}^*\psi_0^2, \qquad (B.18)\\
\mathrm{i}\hbar\partial_t\psi_0 &= \left\{-\frac{\hbar^2}{2m}\nabla^2+V_{\mathrm{ext}}+(c_0+c_2)\left[|\psi_1|^2+|\psi_{-1}|^2\right]+c_0|\psi_0|^2\right\}\psi_0 \\
&\quad +2c_2\psi_0^*\psi_1\psi_{-1}, \qquad (B.19)\\
\mathrm{i}\hbar\partial_t\psi_{-1} &= \left\{-\frac{\hbar^2}{2m}\nabla^2+V_{\mathrm{ext}}+(c_0+c_2)\left[|\psi_{-1}|^2+|\psi_0|^2\right]+(c_0-c_2)|\psi_1|^2\right\}\psi_{-1} \\
&\quad +c_2\psi_1^*\psi_0^2. \qquad (B.20)
\end{aligned}$$

Note special cases exist in the dynamics of the spinor condensates if I only consider two spin states. As an example, if there is no initial atoms in $m_F=0$ or $\psi_0(\mathbf{r},0)=0$, and there is no spin coupling from the single-particle Hamiltonian and external potential, the GPEs reduce to

$$\begin{aligned}
\mathrm{i}\hbar\partial_t\psi_1 &= \left\{-\frac{\hbar^2}{2m}\nabla^2+V_{\mathrm{ext}}+(c_0+c_2)|\psi_1|^2+(c_0-c_2)|\psi_{-1}|^2\right\}\psi_1, \qquad (B.21)\\
\mathrm{i}\hbar\partial_t\psi_{-1} &= \left\{-\frac{\hbar^2}{2m}\nabla^2+V_{\mathrm{ext}}+(c_0+c_2)|\psi_{-1}|^2+(c_0-c_2)|\psi_1|^2\right\}\psi_{-1}. \qquad (B.22)
\end{aligned}$$

Despite their complexities, the set of coupled GPEs in Eqs. B.18-B.20 can be further simplified and understood by drawing analogies to other physical systems. In a specific condition where the available spin interaction energy $|c_2|\, n$ is less than that required to create spatial spin structures in the condensates, or the spin healing length scale $\xi_s = h/\sqrt{2m\,|c_2|\, n}$ is larger than the size of the condensate, I can separate the spatial dynamics and the internal spinor dynamics. This is known as the single-mode approximation (SMA) [26, 27]. Separation of variables for the spinor wave functions lead to

$$\Psi(\mathbf{r},t) = \begin{pmatrix} \psi_1(\mathbf{r},t) \\ \psi_0(\mathbf{r},t) \\ \psi_{-1}(\mathbf{r},t) \end{pmatrix} = \sqrt{N}\phi\left(\mathbf{r}\right) \mathrm{e}^{-\mathrm{i}\mu t/\hbar} \begin{pmatrix} \chi_1(t) \\ \chi_0(t) \\ \chi_{-1}(t) \end{pmatrix}, \tag{B.23}$$

where N is the total number of atoms, $\phi\left(\mathbf{r}\right)$ is the common spatial mode function, and $\chi_\alpha\left(t\right)$ are the position-independent spinor wavefunctions with the normalization $\sum_\alpha \left|\chi_\alpha\left(t\right)\right|^2 = 1$. The spatial mode function $\phi\left(\mathbf{r}\right)$ describes the normalized atomic density distribution $\left|\phi\left(\mathbf{r}\right)\right|^2 = n\left(\mathbf{r}\right)$ and it satisfies the normalization condition $\int \mathrm{d}^3\mathbf{r}\ n\left(\mathbf{r}\right) = 1$. The chemical potential μ is determined by the stationary spin-independent GPE for the spatial mode

$$\mu\phi\left(\mathbf{r}\right) = \left[-\frac{\hbar^2}{2m}\nabla^2 + V_{\mathrm{ext}} + c_0 n\left(\mathbf{r}\right)\right]\phi\left(\mathbf{r}\right). \tag{B.24}$$

In the SMA, the coupled spinor equations become

$$\mathrm{i}\hbar\partial_t\chi_1 = E_1\chi_1 + c\left[\left(\rho_1+\rho_0-\rho_{-1}\right)\chi_1 + \chi_0^2\chi_{-1}^*\right], \tag{B.25}$$

$$\mathrm{i}\hbar\partial_t\chi_0 = E_0\chi_0 + c\left[\left(\rho_1+\rho_{-1}\right)\chi_0 + 2\chi_1\chi_{-1}\chi_0^*\right], \tag{B.26}$$

$$\mathrm{i}\hbar\partial_t\chi_{-1} = E_{-1}\chi_{-1} + c\left[\left(\rho_{-1}+\rho_0-\rho_1\right)\chi_{-1} + \chi_0^2\chi_1^*\right], \tag{B.27}$$

where $c = c_2 N \int \mathrm{d}^3\mathbf{r}\, n(\mathbf{r})^2$ is the integrated spin mean-field coefficient and $\rho_\alpha = |\chi_\alpha|^2$ is the spin fractional population. In above, I have included energy shifts from the Zeeman hyperfine structure, where I parameterize the linear and quadratic Zeeman effects respectively as $\eta = (E_{-1} - E_1)/2$ and $\delta = (E_{-1} + E_1 - 2E_0)/2$. Besides the total number of atoms $\sum_\alpha \rho_\alpha = 1$ is conserved, the equations of motion within the SMA also guarantee the magnetization $M = \rho_1 - \rho_{-1}$ to stay conserved.

In above, I have discussed the dynamics of spinor Bose condensates in the magnetic hyperfine structure where atomic interactions are governed by the two-body collisions. This treatment can be extended to other engineered physical systems, i.e. the so-called "spin" states are realized in the optical lattice or double-well potential, and the interactions can be tuned accordingly via laser-assisted tunneling [96].

APPENDIX C

Machine drawing of camera mounts

In Bragg signal detection, I used an `iXon Ultra 888` electron-multiplying charge-coupled device (EMCCD) camera from Andor Technology. I designed custom-made plates for mounting purpose and extra drift stability, which inspired by Fig. 3 in Ref. [20]. The camera was mounted on two translation stages, as displayed in Fig. C.1. Machine drawings of the mounting plates are shown in Figs. C.2-C.3.

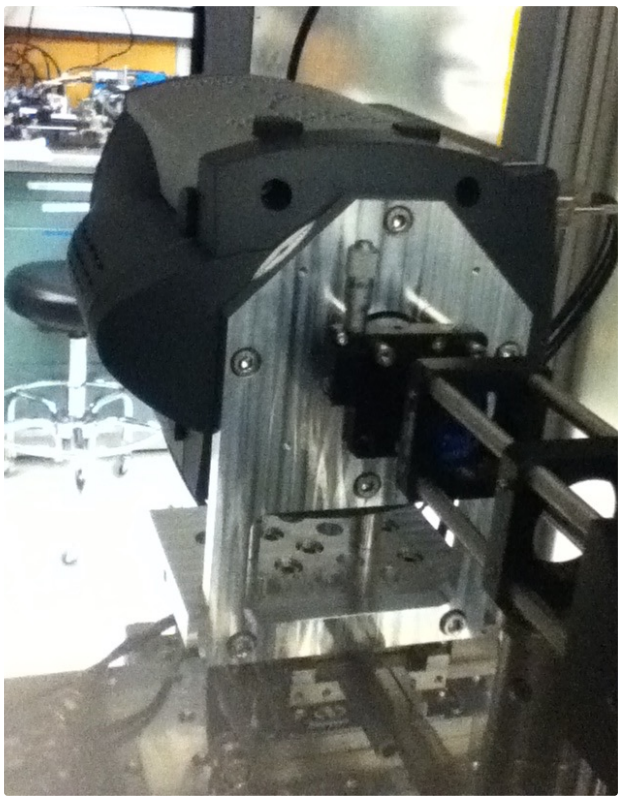

FIGURE C.1. Andor EMCCD camera (`iXon Ultra 888`) mounted on translational stages with custom-made plates.

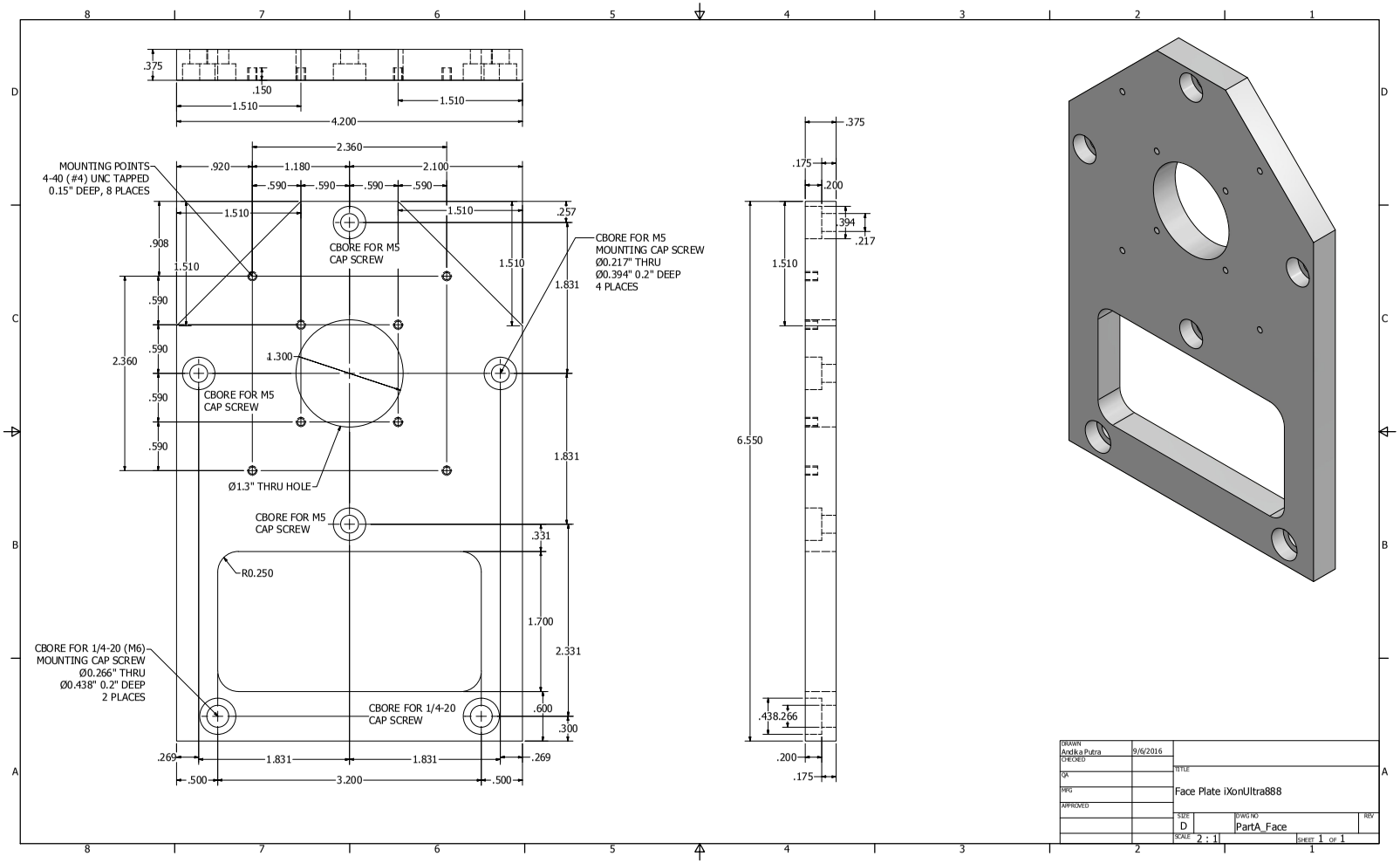

FIGURE C.2. Machine drawing (not to scale) of the front mounting plate for `iXon Ultra 888`.

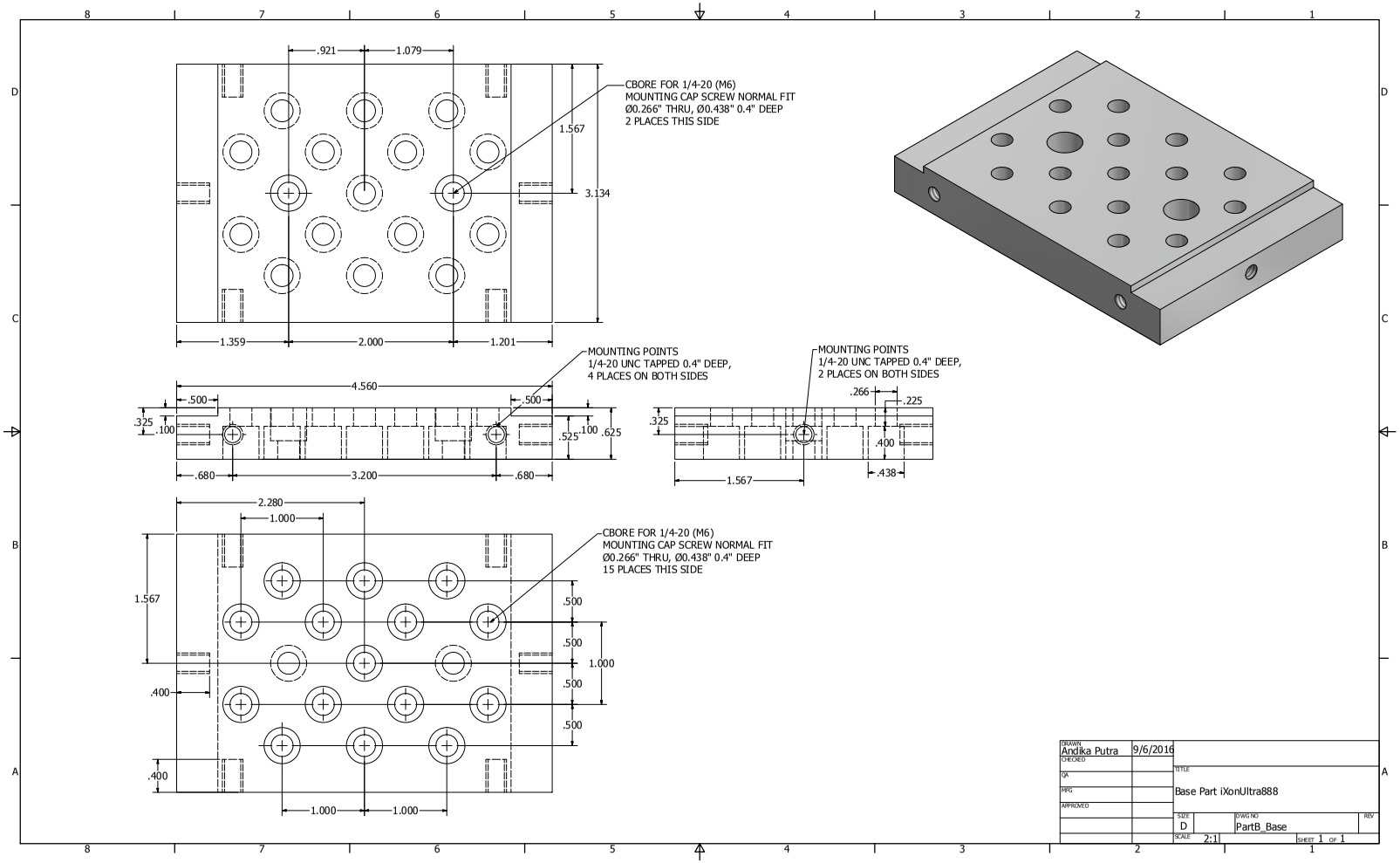

FIGURE C.3. Machine drawing (not to scale) of the base mounting plate for `iXon Ultra 888`.

APPENDIX D

Floquet theory for periodic time-dependent Hamiltonian

In this appendix, I discuss the Floquet formalism to treat a time-periodic Hamiltonian [32, 60]. I am interested in a Hamiltonian with time periodicity T satisfying the relation

$$\hat{H}(\mathbf{r},t) = \hat{H}(\mathbf{r},t+T), \tag{D.1}$$

where the driving frequency of the system is defined by $\omega = 2\pi/T$. Similar to the application of Bloch's theorem in a spatially periodic Hamiltonian, the application of Floquet theory to the time-dependent Schrödinger equation

$$\hat{H}(\mathbf{r},t)\psi(\mathbf{r},t) = \mathrm{i}\hbar\frac{\partial}{\partial t}\psi(\mathbf{r},t), \tag{D.2}$$

gives solutions of the form

$$\psi_\alpha(\mathbf{r},t) = \exp\left(-\mathrm{i}\epsilon_\alpha t/\hbar\right)\phi_\alpha(\mathbf{r},t), \quad \text{where } \phi_\alpha(\mathbf{r},t+T) = \phi_\alpha(\mathbf{r},t). \tag{D.3}$$

This leads to the concept of quasi-energy ϵ_α which is a real parameter and is unique within energy band $\hbar\omega$ (identical to the Brillouin zone in the Bloch's theorem).

The eigenvalues of the quasi-energy is determined by the Hermitian operator $\hat{\mathcal{H}}(t)$

$$\hat{\mathcal{H}}(\mathbf{r},t)\,\phi_\alpha(\mathbf{r},t) = \left[\hat{H}(\mathbf{r},t) - \mathrm{i}\hbar\frac{\partial}{\partial t}\right]\phi_\alpha(\mathbf{r},t) = \epsilon_\alpha\phi_\alpha(\mathbf{r},t), \tag{D.4}$$

where the choice of the eigenvalues and eigenvectors are non-unique. Specifically, the Floquet modes

$$\phi_{\alpha'}(\mathbf{r},t) = \exp\left(\mathrm{i}m\omega t\right)\phi_{\alpha}(\mathbf{r},t), \qquad m \in \text{integers}, \tag{D.5}$$

are also solutions to the eigenvalue problem in Eq. D.4 with shifted quasi-energy

$$\epsilon_{\alpha'} = \epsilon_{\alpha} + m\hbar\omega. \tag{D.6}$$

Consequently, I obtain a whole class of solutions indexed by $\alpha' = (\alpha, m)$ with $m \in \mathbb{Z}$, and the eigenvalues $\{\epsilon_\alpha\}$ can be mapped into the first Brillouin zone defined by $-\hbar\omega/2 \leq \epsilon_\alpha < \hbar\omega/2$.

It is then convenient to extend the initial Hilbert space $\mathcal{R}$ of square integrable functions to the composite Hilbert space $\mathcal{R} \otimes \mathcal{T}$, where I include the Fourier space $\mathcal{T}$of the time-periodic functions with period T describing the "band" index m. In the initial Hilbert space $\mathcal{R}$, the inner product of two square integrable functions $f(\mathbf{r})$ and $g(\mathbf{r})$ is defined by

$$\langle f|g\rangle := \int_{-\infty}^{\infty} \mathrm{d}^3\mathbf{r}\ f^*(\mathbf{r})\, g(\mathbf{r}), \tag{D.7}$$

which form a complete set of orthonormal basis if the functions $\varphi_\alpha(\mathbf{r})$ and $\varphi_\beta(\mathbf{r})$ satisfy the relation

$$\langle \varphi_\beta(\mathbf{r}) | \varphi_\alpha(\mathbf{r})\rangle := \delta_{\alpha,\beta}. \tag{D.8}$$

Meanwhile, in the Fourier space $\mathcal{T}$, the temporal part is spanned by the orthonormal set of Fourier vectors $\langle t|m\rangle = \exp\left(\mathrm{i}m\omega t\right)$ which satisfy the inner product relation:

$$(n,m) = \frac{1}{T}\int_0^T \mathrm{d}t\ \exp\left[\mathrm{i}\left(m-n\right)\omega t\right] = \delta_{m,n}. \tag{D.9}$$

In the extended Hilbert space, the eigenvectors of the operator $\hat{\mathcal{H}}(t)$ with indices $\alpha' = (\alpha, m)$ and $\beta' = (\beta, n)$ obey the orthonormality condition

$$\left\langle \langle \phi_{\alpha'} | \phi_{\beta'} \rangle_{\mathcal{R}} \right\rangle_{\mathcal{T}} := \frac{1}{T} \int_0^T \mathrm{d}t \int_{-\infty}^{\infty} \mathrm{d}^3\mathbf{r}\ \phi^*_{\alpha'}(\mathbf{r}, t)\ \phi^*_{\beta'}(\mathbf{r}, t) = \delta_{\alpha',\beta'} = \delta_{\alpha,\beta}\delta_{m,n}, \tag{D.10}$$

and fulfill the completeness relation

$$\sum_{\alpha} \sum_{m} \phi^*_{\alpha m}(\mathbf{r}, t)\, \phi_{\alpha n}(\mathbf{r}', t') = \delta(\mathbf{r} - \mathbf{r}')\, \delta(t - t'). \tag{D.11}$$

Thus, the Floquet modes are mutually orthogonal for each instant of time and they form a complete orthonormal set.

I now consider a total Hamiltonian given by the form[1]

$$\hat{H}(\mathbf{r}, t) = \hat{H}_0(\mathbf{r}) + \hat{V}(\mathbf{r}, t), \tag{D.12}$$

where $\hat{V}(\mathbf{r}, t) = \hat{V}(\mathbf{r}, t + T)$ is the periodic perturbation with monochromatic frequency $\omega = 2\pi/T$ and the unperturbed Hamiltonian has a complete orthonormal set of eigenfunctions:

$$\hat{H}_0(\mathbf{r}) |\varphi_\alpha(\mathbf{r})\rangle = E^0_\alpha |\varphi_\alpha(\mathbf{r})\rangle, \tag{D.13}$$

with orthonormal relation satisfying Eq. D.8. I then expand the wavefunction as

$$\psi_\alpha(\mathbf{r}, t) = \exp(-\mathrm{i}\epsilon_\alpha t/\hbar)\, \phi_\alpha(\mathbf{r}, t) = \exp(-\mathrm{i}\epsilon_\alpha t/\hbar) \sum_{n=-\infty}^{\infty} \sum_{\alpha} c^n_\alpha |\varphi_\alpha(\mathbf{r})\rangle\, \mathrm{e}^{-\mathrm{i}n\omega t}, \tag{D.14}$$

where the expansion coefficients c^n_α are time-independent. Here I have two indices on the $c^n_\alpha-$coefficients:

(1) α from the initial Hamiltonian $\hat{H}_0(\mathbf{r})$ which sets the Hilbert space $\mathcal{R}$, and

[1]Without losing any generality, I define our time $t = 0$ when the overall Hamiltonian is described by $\hat{H}_0(\mathbf{r})$ and its eigenvectors set the completeness relation in the initial Hilbert space $\mathcal{R}$.

(2) n from the Fourier expansion of the time-periodic perturbation $\hat{V}(\mathbf{r},t)$.

To solve for the quasi-energies of the periodic Hamiltonian, I use the matrix (linear algebra) approach. Insertion of the expanded wavefunction in Eq. D.14 into the Schrödinger equation in Eq. D.2 gives

$$\sum_{n=-\infty}^{\infty}\sum_{\alpha}\left[\hat{H}(t)-\epsilon_\alpha-n\hbar\omega\right]c_\alpha^n\left|\varphi_\alpha(\mathbf{r})\right\rangle \mathrm{e}^{-\mathrm{i}n\omega t}=0. \tag{D.15}$$

Next, I multiply Eq. D.15 by $\langle\varphi_\beta(\mathbf{r})|\,\mathrm{e}^{\mathrm{i}m\omega t}$ and integrate over $(1/T)\int_0^T \mathrm{d}t$ to obtain:

$$\sum_{n=-\infty}^{\infty}\sum_{\alpha}\left[\langle\varphi_\beta|\frac{1}{T}\int_0^T \mathrm{d}t\;\hat{H}(t)\mathrm{e}^{\mathrm{i}(m-n)\omega t}\left|\varphi_\alpha\right\rangle-(\epsilon_\alpha+n\hbar\omega)\,\delta_{mn}\delta_{\alpha\beta}\right]c_\alpha^n=0, \tag{D.16}$$

$$\sum_{n=-\infty}^{\infty}\sum_{\alpha}\left[\left(E_\alpha^0-n\hbar\omega\right)\delta_{\alpha\beta}\delta_{mn}+\langle\varphi_\beta|\frac{1}{T}\int_0^T \mathrm{d}t\;\hat{W}(t)\mathrm{e}^{\mathrm{i}(m-n)\omega t}\left|\varphi_\alpha\right\rangle\right]c_\alpha^n=\epsilon_\beta c_\beta^m. \tag{D.17}$$

The above form in Eq. D.17 gives the explicit matrix elements for the eigenvalue problem to find the quasi-energies.

For a perturbation with harmonic time dependence, i.e. $\hat{W}(t)=\hat{W}_0\cos(\omega t)$, the only surviving indices in the integral term of Eq. D.17 are $(m-n)=\pm1$. The eigenvalue problem in Eq. D.17 accordingly can be written in the matrix form as:

$$\begin{array}{c} \vdots \\ m=-1 \\ m=0 \\ m=1 \\ \vdots \end{array}\begin{bmatrix} \ddots & & \vdots & & \iddots \\ & \mathbf{E_0}+\hbar\omega\mathbf{I} & \mathbf{W} & 0 & \\ \cdots & \mathbf{W} & \mathbf{E_0} & \mathbf{W} & \cdots \\ & 0 & \mathbf{W} & \mathbf{E_0}-\hbar\omega\mathbf{I} & \\ \iddots & & \vdots & & \ddots \end{bmatrix}\mathbf{\Phi}_\alpha=\epsilon_\alpha\mathbf{\Phi}_\alpha, \tag{D.18}$$

$$\cdots \quad n=-1 \quad n=0 \quad n=1 \quad \cdots$$

where I have defined the eigenvectors as $\mathbf{\Phi}_\alpha = (\ldots, c_\alpha^{-2}, c_\alpha^{-1}, c_\alpha^0, c_\alpha^1 \ldots)^T$. The diagonal matrix $\mathbf{E_0}$ represents the eigenvalues of the unperturbed Hamiltonian and $\mathbf{W}$ represents the off-diagonal coupling with its matrix elements is given by $\langle\varphi_\beta|\hat{W}_0|\varphi_\alpha\rangle/2$.

Finally, I give an example of Floquet formalism to calculate the quasi-energies of a time-periodic Hamiltonian. Here I consider our engineered Hamiltonian to realize a spin-1 spin-orbit coupling system (see Subsection 5.4.3). The Hamiltonian operator of our system after rotating-wave approximation consists of the terms

$$\hat{H}_0 \to \mathbf{E_0} = \hbar^2 \begin{bmatrix} \frac{(q-2k_R)^2}{2m} + \frac{\epsilon_{\text{quad}}}{\hbar} & 0 & 0 \\ 0 & \frac{q^2}{2m} & 0 \\ 0 & 0 & \frac{(q+2k_R)^2}{2m} + \frac{\epsilon_{\text{quad}}}{\hbar} \end{bmatrix}, \quad \text{(D.19)}$$

$$\hat{W}(t) \to \mathbf{W} = \frac{1}{\sqrt{2}} \begin{bmatrix} 0 & \Omega_1 & 0 \\ \Omega_1 & 0 & \Omega_1 \\ 0 & \Omega_1 & 0 \end{bmatrix}, \quad \text{(D.20)}$$

where m is the atomic mass, k_R is the single-photon recoil momentum, q is the quasi-momentum space, ϵ_{quad} is the Zeeman quadratic shift, and Ω_1 is the Raman coupling strength. Substitution of Eqs. D.19-D.20 into Eq. D.18 gives me the explicit form of the eigenvalue problem to be solved. I then solve the quasi-energies of the spin-orbit-coupled (SOC) Hamiltonian $\epsilon(q)$ as a function of q.

Figure D.1 displays the quasi-energy dispersion relation $\epsilon(q)$ of the spin-1 SOC Bose gases, where I set the energy scale in the units of $E_R = \hbar k_R^2/2m$. The frequency of the time-periodic perturbation is equal to the quadratic Zeeman shift, i.e $\hbar\omega = 12.7E_R$, in our system. Here I consider the case where the coupling strength is $\Omega_1 = E_R$. I observe the band diagram to be repeating itself in each Brillouin zone with a period of $\hbar\omega$, as bounded by the shaded region in Fig. D.1.

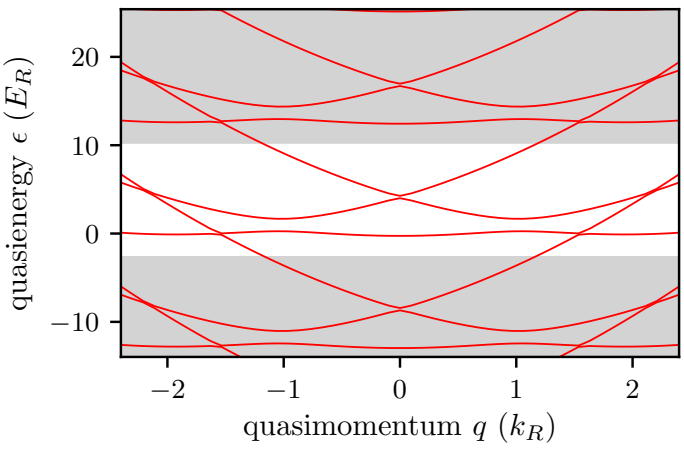

FIGURE D.1. Quasi-energy dispersion relation $\epsilon(q)$ of spin-1 SOC Hamiltonian with coupling strength $\Omega_1 = E_R$ and periodic driving $\hbar\omega = 12.7E_R$.

Bibliography

[1] Abragam, A., "Nuclear ferromagnetism and ant ferromagnetism," *Contemporary Physics*, vol. 33, no. 5, pp. 305–312, 1992.

[2] Adhikari, S. K., "Expansion of a Bose-Einstein condensate formed on a joint harmonic and one-dimensional optical-lattice potential," *Journal of Physics B: Atomic, Molecular and Optical Physics*, vol. 36, no. 19, p. 3951, 2003.

[3] Aharoni, A., *Introduction to the Theory of Ferromagnetism*. International Series of Monographs on Physics, Oxford University Press, 2001.

[4] Aidelsburger, M., Atala, M., Nascimbène, S., Trotzky, S., Chen, Y.-A., and Bloch, I., "Experimental realization of strong effective magnetic fields in an optical lattice," *Phys. Rev. Lett.*, vol. 107, p. 255301, Dec 2011.

[5] Aidelsburger, M., *Artificial gauge fields with ultracold atoms in optical lattices*. PhD thesis, Ludwig-Maximilians-Universität München, München, 2015.

[6] Anderson, B. M., Spielman, I. B., and Juzeliūnas, G., "Magnetically generated spin-orbit coupling for ultracold atoms," *Phys. Rev. Lett.*, vol. 111, p. 125301, Sep 2013.

[7] Anderson, M. H., Ensher, J. R., Matthews, M. R., Wieman, C. E., and Cornell, E. A., "Observation of Bose-Einstein condensation in a dilute atomic vapor," *Science*, vol. 269, no. 5221, pp. 198–201, 1995.

[8] Arimondo, E., Inguscio, M., and Violino, P., "Experimental determinations of the hyperfine structure in the alkali atoms," *Rev. Mod. Phys.*, vol. 49, pp. 31–75, Jan 1977.

[9] Arora, B., Safronova, M. S., and Clark, C. W., "Tune-out wavelengths of alkali-metal atoms and their applications," *Phys. Rev. A*, vol. 84, p. 043401, Oct 2011.

[10] Ashcroft, N. and Mermin, N., *Solid State Physics*. Cengage Learning, 2011.

[11] Atala, M., Aidelsburger, M., Lohse, M., Barreiro, J. T., Paredes, B., and Bloch, I., "Observation of chiral currents with ultracold atoms in bosonic ladders," *Nat Phys*, vol. 10, pp. 588–593, 08 2014.

[12] Auzinsh, M., Budker, D., and Rochester, S. M., *Optically Polarized Atoms: Understanding Light-Atom Interactions*. Oxford University Press, 2010.

[13] Bakr, W. S., Peng, A., Tai, M. E., Ma, R., Simon, J., Gillen, J. I., Fölling, S., Pollet, L., and Greiner, M., "Probing the superfluid–to–Mott insulator transition at the single-atom level," *Science*, vol. 329, no. 5991, pp. 547–550, 2010.

[14] Bao, W., Jaksch, D., and Markowich, P. A., "Numerical solution of the Gross–Pitaevskii equation for Bose-Einstein condensation," *Journal of Computational Physics*, vol. 187, no. 1, pp. 318 – 342, 2003.

[15] Bao, W. and Wang, H., "A mass and magnetization conservative and energy-diminishing numerical method for computing ground state of spin-1 Bose-Einstein condensates," *SIAM Journal on Numerical Analysis*, vol. 45, no. 5, pp. 2177–2200, 2007.

[16] Barnett, R., Turner, A., and Demler, E., "Classifying novel phases of spinor atoms," *Phys. Rev. Lett.*, vol. 97, p. 180412, Nov 2006.

[17] Birkl, G., Gatzke, M., Deutsch, I. H., Rolston, S. L., and Phillips, W. D., "Bragg scattering from atoms in optical lattices," *Phys. Rev. Lett.*, vol. 75, pp. 2823–2826, Oct 1995.

[18] Blakie, P., Bradley, A., Davis, M., Ballagh, R., and Gardiner, C., "Dynamics and statistical mechanics of ultra-cold Bose gases using c-field techniques," *Advances in Physics*, vol. 57, no. 5, pp. 363–455, 2008.

[19] Bransden, B. H. and Joachain, C. J., *Many-electron atoms*, ch. 7, pp. 290–351. Physics of Atoms and Molecules, Longman Group, 1990.

[20] Brian P. English, R. H. S., "A three-camera imaging microscope for high-speed single-molecule tracking and super-resolution imaging in living cells," in *Biosensing and Nanomedicine VIII* (Inguscio, M., Stringari, S., and Wieman, C., eds.), vol. 9550, p. 955008, SPIE, 2015.

[21] Burt, E. A., Ghrist, R. W., Myatt, C. J., Holland, M. J., Cornell,

E. A., and Wieman, C. E., "Coherence, correlations, and collisions: what one learns about Bose-Einstein condensates from their decay," *Phys. Rev. Lett.*, vol. 79, pp. 337–340, Jul 1997.

[22] Campbell, D. L., Price, R. M., Putra, A., Valdés-Curiel, A., Trypogeorgos, D., and Spielman, I. B., "Magnetic phases of spin-1 spin–orbit-coupled Bose gases," *Nature Communications*, vol. 7, p. 10897, 03 2016.

[23] Castin, Y. and Dum, R., "Bose-Einstein condensates in time dependent traps," *Phys. Rev. Lett.*, vol. 77, pp. 5315–5319, Dec 1996.

[24] Castin, Y., Wallis, H., and Dalibard, J., "Limit of Doppler cooling," *J. Opt. Soc. Am. B*, vol. 6, pp. 2046–2057, Nov 1989.

[25] Castin, Y. and Mølmer, K., "Maxwell-Bloch equations: a unified view of nonlinear optics and nonlinear atom optics," *Phys. Rev. A*, vol. 51, pp. R3426–R3428, May 1995.

[26] Chang, M.-S., *Coherent Spin Dynamics of a Spin-1 Bose-Einstein Condensate*. Doctoral thesis, Georgia Institute of Technology, 2006.

[27] Chang, M.-S., Qin, Q., Zhang, W., You, L., and Chapman, M. S., "Coherent spinor dynamics in a spin-1 Bose condensate," *Nat Phys*, vol. 1, pp. 111–116, 11 2005.

[28] Chen, X.-L., Liu, X.-J., and Hu, H., "Quantum and thermal fluctuations in a Raman spin-orbit-coupled Bose gas," *Phys. Rev. A*, vol. 96, p. 013625, Jul 2017.

[29] Cheuk, L. W., Sommer, A. T., Hadzibabic, Z., Yefsah, T., Bakr, W. S., and Zwierlein, M. W., "Spin-injection spectroscopy of a spin-orbit coupled Fermi gas," *Phys. Rev. Lett.*, vol. 109, p. 095302, Aug 2012.

[30] Choi, J.-y., Seo, S. W., Kwon, W. J., and Shin, Y.-i., "Probing phase fluctuations in a 2D degenerate Bose gas by free expansion," *Phys. Rev. Lett.*, vol. 109, p. 125301, Sep 2012.

[31] Chomaz, L., van Bijnen, R. M. W., Petter, D., Faraoni, G., Baier, S., Hendrik Becher, J., Mark, M. J., Waechtler, F., Santos, L., and Ferlaino, F., "Observation of the roton mode in a dipolar quantum gas," *ArXiv e-prints*, May 2017.

[32] Chu, S.-I., *Generalized Floquet Theoretical Approaches to Intense-Field Multiphoton and Nonlinear Optical Processes*, pp. 739–799. John Wiley & Sons, Inc., 2007.

[33] Cohen-Tannoudji, C., "Atomic motion in laser light," in *"Fundamental Systems in Quantum Optics", Les Houches, Session LIII, 1990* (Dalibard, J., Raimond, J., and Justin, J. Z., eds.), pp. 1–164, Elsevier Science Publisher BV, 1992.

[34] Cohen-Tannoudji, C., Diu, B., and Laloe, F., *Quantum Mechanics, Volume 2*, vol. 2. Wiley-VCH, June 1986.

[35] Cohen-Tannoudji, C., Dupont-Roc, J., and Grynberg, G., *Atom-Photon Interactions: Basic Processes and Applications*. Weinheim, Germany: Wiley-VCH Verlag GmbH, 1998.

[36] Dalfovo, F., Giorgini, S., Pitaevskii, L. P., and Stringari, S., "Theory of Bose-Einstein condensation in trapped gases," *Rev. Mod. Phys.*, vol. 71, pp. 463–512, Apr 1999.

[37] Dalibard, J. and Cohen-Tannoudji, C., "Laser cooling below the Doppler limit by polarization gradients: simple theoretical models," *J. Opt. Soc. Am. B*, vol. 6, pp. 2023–2045, Nov 1989.

[38] Davis, K. B., Mewes, M. O., Andrews, M. R., van Druten, N. J., Durfee, D. S., Kurn, D. M., and Ketterle, W., "Bose-Einstein condensation in a gas of sodium atoms," *Phys. Rev. Lett.*, vol. 75, pp. 3969–3973, Nov 1995.

[39] Davis, K. B., Mewes, M.-O., Joffe, M. A., Andrews, M. R., and Ketterle, W., "Evaporative cooling of sodium atoms," *Phys. Rev. Lett.*, vol. 74, pp. 5202–5205, Jun 1995.

[40] De, S., Campbell, D. L., Price, R. M., Putra, A., Anderson, B. M., and Spielman, I. B., "Quenched binary Bose-Einstein condensates: spin-domain formation and coarsening," *Phys. Rev. A*, vol. 89, p. 033631, Mar 2014.

[41] Dedman, C. J., Nes, J., Hanna, T. M., Dall, R. G., Baldwin, K. G. H., and Truscott, A. G., "Optimum design and construction of a Zeeman slower for use with a magneto-optic trap," *Review of Scientific Instruments*, vol. 75, no. 12, pp. 5136–5142, 2004.

[42] Dettmer, S., Hellweg, D., Ryytty, P., Arlt, J. J., Ertmer, W., Sengstock, K., Petrov, D. S., Shlyapnikov, G. V., Kreutzmann, H., Santos, L., and Lewenstein, M., "Observation of phase fluctuations in elongated Bose-Einstein condensates," *Phys. Rev. Lett.*, vol. 87, p. 160406, Oct 2001.

[43] Donley, E. A., Heavner, T. P., Levi, F., Tataw, M. O., and Jefferts, S. R., "Double-pass acousto-optic modulator system," *Review of Scientific Instruments*, vol. 76, no. 6, p. 063112, 2005.

[44] Dresselhaus, G., "Spin-orbit coupling effects in zinc blende structures," *Phys. Rev.*, vol. 100, pp. 580–586, Oct 1955.

[45] Duarte-Gelvez, P. M., *Observation of antiferromagnetic correlations in the Fermi-Hubbard model*. PhD thesis, Rice University, Houston, TX, 2014.

[46] Feit, M. D. and Fleck, J. A., "Light propagation in graded-index optical fibers," *Appl. Opt.*, vol. 17, pp. 3990–3998, Dec 1978.

[47] Folling, S., Gerbier, F., Widera, A., Mandel, O., Gericke, T., and Bloch, I., "Spatial quantum noise interferometry in expanding ultracold atom clouds," *Nature*, vol. 434, pp. 481–484, 03 2005.

[48] Gadway, B., Pertot, D., Reimann, R., Cohen, M. G., and Schneble, D., "Analysis of Kapitza-Dirac diffraction patterns beyond the Raman-Nath regime," *Opt. Express*, vol. 17, pp. 19173–19180, Oct 2009.

[49] Galitski, V. and Spielman, I. B., "Spin-orbit coupling in quantum gases," *Nature*, vol. 494, pp. 49–54, 02 2013.

[50] Gerbier, F., Thywissen, J. H., Richard, S., Hugbart, M., Bouyer, P., and Aspect, A., "Experimental study of the thermodynamics of an interacting trapped Bose-Einstein condensed gas," *Phys. Rev. A*, vol. 70, p. 013607, Jul 2004.

[51] Gerlach, W. and Stern, O., "Der experimentelle nachweis des magnetischen moments des silberatoms," *Zeitschrift für Physik*, vol. 8, pp. 110–111, Dec 1922.

[52] Glauber, R. J., *The Quantum Theory of Optical Coherence*. Weinheim: Wiley-VCH Verlag GmbH & Co. KGaA, 2007.

[53] Goldman, N., Juzeliūnas, G., Öhberg, P., and Spielman, I. B., "Light-induced gauge fields for ultracold atoms," *Reports on Progress in Physics*, vol. 77, no. 12, p. 126401, 2014.

[54] Gordon, J. P. and Ashkin, A., "Motion of atoms in a radiation trap," *Phys. Rev. A*, vol. 21, pp. 1606–1617, May 1980.

[55] Gould, P. L., Ruff, G. A., and Pritchard, D. E., "Diffraction of atoms by light: the near-resonant Kapitza-Dirac effect," *Phys. Rev. Lett.*, vol. 56, pp. 827–830, Feb 1986.

[56] Granade, S. R., Gehm, M. E., O'Hara, K. M., and Thomas, J. E., "All-optical production of a degenerate Fermi gas," *Phys. Rev. Lett.*, vol. 88, p. 120405, Mar 2002.

[57] Greif, D., Uehlinger, T., Jotzu, G., Tarruell, L., and Esslinger, T., "Short-range quantum magnetism of ultracold fermions in an optical lattice," *Science*, vol. 340, no. 6138, pp. 1307–1310, 2013.

[58] Greiner, M., Mandel, O., Esslinger, T., Hansch, T. W., and Bloch, I., "Quantum phase transition from a superfluid to a Mott insulator in a gas of ultracold atoms," *Nature*, vol. 415, pp. 39–44, 01 2002.

[59] Griffin, A., Snoke, D. W., and Stringari, S., *Bose-Einstein Condensation*. Cambridge University Press, 1996.

[60] Grifoni, M. and Hänggi, P., "Driven quantum tunneling," *Physics Reports*, vol. 304, no. 5, pp. 229 – 354, 1998.

[61] Grimm, R., Weidemüller, M., and Ovchinnikov, Y. B., "Optical dipole traps for neutral atoms," *Advances In Atomic, Molecular, and Optical Physics*, vol. 42, pp. 95 – 170, 2000.

[62] Ha, L.-C., Clark, L. W., Parker, C. V., Anderson, B. M., and Chin, C., "Roton-maxon excitation spectrum of Bose condensates in a shaken optical lattice," *Phys. Rev. Lett.*, vol. 114, p. 055301, Feb 2015.

[63] Hall, D. S., Matthews, M. R., Ensher, J. R., Wieman, C. E., and Cornell, E. A., "Dynamics of component separation in a binary mixture of Bose-Einstein condensates," *Phys. Rev. Lett.*, vol. 81, pp. 1539–1542, Aug 1998.

[64] Happer, W. and Mathur, B. S., "Effective operator formalism in optical pumping," *Phys. Rev.*, vol. 163, pp. 12–25, Nov 1967.

[65] Hart, R. A., Duarte, P. M., Yang, T.-L., Liu, X., Paiva, T., Khatami, E., Scalettar, R. T., Trivedi, N., Huse, D. A., and Hulet, R. G., "Observation of antiferromagnetic correlations in the Hubbard model with ultracold atoms," *Nature*, vol. 519, pp. 211–214, 03 2015.

[66] Hickey, C. and Paramekanti, A., "Thermal phase transitions of strongly correlated bosons with spin-orbit coupling," *Phys. Rev. Lett.*, vol. 113, p. 265302, Dec 2014.

[67] Higbie, J. and Stamper-Kurn, D. M., "Periodically dressed Bose-Einstein condensate: a superfluid with an anisotropic and variable critical velocity," *Phys. Rev. Lett.*, vol. 88, p. 090401, Feb 2002.

[68] Ho, T.-L., "Spinor Bose condensates in optical traps," *Phys. Rev. Lett.*, vol. 81, pp. 742–745, Jul 1998.

[69] Ho, T.-L. and Zhang, S., "Bose-Einstein condensates with spin-orbit interaction," *Phys. Rev. Lett.*, vol. 107, p. 150403, Oct 2011.

[70] Hoefer, M. A., Chang, J. J., Hamner, C., and Engels, P., "Dark-dark solitons and modulational instability in miscible two-component Bose-Einstein condensates," *Phys. Rev. A*, vol. 84, p. 041605, Oct 2011.

[71] Horowitz, P. and Hill, W., *The Art of Electronics*. New York, NY, USA: Cambridge University Press, 1989.

[72] Huckans, J. H., Spielman, I. B., Tolra, B. L., Phillips, W. D., and Porto, J. V., "Quantum and classical dynamics of a Bose-Einstein condensate in a large-period optical lattice," *Phys. Rev. A*, vol. 80, p. 043609, Oct 2009.

[73] Hung, C.-L., Zhang, X., Ha, L.-C., Tung, S.-K., Gemelke, N., and Chin, C., "Extracting density–density correlations from in situ images of atomic quantum gases," *New Journal of Physics*, vol. 13, no. 7, p. 075019, 2011.

[74] Inoue, S. and Oldenbourg, R., *Optical instruments. Microscopes.*, vol. 2 of *Handbook of Optics*, ch. 17, pp. 17.1–17.52. McGraw-Hill, 2 ed., 1995.

[75] Ising, E., "Beitrag zur theorie des ferromagnetismus," *Zeitschrift für Physik*,

vol. 31, pp. 253–258, Feb 1925.

[76] J. A. Fleck, J., "Solution of the scalar Helmholtz wave equation by Lanczos reduction," *Progress in Electromagnetics Research*, vol. 11, pp. 103–141, 1995.

[77] Jaksch, D., Bruder, C., Cirac, J. I., Gardiner, C. W., and Zoller, P., "Cold bosonic atoms in optical lattices," *Phys. Rev. Lett.*, vol. 81, pp. 3108–3111, Oct 1998.

[78] Ji, S.-C., Zhang, J.-Y., Zhang, L., Du, Z.-D., Zheng, W., Deng, Y.-J., Zhai, H., Chen, S., and Pan, J.-W., "Experimental determination of the finite-temperature phase diagram of a spin-orbit coupled Bose gas," *Nature Physics*, vol. 10, pp. 314–320, 04 2014.

[79] Ji, S.-C., Zhang, L., Xu, X.-T., Wu, Z., Deng, Y., Chen, S., and Pan, J.-W., "Softening of roton and phonon modes in a Bose-Einstein condensate with spin-orbit coupling," *Phys. Rev. Lett.*, vol. 114, p. 105301, Mar 2015.

[80] Juzeliūnas, G. and Spielman, I. B., "Flux lattices reformulated," *New Journal of Physics*, vol. 14, no. 12, p. 123022, 2012.

[81] Ketterle, W., Durfee, D. S., and Stamper-Kurn, D. M., "Making, probing and understanding Bose-Einstein condensates," in *Proceedings of the International School of Physics "Enrico Fermi", Course CXL* (Inguscio, M., Stringari, S., and Wieman, C., eds.), (Amsterdam), p. 67, IOS Press, 1999.

[82] Ketterle, W. and Inouye, S., "Collective enhancement and suppression in dilute Bose-Einstein condensates," *eprint arXiv:cond-mat/0101424*, Jan. 2001.

[83] Ketterle, W. and Druten, N. V., "Evaporative cooling of trapped atoms," *Advances In Atomic, Molecular, and Optical Physics*, vol. 37, pp. 181 – 236, 1996.

[84] Kibble, T. W. B., "Topology of cosmic domains and strings," *Journal of Physics A: Mathematical and General*, vol. 9, no. 8, p. 1387, 1976.

[85] Klempt, C., van Zoest, T., Henninger, T., Topic, O., Rasel, E., Ertmer, W., and Arlt, J., "Ultraviolet light-induced atom desorption for large rubidium and potassium magneto-optical traps," *Phys. Rev. A*, vol. 73, p. 013410, Jan 2006.

[86] Koralek, J. D., Weber, C. P., Orenstein, J., Bernevig, B. A., Zhang, S.-C., Mack, S., and Awschalom, D. D., "Emergence of the persistent spin helix in semiconductor quantum wells," *Nature*, vol. 458, pp. 610–613, 04 2009.

[87] Korpel, A., Lonngren, K. E., Banerjee, P. P., Sim, H. K., and Chatterjee, M. R., "Split-step-type angular plane-wave spectrum method for the study of self-refractive effects in nonlinear wave propagation," *J. Opt. Soc. Am. B*, vol. 3, pp. 885–890, Jun 1986.

[88] Krämer, M., Menotti, C., Pitaevskii, L., and Stringari, S., "Bose-Einstein condensates in 1D optical lattices," *The European Physical Journal D - Atomic, Molecular, Optical and Plasma Physics*, vol. 27, no. 3, pp. 247–261, 2003.

[89] Kronjäger, J., Becker, C., Soltan-Panahi, P., Bongs, K., and Sengstock, K., "Spontaneous pattern formation in an antiferromagnetic quantum gas," *Phys. Rev. Lett.*, vol. 105, p. 090402, Aug 2010.

[90] Lan, Z. and Öhberg, P., "Raman-dressed spin-1 spin-orbit-coupled quantum gas," *Phys. Rev. A*, vol. 89, p. 023630, Feb 2014.

[91] Langen, T., Geiger, R., Kuhnert, M., Rauer, B., and Schmiedmayer, J., "Local emergence of thermal correlations in an isolated quantum many-body system," *Nature Physics*, vol. 9, pp. 640 EP –, 09 2013.

[92] Langen, T., "Comment on 'probing phase fluctuations in a 2D degenerate Bose gas by free expansion'," *Phys. Rev. Lett.*, vol. 111, p. 159601, Oct 2013.

[93] LeBlanc, L. J., Jiménez-García, K., Williams, R. A., Beeler, M. C., Phillips, W. D., and Spielman, I. B., "Gauge matters: observing the vortex-nucleation transition in a Bose condensate," *New Journal of Physics*, vol. 17, no. 6, p. 065016, 2015.

[94] Léonard, J., Morales, A., Zupancic, P., Esslinger, T., and Donner, T., "Supersolid formation in a quantum gas breaking a continuous translational symmetry," *Nature*, vol. 543, pp. 87–90, 03 2017.

[95] Li, J.-R., Lee, J., Huang, W., Burchesky, S., Shteynas, B., Top, F. c.,

Jamison, A. O., and Ketterle, W., "A stripe phase with supersolid properties in spin–orbit-coupled Bose-Einstein condensates," *Nature*, vol. 543, pp. 91–94, 03 2017.

[96] Li, J., Huang, W., Shteynas, B., Burchesky, S., Top, F. i. m. c. b. u. i. e. i. f., Su, E., Lee, J., Jamison, A. O., and Ketterle, W., "Spin-orbit coupling and spin textures in optical superlattices," *Phys. Rev. Lett.*, vol. 117, p. 185301, Oct 2016.

[97] Li, Y., Martone, G. I., Pitaevskii, L. P., and Stringari, S., "Superstripes and the excitation spectrum of a spin-orbit-coupled Bose-Einstein condensate," *Phys. Rev. Lett.*, vol. 110, p. 235302, Jun 2013.

[98] Li, Y., Pitaevskii, L. P., and Stringari, S., "Quantum tricriticality and phase transitions in spin-orbit coupled Bose-Einstein condensates," *Phys. Rev. Lett.*, vol. 108, p. 225301, May 2012.

[99] Lieb, E. H., Seiringer, R., and Yngvason, J., "Bosons in a trap: a rigorous derivation of the Gross-Pitaevskii energy functional," *Phys. Rev. A*, vol. 61, p. 043602, Mar 2000.

[100] Lin, Y.-J., Compton, R. L., Jimenez-Garcia, K., Phillips, W. D., Porto, J. V., and Spielman, I. B., "A synthetic electric force acting on neutral atoms," *Nat Phys*, vol. 7, pp. 531–534, 07 2011.

[101] Lin, Y. J., Compton, R. L., Jimenez-Garcia, K., Porto, J. V., and Spielman, I. B., "Synthetic magnetic fields for ultracold neutral atoms," *Nature*, vol. 462, pp. 628–632, 12 2009.

[102] Lin, Y.-J., Compton, R. L., Perry, A. R., Phillips, W. D., Porto, J. V., and Spielman, I. B., "Bose-Einstein condensate in a uniform light-induced vector potential," *Phys. Rev. Lett.*, vol. 102, p. 130401, Mar 2009.

[103] Lin, Y. J., Jimenez-Garcia, K., and Spielman, I. B., "Spin-orbit-coupled Bose-Einstein condensates," *Nature*, vol. 471, pp. 83–86, 03 2011.

[104] Lin, Y.-J., Perry, A. R., Compton, R. L., Spielman, I. B., and Porto, J. V., "Rapid production of ^{87}Rb Bose-Einstein condensates in a combined magnetic and optical potential," *Phys. Rev. A*, vol. 79, p. 063631, Jun 2009.

[105] London, F., "The λ-phenomenon of liquid helium and the Bose-Einstein degeneracy," *Nature*, vol. 141, p. 643, 04 1938.

[106] Maguire, L. P., Szilagyi, S., and Scholten, R. E., "High performance laser shutter using a hard disk drive voice-coil actuator," *Review of Scientific Instruments*, vol. 75, no. 9, pp. 3077–3079, 2004.

[107] Martin, W. C. and Wiese, W. L., *Atomic Spectroscopy*, ch. 10, pp. 135–153. Atomic, Molecular, and Optical Physics Handbook, Woodbury, NY: AIP Press, 1996.

[108] Martone, G., *Static and dynamic properties of spin-orbit coupled Bose-Einstein condensates*. Doctoral thesis, University of Trento, 2014.

[109] Martone, G. I., Li, Y., Pitaevskii, L. P., and Stringari, S., "Anisotropic dynamics of a spin-orbit-coupled Bose-Einstein condensate," *Phys. Rev. A*, vol. 86, p. 063621, Dec 2012.

[110] McKay, D. and DeMarco, B., "Thermometry with spin-dependent lattices," *New Journal of Physics*, vol. 12, no. 5, p. 055013, 2010.

[111] McKay, D. C. and DeMarco, B., "Cooling in strongly correlated optical lattices: prospects and challenges," *Reports on Progress in Physics*, vol. 74, no. 5, p. 054401, 2011.

[112] McKay, D., *Quantum simulation in strongly correlated optical lattices*. PhD thesis, University of Illinois at Urbana-Champaign, 2013.

[113] McKay, D. C., Meldgin, C., Chen, D., and DeMarco, B., "Slow thermalization between a lattice and free Bose gas," *Phys. Rev. Lett.*, vol. 111, p. 063002, Aug 2013.

[114] Mertes, K. M., Merrill, J. W., Carretero-González, R., Frantzeskakis, D. J., Kevrekidis, P. G., and Hall, D. S., "Nonequilibrium dynamics and superfluid ring excitations in binary Bose-Einstein condensates," *Phys. Rev. Lett.*, vol. 99, p. 190402, Nov 2007.

[115] Metcalf, H. J. and van der Straten, P., "Laser cooling and trapping of atoms," *J. Opt. Soc. Am. B*, vol. 20, pp. 887–908, May 2003.

[116] Mewes, M.-O., Andrews, M. R., Kurn, D. M., Durfee, D. S.,

Townsend, C. G., and Ketterle, W., "Output coupler for Bose-Einstein condensed atoms," *Phys. Rev. Lett.*, vol. 78, pp. 582–585, Jan 1997.

[117] Mewes, M.-O., Andrews, M. R., van Druten, N. J., Kurn, D. M., Durfee, D. S., and Ketterle, W., "Bose-Einstein condensation in a tightly confining dc magnetic trap," *Phys. Rev. Lett.*, vol. 77, pp. 416–419, Jul 1996.

[118] Mewes, M.-O., Andrews, M. R., van Druten, N. J., Kurn, D. M., Durfee, D. S., Townsend, C. G., and Ketterle, W., "Collective excitations of a Bose-Einstein condensate in a magnetic trap," *Phys. Rev. Lett.*, vol. 77, pp. 988–991, Aug 1996.

[119] Milonni, P., "Semiclassical and quantum-electrodynamical approaches in nonrelativistic radiation theory," *Physics Reports*, vol. 25, no. 1, pp. 1 – 81, 1976.

[120] Miyake, H., Siviloglou, G. A., Puentes, G., Pritchard, D. E., Ketterle, W., and Weld, D. M., "Bragg scattering as a probe of atomic wave functions and quantum phase transitions in optical lattices," *Phys. Rev. Lett.*, vol. 107, p. 175302, Oct 2011.

[121] Mohr, P. J., Newell, D. B., and Taylor, B. N., "Codata recommended values of the fundamental physical constants: 2014," *Rev. Mod. Phys.*, vol. 88, p. 035009, Sep 2016.

[122] Morice, O., Castin, Y., and Dalibard, J., "Refractive index of a dilute Bose gas," *Phys. Rev. A*, vol. 51, pp. 3896–3901, May 1995.

[123] Mottl, R., Brennecke, F., Baumann, K., Landig, R., Donner, T., and Esslinger, T., "Roton-type mode softening in a quantum gas with cavity-mediated long-range interactions," *Science*, vol. 336, no. 6088, pp. 1570–1573, 2012.

[124] Müller, C. A., Miniatura, C., Wilkowski, D., Kaiser, R., and Delande, D., "Multiple scattering of photons by atomic hyperfine multiplets," *Phys. Rev. A*, vol. 72, p. 053405, Nov 2005.

[125] Natu, S. S., Li, X., and Cole, W. S., "Striped ferronematic ground states in a spin-orbit-coupled $S = 1$ Bose gas," *Phys. Rev. A*, vol. 91, p. 023608, Feb 2015.

[126] Novotny, L. and Hecht, B., *Principles of Nano-Optics*. Cambridge University Press, 2006.

[127] Ohmi, T. and Machida, K., "Bose-Einstein condensation with internal degrees of freedom in alkali atom gases," *Journal of the Physical Society of Japan*, vol. 67, no. 6, pp. 1822–1825, 1998.

[128] Parker, C. V., Ha, L.-C., and Chin, C., "Direct observation of effective ferromagnetic domains of cold atoms in a shaken optical lattice," *Nat Phys*, vol. 9, pp. 769–774, 12 2013.

[129] Pathria, R. and Beale, P. D., *Statistical Mechanics*. Boston: Academic Press, 3 ed., 2011.

[130] Perrin, H. and Garraway, B. M., "Chapter four - trapping atoms with radio frequency adiabatic potentials," vol. 66 of *Advances In Atomic, Molecular, and Optical Physics*, pp. 181 – 262, Academic Press, 2017.

[131] Perry, A. R., *An apparatus for light-less artificial gauge fields and new imaging techniques*. PhD thesis, University of Maryland, College Park, 2015.

[132] Pethick, C. and Smith, H., *Bose-Einstein condensation in dilute gases*. Cambridge University Press, 2002.

[133] Ph.D., E. C. S., "LXXX. Atomic moments in ferromagnetic metals and alloys with non-ferromagnetic elements," *The London, Edinburgh, and Dublin Philosophical Magazine and Journal of Science*, vol. 15, no. 101, pp. 1018–1034, 1933.

[134] Phillips, W. D., "Nobel lecture: laser cooling and trapping of neutral atoms," *Rev. Mod. Phys.*, vol. 70, pp. 721–741, Jul 1998.

[135] Pitaevskii, L. P. and Stringari, S., *Bose-Einstein condensation*. No. 116 in International Series of Monographs on Physics, Oxford University Press, 2003.

[136] Pomeau, Y. and Rica, S., "Dynamics of a model of supersolid," *Phys. Rev. Lett.*, vol. 72, pp. 2426–2429, Apr 1994.

[137] Preston, D. W., "Doppler-free saturated absorption: laser spectroscopy," *American Journal of Physics*, vol. 64, no. 11, pp. 1432–1436, 1996.

[138] Price, R. M., Trypogeorgos, D., Campbell, D. L., Putra, A., Valdés-Curiel, A., and Spielman, I. B., "Vortex nucleation in a Bose-Einstein condensate: from the inside out," *New Journal of Physics*, vol. 18, no. 11, p. 113009, 2016.

[139] Price, R. M., *Phase Transitions in Engineered Ultracold Quantum Systems*. PhD thesis, University of Maryland, College Park, 2015.

[140] Putra, A., Campbell, D. L., Price, R. M., De, S., and Spielman, I. B., "Optimally focused cold atom systems obtained using density-density correlations," *Review of Scientific Instruments*, vol. 85, no. 1, p. 013110, 2014.

[141] Radić, J., Natu, S. S., and Galitski, V., "Stoner ferromagnetism in a thermal pseudospin-1/2 Bose gas," *Phys. Rev. Lett.*, vol. 113, p. 185302, Oct 2014.

[142] Ramanathan, A., Muniz, S. R., Wright, K. C., Anderson, R. P., Phillips, W. D., Helmerson, K., and Campbell, G. K., "Partial-transfer absorption imaging: a versatile technique for optimal imaging of ultracold gases," *Review of Scientific Instruments*, vol. 83, no. 8, p. 083119, 2012.

[143] Ramsey, N., *Molecular Beams*. Oxford University Press, 1956.

[144] Rashba, E. I., "Properties of semiconductors with an extremum loop. I. Cyclotron and combinational resonance in a magnetic field perpendicular to the plane of the loop," *Sov. Phys. Solid State*, vol. 2, p. 1109, 1960.

[145] Regal, C. A., Greiner, M., and Jin, D. S., "Observation of resonance condensation of fermionic atom pairs," *Phys. Rev. Lett.*, vol. 92, p. 040403, Jan 2004.

[146] Regal, C. A., Ticknor, C., Bohn, J. L., and Jin, D. S., "Creation of ultracold molecules from a Fermi gas of atoms," *Nature*, vol. 424, pp. 47–50, 07 2003.

[147] Reinaudi, G., Lahaye, T., Wang, Z., and Guéry-Odelin, D., "Strong saturation absorption imaging of dense clouds of ultracold atoms," *Opt. Lett.*, vol. 32, pp. 3143–3145, Nov 2007.

[148] Sadler, L. E., Higbie, J. M., Leslie, S. R., Vengalattore, M., and Stamper-Kurn, D. M., "Spontaneous symmetry breaking in a quenched ferromagnetic spinor Bose-Einstein condensate," *Nature*, vol. 443, pp. 312–315, 09

2006.

[149] Sanner, C., Su, E. J., Huang, W., Keshet, A., Gillen, J., and Ketterle, W., "Correlations and pair formation in a repulsively interacting Fermi gas," *Phys. Rev. Lett.*, vol. 108, p. 240404, Jun 2012.

[150] Santra, B., Baals, C., Labouvie, R., Bhattacherjee, A. B., Pelster, A., and Ott, H., "Measuring finite-range phase coherence in an optical lattice using Talbot interferometry," *Nature Communications*, vol. 8, p. 15601, 06 2017.

[151] Schwartz, C., "Theory of hyperfine structure," *Phys. Rev.*, vol. 97, pp. 380–395, Jan 1955.

[152] Schwartz, C., "Theory of hyperfine structure," *Phys. Rev.*, vol. 105, pp. 173–183, Jan 1957.

[153] Seo, S. W., Choi, J.-y., and Shin, Y.-i., "Free expansion of quasi-2D Bose-Einstein condensates with quantized vortices," *Journal of the Korean Physical Society*, vol. 64, pp. 53–57, Jan 2014.

[154] Sherson, J. F., Weitenberg, C., Endres, M., Cheneau, M., Bloch, I., and Kuhr, S., "Single-atom-resolved fluorescence imaging of an atomic Mott insulator," *Nature*, vol. 467, pp. 68–72, 09 2010.

[155] Simon, J., Bakr, W. S., Ma, R., Tai, M. E., Preiss, P. M., and Greiner, M., "Quantum simulation of antiferromagnetic spin chains in an optical lattice," *Nature*, vol. 472, pp. 307–312, 04 2011.

[156] Slama, S., von Cube, C., Ludewig, A., Kohler, M., Zimmermann, C., and Courteille, P. W., "Dimensional crossover in Bragg scattering from an optical lattice," *Phys. Rev. A*, vol. 72, p. 031402, Sep 2005.

[157] Söding, J., Guéry-Odelin, D., Desbiolles, P., Chevy, F., Inamori, H., and Dalibard, J., "Three-body decay of a rubidium Bose-Einstein condensate," *Applied Physics B*, vol. 69, no. 4, pp. 257–261, 1999.

[158] Spielman, I. B., "Raman processes and effective gauge potentials," *Phys. Rev. A*, vol. 79, p. 063613, Jun 2009.

[159] Stamper-Kurn, D. M. and Ueda, M., "Spinor Bose gases: symmetries, magnetism, and quantum dynamics," *Rev. Mod. Phys.*, vol. 85, pp. 1191–1244, Jul

2013.

[160] Stanescu, T. D. and Galitski, V., "Spin relaxation in a generic two-dimensional spin-orbit coupled system," *Phys. Rev. B*, vol. 75, p. 125307, Mar 2007.

[161] Starkey, P. T., Billington, C. J., Johnstone, S. P., Jasperse, M., Helmerson, K., Turner, L. D., and Anderson, R. P., "A scripted control system for autonomous hardware-timed experiments," *Review of Scientific Instruments*, vol. 84, no. 8, p. 085111, 2013.

[162] Steck, D. A., "Rubidium 87 D line data." available online at http://steck.us/alkalidata/ (revision 2.1.5, 13 Jan 2015), 2001.

[163] Steck, D. A., "Quantum and atom optics." available online at http://steck.us/teaching (revision 0.12.0, 16 May 2017), 2007.

[164] Stenger, F., *Numerical Methods Based on Sinc and Analytic Functions*, vol. 20 of *Springer Series in Computational Mathematics*. New York: Springer-Verlag, 2002.

[165] Stenger, J., Inouye, S., Stamper-Kurn, D. M., Miesner, H. J., Chikkatur, A. P., and Ketterle, W., "Spin domains in ground-state Bose-Einstein condensates," *Nature*, vol. 396, pp. 345–348, 11 1998.

[166] Struck, J., Ölschläger, C., Le Targat, R., Soltan-Panahi, P., Eckardt, A., Lewenstein, M., Windpassinger, P., and Sengstock, K., "Quantum simulation of frustrated classical magnetism in triangular optical lattices," *Science*, vol. 333, no. 6045, pp. 996–999, 2011.

[167] Sueda, K., Miyaji, G., Miyanaga, N., and Nakatsuka, M., "Laguerre-Gaussian beam generated with a multilevel spiral phase plate for high intensity laser pulses," *Opt. Express*, vol. 12, pp. 3548–3553, Jul 2004.

[168] Talbot Esq. F.R.S., H., "LXXVI. Facts relating to optical science. No. IV," *The London, Edinburgh, and Dublin Philosophical Magazine and Journal of Science*, vol. 9, no. 56, pp. 401–407, 1836.

[169] Twersky, V., "Rayleigh scattering," *Appl. Opt.*, vol. 3, pp. 1150–1162, Oct 1964.

[170] van Kempen, E. G. M., Kokkelmans, S. J. J. M. F., Heinzen, D. J., and Verhaar, B. J., "Interisotope determination of ultracold rubidium interactions from three high-precision experiments," *Phys. Rev. Lett.*, vol. 88, p. 093201, Feb 2002.

[171] Vitanov, N. V., Halfmann, T., Shore, B. W., and Bergmann, K., "Laser-induced population transfer by adiabatic passage," *Annual Review of Physical Chemistry*, vol. 52, no. 1, pp. 763–809, 2001. PMID: 11326080.

[172] Wang, C., Gao, C., Jian, C.-M., and Zhai, H., "Spin-orbit coupled spinor Bose-Einstein condensates," *Phys. Rev. Lett.*, vol. 105, p. 160403, Oct 2010.

[173] Wang, P., Yu, Z.-Q., Fu, Z., Miao, J., Huang, L., Chai, S., Zhai, H., and Zhang, J., "Spin-orbit coupled degenerate Fermi gases," *Phys. Rev. Lett.*, vol. 109, p. 095301, Aug 2012.

[174] Weidemüller, M., Hemmerich, A., Görlitz, A., Esslinger, T., and Hänsch, T. W., "Bragg diffraction in an atomic lattice bound by light," *Phys. Rev. Lett.*, vol. 75, pp. 4583–4586, Dec 1995.

[175] Weitenberg, C., Schauss, P., Fukuhara, T., Cheneau, M., Endres, M., Bloch, I., and Kuhr, S., "Coherent light scattering from a two-dimensional Mott insulator," *Phys. Rev. Lett.*, vol. 106, p. 215301, May 2011.

[176] Weld, D. M., Medley, P., Miyake, H., Hucul, D., Pritchard, D. E., and Ketterle, W., "Spin gradient thermometry for ultracold atoms in optical lattices," *Phys. Rev. Lett.*, vol. 103, p. 245301, Dec 2009.

[177] Widera, A., Gerbier, F., Fölling, S., Gericke, T., Mandel, O., and Bloch, I., "Precision measurement of spin-dependent interaction strengths for spin-1 and spin-2 ^{87}Rb atoms," *New Journal of Physics*, vol. 8, no. 8, p. 152, 2006.

[178] Yu, Z.-Q., "Equation of state and phase transition in spin-orbit-coupled Bose gases at finite temperature: a perturbation approach," *Phys. Rev. A*, vol. 90, p. 053608, Nov 2014.

[179] Zener, C., "Non-adiabatic crossing of energy levels," *Proceedings of the Royal Society of London A: Mathematical, Physical and Engineering Sciences*, vol. 137, no. 833, pp. 696–702, 1932.

[180] Zhang, J.-Y., Ji, S.-C., Chen, Z., Zhang, L., Du, Z.-D., Yan, B., Pan, G.-S., Zhao, B., Deng, Y.-J., Zhai, H., Chen, S., and Pan, J.-W., "Collective dipole oscillations of a spin-orbit coupled Bose-Einstein condensate," *Phys. Rev. Lett.*, vol. 109, p. 115301, Sep 2012.

[181] Zhang, S.-S., Ye, J., and Liu, W.-M., "Itinerant magnetic phases and quantum Lifshitz transitions in a three-dimensional repulsively interacting Fermi gas with spin-orbit coupling," *Phys. Rev. B*, vol. 94, p. 115121, Sep 2016.

[182] Zurek, W. H., "Cosmological experiments in superfluid helium?," *Nature*, vol. 317, pp. 505–508, 10 1985.